Multiscale Computational Framework for Analysis and Design of Ultra-High Performance Concrete Structural Components and Systems

Rafic G. El-Helou

Dissertation submitted to the faculty of the
Virginia Polytechnic Institute and State University
in partial fulfillment of the requirements for the degree of

Doctor of Philosophy
in
Civil Engineering

Cristopher D. Moen, Chair
Gianluca Cusatis
Ioannis Koutromanos
Carin Roberts-Wollmann
Zachary C. Grasley

September 27, 2016
Blacksburg, Virginia

Keywords: Ultra-high performance concrete, Lattice discrete particle model, Continuum triaxial model, Material characterization, Structural analysis

Multiscale Computational Framework for Analysis and Design of Ultra-High Performance Concrete Structural Components and Systems

Rafic G. El-Helou

ABSTRACT (ACADEMIC)

This research develops and validates computational tools for the design and analysis of structural components and systems constructed with Ultra-High Performance Concrete (UHPC). The modeling strategy utilizes the Lattice Discrete Particle Model (LDPM) to represent UHPC material and structural member response, and extends a structural-level triaxial continuum constitutive law to account for the addition of discrete fibers. The approach is robust, general, and could be utilized by other researchers to expand the computational capability and simulate the behavior of different composite materials. The work described herein identifies the model material parameters by conducting a complete material characterization for UHPC, with and without fiber reinforcement, describing its behavior in unconfined compression, uniaxial tension, and fracture toughness. It characterizes the effect of fiber orientations, fiber-matrix interaction, and resolves the issue of multi-axial stress states on fiber pullout. The capabilities of the computational models are demonstrated by comparing the material test data that were not used in the parameter identification phase to numerical simulations to validate the models' predictive capabilities. These models offer a mechanics-based shortcut to UHPC analysis that can strategically support ongoing development of material and structural design codes and standards.

Multiscale Computational Framework for Analysis and Design of Ultra-High Performance Concrete Structural Components and Systems

Rafic G. El-Helou

ABSTRACT (PUBLIC)

This research develops and validates new computer-based methods to analyze and design civil infrastructure constructed with ultra-high performance concrete (UHPC), achieved when steel fibers are combined with a finely graded cement matrix. With superior performance characteristics in comparison to regular concrete, UHPC is studied herein for its strong potential to advance the durability, efficiency, and resiliency of new and existing infrastructure. The simulation-based methods are extensively verified with novel experiments that evaluate the material limits and failure modes when compressed, bent, or stretched, considering fiber volume and orientation. The computer-based tools can be used to realistically assess the structural performance of innovative UHPC applications in buildings, bridges, and tunnels under natural hazards, leading to surpassed levels of structural efficiency and resiliency across civil infrastructure.

To my family

for their endless love and unwavering support

Acknowledgments

Sincere thank you to my advisor Dr. Cris Moen for his patience, motivation, and mentorship. Thank you for choosing me to be your student, for encouraging me with my research, and for coaching me to grow as a critical thinker throughout the past four years. Most importantly, thank you for showing me that it is possible to have fun and keep a positive attitude while handling the pressures of professional commitments. My deepest appreciation also goes to Dr. Gianluca Cusatis for his continuous support, help, and guidance. Thank you for giving me the opportunity to work closely with you and your research team, for turning my three-month research visit at Northwestern University into such a stimulating, rewarding, and memorable experience. A special thank you to Dr. Ioannis Koutromanos for his guidance and support. It has been a pleasure learning from you about continuum modeling and I thank you for all the time and support you invested in me. Thank you to Dr. Carin Roberts-Wollmann and Dr. Zachary Grasley for their advice on my research and career aspirations. Thank you for sharing your own experiences and carving out the best pathways to move forward in my research. To my dear friend Lindy Cranwell, thank you for helping me navigate the world of international student administration.

I would like to thank Dr. David Mokarem, Mac McCord, Brett Farmer, and Dennis Huffman for their continuous help with the UHPC experimental testing. Special thanks goes to Dr. Mokarem for the supportive assistance, guidance, and the many laughs! I sincerely appreciate Dr. Erol Lale's support with LDPM modeling and the friendship we've formed as a result of our close collaboration. Thank you to Dr. Kacie D'Alessandro for the insightful discussion on UHPC material testing. I would also like to thank Dr. Benjamin Graybeal and Dr. Luis Felipe Maya Duque for sharing their expertise on UHPC tension testing.

The experimental portion of this work could not have been possible without the help of my fellow comrades in the IGT research group at Virginia Tech: Valerie Black, Tommy

Dacanay, Rachel Gordon, and Evan May, thank you for keeping me sane and filling my last four years with fun and laughter. I will miss cleaning those concrete molds with you while blasting Wagon Wheel at the lab on Saturday morning!

A heartfelt thank you to my parents, Gerges and Norma, my sister and brother-in-law, Amale and Wissam, for their steadfast support and love throughout my life, and to whom I dedicate this work. My deepest gratitude goes to my wonderful Sandy, for being present in my times of need, for her complete confidence in me, and for her unconditional love and patience.

Last but not least, thank you to all my friends at Virginia Tech, especially Dr. David Padilla and Fannie Tao. I am grateful for the strong friendship that I have formed with y'all and that will last us a lifetime.

Go Hokies!

Funding Support

This study is based upon work supported by the National Science Foundation under Grant No. 1201087 to Virginia Tech with subcontract to Northwestern University, and by the Qatar National Research Fund under NPRP No. 7-1518-2-547 to Virginia Tech. The concrete was donated by LaFarge Ductal®. Any opinions, findings, and conclusions or recommendations expressed in this material are those of the authors and do not necessarily reflect the views of the sponsors.

Contents

List of Figures

List of Tables

Chapter 1

Research Vision

Ultra-High Performance Concrete (UHPC) is an emerging class of cementitious composites with superior performance characteristics compared to conventional concrete, achieved when discrete steel fibers are combined with optimized particle densities of cement, silica fume, fine sand, and water. The discrete fibers improve the composite's durability and ductility by providing resistance to tensile stresses, bridging crack surfaces, and limiting crack propagation (Lin and Li, 1997; Li et al., 1998; Li, 2003; Lepech and Li, 2009; Bencardino et al., 2010; Wille et al., 2010; Wille and Naaman, 2012). UHPC is generally characterized by a minimum compressive strength of 150 MPa, with a sustained post-cracking tensile strength exceeding 5 MPa, and enhanced durability, resulting from the elimination of interconnected pores that transmit water and chloride into the material internal structure (Graybeal, 2014). These superior mechanical and durability properties are unlocking innovative design concepts for engineers with design-life and efficiencies several orders of magnitude greater than conventional concrete construction, even in extremely corrosive environmental conditions. Several proof-of-concept studies and structural applications were initiated by the government and industry for broader implementation of UHPC across civil infrastructure. However, these efforts are taking time to catalyze, largely because structural design guidelines and computational tools for analyzing UHPC structural components are yet to be developed.

1.1 Research objectives

The goal of this research work is to develop validated computational modeling tools for analysis and design of structural components and systems constructed with UHPC. These tools could be utilized to develop innovative design concepts and structural applications, that optimize material use and efficiently take advantage of its enhanced mechanical properties. Virtual experiments covering a large number of parameters that are difficult to produce experimentally could be conducted, offering a mechanics-based shortcut to UHPC analysis that can strategically support ongoing development of material and structural design codes and standards.

The modeling strategy utilizes the existing Lattice Discrete Particle Model (LDPM) to represent UHPC material and structural member response. The LDPM is a mesoscale discrete computational framework that can realistically simulate all aspects of concrete response including discrete cracking, aggregate size, and effect of fiber reinforcement (Cusatis et al., 2011a; Schauffert and Cusatis, 2012). This framework was chosen for this study for its distinctive ability to predict concrete failure mode, including the development of multiple crack planes in fiber-reinforced composites. To simulate the behavior of large-scale structural systems made with UHPC, the macroscopic triaxial continuum constitutive law, developed by Moharrami and Koutromanos (2016), is extended to account for the effect of fibers. The newly developed formulation is calibrated and validated to capture UHPC material behavior and mechanical properties.

Predictive structural-scale concrete computational simulations rely on careful material characterization that captures the material behavior in compression, tension, fracture, and fiber-matrix interaction. The research described herein contributes to this characterization by conducting a set of experimental tests including unconfined compression, direct tension, split cylinder, fracture toughness, and single fiber pullout tests. The investigated variables include fiber volume in the matrix, fiber orientation, and confinement pressure in fiber pullout tests. Material test data that were not used in the parameter identification phase are compared to numerical simulations to validate the models' predictive capabilities.

1.2 Original contributions

This research effort documents a complete material characterization for UHPC, without and with fiber reinforcement, describing its behavior in unconfined compression, tension, and fracture. It provides insights on the fiber-matrix interaction and resolves the issue of multi-axial stress states on fiber pullout. The work couples the material tests with robust and general state-of-the-art computational techniques, that could be utilized by other researchers to expand their computational capability and simulate the behavior of different composite materials. The models can accept both discrete and continuum based material laws to simulate structural response at the level of detail required for a certain UHPC application and at a reasonable computational cost. Particularly for UHPC, the mesoscale input parameters of the lattice discrete particle model are obtained and validated against experimental data; they could be used to simulate the behavior of UHPC structural components and to predict the effect of fiber content and orientation on the failure mode and crack network. Moreover, a macroscopic continuum smeared-crack approach is developed, as an extension of a parent concrete model, to account for the addition of fibers in the matrix. The newly developed model input parameters are identified and validated to capture UHPC intrinsic properties and material behavior, which will be used in the near future to predict the behavior of large-scale structural systems made with UHPC.

1.3 Dissertation organization

The research progression starts in Chapter 2 with an overview of the existing numerical methods used to simulate cement composites. Chapter 3 summarizes the formulation of the lattice discrete particle model (LDPM), and discusses its adopted modeling techniques for UHPC. Chapter 4 briefly describes the formulation of an existing triaxial continuum model for concrete, and extends it with an original formulation to account for the effect of fibers. Chapter 5 presents the material characterization experimental program conducted for this research, and describes the UHPC mixing, placing, and curing procedures. Chapter 6 documents the unconfined compression behavior of UHPC including the linear, non-linear, peak, and post-peak portions of the stress-strain response. Chapter 7 characterizes the basic behaviors of individual cracks in UHPC through a set of three point bending tests performed on notched beams. Chapter 8 examines the direct and indirect tension behavior of UHPC

including the effect of fiber content and orientations. Chapter 9 describes the interfacial properties between fibers and the surrounding UHPC matrix including the effect of mutli-axial stress states on fiber pullout. The experimental results, presented in Chapters 6-9, are utilized in Chapter 10 to identify the LDPM mesoscale material input parameters and validate its predictive capabilities. Chapter 11 lays out the calibration procedure for the continuum model material parameters and verifies the capability of the model to simulate the behavior of UHPC with and without fiber reinforcement. Chapter 12 summarizes the major findings of this work and provides recommendations for future research.

Chapter 2

Computational Models to Simulate Cement-Based Composites Behavior

Cement-based composites, such as concrete, are complex multiscale materials whose behavior at the engineering scale is strongly dependent on the heterogeneity of their internal structure. Failure of concrete structures are generally the consequence of the development and propagation of a crack network that deteriorates the material's intrinsic ability to withstand service loads. Therefore, it is imperative that any predictive simulation model accurately predicts concrete internal fracture mechanisms and their influence on its macroscopic response.

There are six different scales of observation at which concrete internal fracture processes can be modeled (Cusatis et al., 2006; Lewis-Smith, 2014). The smallest is the atomistic scale, where the micro-crystalline particles of hydrated cement are simulated. Nano-scale (10^{-9} m) models are next, where the hardened cement gel with pores few nanometers in width (fully or partially filled with water) are modeled. Micro-scale (10^{-6} m) models simulate the cement paste containing cement gel and capillary pores (comprised of liquid water and water vapor). At the mini-scale (10^{-3} m), concrete is modeled as a three-phase material composed of cement paste, aggregate particles, and a thin layer of weak hydrated cement surrounding the aggregates, entitled the interfacial transition zone (ITZ) (Tregger et al., 2006). At the mesoscale (10^{-2} m), concrete is considered as a two phase material in which stiffer aggregate pieces are embedded in a weaker mortar matrix (Cusatis et al., 2014). Finally, macroscale (10^{-1} m) models, also known as plain concrete models, treat concrete as a homogeneous

continuum.

The choice of concrete numerical modeling approach depends on its ability to predict concrete behavior and failure modes at the level of detail required for a particular structural application. A brief overview of the two main trends to study fracture of quasi-brittle materials like concrete is briefly discussed in sections 2.1 and 2.2, namely continuum based models and discrete models. Notable contributions to capture the effect of fiber reinforcing in concrete computational models are highlighted in section 2.3.

2.1 Discrete fracture models

Discrete models provide a detailed representation of concrete's internal heterogeneity by discretizing its internal structure using discrete approaches (i.e. lattice and particle models). These methods were developed in search for accurate prediction of quasi-brittle materials ultimate strength, inelastic response, softening behavior, and micro-cracking zone spread after fracture initiation.

2.1.1 Lattice models

Lattice models, first proposed by Hrennikoff in 1941, represent the material by a network of lattices, or trusses, following the truss analogy. Motivated by Von Mises' criterion and Cosserat theory, square lattice models were developed by Herrmann et al. in 1989 to simulate fracture of metals. The model was later modified and applied to concrete fracture mechanics by a number of researchers (Bažant, 1990; Herrmann, 1990; Schlangen and van Mier, 1992; Schlangen and Garboczi, 1997). Concrete lattice models use triangular lattice network (Fig. 2.1) to simulate concrete heterogeneity using a fuller grading curve where the lattices are assumed to fail when the axial stress reaches concrete's tensile strength (Arslan et al., 2002). Such models were effective in capturing the crack patterns but often resulted in unexpected load-displacement curves. To overcome this problem, several updates were later developed (Jirásek and Bažant, 1994a,b) including the introduction of tensile softening and shear lattices. Notable contributions are the development of irregular random lattice systems through Voronoi tessellation (Bolander Jr. et al., 1996; Bolander Jr. and Saito, 1998), and the confinement-shear lattice (CSL) using Delaunay triangulation (Cusatis et al., 2006; Cusatis and Nakamura, 2011), which successfully replicated concrete's tensile and cohesive

fracture, softening, hardening, and size effect.

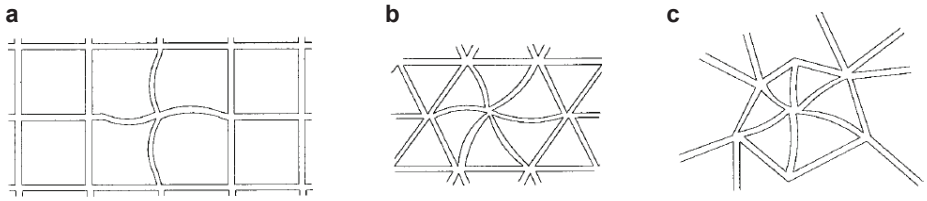

Figure 2.1: Lattice types: a) square lattice, b) triangular lattice, c) random lattice (Arslan et al., 2002). Under fair use 2016.

2.1.2 Particle models

The first particle model, known as distinct element method (DEM), was introduced by Cundall in 1971, to simulate the behavior of loose granular solids. In this method, the material's internal structure is represented by assemblies of discs or spheres. The motion of these particles, which interact with each other by contact, is modeled (Cundall and Strack, 1979). Inspired by the Cundall's theory and others (Cundall, 1971; Cundall and Strack, 1979), Zubelewicz and Bazant (1987) modeled concrete in two dimensions as a system of perfectly rigid circular particles of various sizes that interact at interfaces following a force-displacement relationship for normal and tangential components (Fig. 2.2).

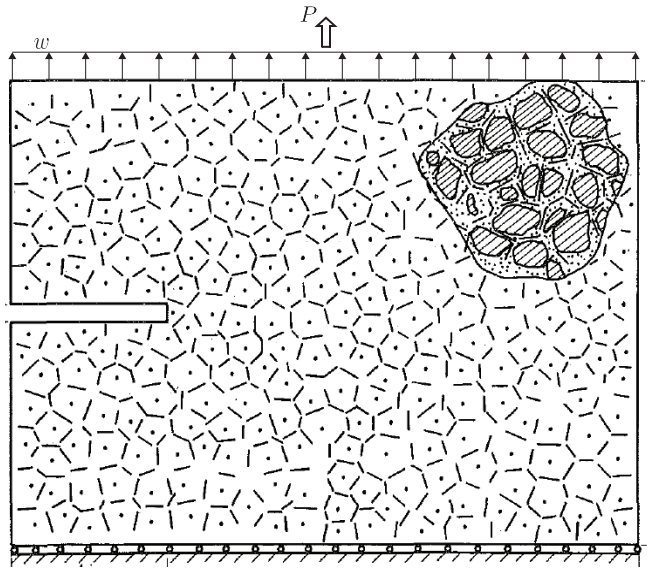

Figure 2.2: Fracture specimen consisting of an array of rigid particles and their interfaces (Zubelewicz and Bažant, 1987). Under fair use 2016.

Recent publications proposed modeling concrete's internal structure and heterogeneity through atomistic, molecular systems, and mini-scale models (Cusatis et al., 2006; Schlangen and van Mier, 1992; Arslan et al., 2002; Bolander Jr. et al., 1996; Caballero et al., 2006; Yip et al., 2006). Miniscale models describe concrete as three-phase material composed of cement paste, aggregate, and interfacial transitional zone. These models capture concrete cracks, simulate localized cracking behavior, and reproduce fracture propagation. However, they are computationally intensive especially for three dimensional modeling.

To reduce computational costs associated with numerical discretization, mesoscale models have been introduced (Cusatis et al., 2006; Bažant et al., 1990; Cusatis et al., 2003a,b). Mesoscale models simulate the basic material components of concrete, aggregate pieces and their surrounding layer of mortar, by discrete elements which are themselves not discretized on a finer scale. Such discretization reduces the size of numerical problems and captures the fundamental aspects of concrete heterogeneity. For this reason, the mesoscale Lattice Discrete Particle Model (LDPM) formulated, calibrated, and validated by Cusatis and coworkers (Cusatis et al., 2011a) was selected in this study to simulate the behavior of UHPC without fibers. A detailed description of the model constitutive law is provided in Chapter 3.

2.2 Continuum based models

In a continuum model, the nonlinear mechanical properties of concrete are represented by mathematical constitutive models within the framework of continuum mechanics. Continuum models significantly reduce the computational cost associated with finer scale models making them desirable for the simulation of large-scale structural components and systems, where a detailed representation of concrete's internal structure is not required. Numerous approaches have been developed that utilize this concept. For example, damage continuum models do not reproduce concrete cracks but considers their effect through a degradation of the material elastic properties. This section discusses the smeared crack and embedded discontinuity approaches.

2.2.1 Smeared crack models

Smeared crack models are based on the idea that the heterogeneity of concrete and the presence of steel reinforcement induce small cracks that later develop to larger or more dominant ones during the loading process. The cracks are not individually replicated but smeared over the continuum (Borst et al., 2004). In a one dimensional setting, the total strain is separated into two components, the elastic strain, ε^e, and the crack strain, ε^c, which represented the deformation due to crack opening (Fig. 2.3). The strain decomposition is written as follows: $\varepsilon = \varepsilon^e + \varepsilon^c$. It is assumed that no stress is developed from the crack strain and thus the stress transmitted is: $\sigma = E\varepsilon^e$. The crack strains develop when the tensile stress exceeds the tensile strength of the material. A constitutive law governing the stress evolution is typically determined experimentally as a function of the crack strain ε^c: $\sigma = f(\varepsilon^c)$ (Jirásek, 2011). The original smeared crack model was proposed by Rashid in 1968. Several researchers have updated the theory to address several issues such as the divergence of the results with mesh refinement leading to the incorporation of fracture energy criterion instead of strength based fracture criterion (Hillerborg et al., 1976; Bažant and Oh, 1983). In a triaxial state of stresses, strain softening tensorial constitutive equations have been developed (Bićanić and Pearce, 1996; Comi and Perego, 2001; Grassl and Jirásek, 2006; Mazars and Pijaudier Cabot, 1989) including the micro-plane theory (Bažant et al., 2000; Di Luzio and Cusatis, 2013; Caner and Bažant, 2013; Ožbolt et al., 2001; Luzio, 2007). However, these types of models cannot represent local fracture as they suffer from mesh sensitivity and spurious energy dissipation upon mesh refinement (Lewis-Smith, 2014; Bažant and Planas, 1997; Cedolin and Bažant, 1980; De Borst et al., 1993).

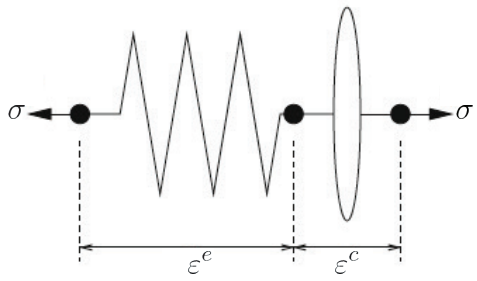

Figure 2.3: Schematic representation of smeared-crack approach as an elastic unit coupled in series with a crack unit (Jirásek, 2011). Under fair use 2016.

2.2.2 Embedded discontinuity models

To account for the development of strong discontinuities or cracks in concrete, several meshing methods are sometimes employed (Belytschko et al., 2014). One method is to predefine a failure surface and use boundary elements along that surface. However, predefining a failure surface is not practical as it means knowing the failure mode beforehand. Another method is to iteratively regenerate the mesh to account for the discontinuity growth. Mesh regeneration adds significant computational burden especially for large complex models. One could also delete the elements along the crack but this can also be problematic as the internal energies of the other elements must be adjusted to account for what is lost with the deleted elements. In addition, all of these methods are mesh dependent.

The embedded discontinuity approach (EDA) is envisioned as a combination of fracture and continuum mechanics and accounts for many problems associated with meshing techniques. The method was introduced by Ortiz et al. (1987) and captures the localized bands of intense straining in a material. At the onset of localization, the EDA set up additional shape functions within the isoparametric elements to closely reproduce the deformation patterns. Huespe and Oliver (2011) describe the fracture process zone (FPZ) as a progression of four stages (Fig. 2.4). First, the material exhibits a stable response and becomes nonlinear. Weak discontinuities are detected when the strain localizes into a band of finite width. When the width of strain localization becomes zero (i.e. a surface is formed), strong discontinuities are detected but cohesive forces remain (i.e. crack is closed). A stress-free zone is formed when the cohesive forces become zero generating a strong discontinuity. The EDA includes the strong discontinuity approach (SDA), the embedded finite element method (EFEM), the extended finite element approach (XFEM), and the enhanced strain method (EAS) (Belytschko et al., 2014; Oliver et al., 2006; Sancho et al., 2007). However, these models suffer from conceptual complexity and are not able to capture the effect of random localized effects induced by the heterogeneity of concrete's internal structure.

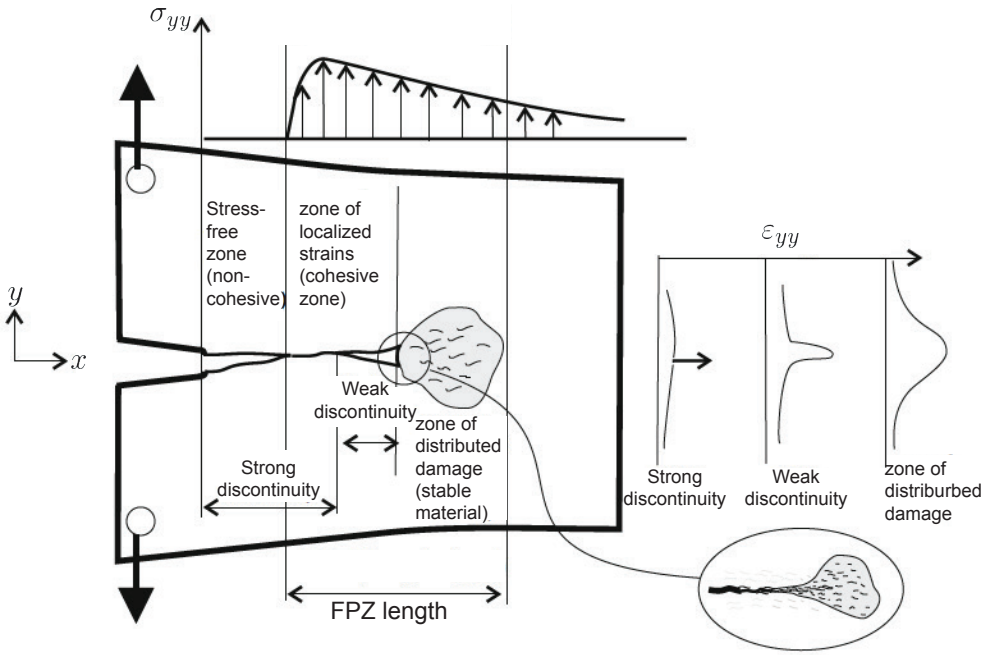

Figure 2.4: Phenomenological description of a quasi-brittle fracture process (Huespe and Oliver, 2011). Under fair use 2016.

Recent efforts by Moharrami and Koutromanos (2016) formulated, calibrated, and validated a triaxial continuum model for the analysis of concrete under multiaxial cyclic loading conditions. The formulation is based on an elastoplastic formulation, to capture compression-dominated behavior, with a rotating smeared-crack approach, to capture tension-dominated behavior. This approach resolves the issues existing with many available models to properly capture the crack opening and closing behavior and accounts for the effect of confinement on the strength and ductility under compression-dominated stress states. For this reason, this model was selected in this research to model large-scale structural UHPC components and systems. A detailed description of the triaxial continuum model formulation by Moharrami and Koutromanos (2016) is presented in Chapter 4.

2.3 Fiber-reinforced concrete models

Several researchers have extended their concrete numerical models to account for the effect of fiber reinforcing on the macroscopic behavior of concrete. Fibers transfer load between crack surfaces providing resistance to crack initiation and propagation (Cunha et al., 2009).

The crack-bridging mechanism is governed by the interfacial bond load-slip response as the fibers crossing a crack are pulled out of the cement matrix. Increases in the fiber-matrix bond strength lead to smaller crack openings and allow the composite to undergo multiple cracking (Lin and Li, 1997). This behavior increases the failure strain, fracture toughness, and tensile strength of the composite, providing residual strength and resistance to chemical attacks and penetration (Li et al., 1998; Lepech and Li, 2009; Wille and Naaman, 2012; Belletti et al., 2008; Naaman and Najm, 1991).

To simulate fiber-matrix interaction, Yang et al. (2008) developed a fiber crack bridging micromechanical model utilizing earlier studies by many, first introduced by Lin et al. (1999). A number of researchers incorporated this crack-bridging model to simulate the physical phenomena at the interface between fibers and the concrete matrix. For instance, Schauffert and Cusatis (2012) incorporated the fiber-bridging model by Yang et al. (2008) to extend the LDPM formulation to incorporate the effect of discrete short straight fiber reinforcement on concrete behavior. The LDPM generates all fibers occupying a volume and overlaps the fiber system with the lattice system. The approach is validated to predict the effect of fiber content and orientation on the macroscopic behavior of concrete and therefore, it was chosen in this research to model UHPC with fiber reinforcement. A complete summary of the LDPM formulation for fiber reinforcement is provided in Chapter 3.

Another approach to account for the fiber-matrix interaction in discrete formulations is developed by Bolander et al. (2009). The fibers in this approach are represented by a rigid body spring network that is overlapped with a Voronoi discretization of the cement matrix to simulate tensile fracturing as shown in Fig. 2.5.

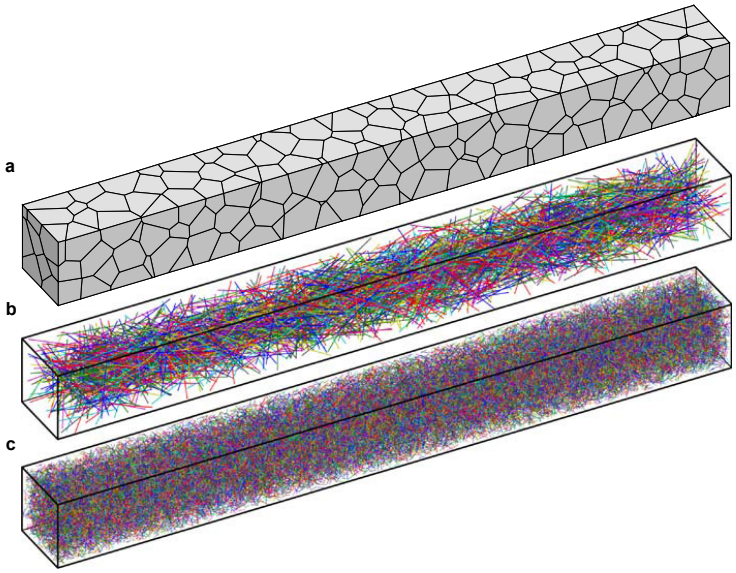

Figure 2.5: Fiber modeling by a rigid body spring network: a) Voronoi discretization of tension prism, b) macro-fiber inclusions, and c) micro-fiber inclusions (Bolander et al., 2009). Under fair use 2016.

In the realm of continuum modeling, Kabele (2007) presented a multiscale finite element approach capable of simulating multiple closely spaced cracks. His method is based on the concept of spacial averaging, in which it is assumed that finer scale substructures, like fibers and cracks, are small enough to be represented by a spatially uniform constitutive law in the spacial element, entitled representative volume element (RVE). Radtke et al. (2010) also utilized Yang et al. (2008) crack-bridging approach to represent the fiber contribution in a two dimensional mesh. In this approach, concrete is represented by a uniform background mesh in which the regularized damage model is employed to simulate concrete cracks. Fibers are randomly distributed over the concrete area and are not related to the discretization of the background mesh. The fiber-matrix interaction is then implemented by applying the reaction forces from the fiber to the matrix at the vicinity of a crack as shown in Fig. 2.6. Cunha et. al. (2011) simulated the structural response of direct tension tests by random distribution of fibers over a continuum concrete mesh utilizing the smeared-crack approach. Beghini et al. (2007) extended the microplane model to include fiber-reinforcing by providing a separate traction law for fiber contribution coupled with concrete softening.

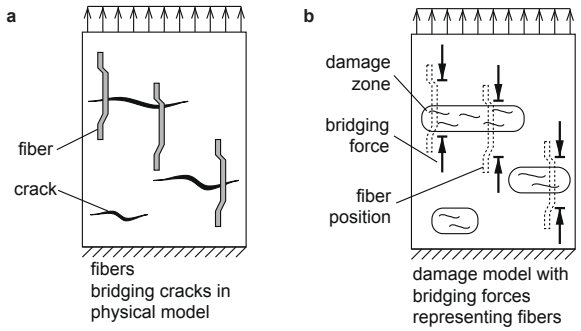

Figure 2.6: Fiber model in two dimensions: a) Fibers bridging cracks in physical model, and b) damage model with bridging forces representing fibers (Radtke et al., 2010). Under fair use 2016.

Chapter 3

Cement-Based Composites Fracture Modeling with the Lattice Discrete Particle Model

Based on the published work of Cusatis and coworkers (2011a; 2012), this chapter details the lattice discrete particle model (LDPM) formulation and its extension to include the effect of fiber reinforcement (LDPM-F). Section 3.1 investigates the underlying concepts and governing equations of the framework for concrete without and with fibers. Section 3.2 discusses the LDPM-based multi-scale techniques typically adopted with LDPM UHPC simulations. Finally, a summary of the mesoscale input parameters for UHPC is provided in section 3.3.

3.1 Lattice discrete particle model formulation for UHPC

The LDPM simulates concrete as a two-phase material composed of aggregate pieces held together by a cementitious matrix. Concrete behavior is captured through mesoscale constitutive equations where material failure is represented through fracture and cohesion under tension and tension-shear, compaction and pore collapse under compression, and friction from compression shear. The geometrical representation of the concrete mesostructure, the

LDPM constitutive law, and the fiber-matrix interaction law are detailed herein.

3.1.1 Geometrical representation of UHPC mesostructure

The LDPM geometry is characterized following a four-step procedure that defines the number and size of generated particles, particle position, interparticle connection, and facets, through which interparticle forces are transmitted. These facets represent weak locations in the material where potential cracks could initiate and propagate.

Particle generation

Particle generation is accomplished by approximating concrete coarse aggregates as spheres and utilizing Stroeven's (2000) particle size distribution (psd) function given in Eq. 3.1 to generate particle diameters.

$$f(d) = \frac{q d_0^q}{[1 - (\frac{d_0}{d_a})^q] d^{q+1}}. \tag{3.1}$$

In Eq. 3.1, $f(d)$ is the incidence of a particle by its diameter d, q is a material parameter, d_a is the maximum particle size, and d_0 is the minimum particle size which governs the number of simulated particles. The psd can be interpreted as a probability density function (pdf) for the occurrence of a certain diameter d, computed in Eq. 3.2 as cumulative density function (cdf).

$$P(d) = \int_{d_0}^{d} f(d) dd = \frac{1 - (d_0/d)^q}{1 - (d_0/d_a)^q}. \tag{3.2}$$

As shown by Stroeven (2000), Eq. 3.1 is associated to a sieve curve (percent of aggregate by weight retained by sieve of characteristic size d) in the form:

$$F(d) = \left(\frac{d}{d_a}\right)^{n_F} \tag{3.3}$$

where $n_F = 3 - q$. The classical Fuller curve, which is extensively used for optimal packing of aggregates in concrete, correspond to $q = 2.5$ or $n_F = 0.5$ in Eq. 3.3 (Fig. 3.1a).

The particle number and size to be placed inside a volume of concrete, V, is calculated for a given cement content, c, water-to-cement ratio, w/c, d_a, and d_0 as detailed in Cusatis et al. (2011b). The aggregate volume fraction v_a can be taken as 1 − volume fraction of cement, water, and air. The volume fraction of simulated aggregates (dictated by the choice of d_0) is computed as $v_{a0} = [1 - F(d_0)]v_a$. The particle diameters are assigned by a random sampling of the cdf in Eq. 3.2 through a random particle number generator, i (i.e. $d = d_i$), and following a sequence of random numbers for $P_i(d_i)$ between 0 and 1. For each generated particle in the sequence, the total volume of generated particles is checked to make sure that the total volume of simulated aggregates $V_{a0} = v_{a0}V$ is not exceeded. The external surfaces of the volume are simulated with zero-diameter particles (nodes) which are added to the external vertexes, edges, and polyhedral faces forming the volume in consideration.

Particle position

Once particle generation is completed, the particles are randomly distributed over the volume of the specimen. The vertex nodes are placed first by a random distribution of the nodes on edges and surfaces of the volume using an optimized minimum routine to minimize geometrical bias. The centers of the LDPM particles are then positioned one by one, from largest to smallest, inside the specimen volume following the procedure by Bažant (1990) and Cusatis et al. (2003a) which ensures that the new particle does not overlap with a previously positioned particle (Fig. 3.1b).

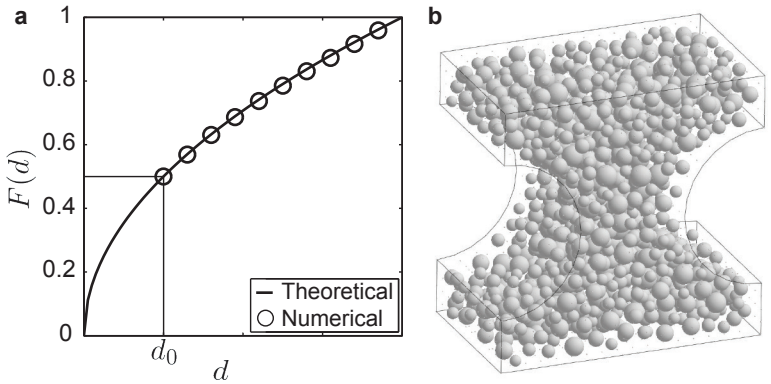

Figure 3.1: LDPM particle generation: a) Theoretical (solid line) and simulated (circles) sieve curves, and b) particle system (Cusatis et al., 2011a). Under fair use 2016.

Lattice system

The construction of the concrete mesostructure topology is defined by a Delaunay tetrahedralization (Delaunay, 1934; Barber et al., 1996). The nodal coordinates of the particle centers are connected by lattices creating a three-dimensional tetrahedra mesh that fill all the volume of the specimen as shown in Fig. 3.2.

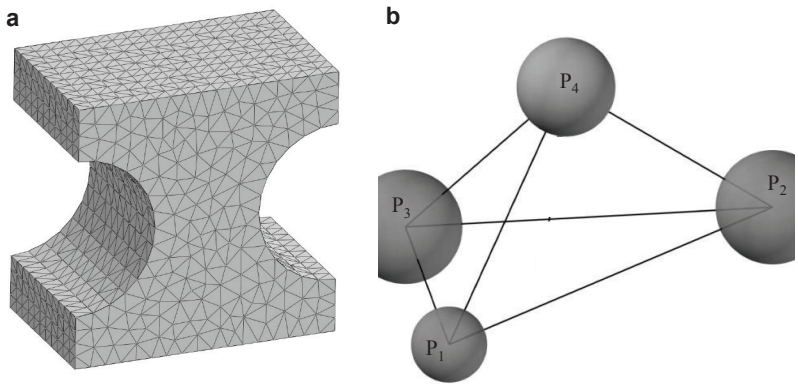

Figure 3.2: LDPM lattice system: a) Tetrahedralization of volume surfaces, and b) lattice system (Cusatis et al., 2011a). Under fair usė 2016.

Potential crack surfaces

In the LDPM formulation, cracks initiate and propagate in the concrete mortar and the aggregate pieces are assumed remain undamaged during the loading process. This is reflected by a three-dimensional tetrahedron tessellation which defines a set of triangular facets pertaining to each particle and forming a potential crack network. Each triangular facet is obtained by connecting three points namely: (1) an edge point, E, defined at midway of the clear distance between two particles on a lattice connection (Fig. 3.3a); (2) a face point, F, defined as the centroid of the triangle formed by the intermediate face points, F*, which are located midway of the clear distance (identified as straight line) between a particle center and opposite edge point E (Fig. 3.3b); and (3) a tet-point, T, defined as the centroid of the four intermediate points, T*, which are located midway of the clear distance (straight line) between a particle center and opposite face point, F (Fig. 3.3c). This tessalation results in the creation of twelve faces in each tetrahedron, six of which are pertaining to one of the four particle in the tetrahedron (Figs. 3.3d-e). The combination of these faces from all adjacent tetrahedra creates a system of polyhedral cells containing the particle as shown in Fig. 3.3f.

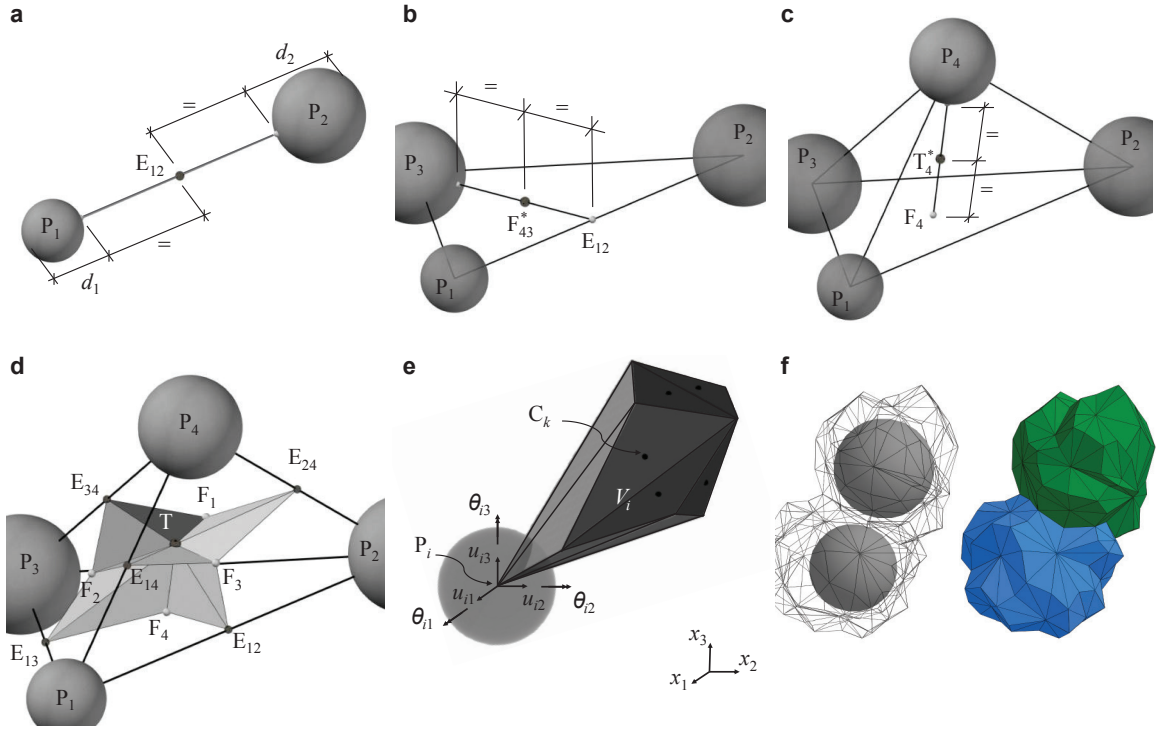

Figure 3.3: LDPM domain tesselation: a) Edge point E, b) intermediate face point F*, c) intermediate tet-point T*, d) tetrahedron tesselation, e) portion of a tetrahedron associated with a particle, and f) polyhedral cells for two adjacent particles (Cusatis et al., 2011a). Under fair use 2016.

3.1.2 LDPM constitutive law for UHPC without fibers

Each tetrahedron can be divided into four subdomains, V_i ($i = 1, ..., 4$), comprising of one particle, P_i, a portion of the three tetrahedron edges, and six triangular tessellation facets (Fig. 3.3e). Rigid body kinematics describe the displacement field in each subdomain, $\mathbf{u}(\mathbf{x})$, where $\mathbf{x} = [x_1, x_2, x_3]^T \in V_i$ (Eq. 3.4), and the displacement jump, $[\mathbf{u}_c]$, at the centroid of each facet (Eq. 3.5), where i and j refer to the two nodes adjacent to each facet. In Eq. 3.4, $\mathbf{u}_i$ is the translational degree of freedom, $\mathbf{u}_i = [u_{1i}, u_{2i}, u_{3i}]^T$, and rotational degree of freedom, $\theta_i = [\theta_{1i}, \theta_{2i}, \theta_{3i}]^T$, for particle i.

$$\mathbf{u}(\mathbf{x}) = \mathbf{u}_i + \theta_i \times (\mathbf{x} - \mathbf{x}_i). \tag{3.4}$$

$$\mathbf{u}_C = \mathbf{u}_{Cj} - \mathbf{u}_{Ci}. \tag{3.5}$$

The strain vector is defined as the displacement jump at the contact point divided by the interparticle clear distance, $\ell_e = \| \mathbf{x}_j - \mathbf{x}_i \|$. The constitutive law is formulated with reference to the projected facets into planes orthogonal to the lattices characterized by the unit vectors $\mathbf{n}$, $\mathbf{l}$, and $\mathbf{m}$. Such formulation adopts the classical tension-compression asymmetry of concrete behavior and avoids non-symmetric behavior under pure shear. The components of the strain vector (normal and shear) in a local system of reference are shown in Eq. 3.6 below:

$$\varepsilon_N = \frac{\mathbf{n}^T[\mathbf{u}_C]}{\ell_e};\ \varepsilon_M = \frac{\mathbf{m}^T[\mathbf{u}_C]}{\ell_e};\ \varepsilon_L = \frac{\mathbf{l}^T[\mathbf{u}_C]}{\ell_e}. \tag{3.6}$$

Equilibrium is imposed using the principle of virtual work by summing all the facet contributions and equating total internal and external work to obtain the discrete equilibrium equations of the LDPM formulation.

Elastic behavior

The elastic behavior is described by assuming that the normal and shear stresses are proportional to the corresponding strains:

$$\sigma_N = E_N\varepsilon_N;\ \sigma_M = E_T\varepsilon_M;\ \sigma_L = E_T\varepsilon_L \tag{3.7}$$

where $E_N = E_0$, $E_T = \alpha E_0$, in which E_0 is the effective normal modulus, and α is the shear-normal coupling parameter. The parameters E_0 and α are assumed to be material properties and are related to the macroscopic properties (modulus of elasticity, E, and Poisson's ratio, ν) in the elastic regime (for $\nu < 0.25$) as described below:

$$E_0 = \frac{1}{1-2\nu}E \ \Leftrightarrow\ E = \frac{2+3\alpha}{4+\alpha}E_0 \tag{3.8}$$

$$\alpha = \frac{1-4\nu}{1+\nu}E \ \Leftrightarrow\ \nu = \frac{1-\alpha}{4+\alpha}E_0. \tag{3.9}$$

Beyond the elastic regime, the inelastic behavior is represented by three physical mechanisms including fracture and cohesion under tension and tension-shear, pore collapse and compaction under compression, and frictional behavior due to compression-shear.

Fracture behavior

For tensile normal strains ($\varepsilon_N < 0$), the fracture and damage evolution is formulated in terms of the effective strain, ε, and effective stress, σ, given by:

$$\varepsilon = \sqrt{\varepsilon_N^2 + \alpha(\varepsilon_M^2 + \varepsilon_L^2)} \qquad \sigma = \sqrt{\sigma_N^2 + (\sigma_M^2 + \sigma_L^2)/\alpha}. \tag{3.10}$$

The normal and shear stresses are related to their corresponding strains through damage-type constitutive equations given by:

$$\sigma_N = \sigma\frac{\varepsilon_N}{\varepsilon}; \quad \sigma_M = \sigma\frac{\alpha\varepsilon_M}{\varepsilon}; \quad \sigma_L = \sigma\frac{\alpha\varepsilon_L}{\varepsilon}. \tag{3.11}$$

The effective stress is incrementally elastic, $\dot{\sigma} = E_0\dot{\varepsilon}$, and satisfies the inequality $0 \leq \sigma \leq \sigma_{bt}(\varepsilon, \omega)$, where ω is a coupling variable representing the interaction between shear and normal loading (Eq. 3.12), and $\sigma_{bt}(\varepsilon, \omega)$ is a limiting boundary defining the maximum effective strain (Eq. 3.13).

$$\tan(\omega) = \frac{\varepsilon_N}{\sqrt{\alpha}\varepsilon_T} = \frac{\sigma_N\sqrt{\alpha}}{\sigma_T}. \tag{3.12}$$

$$\sigma_{bt}(\varepsilon, \omega) = \sigma_0(\omega)\exp\left[-H_0(\omega)\frac{\langle\varepsilon_{max} - \varepsilon_0(\omega)\rangle}{\sigma_0(\omega)}\right]. \tag{3.13}$$

In Eqs. 3.12 and 3.13, $\varepsilon_T = \sqrt{\varepsilon_M^2 + \varepsilon_L^2}$ is the total shear strain, $\sigma_T = \sqrt{\sigma_M^2 + \sigma_L^2}$ is the total shear stress, $\varepsilon_{max} = \sqrt{\varepsilon_{N,max}^2 + \alpha\varepsilon_{T,max}^2}$ is the maximum effective strain formulated as a function of the maximum normal strain, $\varepsilon_{N,max}$, and total shear strain, $\varepsilon_{T,max}$, during the loading history. $\sigma_0(\omega)$ is the strength limit for the effective stress defined in Eq. 3.14, and $H_0(\omega)$ is the softening modulus which governs the exponential decay of the σ_{bt} beyond the elastic limit, $\varepsilon_0(\omega) = \sigma_0(\omega)/E_0$, formulated in Eq. 3.15. The brackets are used in Macaulay sense $\langle x\rangle = max\{x, 0\}$.

$$\sigma_0(\omega) = \sigma_t\frac{-\sin(\omega) + \sqrt{\sin^2(\omega) + 4\alpha\cos^2(\omega)/r_{st}^2}}{2\alpha\cos^2(\omega)/r_{st}^2}. \tag{3.14}$$

$$H_0(\omega) = H_t\left(\frac{2\omega}{\pi}\right)^{n_t}. \tag{3.15}$$

In Eq. 3.14, $r_{st} = \sigma_s/\sigma_t$ is the ratio between the shear strength (cohesion), σ_s, and the

tensile strength, σ_t. The term n_t in Eq. 3.15 defines the nature of the power function, and $H_t = 2E_0/(\ell_t/\ell - 1)$ gives the softening modulus in pure tension, where $\ell_t = 2E_0G_t/\sigma_t^2$ is tensile characteristic length, G_t is the meso-scale fracture energy, and ℓ is the length of the tetrahedron edge associated with the facet.

The unloading-reloading rules in LDPM are defined through the reloading strain limit, $\varepsilon_{tr} = k_t(\varepsilon_\ell - \sigma_{bt}/E_0)$, where k_t is a material parameter, and ε_ℓ is the strain at which the unloading occurred. During reloading, the effective strain, ε, remain zero until it reaches reloading strain limit, ε_{tr}, beyond which it becomes incrementally elastic.

Pore collapse

For compression normal strains ($\varepsilon_N < 0$), the normal stress, σ_N, is incrementally elastic, $\dot{\sigma}_N = E_{Nc}\dot{\varepsilon}_N$, and satisfies the inequality: $-\sigma_{bc}(\varepsilon_D, \varepsilon_V) \leq \sigma_N \leq 0$. E_{Nc} is the loading-unloading stiffness is equal to E_0 for $-\sigma_N < \sigma_{c0}$ and to E_d otherwise, where σ_{c0} and E_d are material parameters describing the mesoscale compression strength and the densified normal modulus, respectively.

The compressive boundary, $\sigma_{bc}(\varepsilon_D, \varepsilon_V)$, is a function of the volumetric strain, ε_D, and the deviatoric strain, ε_V, as described in Eq. 3.16. All of the facets in a tetrahedron are assumed to have the same volumetric strain, $\varepsilon_V = (V - V_0)/V_0$, where V_0 is the initial volume of the tetrahedron and V is its current volume. However, the deviatoric strain at each facet varies as follows: $\varepsilon_D = \varepsilon_N - \varepsilon_V$.

$$\sigma_{bc}(\varepsilon_D, \varepsilon_V) = \begin{cases} \sigma_{c0} & \text{if } -\varepsilon_{DV} \leq 0 \\ \sigma_{c0} + \langle -\varepsilon_{DV} - \varepsilon_{c0} \rangle H_c(r_{DV}) & \text{if } \varepsilon_{c0} \leq -\varepsilon_{DV} \leq \varepsilon_{c1} \\ \sigma_{c1}(r_{DV}) \exp\left[(-\varepsilon_{DV} - \varepsilon_{c1})H_c(r_{DV})/\sigma_{c1}(r_{DV})\right] & \text{otherwise} \end{cases} \quad (3.16)$$

In Eq. 3.16, $\varepsilon_{DV} = \varepsilon_V + \beta\varepsilon_D$ is the compaction strain, β is a material parameter, $\varepsilon_{c0} = \sigma_{c0}/E_0$ is the compaction strain right before pore collapse (elastic limit), $r_{DV} = \varepsilon_D/\varepsilon_V$ is the deviatoric-to-volumetric strain ratio, $\varepsilon_{c1} = \kappa_{c0}\varepsilon_{c0}$ is the compaction strain at which rehardening begins, κ_{c0} is a material parameter governing the onset of rehardening, $\sigma_{c1}(r_{DV}) = \sigma_{c0} + (\varepsilon_{c1} - \varepsilon_{c0})H_c(r_{DV})$, and $H_c(r_{DV})$ is the initial hardening modulus given as:

$$H_c(r_{DV}) = \frac{H_{c0}}{1 + \kappa_{c2}\langle r_{DV} - \kappa_{c1} \rangle} \quad (3.17)$$

where H_{c0}, κ_{c1}, κ_{c2} are material parameters.

The above formulation mathematically represent pore collapse and yielding by a constant upper limit for the compressive boundary, σ_{bc}, within the elastic range ($-\varepsilon_{DV} < \varepsilon_{c0}$), beyond which σ_{bc} linearly evolve until the volumetric strain limit, ε_{c1}, is reached. For values of ε_{DV} greater than ε_{c1}, the compaction and rehardening of the material are modeled by an exponential evolution of σ_{bc}, and by ensuring that the hardening modulus $H_c(r_{DV})$ tends to zero with increasing r_{DV} so that the experimentally observed plateau for lateral confinement is captured.

Frictional behavior

To simulate the increases in shear strength due to the frictional effects under compressive loading, the classical incremental plasticity is used (Drucker and Prager, 1952). The incremental increases of the shear stresses are calculated using the plastic strain increments, $\dot{\varepsilon}^p_M = \dot{\lambda}\partial\varphi/\partial\sigma_M$ and $\dot{\varepsilon}^p_L = \dot{\lambda}\partial\varphi/\partial\sigma_L$, as follows: $\dot{\sigma}_M = E_T(\dot{\varepsilon}_M - \dot{\varepsilon}^p_M)$ and $\dot{\sigma}_L = E_T(\dot{\varepsilon}_L - \dot{\varepsilon}^p_L)$. λ is a plastic multiplier, and $\varphi = \sqrt{\sigma^2_M + \sigma^2_L} - \sigma_{bs}(\sigma_N)$ is the plastic potential, where σ_{bs} is the shear strength formulated as follows:

$$\sigma_{bs}(\sigma_N) = \sigma_s - \mu_\infty\sigma_N + \sigma_{N0}(\mu_0 - \mu_\infty)\left[1 - \exp\left(\sigma_N/\sigma_{N0}\right)\right] \tag{3.18}$$

where σ_{N0} is the normal stress at which the internal friction coefficients transition from the initial value, μ_0, to the final value, μ_∞. Finally, the loading-unloading for shear stress evolution are expressed through the following conditions: $\varphi\dot{\lambda} \leq 0$ and $\dot{\lambda} \geq 0$.

3.1.3 LDPM constitutive law for fiber-reinforcement

Schauffert and Cusatis (2012) extended the LDPM formulation to incorporate the effect of discrete short circular straight fiber reinforcement on concrete behavior. The LDPM fiber formulation, entitled LDPM-F, retains the discrete nature of the model by generating all the fibers in a given concrete volume, V, and overlapping it with the cell system of the LDPM mesostructure. The number of fibers, $N_f = INT\left[4v_fV/(\pi d^2_f A_f)\right]$, is first calculated and each generated fiber is then inserted into the LDPM geometry with random position, and arbitrary or preferred orientation. v_f is the fiber volume fraction, d_f is the diameter of individual fibers, and $A_f = \pi d^2_f/4$ is the cross-sectional area of the individual fibers. The

intersection of the generated fibers with the LDPM facets are determined as shown in Fig. 3.4, where the shorter and longer fiber lengths on each side of the facet-fiber intersection are denoted by L_s and L_l. The fiber orientation is characterized by a unit vector $\mathbf{n}_f$.

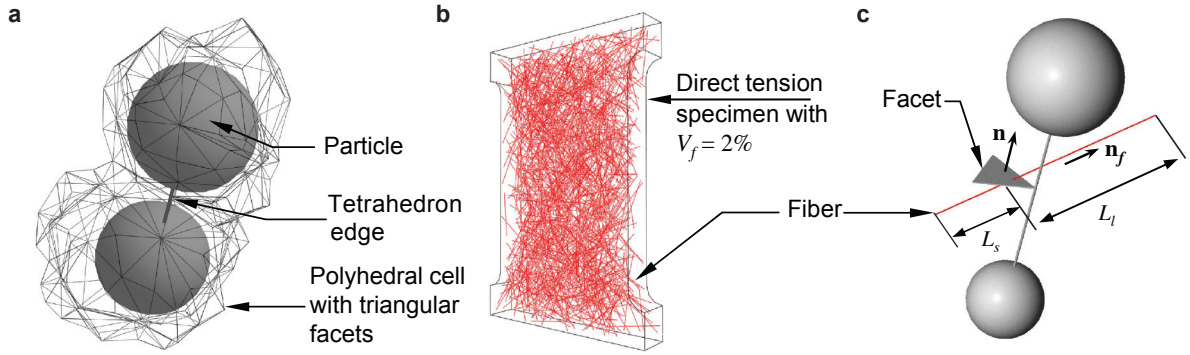

Figure 3.4: LDPM fiber generation: a) Two adjacent cells, b) specimen with random fiber content, and c) facet with intersecting fiber (Schauffert and Cusatis, 2012). Under fair use 2016.

The total stress on each LDPM facet, σ, is computed by adding the force contribution of each fiber crossing a facet, P_f, to the facet stress, σ_c, as follows:

$$\sigma = \sigma_c + \frac{1}{A_c} \sum_{f \in A_c} P_f \tag{3.19}$$

where, $\sigma_c = \sigma_N \mathbf{n} + \sigma_M \mathbf{m} + \sigma_L \mathbf{l}$, and A_c is the facet area.

The crack-bridging force for each fiber crossing a given facet, $P_f = P_f(w)$, is a function of the mesoscale crack opening, $\mathbf{w}$, which starts when the facet strains exceed the tensile elastic limit and is calculated below:

$$\mathbf{w} = \omega_N \mathbf{n} + \omega_M \mathbf{m} + \omega_L \mathbf{l} \tag{3.20}$$

where $\omega_N = \ell_e(\varepsilon_N - \sigma_N/E_N)$, $\omega_M = \ell_e(\varepsilon_M - \sigma_M/E_T)$, and $\omega_L = \ell_e(\varepsilon_L - \sigma_L/E_T)$.

The fiber-matrix analysis is analyzed independent of the LDPM mesoscale framework using the semi-empirical analytical formulation of Yang et al. (2008) which assumes that the fibers are initially straight, elastic, and have negligible bending stiffness.

Debonding and frictional slip

The overall pullout behavior is typically represented by a relationship between the pullout load, P_f, and slippage, υ, between the fiber and the matrix as shown in Fig. 3.5. The load-slip ($P_f - \upsilon$) is characterized by a debonding stage at which the pullout load, P_f, increases until reaching a reaching a maximum load, after which a load drop occurs (Fig. 3.5). The load drop indicates the transition from both chemical and frictional controlled debonding to frictional bond only, and would not occur if the interface has no initial chemical bond (Lin et al., 1999; Kim et al., 2008; Robins et al., 2002; Sujivorakul, 2002). After debonding, and depending on the matrix packing density and fiber surface properties (Wille et al., 2010; Wille and Naaman, 2012; Naaman and Najm, 1991; Orange et al., 1999; Sugama et al., 1992; Stengel, 2009), the frictional pullout load, P_f, decreases or increases with increasing slip, υ. For example, straight steel fibers embedded in normal strength concrete exhibit a linear decrease in pullout load or slip-softening frictional behavior (Naaman and Najm, 1991). In contrast, a slip-hardening behavior is generally observed when the particle packing density of the cementitious composite is enhanced (Wille et al., 2010).

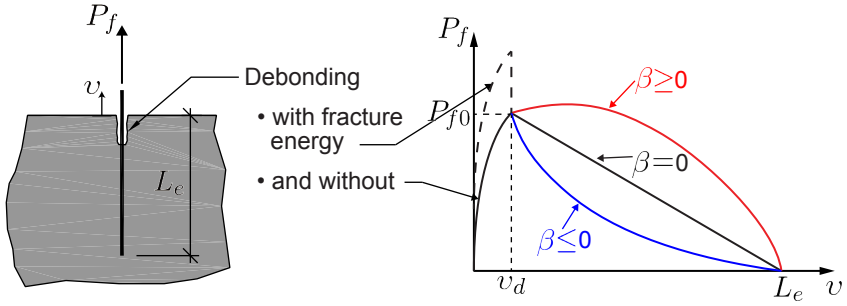

Figure 3.5: Typical pullout load versus slippage ($P_f - \upsilon$) relationship (Schauffert and Cusatis, 2012). Under fair use 2016.

The fiber-matrix interaction law in LDPM formulates the load-slip ($P - \upsilon$) relation considering combined chemical bonding, expressed in terms of bond fracture energy, G_d, and frictional bonding, expressed in terms of frictional stress, τ_0. Following Lin et al. (1999), the slippage, υ, has a critical value, υ_d, marking the end of the debonding stage, given by:

$$\upsilon_d = \frac{2\tau_0 L_e^2}{E_f d_f} + \left(\frac{8 G_d L_e^2}{E_f d_f}\right)^{1/2} \tag{3.21}$$

where L_e, E_f, and d_f represent the fiber embedded length, modulus of elasticity, and

diameter, respectively. Before debonding ($\upsilon < \upsilon_d$), the fiber resistance is formulated as shown:

$$P_f(\upsilon) = \left[\frac{\pi^2 E_f d_f^3}{2}\left(\tau_0 \upsilon + G_d\right)\right]^{1/2} \tag{3.22}$$

and after debonding ($\upsilon > \upsilon_d$), it is given as:

$$P_f(\upsilon) = P_{f0}\left(1 - \frac{\upsilon - \upsilon_d}{L_e}\right)\left[1 + \beta\frac{(\upsilon - \upsilon_d)}{d_f}\right] \tag{3.23}$$

where $P_{f0} = \pi L_e d_f \tau_0$ is the initial frictional force, and β is the interfacial friction coefficient, governing the behavior of the friction pullout stage. The interfacial friction coefficient, β, can take values of $0, > 0$, or < 0, if the interfacial friction does not depend on slippage, or if it increases or decreases with slippage, respectively (Fig. 3.5).

Matrix spalling

In the two-way fiber pullout model adopted in the LDPM-F formulation, the orientations of the mesoscale crack opening, $\mathbf{w}$, and the bridging fibers, $\mathbf{u}_f$, might be different as shown in Fig. 3.6a. In this case, localized bearing stress fields are developed at the points where the fiber exists the matrix. When these stresses exceed a certain threshold, localized fracture and fragmentation, or spalling, of the matrix occur (Fig. 3.6b). Matrix spalling reduces the corresponding fiber embedded length (L_s or L_l) inducing a sudden drop the crack-bridging force P_f. The reduction in the embedment length, denoted by s_f, is given below Yang et al. (2008):

$$s_f = \frac{P_{fN}\sin(\theta/2)}{k_{sp}\sigma_t d_f \cos^2(\theta/2)} \tag{3.24}$$

where P_{fN} is the normal component of the total force P_f (Fig. 3.6b) that contributes to spalling, k_{sp} is a dimensionless parameter, and $\theta = \arccos(\mathbf{n}_f^T\mathbf{n})$ is the deflection angle between the fiber embedded segment and the facet (crack surface) unit normal vector (Fig. 3.6b).

Matrix snubbing

When the fiber is shortened due to spalling, the LDPM-F formulation assumes that it wraps around the intact fiber in a perfectly flexible manner. The additional friction and bearing forces acting at the exit point between the tunnel crack and fiber (Fig. 3.6c) imply that P_f is greater than the calculated value from Eqs. 3.22 and 3.23. $P(\upsilon)$. This is reflected by utilizing Li et al. (1990) formula shown below:

$$P_f = \exp(k_{sn}\varphi'_f)P(\upsilon) \tag{3.25}$$

where k_{sn} is the snubbing parameter, φ'_f is the deflection angle between the two fiber segments.

The fiber axial strength strength reduction, due to bending stresses, proposed by Kanda and Li (1998) is adopted in LDPM-F, expressed as:

$$\sigma_f \leq \sigma_{uf} e^{-k_{rup}\varphi'_f} \tag{3.26}$$

where k_{rup} is a material parameter, $\sigma_c = 4P_f/\pi d_f^2$ is the axial stress in the fiber, and σ_{uf} is the fiber ultimate tensile strength.

The above snubbing model does not properly represent the microscale bending and shear phenomena for brittle fibers or semi-flexible, like carbon and steel fibers, respectively. However, the effect of these phenomena is not primary on the crack resistance, strength increase, and ductility at the structural scale. Therefore, the snubbing model could be considered in steel fiber simulations with LDPM-F since (1) the overall net effect of crack-bridging of the steel fibers on the concrete mesostructure is adequately captured, and (2) the effect of the bending stresses on the fiber axial force is properly accounted for in Eq. 3.26.

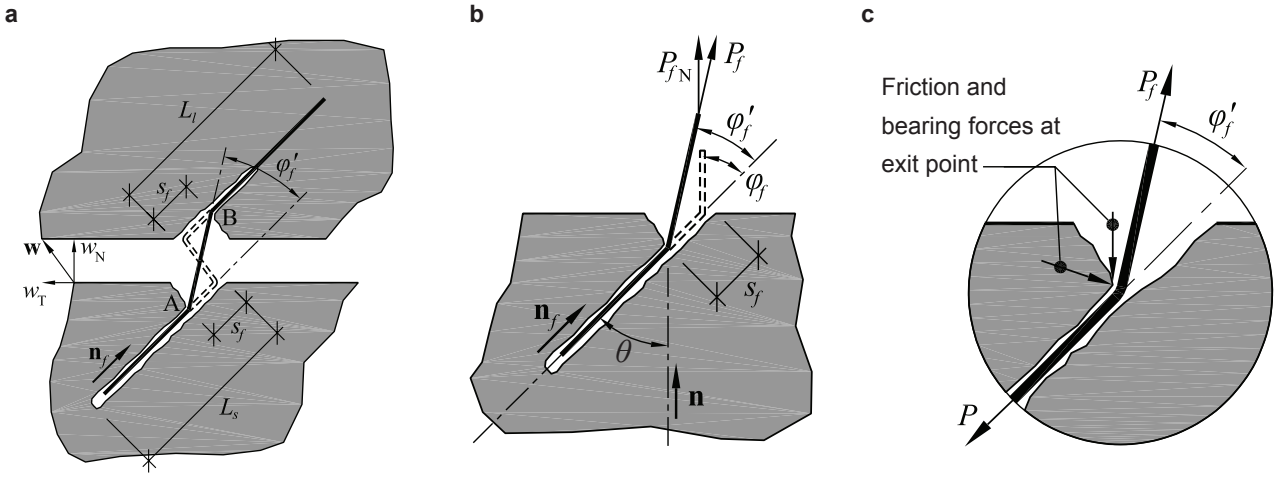

Figure 3.6: Bridging fiber phenomena: a) Crack-bridging fiber, b) matrix spalling, and d) fiber snubbing (Schauffert and Cusatis, 2012). Under fair use 2016.

Governing equations

The equilibrium and compatibility equations that govern the fiber-bridging segment formulation in LDPM-F are detailed herein. Assuming that the fiber spalling length, s_f, is the same on both sides of the crack, the crack bridging segment can computed as $\mathbf{w}' = \mathbf{w} + 2s_f\mathbf{n}_f$. The crack bridging segment compatibility is enforced as follows:

$$\|\mathbf{w}'\| = 2s_f + \upsilon_s + \upsilon_l \tag{3.27}$$

where υ_s and υ_l are the relative slippage values associated with the initial embedded fiber lengths L_s and L_l at each side of the crack. Accordingly, the pullout resisting forces in each embedded length are denoted by P_s and P_l.

Equilibrium of the fiber-bridging segment is expressed in the following expression:

$$P_f = \exp(k_{sn}\varphi'_f)P_s(\upsilon_s) = \exp(k_{sn}\varphi'_f)P_l(\upsilon_l) \tag{3.28}$$

where $P_s(\upsilon_s)$ and $P_l(\upsilon_l)$ are evaluated using Eqs. 3.21, 3.22, and 3.23, in which $L_e = L_s - s_f$ or $L_e = L_l - s_f$. This implies that pullout resisting forces on each side of the crack are equal regardless of the pullout state as shown in Eq. 3.29.

$$P_s(\upsilon_s) = P_l(\upsilon_l) \tag{3.29}$$

3.2 Coarse grained particle particle approximation for UHPC simulations

The first step in the LDPM formulation is a proper estimation of the concrete internal structure heterogeneity through particle generation and positioning. This step defines the LDPM mesoscale topology and establishes a network of potential cracks created by a Delaunay tetrahedralization of the particle centers followed by a three dimensional domain tesselation. The number and size of the generated particles depend on the user's choice of the minimum and maximum particle sizes in the model, denoted by d_0 and d_a, respectively. Cusatis et al. (2011b) performed a parametric study to investigate the effect of these two parameters on the model's response. It was concluded that simulating about 30% of the actual aggregate mass results in adequate macroscopic response while keeping computational cost manageable.

The maximum particle size in a typical UHPC mix is about 0.6 mm, setting the choice of d_a at 0.6 mm. To simulate about 30% of the aggregate mass, the minimum aggregate size d_0 is typically taken as $d_a/2$ in LDPM simulations with a Fuller curve coefficient, n_F, of 0.5. This will generate approximately 1 million particles in a compression cylinder test with 51 mm diameter and 102 mm height and about 20 million particles in a slab model having 305 $\times$ 305 mm cross sectional dimensions with 51 mm thickness (Smith et al., 2014). Given the very large number of particles generated in typical simulations, the computational cost for UHPC simulations is quite high. To reduce the computational cost, Smith et al. (2014) utilized a coarse graining technique developed by Alnaggar and Cusatis (2012) when simulating projectile penetration in UHPC slabs.

The coarse graining technique increases the particle size of the simulated material relying on the observation that the particle size mainly influences the LDPM strain softening macroscopic response and damage localization, which are governed by the tensile characteristic length, $\ell_t = 2E_0G_t/\sigma_t$. The method defines a coarse-graining factor $\kappa = d_a^{coarse}/d_a = d_0^{coarse}/d_0$ with the same fuller coefficient for both the coarse and fine systems. The coarse model new characteristic length, ℓ_t^{coarse}, is calculated in Eq. 3.30 as function of the mean value of the locally variable interparticle distances for both the coarse and fine models,

denoted by $\bar{\ell}^{coarse}$ and $\bar{\ell}$ respectively, with $\bar{\ell}^{coarse}/\bar{\ell} \neq \kappa$.

$$\ell_t^{coarse} = \ell_t \frac{\bar{\ell}^{coarse}}{\bar{\ell}} \tag{3.30}$$

Smith et al. (2014) showed that a maximum aggregate size of 4 mm with a Fuller coefficient of 0.5 ($n_F = 0.5$) gives a coarse grained mesostructure that sufficiently matches the fine model results. The accuracy and effectiveness of this method is illustrated in Figs. 3.7 and 3.8. Fig.3.7a shows the particle generation for the coarse (right) and fine (left) systems. Figs. 3.7b and c show the results of the coarse (solid line) and fine (dashed line) models for a uniaxial compression and split tests performed on 20 mm concrete cubes respectively. Finally, Figs. 3.8 show the simulated and experimental results of 3-point bending and triaxial compression tests for UHPC samples simulated with the coarse graining technique (Smith et al., 2014).

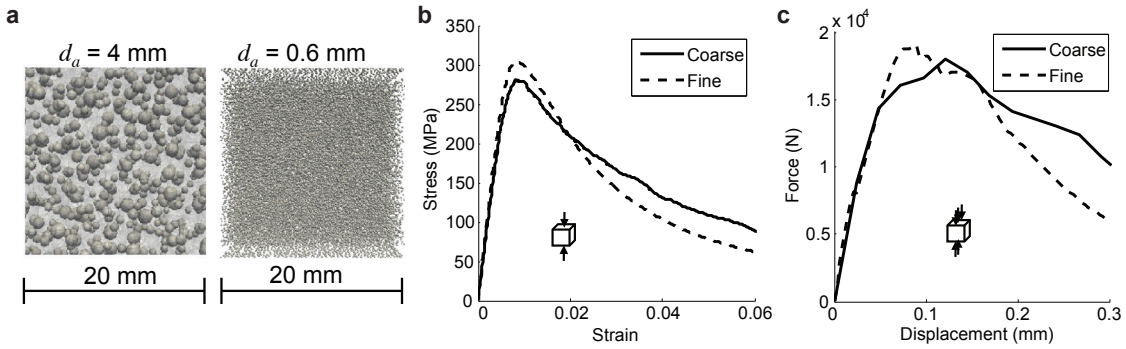

Figure 3.7: Coarse grained particle approximation: a) coarse and fine scale aggregate distribution, b) uniaxial compression, and d) split test (Smith et al., 2014). Under fair use 2016.

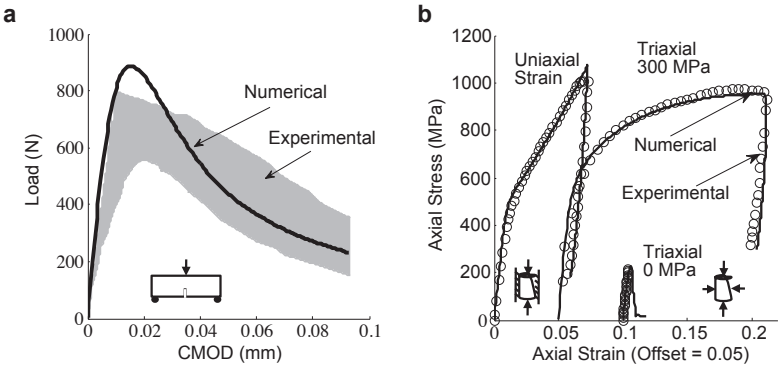

Figure 3.8: UHPC test results for LDPM-F parametric identification: a) 3-point bending, b) uniaxial strain and triaxial compression (Smith et al., 2014). Under fair use 2016.

3.3 Description of LDPM mesoscale parameters for UHPC

The LDPM and LDPM-F can realistically simulate all aspects of concrete response under quasi-static loading, including tensile and compressive strength, cohesive fracture and size effect, damage in compression, compression-shear behavior with softening at zero and low-confinement and hardening at high confined compression, strength increase under biaxial loading, and effect of fiber reinforcing. The method's numerical formulation is implemented into the Modeling and Analysis of the Response of Structures (MARS) software (Pelessone, 2016). MARS is an objected-oriented software with a robust dynamic explicit solver that uses a combination of finite element and discrete element features. The stability of the LDPM solution is established by decreasing the time step.

The following is a list of the LDPM input parameters and their effect on the macroscopic model response:

- The normal modulus (MPa), E_0, governs the stiffness of the normal facet behavior. At the macroscopic level, it determines the elastic stiffness of the material, namely the modulus of elasticity, E. The value of E_0 is informed from modulus of elasticity and Poisson's ratio tests: $E_0 = 1/(1-2\nu)E$, where ν is the Poisson's ratio.

- The shear-normal coupling parameter, α, governs the LDPM response in the elastic regime (along with the normal modulus, E_0). The value of α is informed from Poisson's ratio tests: $\alpha = (1-4\nu)/(1+\nu)$.

- The densification ratio, E_d/E_0, governs the tangential volumetric stiffness at high confinement levels and the volumetric loading/reloading stiffness. The value of E_d is informed from uniaxial strain tests.

- The tensile strength (MPa), σ_t, and the tensile characteristic lengths (mm), ℓ_t, governs the facet softening tensile fracturing behavior. At the macroscopic level, they determine the softening behavior including tensile fracturing and unconfined compression. The values of σ_t and ℓ_t are informed from three-point bending notch beam and tension tests.

- The shear strength ratio, σ_s/σ_t, governs the facet strength for pure shear. At the

macroscopic level, it governs the compression behavior and has no effect on the tensile strength. The value of σ_s is informed from uniaxial unconfined compression tests.

- The yielding compressive strength (MPa), σ_{c0} governs the macroscopic volumetric stress at which pore collapse begins (compression). The value of σ_{c0} is informed from uniaxial strain tests.

- The softening exponent, n_t, governs the interaction between shear and tensile behavior during softening at the facet level. At the macroscopic level, it determines the toughness and ductility of the material with a more pronounced effect on compression. The value of n_t is informed from uniaxial unconfined compression tests.

- The initial hardening modulus ratio, H_{c0}/E_0, governs the slope of the volumetric stress-strain curve at the onset of compression yielding. The value of H_{c0} is informed from uniaxial strain tests.

- The transitional strain ratio, κ_{c0}, governs the volumetric strain at onset of rehardening due to material densification. The value of κ_{c0} is informed from uniaxial strain tests.

- The initial friction, μ_0, is a shear boundary parameter the determine the LDPM response in compression with no effect on the tensile behavior. The value of μ_0 is informed form uniaxial unconfined compression tests.

- The asymptotic friction, μ_∞, is a shear boundary parameter that determine the triaxial behavior at high-confinement. It is typically taken as zero to capture the exponential plateau usually observed with increasing strain. The value of μ_∞ is informed from triaxial compression tests.

- The transitional stress (MPa), σ_{N0}, contribute the LDPM response in triaxial compression and has no effect on the tensile behavior. The value of σ_{N0} is informed from triaxial compression tests.

- The deviatoric strain threshold ratio, κ_{c1}, determines when rehardening after yielding is prevented due to induced damage from the deviatoric strain. The value of κ_{c1} is informed from triaxial compression tests.

- The deviatoric damage parameter, κ_{c2}, governs the deviatoric effect on rehardoning behavior. Both κ_{c1} and κ_{c2} determine the nonlinear behavior of the compression normal facet stress. The value of κ_{c2} is informed from triaxial compression tests.

- The unloading-reloading parameter, k_l, governs the cyclic behavior for both compression and tension. The value of k_l is informed from cyclic tests.

The LDPM-F is governed by the following additional input parameters pertaining the the fiber reinforcement:

- The fracture energy (N/mm), G_d, determine the effect of initial chemical bonding between the fiber and the surrounding matrix. The value of G_d is informed from single fiber pullout tests.

- The frictional stress (MPa), τ_0, governs the friction controlled debonding as the fiber exits the matrix. The value of τ_0 is informed from single fiber pullout tests.

- The interfacial friction coefficient, β, determine the shape of the pullout curve after debonding, i.e. slip-hardening or slip-softening behavior. The value of β is informed from single fiber pullout tests.

- The spalling parameter, k_{sp}, determines the threshold at which localized fracture and fragmentation (spalling) occurs at the level of the facet. It is typically taken as $k_{sp} = 0.6f'_c$, where f'_c is the macroscopic compression strength (Schauffert et al., 2012).

- The snubbing parameter, k_{sn}, governs the snubbing effect after matrix spalling. In absence of literature review to determine this parameter for steel fibers in concrete, a value of 0.4 was found appropriate (Schauffert et al., 2012).

- The fiber strength decay parameter, k_{rup}, determines the fiber axial strength reduction due to bending. For steel fibers, this value is taken as twice of the value reported by Kanda and Li (1998) for polyvinyl alcohol (PVA) fibers: $k_{sup} = 0.6$ for steel fibers.

Chapter 4

Cement-Based Composites Fracture Modeling with a Triaxial Continuum Constitutive Law

This chapter details the formulation of an existing, phenomenological macroscopic continuum material model for the analysis of concrete under multiaxial cyclic loading conditions and its extension to include the effect of dispersed fibers within the matrix. Section 4.1 investigates the model underlying concepts and governing equations for the model when applied to concrete without fibers, as described by Moharrami and Koutromanos (2016). Section 4.2 develops a new smeared-crack model formulation for fiber-reinforcement, and section 4.3 summarizes the model's macroscopic input parameters for UHPC.

4.1 Triaxial continuum model formulation for UHPC without fibers

This constitutive model is described in detail in Moharrami and Koutromanos (2016), but the salient features will be provided herein for completeness. The model simulates concrete macroscopic behavior through an elastoplastic formulation, having a nonassociative flow rule to capture compression-dominated behavior, combined with a rotating smeared-crack model to capture tension-dominated behavior. The total strain vector, $\boldsymbol{\varepsilon}$, is decomposed into three

parts: an elastic part, $\boldsymbol{\varepsilon}^{(el)}$, a plastic part, $\boldsymbol{\varepsilon}^{(pl)}$, and a cracking part, $\boldsymbol{\varepsilon}^{(cr)}$.

4.1.1 Uncracked elastoplastic material constitutive law

An elastoplastic formulation governs the behavior of uncracked material where the total stress vector, $\boldsymbol{\sigma}$, is expressed as a function of the elastic stiffness matrix, $[D]$, and the elastic strain vector, $\boldsymbol{\varepsilon}^{(e)}$, as shown below:

$$\boldsymbol{\sigma} = [D]\boldsymbol{\varepsilon}^{(el)} = [D](\boldsymbol{\varepsilon} - \boldsymbol{\varepsilon}^{(pl)}). \tag{4.1}$$

In terms of principal stresses and strain, the stress-strain law is be formulated as follows:

$$\hat{\boldsymbol{\sigma}} = [\hat{D}]\hat{\boldsymbol{\varepsilon}}^{(el)} \tag{4.2}$$

where $\hat{\boldsymbol{\sigma}}$ and $\hat{\boldsymbol{\varepsilon}}^{(el)}$ are the principal stress and strain vectors. Assuming an isotropic behavior in the elastic regime, the elastic stiffness matrix, $[\hat{D}]$, can be expressed in terms of the elastic modulus, E, and Poisson's ratio, ν, as follows:

$$[\hat{D}] = \frac{E}{(1+\nu)(1-2\nu)} \begin{bmatrix} 1-\nu & \nu & \nu \\ \nu & 1-\nu & \nu \\ \nu & \nu & 1-\nu \end{bmatrix} \tag{4.3}$$

Yield criteria

Moharrami and Koutromanos (2016) implemented a new yield surface criterion for the elastoplastic law to improve the multiaxial response of concrete while maintaining numerical efficiency. The modified yield criterion is described by the following equation:

$$f(\hat{\boldsymbol{\sigma}}, \kappa) = \frac{1}{1-\alpha}[\alpha \cdot I_1 + r(\theta, e)\sqrt{3J_2}] - c_c(\kappa) = 0 \tag{4.4}$$

where $\alpha = (f_b - f_c)/(2f_b - f_c)$ is a material parameter (Lubliner et al., 1989), f_c is the uniaxial compressive strength of the material, f_b is the biaxial compressive strength, I_1 and J_2 are the first and second invariant of the stress tensor, c_c is a strength parameter equal to the uniaxial compressive strength, κ is a hardening parameter expressing the cumulative

effect of inelastic deformation, $r(\theta, e)$ is dimensionless factor named radial distance, e is the eccentricity, defined in Eq. 4.5, describing the deviation of yield surface shape in the deviatoric plane from a circle, and θ is Lode angle, given in Eq. 4.6, ranging from 0 and $\pi/3$ in Haigh-Westergaard coordinates.

$$e = \frac{\sqrt{3}c_t - 5.5c_c}{I_1/\sqrt{3} - 5.5c_c} \tag{4.5}$$

$$\theta = \frac{1}{3}\cos^{-1}\left(\frac{3\sqrt{3}}{2}\frac{J_3}{\sqrt{J_2}}\right) \tag{4.6}$$

Plastic Strain

The plastic strain increments are obtained from the rate equation below:

$$\dot{\varepsilon}_{ij}^{(pl)} = \dot{\lambda}\frac{\partial g}{\partial \sigma_{ij}} \tag{4.7}$$

where $\dot{\lambda}$ is a scalar plastic multiplier, and g is a plastic potential function given in Eq. 4.8.

$$g = \alpha_p \cdot I_1 + \sqrt{2J_2} \tag{4.8}$$

In Eq. 4.8, α_p is the dilatancy parameter that controls the volumetric expansion of the material in the inelastic regime.

Compressive Strength

The evolution of the material compressive strength with the accumulation of inelastic strains follows the hardening-softening law of Lee and Fenves (1998) as shown in Fig. 4.1:

$$c_c(\kappa) = \frac{f_o}{a}\left[(1+a)\sqrt{\varphi(\kappa)} - \varphi(\kappa)\right] \geq f_{res} \tag{4.9}$$

where f_{res} is the residual compressive strength of the material, f_o is a material constant indicating the initiation of the plastic deformations, a is a material constant, and $\varphi(\kappa)$ is an

increasing function given by:

$$\varphi(\kappa) = 1 + a(2 + a)\kappa. \tag{4.10}$$

The hardening variable, κ, is positive, initially equal to zero, and changes following the following rate equation:

$$\dot{\kappa} = \frac{c_c}{g_c} \cdot \frac{\partial g}{\partial \hat{\sigma}}\bigg|_{\hat{\sigma}_{min}} \cdot e^{d(1+X)(p/f_c)} \tag{4.11}$$

where $g_c = g_{c0} + g_{c1}$ or $g_c = g_{c1}$ (Fig. 4.1b), g_{c0} is the area under the hardening portion of the hardening-softening law, $g_{c1} = G_c/h$ is set equal to the area under the softening portion of the hardening-softening law (which resolves the issue of spurious mesh effects on the model compression results) and is calculated by dividing the compressive fracture energy, G_c, by the mesh size of the model, h, $\partial g/\partial \hat{\sigma}|_{\hat{\sigma}_{min}}$ is the component of the plastic strain rate in the direction of the minimum principal stress, d is a user defined constant that expresses the effect of pressure on the hardening variable evolution, $p = -I_1/3$ is the pressure, and $X = I_1/\sqrt{3J_2}$ is expressed in terms of the first and second invariants. In absence of pertinent material test data and in accordance with the work of Moharrami and Koutromanos (2016), G_c can be obtained by multiplying the tensile (Mode I) fracture energy, G_t, by 100.

The exponantial term in Eq. 4.11 was introduced by Moharrami and Koutromanos (2016) to account for the increased ductility of confined concrete. For example, the exponential term is equal to 1 ($p = 0$) for uniaxial compression and then it decreases when the material is subjected to multiaxial compressive states leading to slower evolution of the hardening-softening variable.

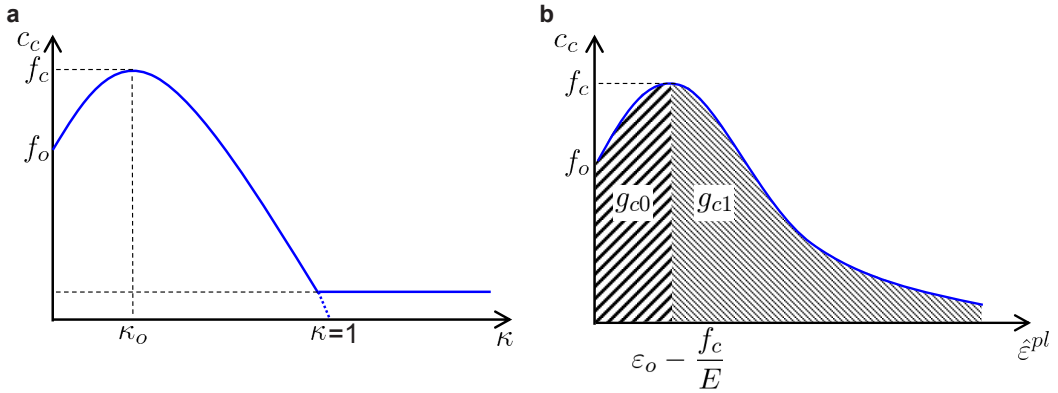

Figure 4.1: Compression law of elastoplastic model: a) hardening-softening law, and b) area under hardening and softening portions (Moharrami Gargari, 2016). Under fair use 2016.

4.1.2 Cracked material constitutive law

When the stress in one of the principal directions, $\hat{\sigma}_i$, exceeds the material cracking strength, it is corrected to account for the active crack following the equation below:

$$\hat{\sigma}_i = c_t \cdot \left\{(1-M)e^{-\lambda_t[\hat{\varepsilon}_i - \hat{\varepsilon}_{ini}/f_t]} + M\right\} \tag{4.12}$$

where c_t is the material tensile strength, f_t is the initial tensile strength, M is the ratio of residual tensile strength over tensile strength, $\hat{\varepsilon}_{ini}$ is the strain at the onset of softening, and $\lambda_t = G_t/h$ is the area under the softening portion of the stress-strain law (which resolves the issue of spurious mesh effects on the model tension results).

The value of c_t is equal to f_t when the material is subjected to compression hardening ($\kappa \leq \kappa_o$). When the material reaches the compressive degradation stage ($\kappa > \kappa_o$), the tensile strength is subjected to the same reduction, $c_t = (c_c/f_c)f_t$. The crack stress-strain model the unloading-reloading law in the cracked regime are shown in Fig. 4.2a. The parameter λ_t is depicted in Fig. 4.2b.

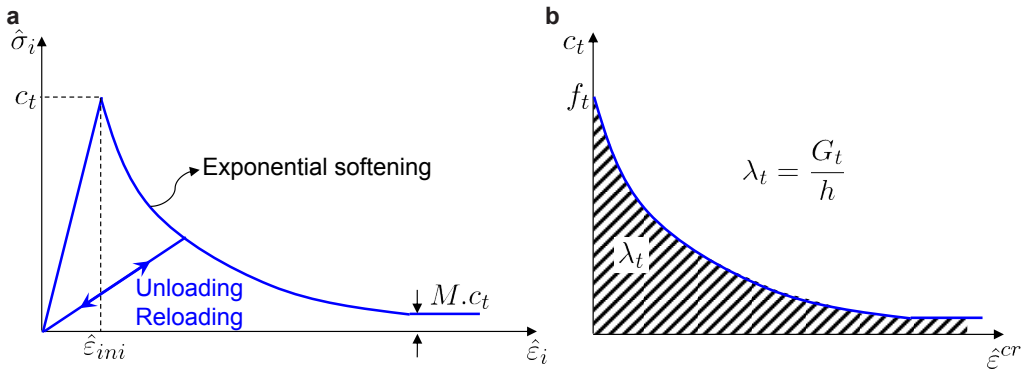

Figure 4.2: Crack stress-strain model: a) material response for uniaxial tension, and b) definition of mode-I fracture (Moharrami Gargari, 2016). Under fair use 2016.

4.1.3 Compatibility between uncracked and cracked models

The cracking correction is made in the principal stress state and only for the tensile stresses. A crack opens when the tensile strength, c_t, is exceeded and closes once compression develops. A cracking correction is performed for the principal stress and a crack opening strain vector is developed. c_t is set to zero when a previously closed crack reopens once

subjected to tensile stresses. When cracking occurs, two stress vectors, $\sigma^{+(uc)}$ and $\sigma^{+(cr)}$, are obtained from the elastoplastic and crack model, respectively. Each of these vector's components is equal to $\hat{\sigma}_i$ is a crack opens in principal direction, i, and zero otherwise.

The total strain vector is calculated by summing the elastic, plastic, and cracking parts as shown below:

$$\hat{\boldsymbol{\varepsilon}} = \hat{\boldsymbol{\varepsilon}}^{(el)} + \hat{\boldsymbol{\varepsilon}}^{(pl)} + \hat{\boldsymbol{\varepsilon}}^{(cr)}. \tag{4.13}$$

4.2 Smeared-crack model formulation for fiber reinforcement

The model by Moharrami and Koutromanos (2016) is extended in this section to incorporate the effect of fiber reinforcement on concrete behavior. The approach retains the continuum nature of the model by averaging the overall fiber contribution in a given volume over three mutually orthogonal directions ($i = 1, 2, 3$) as shown in Figs. 4.3 and 4.4. Each element in the model is treated as a representative volume element (RVE) given an overall stress vector, $\boldsymbol{\sigma}$, and strain vector, $\boldsymbol{\varepsilon}$. The total stress in each direction, σ_i, is calculated by adding the average total fiber stress, σ_{F_i}, to the matrix stress, σ_{c_i}, as shown in the equation below:

$$\sigma_i = \sigma_{c_i} + \sigma_{F_i}. \tag{4.14}$$

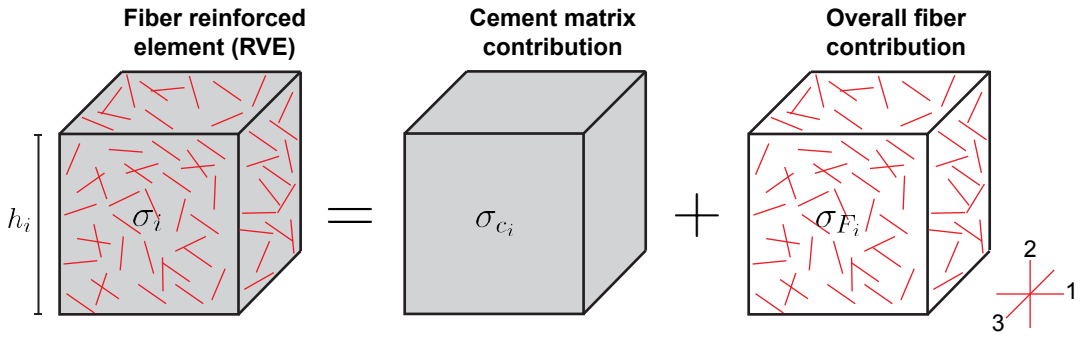

Figure 4.3: Smeared-crack fiber model approach.

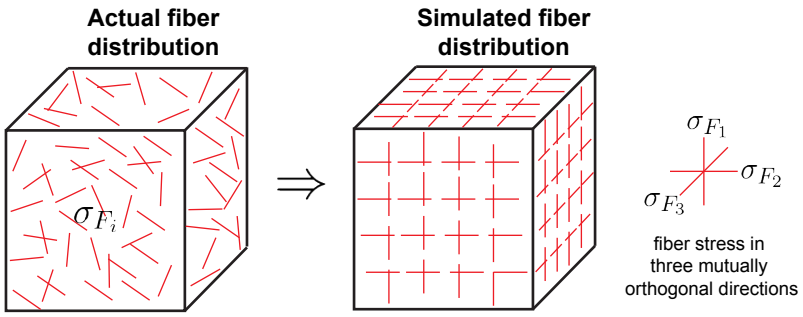

Figure 4.4: Actual and simulated fiber distribution.

4.2.1 Overall fiber contribution

The total smeared fiber area contributing to the response in each direction is calculated using the equation below:

$$A_{F_i} = a_i \frac{V_F}{h_i} = a_i v_f A_{c_i} \tag{4.15}$$

where a_i is the fiber orientation weight factor, $V_F = v_f V_c$ is the total fiber volume contained in a volume, V_c, at a given fiber volume ratio, v_f, $A_{c_i} = V_c/h_i$ is the cross-sectional area of the RVE, and h_i is the RVE side length in direction i.

The overall fiber stress, σ_{F_i}, is defined as

$$\sigma_{F_i} = \frac{P_{F_i}}{A_c} \tag{4.16}$$

where P_{F_i} is the total fiber force in each direction defined in terms of the average stress of all the fibers bridging a crack, σ_{f_i}, and calculated as follows:

$$P_{F_i} = A_{F_i} \sigma_{f_i}. \tag{4.17}$$

By substituting Eqs. 4.15 and 4.17 into Eq. 4.16, one obtains the overall fiber contribution taking into the account fiber content, orientation, and interaction with the matrix at the vicinity of a crack:

$$\sigma_{F_i} = a_i v_f \sigma_{f_i}. \tag{4.18}$$

4.2.2 Fiber-matrix interaction

Similarly to the fiber-matrix interaction law used in the LDPM-F formulation (Section 3.1.3), the average force generated in a fiber bridging a crack is represented by a load-slip relationship ($P - \upsilon$) between the fiber load, P_f, and slippage, υ, as described by Lin et al. (1999). Recalling Eqs. 3.22, and 3.23, the fiber load-slip relationship is established in terms of the bond fracture energy, G_d, the frictional stress, τ_0, and the interfacial friction coefficient, β. These parameters can be directly informed from single fiber pullout tests.

Before fiber debonding ($\upsilon < \upsilon_d$), the fiber resistance is formulated as shown:

$$P_f(\upsilon) = \left[\frac{\pi^2 E_f d_f^3}{2}\left(\tau_0 \upsilon + G_d\right)\right]^{1/2} \tag{4.19}$$

and after debonding ($\upsilon > \upsilon_d$), it is given as:

$$P_f(\upsilon) = P_{f_0}\left(1 - \frac{\upsilon - \upsilon_d}{L_e - \upsilon_d}\right)\left[1 + \beta\frac{(\upsilon - \upsilon_d)}{d_f}\right] \tag{4.20}$$

where $P_{f_0} = \pi L_e d_f \tau_0$ is the initial frictional force. The debonding slip, υ_d, is the value at which the fiber starts pulling out of the matrix and is obtained from Eq. 3.21 rewritten below:

$$\upsilon_d = \frac{2\tau_0 L_e^2}{E_f d_f} + \left(\frac{8 G_d L_e^2}{E_f d_f}\right)^{1/2} \tag{4.21}$$

where L_e, E_f, and d_f are the fiber embedded length, modulus of elasticity, and diameter, respectively.

The average stress of all fibers bridging a crack, σ_{f_i}, is a function of the fiber slip, υ_i, and is defined in terms of the fiber force, P_f, as

$$\sigma_{f_i}(\upsilon_i) = \frac{P_f(\upsilon_i)}{A_f} \tag{4.22}$$

where $A_f = \pi d^2/4$ is the cross-sectional area of a single fiber.

The above definition inherently assumes that fibers within a cross section are bridging a crack at an average location across all fibers. Therefore, it is imperative to characterize a statistically representative value of embedment, L_e, to use in the calculation of σ_{f_i}. To do

that, let x be the shorter embedded fiber length on either side of a cracking plane. Assuming a uniform distribution of x between 0 and $L_f/2$, in which L_f is the fiber length, the following probability density function is obtained:

$$f(x) = \frac{2}{L_f} \text{ for } 0 \leq x \leq \frac{L_f}{2}. \tag{4.23}$$

The expected value of x, L_s, to be used in the fiber model can then be calculated as follows (Naaman, 1972):

$$L_s = \int_0^{L_f/2} x f(x) dx = \frac{L_f}{4}. \tag{4.24}$$

The fiber pullout model applies to both the shorter and longer ends of a fiber bridging a crack plane, with initial lengths $L_s = L_f/4$ and $L_l = 3L_f/4$, and slippages υ_{s_i} and υ_{l_i}, respectively. At each side of the crack, the pullout state could be either debonding ($\upsilon \leq \upsilon_d$), friction only ($\upsilon \geq \upsilon_d$), or an unloading condition. Regardless of the pullout state, equilibrium and compatibility between the fiber resistance and slippages on either side of the crack should be maintained:

$$P_f(\upsilon_{s_i}) = P_f(\upsilon_{l_i}) \tag{4.25}$$

$$\upsilon_{cr_i} = \upsilon_{s_i} + \upsilon_{l_i} \tag{4.26}$$

where υ_{cr_i} is the total crack opening in direction i as shown in Fig. 4.5.

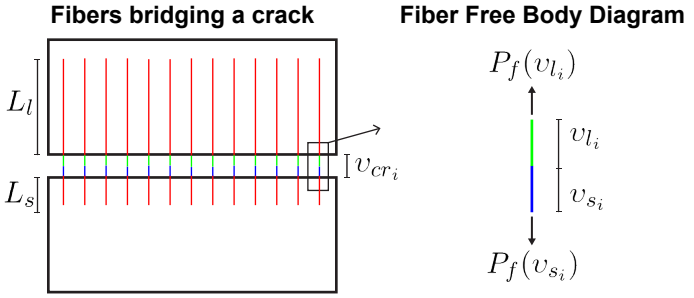

Figure 4.5: Free body diagram of a fiber bridging a crack.

Eq. 4.19 shows that for the same value of fiber slip ($\upsilon_s = \upsilon_l$), the calculated fiber loads at both sides of the crack ($P_f(\upsilon_s)$ and $P_f(\upsilon_l)$) before debonding of the short portion of the fiber ($\upsilon \leq \upsilon_{d_s}$), are equal as shown in Fig. 4.6.

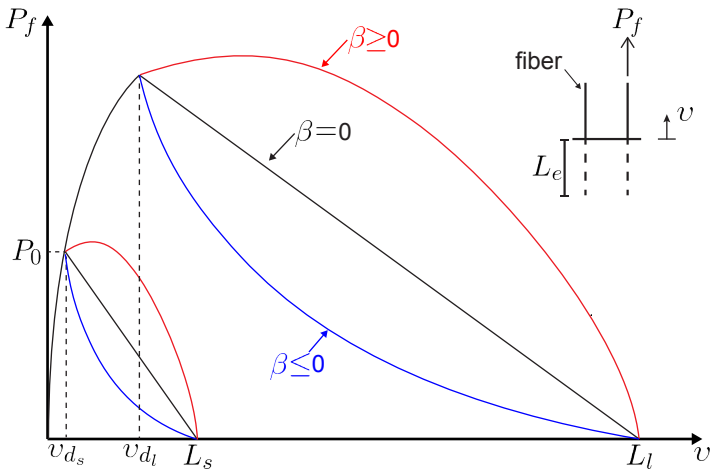

Figure 4.6: Fiber pullout curves for the short and long embedement lengths at both sides of the crack plane.

Therefore, the fiber slippage on both sides of the crack before the debonding of the short embedment length, υ_{d_s}, is half of the total crack opening, υ_{cr_i}. As the crack continue to open, the short part of the fiber enters into the frictional zone of the curve ($\upsilon_s \geq \upsilon_{d_s}$) while the longer portion begins to unload. This is particulary true for all negative or zero values of β as $P_f(\upsilon_{d_s}) = P_0$ is the maximum load sustained by the fiber. For large postive values of β, the maximum value of $P_f(\upsilon_s)$ could be larger than P_0 and the unloading of the longer fiber portion starts after υ_{d_s}. To ensure a robust and efficient computational routine of the two way pullout written as function of the shorter embedment length, $L_e = L_s = L_f/4$, the fiber slip, υ_i, used to determine P_{f_i} is calculated by assuming equal slippage on both sides until the fiber debonds on the shorter side, beyond which the longer portion starts to unload without further pullout and the additional crack opening is only taken by the shorter side as follows:

$$\upsilon_i = \begin{cases} \frac{\upsilon_{cr_i}}{2} & \text{for } \frac{\upsilon_{cr_i}}{2} \leq \upsilon_{d_s} \\ \upsilon_{cr_i} - \upsilon_{d_s} & \text{for } \frac{\upsilon_{cr_i}}{2} \geq \upsilon_{d_s}. \end{cases} \tag{4.27}$$

In fiber reinforced composites, fibers bridge the crack surfaces providing resistance to crack propagation and resulting in the development of multiple crack planes when the composite is subjected to tensile forces (see Fig. 4.7). This phenomenon is a characteristic of fiber reinforced composites where the first crack is followed by multiple cracking until the strain localizes in a single crack at which the material starts to soften. Therefore, the crack opening, υ_{cr_i}, is written in terms of an adjusted cracking strain, ε_{mcr}: $\upsilon_{cr_i} = \varepsilon_{mcr} \times h_i$, where $\varepsilon_{mcr} =$

$f(\varepsilon_{cr})$, is a function of the element cracking strain, $\varepsilon_{cr} = \varepsilon_i - \varepsilon_{ini}$. $f(\varepsilon_{cr})$ reduces ε_{cr} to reflect the increase in stiffness for both the original matrix and fiber stress resulting from multiple cracking. Since the fibers are only activated when the crack opens ($\varepsilon_i \geq \varepsilon_{ini}$), the contribution of fiber reinforcement before the first crack is ignored since its effect on the macroscopic response of the composite is minimal.

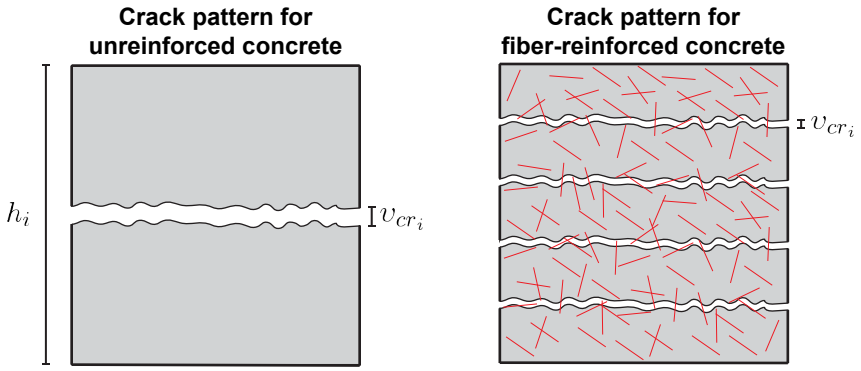

Figure 4.7: Crack pattern for unreinforced and fiber-reinforced concrete.

In the current formulation, an adjusted strain function composed of four straight line segments as shown in Fig. 4.8 was found to capture the multiple cracking behavior of the fiber reinforced composites in tension.

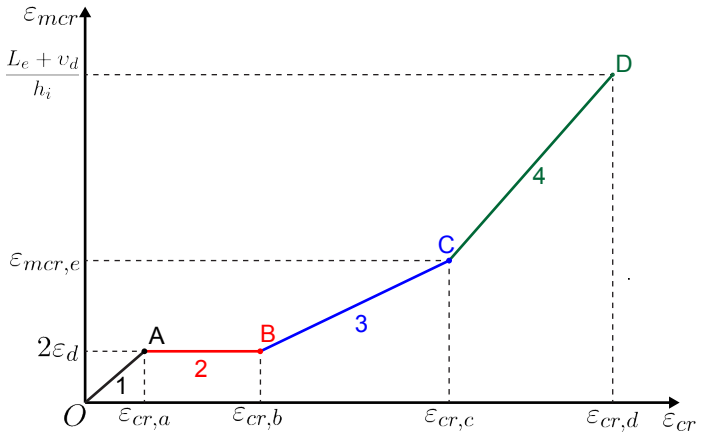

Figure 4.8: Strain adjustment function to account for multiple cracking.

The proposed function (Fig. 4.8) is inspired from the following salient features of the tensile macroscopic behavior:

- Line 1, extending from point O$(0,0)$ to point A$(\varepsilon_{cr,a}, 2\varepsilon_d)$, where $\varepsilon_d = \upsilon_d/h_i$, describes the microcracks forming at the onset of cracking ($\varepsilon_i \geq \varepsilon_{ini}$) until reaching the fiber

peak load, P_0. $\varepsilon_{cr,a}$ must be initialized and is stipulated to be greater than or equal to $2\varepsilon_d$.

- Line 2, extending from point A$(\varepsilon_{cr,a}, 2\varepsilon_d)$ to point B$(\varepsilon_{cr,b}, 2\varepsilon_d)$, accounts for the multiple cracks that simultaneously form resulting in straining the material with minimum increases in tensile strength.

- Line 3, extending from point B$(\varepsilon_{cr,b}, 2\varepsilon_d)$ to point C$(\varepsilon_{cr,c}, \varepsilon_{cr,e})$, initiates the overall tensile softening behavior when several cracks enters the frictional pullout regime.

- Line 4, extending from point C$(\varepsilon_{cr,c}, \varepsilon_{cr,e})$ to point D$((L_e + \upsilon_d)/h_i, \varepsilon_{cr,d})$, indicate that the strain has localized in one crack. The last value of $\varepsilon_{mcr} = (L_e + \upsilon_d)/h_i$ represent the fibers complete pullout.

In finite element modeling of concrete structures, the size of the mesh spuriously influence the model results when softening of the composite occurs. This lack of objectivity creates inconsistencies in the behavior of the softening portions of the stress-strain curves in tension and compression when the mesh size is changed. This problem is addressed in the parent concrete model (Moharrami and Koutromanos, 2016) by setting the area under the softening portions of the tension and compressive constitutive laws to the their respective fracture energies divided by the element size: $g_t = G_t/h_i$ and $g_c = G_c/h_i$. The mesh objectivity of the unreinforced matrix is then inherently maintained when adding fibers. However, since the macroscopic softening of the fiber-reinforced composite is dictated by the strain adjustment function, the cracking strain at onset of localization, $\varepsilon_{cr,a}$ is made independent of mesh size. The regularization of the softening for different mesh/element sizes when macroscopic softening ($\varepsilon_{cr} \geq \varepsilon_{cr,a}$) occurs is performed by providing the remaining parameters of Fig. 4.8 as crack openings instead of strains calculated as follows: $d_b = \varepsilon_{cr,b} \times h_i$, $d_c = \varepsilon_{cr,c} \times h_i$, $d_d = \varepsilon_{cr,d} \times h_i$, and $d_e = \varepsilon_{mcr,e} \times h_i$.

4.2.3 Fiber orientation

The fiber orientation weight factor, a_i, is the ratio between the number of fibers oriented in direction i over the total numbers of fibers occupying the volume of the RVE. The weight factor vary from 0 when no fibers are aligned in a certain direction to 1 when all fibers are oriented in that direction. If the fibers are randomly distributed, the orientation factor in all

three direction is equal to 1/3. At any given fiber distribution, the sum of the weight factor coefficients in the three mutually orthogonal directions must be equal to 1, as shown in Eq. 4.28, to insure that the total amount of fibers in a volume always corresponds to v_f.

$$\sum_{i=1}^{3} a_i = 1 \tag{4.28}$$

Several researchers have developed different approaches, based on a number of assumptions, to estimate the fiber preferential alignment in a specific direction. The following two approaches can be used to calculate a_i depending on the available information from the experimental program.

Bastien-Masse et al. (2016) calculated three orientation factors, $\mu_1, \mu_2,$ and μ_3, to quantitatively estimate the fiber orientation in all three principal directions forming the three-dimensional (3D) space. The orientation factors are defined using stereological principles and geometric probabilities. The fiber position is determined by the orientation angles: θ and φ, where θ is the angle between the fiber axis and one principal direction (i.e. $i = 1$ as shown in Fig. 4.9a), and φ is the angle between the fiber axis projection onto the quadrant made by the other two directions ($i = 2, 3$) and one of the principal directions in that quadrant (i.e. $i = 2$) as shown Fig. 4.9a,b.

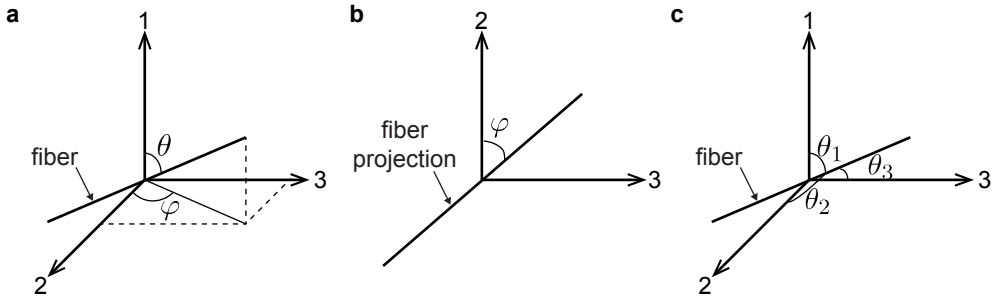

Figure 4.9: Fiber angles.

The approach assumes a uniform distribution of fibers between all possible ranges of θ and φ and ignores extreme angle values in the orientation factors calculation due to their very low probability in appearing in an actual distribution. The orientation factor in each direction can be calculated as follows:

$$\mu_1 = \frac{\cos 2\theta_a - \cos 2\theta_b}{4(\cos \theta_a - \cos \theta_b)} \tag{4.29}$$

$$\mu_2 = \frac{2(\theta_b - \theta_a) + \sin 2\theta_a - \sin 2\theta_b}{4(\varphi_b - \varphi_a)(\cos\theta_a - \cos\theta_b)}(\sin\varphi_b - \sin\varphi_a) \tag{4.30}$$

$$\mu_3 = \frac{2(\theta_b - \theta_a) + \sin 2\theta_a - \sin 2\theta_b}{4(\varphi_b - \varphi_a)(\cos\theta_a - \cos\theta_b)}(\cos\varphi_a - \cos\varphi_b) \tag{4.31}$$

where the angle indexes, a and b, indicate the minimum and maximum limits of the angles described by θ and φ , respectively. If the fibers are randomly oriented in all three directions, angles θ_a and θ_a are respectively equal to 0 and $\pi/2$, and angles φ_a and φ_b are also equal to 0 and $\pi/2$. Therefore, the orientation factor μ_i in all three directions is equal to 0.5.

Another approach assumes that the orientation angles, θ_i, between the fiber axis and the three orthogonal directions ($i = 1, 2, 3$ as shown in 4.9b) of a representative number of fibers are known (Markovic, 2006; Wille et al., 2013; Maya Duque and Graybeal, 2016). The fiber orientation factor in each direction is calculated as follows:

$$\mu_i = \frac{1}{N}\sum_{i=1}^{N}\cos\theta_i \tag{4.32}$$

where N is the total number of fibers. If the fibers are randomly oriented in all three directions, the orientation factor in all three directions is also equal to 0.5.

Regardless of the approach used to estimate the fiber orientation weight factor used in the model calculations, a_i, Eq. 4.28 should be enforced to insure that the total amount of fibers in a volume always corresponds to v_f. This can be achieved by setting:

$$a_i = \frac{\mu_i}{\mu_1 + \mu_2 + \mu_3}. \tag{4.33}$$

4.3 Description of continuum macroscale parameters for UHPC

The continuum model formulation described in this chapter can be used to realistically simulate UHPC large-scale structural components and systems under multiaxial cyclic loading conditions including the effect of fiber content and orientation. The method is robust, computationally efficient, and suitable for the systematic performance assessment of the structural behavior of fiber-reinforced concretes.

The following is a list of the continuum model input parameters for UHPC without fibers and their effect of the macroscopic response of the model:

- The modulus of elasticity, E, and the Poisson's Ratio, ν, governs the behavior of the model in the elastic range. E and ν are directly obtained from modulus of elasticity and Poisson's ratio tests.

- The compressive strength, f_c, is the maximum value of stress that unconfined concrete can withstand before softening begins. f_c is equal to the maximum value of c_c which occurs when $\kappa = \kappa_o$ and is informed from unconfined compression tests.

- The strain at peak compressive strength, ε_o, is strain at onset of compression softening. ε_o is obtained from the material's compressive stress-strain curve recorded during an unconfined compression test.

- The compressive stress, f_o, is the stress at which the plastic behavior of concrete starts. f_o is obtained from pre-peak non-linear response of the compressive stress-strain curve recorded during an unconfined compression test.

- The residual compressive strength, f_{res}, is the residual compressive stress after the material have failed. ε_o is obtained from the post-peak response of the compressive stress-strain curve recorded during an unconfined compression test.

- The tension strength, f_t, is the maximum value of tensile stress at the onset of softening. f_t is equal to the maximum value of c_t at the onset of cracking and is obtained from direct or indirect tension tests.

- Parameter $\lambda_t = G_t/h$ is equal to the area under the softening portion of the cracking stress-strain law and is informed from direct tension tests.

- Parameter, M, is the ratio of residual tensile strength over the tensile strength, f_t, of the material. M is obtained for the post-peak response of concrete under direct tension.

- Parameter $g_c = G_c/h$ is the area under the softening portion of the hardening-softening law. In absence of pertinent material test data and in accordance with the work of Moharrami and Koutromanos (2016), G_c can be obtained by multiplying the value of G_t by 100.

- Parameter a is a material constant influencing the confined concrete ultimate strength. a is informed from triaxial compression tests.
- Parameter α_p is a dilatancy parameter controlling the volumetric expansion of the material due to inelastic behavior. α_p is informed from triaxial compression tests.
- Parameter d is a user defined constant that expresses the effect of pressure on the hardening variable evolution. d is informed from triaxial compression tests.

The smeared-crack fiber model input parameters for UHPC with fibers is governed by the following additional parameters:

- The fracture energy (N/mm), G_d, determine the effect of initial chemical bonding between the fiber and the surrounding matrix. The value of G_d is informed from single fiber pullout tests.
- The frictional stress (MPa), τ_0, governs the friction controlled debonding as the fiber exits the matrix. The value of τ_0 is informed from single fiber pullout tests.
- The interfacial friction coefficient, β, determine the shape of the pullout curve after debonding, i.e. slip-hardening or slip-softening behavior. The value of β is informed from single fiber pullout tests.
- The fiber orientation weight factor, a_i, is the ratio of fibers oriented in direction i over the total number of fibers occupying a volume. a_i is estimated using statistical and geometric probabilities which are informed from experimental procedures.
- The multiple cracks strain adjustment function, $f(\varepsilon_{cr})$, which accounts for the stiffening effect of the fiber contribution to the overall tensile behavior. $f(\varepsilon_{cr})$ is informed from direct tension tests.

Chapter 5

UHPC Material Characterization to Inform Computational Models

This chapter provides an overview of the UHPC material characterization experimental program conducted in this research work to investigate the compression, fracture, and tension properties of UHPC. The tests detailed in the test matrix below will be used to inform and validate the adopted computational models predictive capabilities. Section 4.1 details mix composition specific to the UHPC used in this research work. Section 4.2 describes the mixing, placing, and curing process followed for each of the UHPC batches performed. Finally, section 4.3 lists the overall test matrix detailing the specimens placed in each batch and their associated material tests.

5.1 Ductal® UHPC Mix Composition

The UHPC used in this research work is a proprietary product, commercially available in North America since 2001 under the name Ductal®. It is jointly developed by LaFarge, Bouyegues, and Rhodia and has a typical mix composition shown in Table 5.1 with 2% fibers by volume (Graybeal, 2006). Table 5.2 shows the manufacturer-supplied material properties.

Table 5.1: Typical UHPC composition of Ductal® (Graybeal, 2006).

Material	**Kg/m³**	**Percentage by Weight**
Portland Cement	712	28.5
Fine Sand	1,020	40.8
Silica Fume	231	9.3
Ground Quartz	211	8.4
HRWR	30.7	1.2
Accelerator	30.0	1.2
Steel Fibers	156	6.2
Water	109	4.4

Table 5.2: Manufacturer-supplied material properties of Ductal® (Graybeal, 2006).

Material Property	**Range**
Compressive Strength (MPa)	180-225
Modulus of Elasticity (GPa)	55-58.5
Flexural Strength(MPa)	40-50
Chloride Ion Diffusion (m^2/s)	1.9×10^{-14}
Carbonation Penetration Depth (mm)	< 0.5
Freeze-Thaw Resistance (RDM)	100%
Salt-Cure Shrinkage (micro-strain)	< 0.012
Creep Coefficient	2-4%
Density (Kg/m^3)	2,440-2,550

Ductal® is supplied in the form of dry homogeneous premix bags, superplasticizer (Premia® 150), and steel fibers. The manufacturer recommends the mix proportions shown in Table 5.3, and reinforcing the composite with 2% fiber volume content for optimum flowability. This work, in addition to 2% fiber reinforcement, explores UHPC with 0% and 4% fibers by volume. For these batches, the amount of steel fibers shown in Table 5.3 was removed or doubled, respectively.

Table 5.3: Mix proportions of Ductal® JS1000.

Material	**Kg/m^3**
Premix	2195
Water	130
Premia® 150	30
Steel Fiber (2% by vol.)	156

The fibers used in Ductal® mixes are Dramix® OL 13/.20 smooth high carbon steel fiber, with length, L_f, and diameter, d_f, of 13 mm and 0.2 mm, respectively. The manufacturer specifies a minimum tensile strength of 2,600 MPa. Quality control tension tests performed by Graybeal (2006) determined that these fibers have an average ultimate strength, σ_u, of 3,270 MPa, an average yield strength, σ_y, of 3,160 MPa, and average modulus of elasticity, E_f, of 205 GPa. Figure 5.1 shows a sample tensile stress-strain ($\sigma - \varepsilon$) for the fibers.

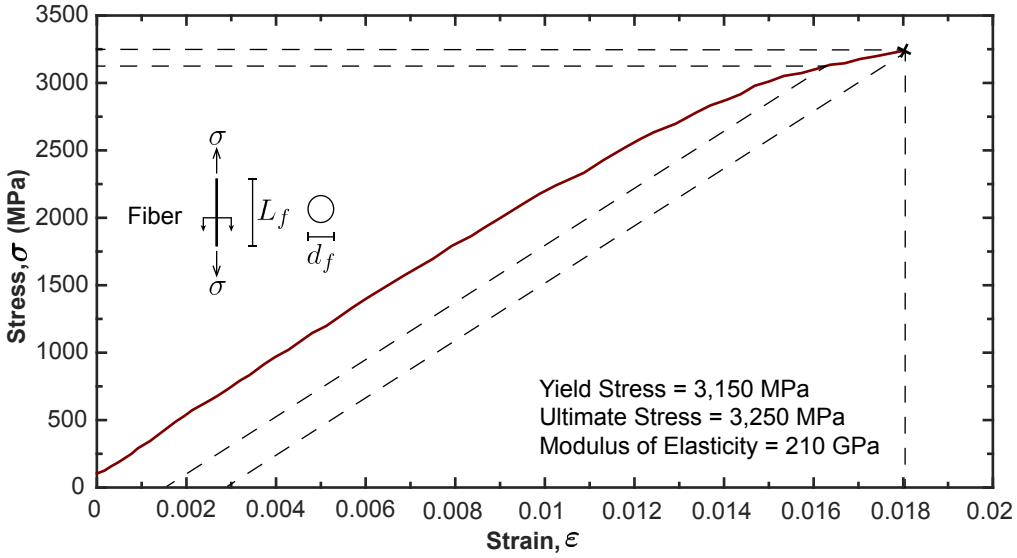

Figure 5.1: Sample tensile stress-strain relationship of fiber reinforcement in Ductal® (Graybeal, 2006).

5.2 Mixing, placing, and curing of UHPC batches

Prior to each batch, the premix was weighed and placed into a Mortarman® 750 mortar mixer, which speed and capacity are 35 rotations per minute (rpm) and 0.14 m^3, respectively

(Figs 5.2a-b). The mixer was started for approximately 2 minutes to disperse any large dry pack-set clumps of premix. Water and superplastizer were weighed, thoroughly mixed, and added to the mixer over a span of 1-3 minutes to allow for proper distribution (Figs 5.2c-b). The products were left to mix for about 15-20 minutes until the mix turned dark grey with a consistency of bread dough (Fig. 5.2e). Fibers, when applicable, were then slowly dispersed and added into the mixer (Fig. 5.2f). Once the fibers are evenly distributed in the mix, the mixer was stopped and a static flow test is performed (Figs 5.2g-h). The total mixing time ranged from 20 to 35 minutes.

Figure 5.2: UHPC mixing process

The static flow test is a test method described in ASTM C230/C230M *Standard Specification for Flow Table for Use in Tests of Hydraulic Cement* (2014) that determines the flow characteristics of concrete mortars. It is used with UHPC preparation to determine if the products have been adequately mixed and are ready to be placed into the molds. Prior to the test, the circular flow table and its brass ring were damped with water. The brass ring was then centered on the table and filled with UHPC, removing excess material from the table and ring area (Figs 5.3a-b). The ring was slowly removed (4 to 5 seconds) and any residual material left inside the ring was scraped off and deposited into the sample (Fig. 5.3c). After 2 minutes, the diameter of UHPC was measured at three locations (Fig. 5.3d). The flow test results, provided in Appendix A, show excellent flowability with the UHPC flowing outside the 254 mm diameter of the table for all batches except for those with 4% fiber volume content, which had an average spread diameter of 215 mm. These mixes took significantly more effort and time to be properly placed into the molds. Groups of fibers were noticed in the paste suggesting that the fiber content of 4% by volume is relatively high to be used with the proportions of Table 5.3. After the flowability test, the mix was then placed into the selected molds, covered with plastic, and left to cure at room temperature for 48 hours (Fig. 5.4). The specimens were demolded afterwards and labeled for testing.

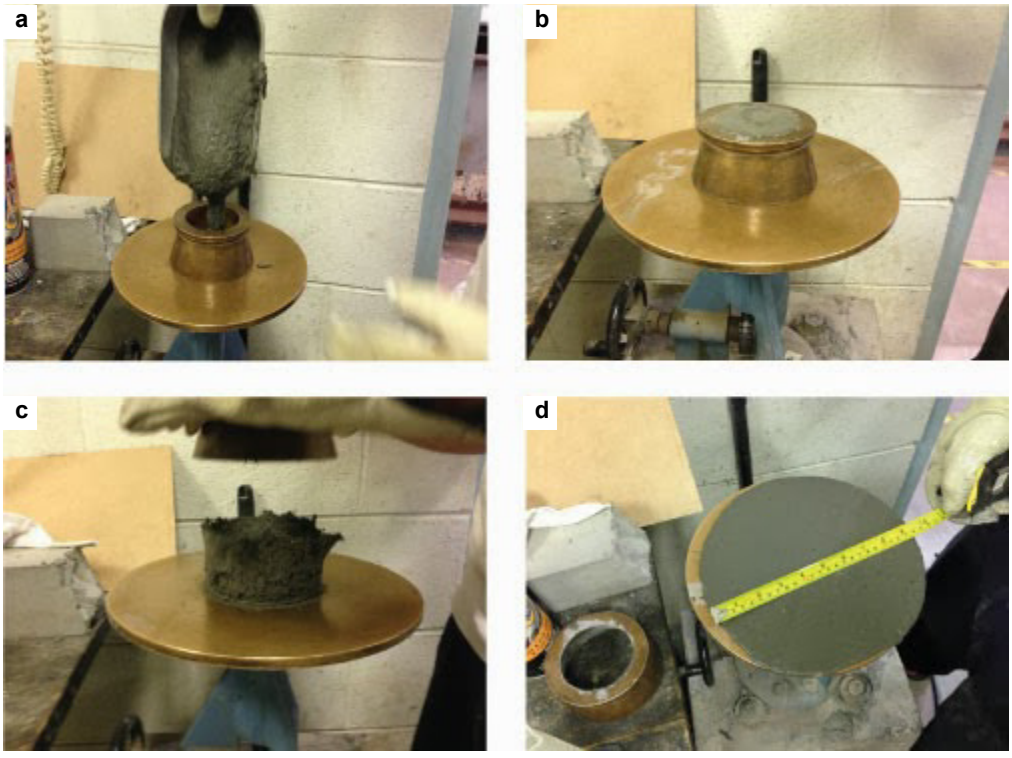

Figure 5.3: UHPC flow test

5.3 Experimental program design

The experimental matrix consisted of 10 batches from which all the experimental tests reported in this document are placed. Table 5.4 lists the batch descriptions with their associated material tests and fiber volume content, v_f. Appendix A provides the experimental data sheets listing the quantities of the manufacturer's constituent materials (premix, superplasticizer, water, and steel fibers) mixed for each batch to produce UHPC.

Figure 5.4: Batch-IV UHPC placement

Table 5.4: Batch descriptions and their associated tests

Batch ID	v_f %	**Tested property**	**Specimens placed**	**Batch size (m^3)**
I	0	Compression: stress-strain	4 76×152 mm cylinders	0.060
		Compression: peak strength	32 51×51 mm cubes	
		Fracture toughness	5 51×102×508 mm prisms	
		Direct tension	10 25×25×76 mm briquettes	
		Split Cylinder	5 102×204 mm cylinders	
II	0	Compression: stress-strain	4 76×152 mm cylinders	0.078
		Compression: peak strength	36 51×51 mm cubes	
		Poisson's ratio	5 102×204 mm cylinders	
		Fracture toughness	6 51×102×508 mm prisms	
		Direct tension	9 25×25×76 mm briquettes	
		Split Cylinder	5 102×204 mm cylinders	
III	0	Compression: peak strength	20 51×51 mm cubes	0.062
		Fiber pullout	10 51×102×508 mm prisms	
IV	2	Compression: stress-strain	12 76×152 mm cylinders	0.085
		Compression: peak strength	31 51×51 mm cubes	
		Poisson's ratio	5 102×204 mm cylinders	
		Fracture toughness	5 51×102×508 mm prisms	
		Direct tension	12 25×25×76 mm briquettes	
		Split cylinder	5 102×204 mm cylinders	
V	2	Compression: peak strength	21 51×51 mm cubes	0.064
		Fracture toughness	6 51×102×508 mm prisms	
VI	2	Compression: peak strength	25 51×51 mm cubes	0.062
		Fiber pullout	10 51×102×508 mm prisms	
VII	2	Compression: peak strength	10 51×51 mm cubes	0.085
		Fiber pullout	10 51×102×508 mm prisms	
VIII	4	Compression: stress-strain	10 76×152 mm cylinders	0.085
		Compression: peak strength	30 51×51 mm cubes	
		Poisson's ratio	5 102×204 mm cylinders	
		Fracture toughness	8 51×102×508 mm prisms	
		Direct tension	10 25×25×76 mm briquettes	
		Split cylinder	5 102×204 mm cylinders	
IX	4	Compression: peak strength	26 51×51 mm cubes	0.072
		Fracture toughness	6 51×102×508 mm prisms	
X	4	Compression: peak strength	23 51×51 mm cubes	0.070
		Fiber pullout	10 51×102×508 mm prisms	

Chapter 6

UHPC Unconfined Compression Behavior to Inform Computational Models

This chapter details the UHPC compression behavior including linear, non-linear, peak, and post-peak portions of the response at fiber volume contents of 0%, 2%, and 4%. The material's strength evolution with concrete age is also highlighted herein. Section 6.1 discusses the compression test matrix. Section 6.2 describes the specimen preparation procedure. Section 6.3 details the test setup, instrumentation, and procedure followed to conduct the compression tests. Sections 6.5 discusses the experimental results including axial stress vs. axial and circumferential strain curves, modulus of elasticity, Poisson's ratio, strength evolution with time, and specimen geometry effect on compressive strength.

6.1 Test matrix

The UHPC material behavior in compression at fiber volume content of 0%, 2%, and 4% was characterized from three different investigations, each tailored to obtain a specific compression property as shown in Table 6.1. The first set of tests characterized the UHPC axial stress - axial/circumferential strain relationships of 30 cylinders, each having a diameter of 76 mm and a height of 152 mm. The second set obtained the material's Poisson's ratio,

ν, of 15 cylinders, each having a diameter of 102 mm and a height of 204 mm. The last set of tests were used to evaluate the ultimate strength, f_c, of 254 cubes, each having a side length of 25 mm, and to analyze the strength evolution with concrete age after placement. The cube ultimate compression strength tests were also performed to monitor f_c of each UHPC batch at the time of conducting a specific material test (i.e. fracture, tension, and fiber-pullout tests).

Table 6.1: UHPC compression test matrix.

Batch ID	v_f (%)	**Tested property**	**Tested specimens**
I	0	Stress - strain	4
		Cube strength	32
II	0	Stress - strain	4
		Poisson's ratio	5
		Cube strength	36
III	0	Cube strength	20
IV	2	Stress - strain	12
		Poisson's ratio	5
		Cube strength	31
V	2	Cube strength	21
VI	2	Cube strength	25
VII	2	Cube strength	10
VIII	4	Stress-strain	10
		Poisson's ratio	5
		Cube strength	30
IX	4	Cube strength	26
X	4	Cube strength	23

6.2 Specimen preparation

The compression specimens used to obtain the stress - strain relationship were placed in cylindrical molds having a diameter of 76 mm and a height of 165 mm. The molds are made of 7 mm thick rigid Plyvinyl Chloride (PVC) plastic to prevent any geometric imperfections in the hardened concrete. Fresh UHPC was placed vertically into the molds as shown in Fig. 6.1a. The specimens were demolded after 48 hours and the top 13 mm of the cylinders were cut using a diamond blade saw to obtain clean smooth top surfaces (Fig. 6.1b). The ends

of the specimens were not capped because the expected UHPC ultimate strength is greater than the sulfur strength. Instead of sulfur capping, the surfaces were manually grinded and their end planeness were measured using a flat steel plate and a dial gage as shown in Fig. 6.1c. The specimens were then labeled, measured, and marked for equipment installation (Fig. 6.1d). The following measurements were recorded for each specimen and reported in Appendix B: the cylinder diameter at 5 locations, and the height at six, including the longest and shortest heights. The final specimens had a average diameter, $\bar{d}$, of 75.4 mm $\pm$ 0.15%, an average height, $\bar{h}$, of 151.3 mm $\pm$ 0.38%, and an average end planeness angle, $\bar{\theta}$, of 0.64°$\pm$ 30.1%.. None of the specimens had an end planeness angle greater than 1° as recommended by Graybeal (2006).

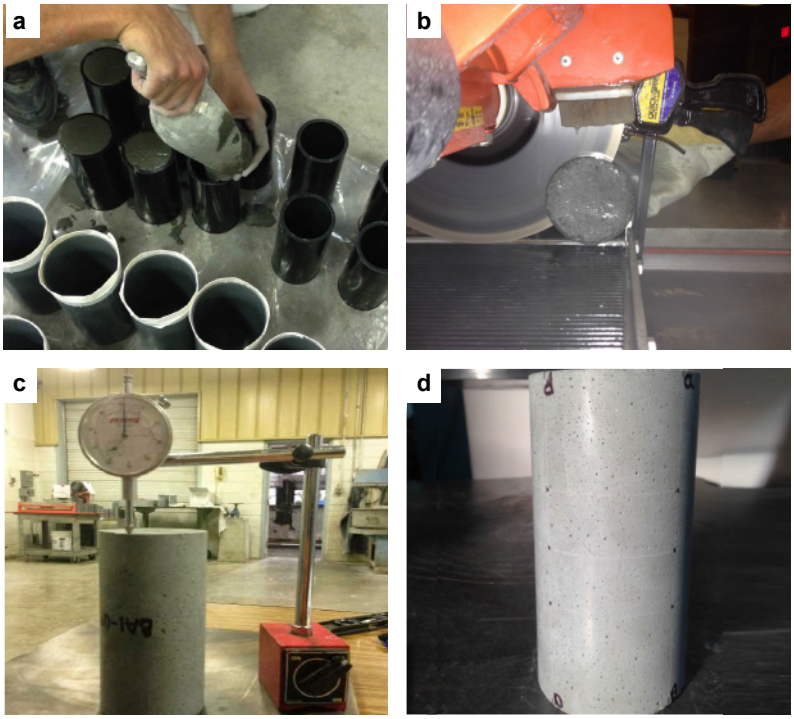

Figure 6.1: Specimen preparation for compression stress-strain relationship.

The Poisson's ratio specimens were placed in cylindrical molds having a diameter of 102 mm and a height of 204 mm. The molds' heights were deliberately increased by approximately 10 mm using duct tape mounted around the top circumference as shown in Fig. 6.2a. The extra height was added to allow room for adequate surface preparation of the hardened UHPC. The extra height was then cut using a concrete saw to remove any rough edges. As these specimens will not be loaded to failure, sulfure caps were molded into both ends of the specimen to provide a smooth, level surface of bearing.

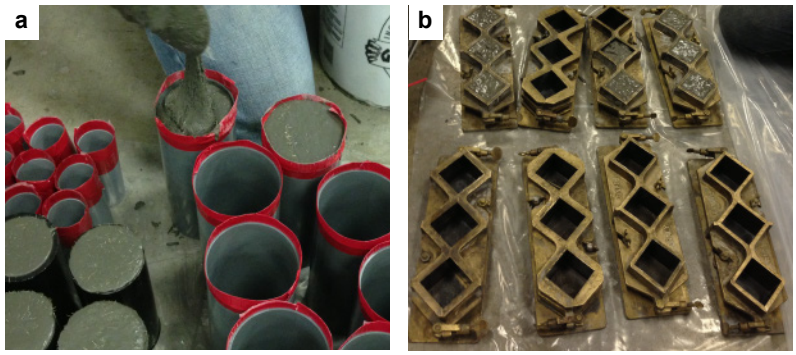

Figure 6.2: Specimen preparation for: a) Poisson's ratio tests and b) cube ultimate strength.

To overcome the hurdles of preparing flat and parallel end surfaces for cylindrical specimens, cubical specimens are often used as a quick and easy compression test to obtain the UHPC ultimate compression strength. For a cubical specimen, the ultimate strength is obtained by applying compressive loads on the cube's plane surfaces that were in contact with the mold true plane surfaces without the need for any grinding or sulfar capping. The cube specimens tested in this research were placed vertically in steel molds having 51 mm sides as shown in Fig. 6.2b.

6.3 Test setup, instrumentation, and procedure

The compressive stress-strain relationships were obtained by placing the 76 mm diameter cylinders in a SATEC 1,334-kN capacity compression machine, having load readings accuracy of 0.2%. An averaging axial extensometer (Epsilon 3542), with 6 mm travel and 0.2% accuracy, was mounted over a 50 mm gauge length at the middle of the cylinder to measure the axial displacement and avoid end effects. The total displacement was measured using two Linear Variable Differential Transformers (Vishay HS10 LVDT), with 13 mm travel and 0.2% accuracy, mounted between the machine platform and top metal socket. The circumferential expansion was recorded using a circumferential extensometer (Epsilon 3544), with 12 mm travel and 0.2% accuracy, connected to a chain device mounted around the circumference at mid-height of the cylinder as shown in Fig. 6.3. To avoid erroneous data at the beginning of each test because of platen seating and cylinder surface irregularities, a preload of 4 MPa was applied prior to the start of each test and the pre-cracking axial displacements were measured using the axial extensometer mounted directly on the cylinder. After cracking, the axial extensometer moved and its data was no longer reliable. The LVDTs data was

used beyond cracking after correcting the pre-cracking LVDT data to coincide with the axial extensometer readings eliminating the testing-frame deformation and concrete-steel frictional end effects.

The compression test procedure was in accordance with ASTM C39/C39M *Standard Test Method for Compressive Strength of Cylindrical Concrete Specimens* (2015) with one exception: the tests were displacement-controlled with a constant circumferential displacement rate of 2.1×10^{-4} mm/s until the peak axial stress was reached, after which the displacement rate was increased to 2.5×10^{-3} mm/s and 8.5×10^{-3} mm/s, respectively. This displacement procedure was adopted after a series of trial-and-error tests to find the loading scheme that captures best the elastic and post-peak portions of the stress-strain compressive curve while keeping test duration below 20 min to avoid long-term effects. The adopted pre-peak circumferential displacement rate corresponds to an average load rate of 0.42 MPa/s. The compression specimens were tested between 400 to 410 days after placement.

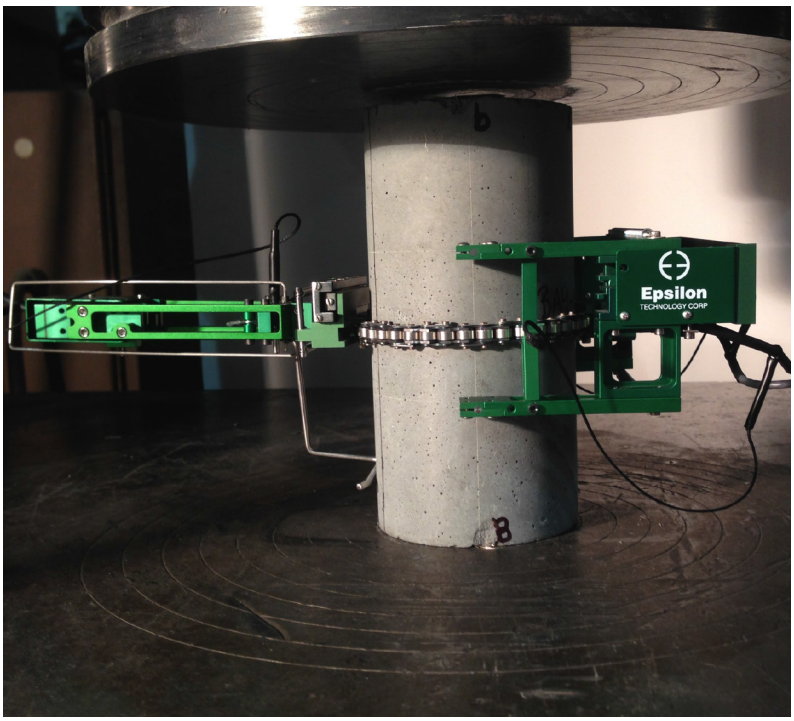

Figure 6.3: Stress-strain compression test setup.

The Poisson's ratio test setup and procedure was in accordance with ASTM C469/C469M *Standard Test Method for Static Modulus of Elasticity and Poissons Ratio of Concrete in Compression* (2014). The 102 mm diameter cylinders were placed in a Forney 1,557 kN capacity compression machine, with 0.2% load reading accuracy. The loading rate of this ma-

chine is controlled manually using a hydraulic valve. A compressometer device was mounted over a 133 mm gage length at the middle of the cylinder as shown in Fig. 6.4. The vertical and circumferential displacement were measured by two digital dial gages (Humboldt BG3500) having a travel distance of 6.35 mm with an accuracy of 0.2%. This test was chosen to determine the UHPC Poisson's ratio over the stress-strain test described above for two main reasons: (1) it follows a standard testing procedure in line with ASTM C469/C469M (2014); and (2) it provides more accurate readings of the initial elastic deformations of the specimen through the use of larger diameter specimens and higher resolution instrumentation.

The cylinders were loaded in compression with a constant load rate of 1.0 MPa/sec. This load rate is higher than the one recommended by ASTM C469/C469M (2014). This increase was necessary to keep the test duration below 20 minutes given the UHPC higher strength (Graybeal, 2006). The cylinders were loaded once before readings were collected. The readings were recorded when the longitudinal strain reached at 0.00005 and until the load attained 40% of the ultimate strength. The Poisson's ratio for each tested cylinder was calculated as follows:

$$\nu = \frac{\varepsilon_{c,40\%} - \varepsilon_{c,0.00005}}{\varepsilon_{a,40\%} - 0.00005} \tag{6.1}$$

where $\varepsilon_{c,40\%}$ is the circumferential strain at 40% of f_c, $\varepsilon_{c,0.00005}$ is the circumferential strain at an axial strain of 0.00005, and $\varepsilon_{a,40\%}$ is the axial strain at at 40% of f_c.

Figure 6.4: Poisson's ratio test setup.

The cube compression test setup and procedure was in accordance with ASTM C109/C109-M *Standard Test Method for Compressive Strength of Hydraulic Cement Mortars (Using 2-in. or [50-mm] Cube Specimens)* (2013) with one exception: the load rate was increased to 0.90 MPa/sec for the same previously discussed reasons (Graybeal, 2006). The specimens were also placed into the Forney machine, with 1,557 kN capacity and 0.2% accuracy, and axially loaded along the plane surfaces that were in contact with the mold surfaces as shown in Fig. 6.5. The ultimate compressive strength was then computed by dividing the maximum attained load by the cube cross sectional area. The cube compression results are expected to show an apparent ultimate strength that is approximately 5% higher than the cylindrical specimens due to the cube's shorter aspect ratio, which generates larger lateral confinement caused by the machine platens (Graybeal, 2006).

Figure 6.5: Cube compression strength test setup.

6.4 Results

6.4.1 Compressive stress-strain response without fibers

A sample axial stress-strain curve of a compression cylinder without fiber reinforcement ($v_f = 0\%$), with the typical failure mode observed at the end of the test and the unloading-reloading cycles, is shown in Fig. 6.6. The unloading-reloading cycles are a consequence of the constant circumferential expansion enforced during testing to account for the sudden decreases in stiffness following the initiation of major cracks. However, obtaining a post-peak response of UHPC without fibers was particularly challenging due to the brittle nature of failure and the material's high sensitivity to slight increases in axial stress, σ_a, at the vicinity of the peak stress. Of the 8 tested cylinders in this group, only the post-peak response of the specimen shown in Fig. 6.6 was captured. The circumferential strain, ε_c, measurements are not reported herein due to major jumps in the displacement readings after cracking.

The individual and average axial stress - axial strain response of all the tested specimens are shown in Fig. 6.7; the unloading-reloading cycles were omitted for clarity, and the average curve, plotted as a thicker solid line, is calculated from the individual axial stresses at one value of axial strain. The average initial stiffness of UHPC without fibers is 53.3 MPa $\pm 5\%$;

it begins to degrade when cracks develops resulting in a non-linear behavior ($\bar{\sigma}_a \gtrsim 107$ MPa). The average ultimate compressive strength, $\bar{f}_c$, is 122 MPa ±18% which occurred at an average ultimate axial strain, $\bar{\varepsilon}_c$, of 0.0026 ±21%.

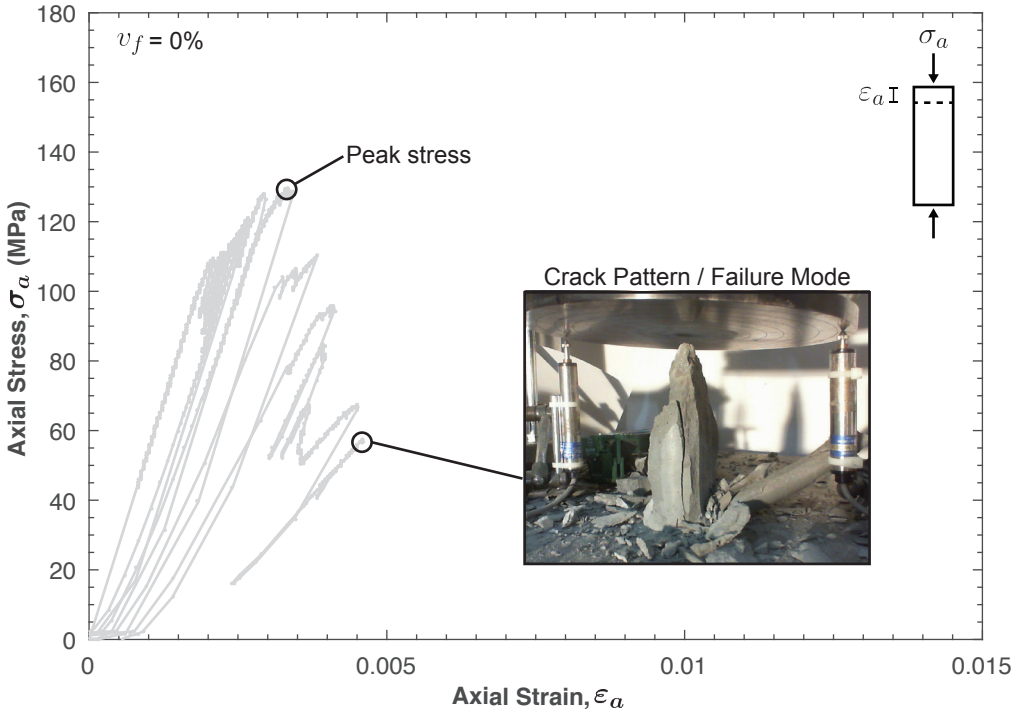

Figure 6.6: Sample compression axial stress - strain response of UHPC without fibers.

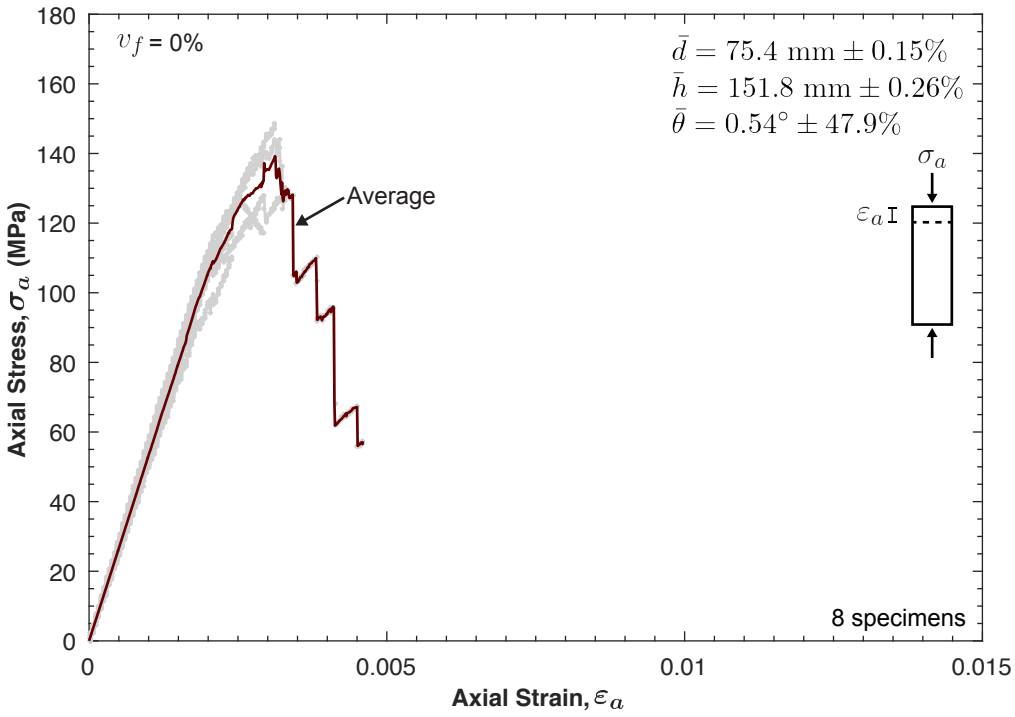

Figure 6.7: Average compression axial stress - strain response of UHPC without fibers.

6.4.2 Compressive stress-strain response with fibers

Sample compression axial stress - axial strain and axial stress - circumferential strain curves for UHPC containing 2% fibers by volume ($v_f = 2\%$), with a typical crack pattern and unloading-reloading cycles, are shown in Figs. 6.8 and 6.9, respectively. The average trends, plotted as thicker solid lines above the individual test results, are shown in Figs. 6.10 and 6.11. The unloading-reloading cycles are omitted for clarity. The average curves are calculated from the individual axial stresses at one value of axial or circumferential strain. Similarly, sample axial stress - axial strain and axial stress - circumferential strain curves for UHPC with 4% fiber volume content ($v_f = 4\%$) are shown in Figs. 6.12 and 6.13; the average trends are shown in Figs. 6.14 and 6.15.

The average initial axial stiffness of UHPC with 2% fibers by volume is 54.4 $\pm$ 3%; it begins to degrade when cracks develops resulting in a non-linear behavior ($\sigma_a \gtrsim 125$ MPa). The average ultimate compressive strength, $\bar{f}_c$, is 158 MPa $\pm$ 3% which occurred at an average ultimate axial strain, $\bar{\varepsilon}_c$, of 0.0033 $\pm$4%.

For the specimens with 4% fibers volume content, the average initial axial stiffness is 54.3

$\pm$ 5% and also begins to degrade when $\sigma_a \gtrsim 125$ MPa. The average ultimate compressive strength, $\bar{f}_c$, is 161 MPa $\pm$ 3% which occurred at an average ultimate axial strain, $\bar{\varepsilon}_c$, of 0.0038 $\pm$12%.

The average trends for UHPC with v_f = 0%, 2%, and 4% are compared in Figs. 6.16 and 6.17. It can be concluded that the UHPC average modulus of elasticity, $\bar{E}$, without and with fibers is similar and equal to 53.7 MPa $\pm$ 4%. The initial stiffness begins to degrade at a compressive stress of approximately 107 MPa for the UHPC without fiber reinforcement compared to 125 MPa for UHPC with fibers. The average ultimate compressive strength, $\bar{f}_c$, increases by about 30% when fibers are added to the matrix. No significant increase in ultimate strength was observed between fiber contents of 2% and 4%. The fibers have improved the ductility of the material by transmitting forces between crack surfaces maintaining confinement as shown in Fig. 6.16 and 6.17. For example, the material was able to withstand 50% of its ultimate capacity at axial strains of 0.006 and 0.009 when fibers are added at 2% and 4% by volume, respectively. Fibers have also limited crack propagation resulting in smaller crack openings and fewer unloading and reloading cycles in the stress-strain curves (Figs. 6.8 and 6.12) compared to the curve without fibers (Fig. 6.6).

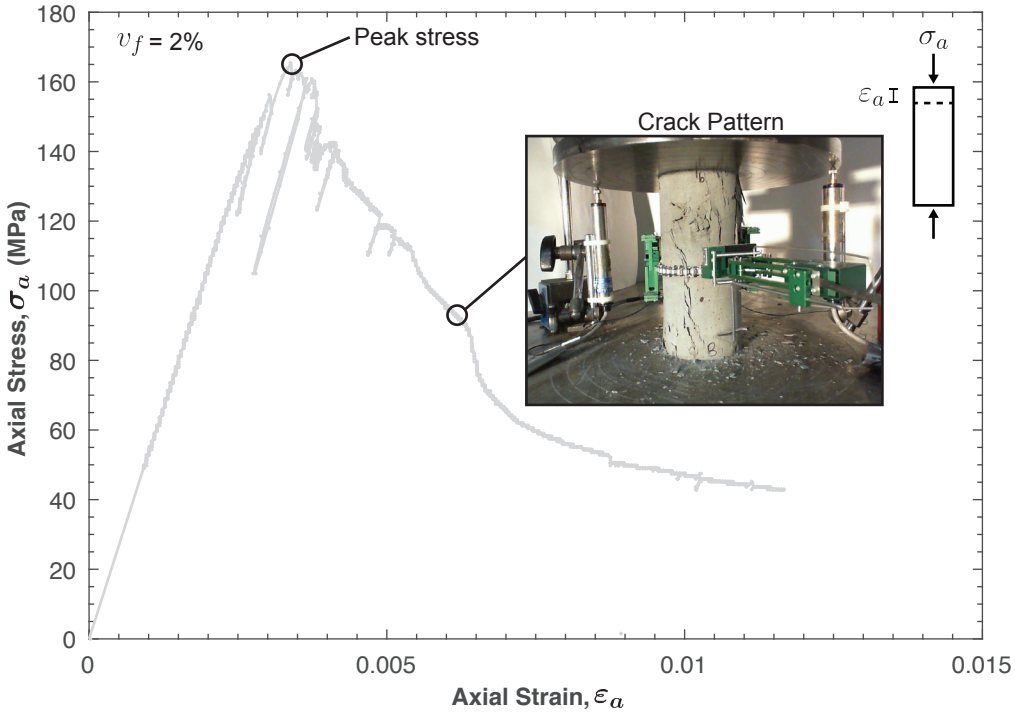

Figure 6.8: Sample compression axial stress - axial strain response of UHPC with 2% fibers by volume.

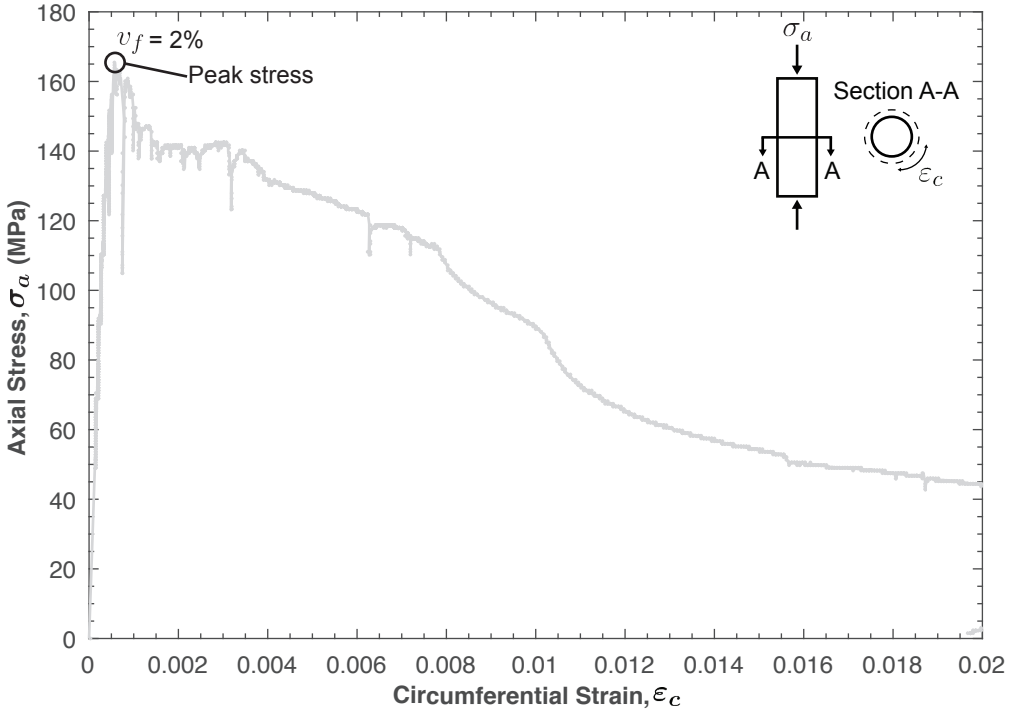

Figure 6.9: Sample compression axial stress - circumferential strain response of UHPC with 2% fibers by volume.

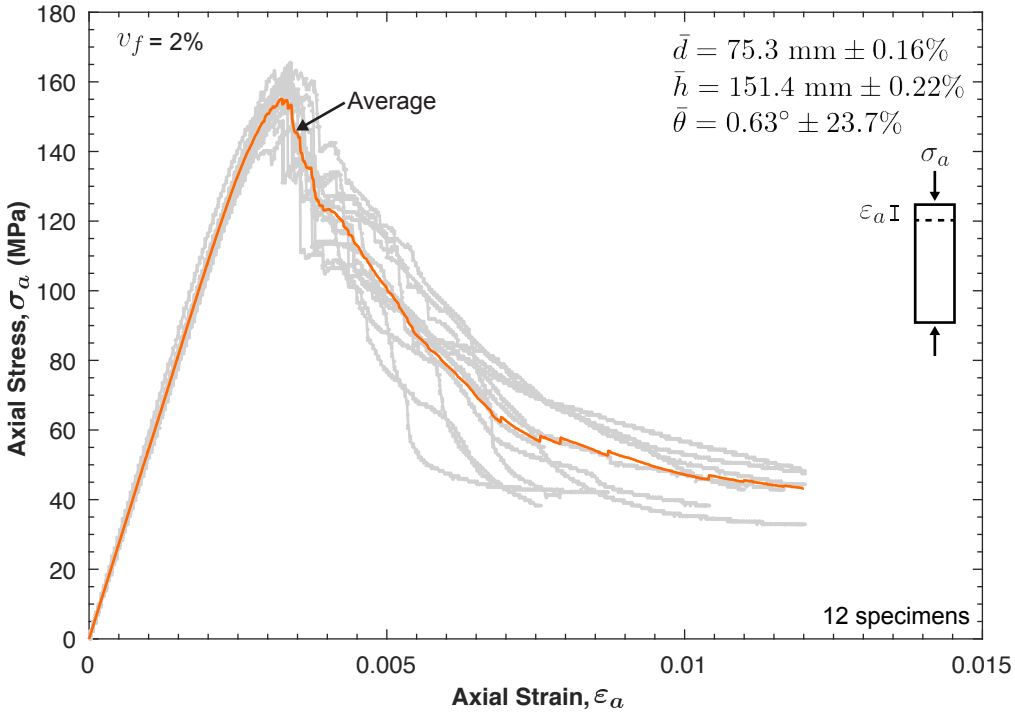

Figure 6.10: Average compression axial stress - axial strain response of UHPC with 2% fibers by volume.

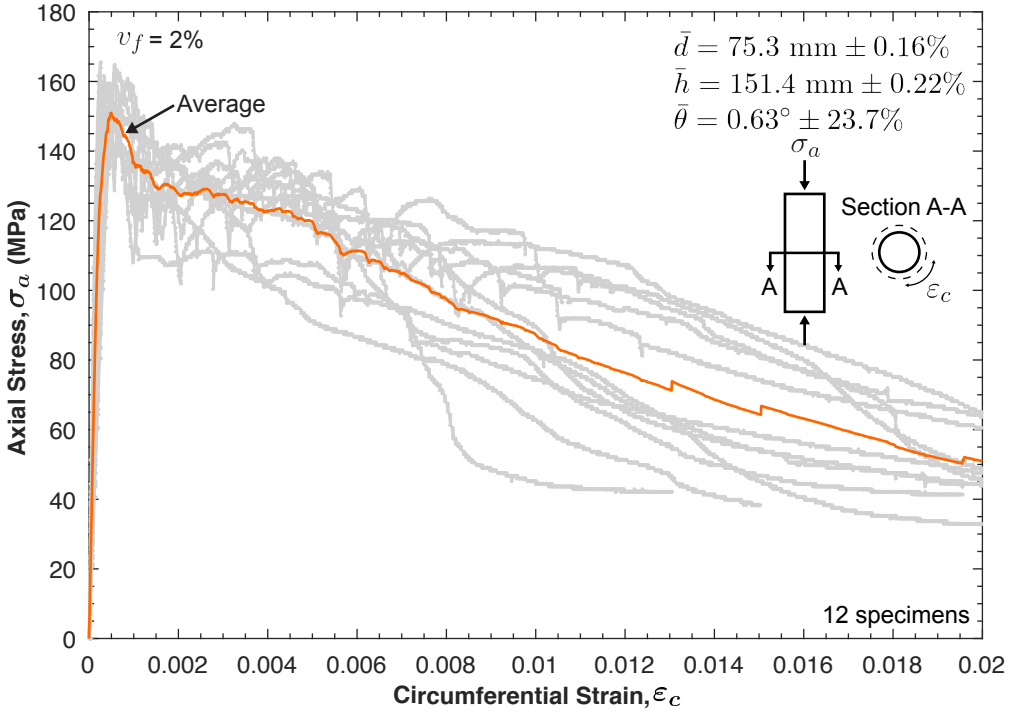

Figure 6.11: Average compression axial stress - circumferential strain response of UHPC with 2% fibers by volume.

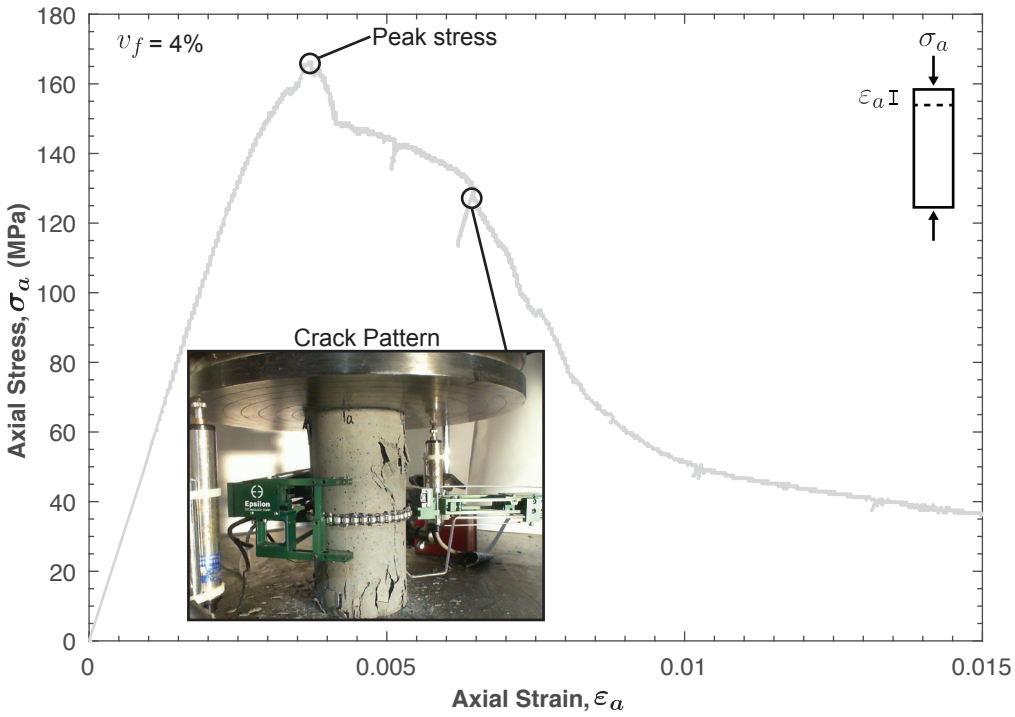

Figure 6.12: Sample compression axial stress - axial strain response of UHPC with 4% fibers by volume.

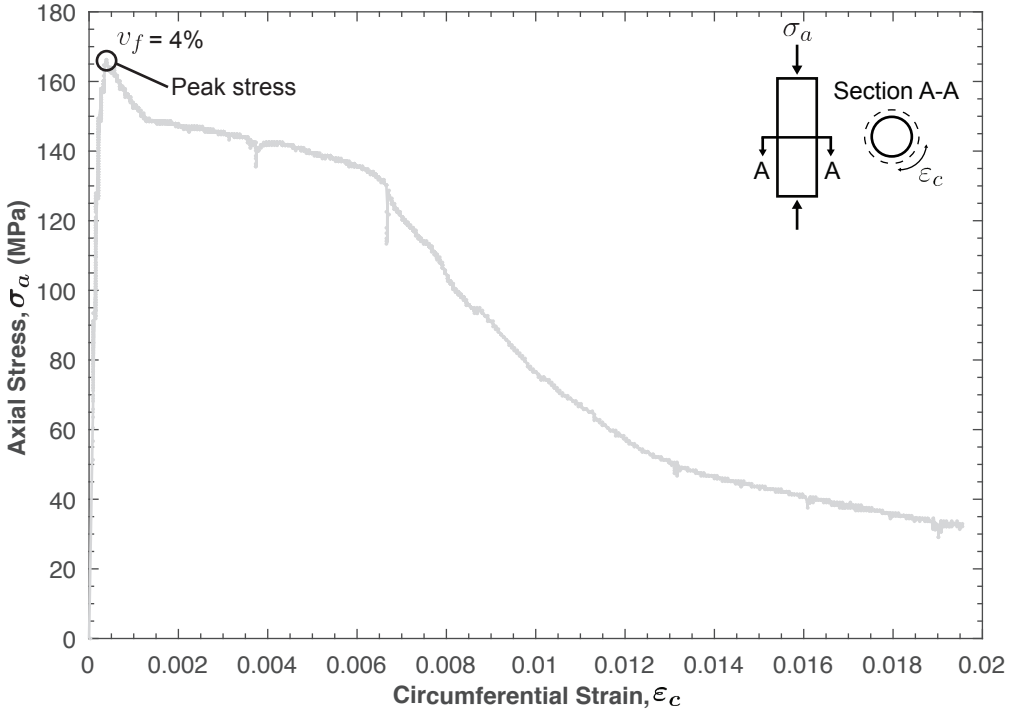

Figure 6.13: Sample compression axial stress - circumferential strain response of UHPC with 4% fibers by volume.

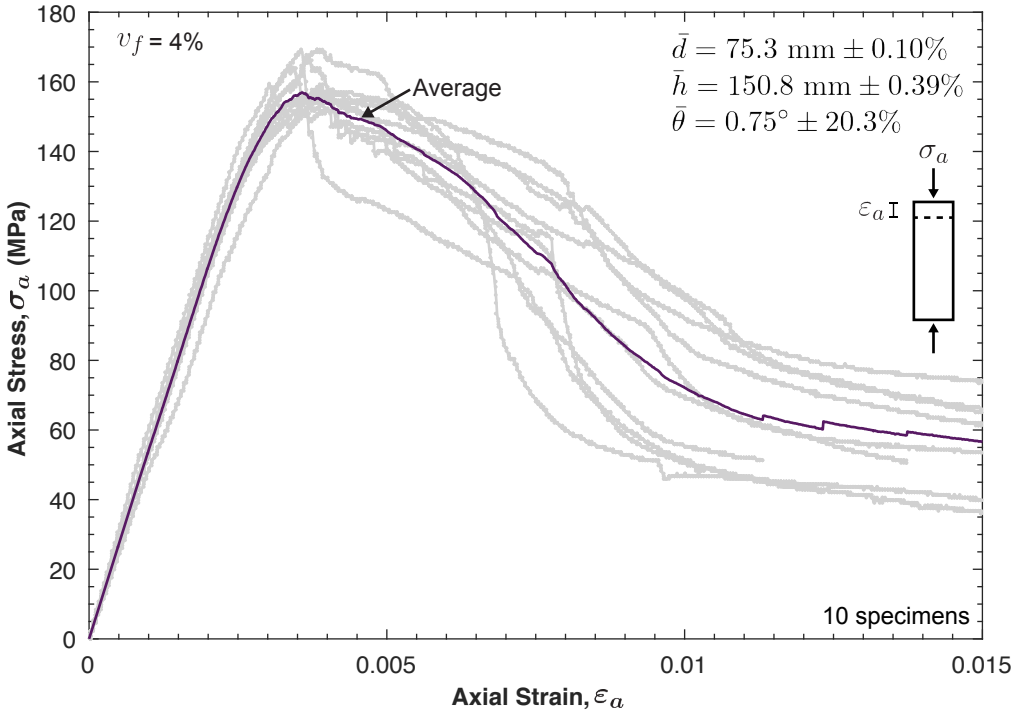

Figure 6.14: Sample compression axial stress - axial strain response of UHPC with 4% fibers by volume.

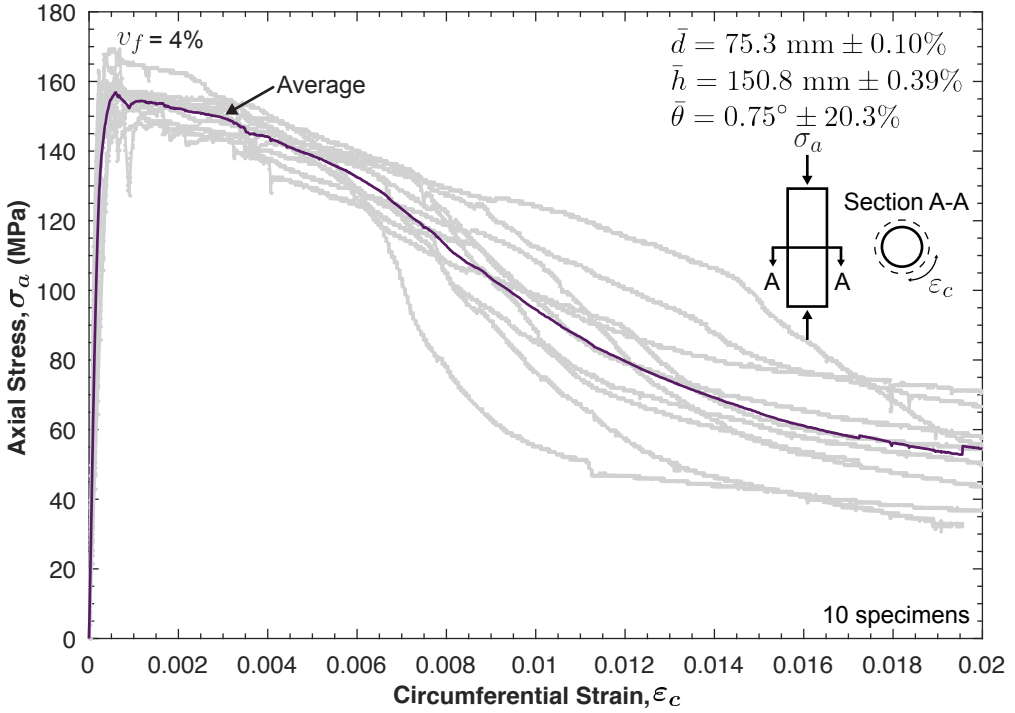

Figure 6.15: Average compression axial stress - circumferential strain response of UHPC with 4% fibers by volume.

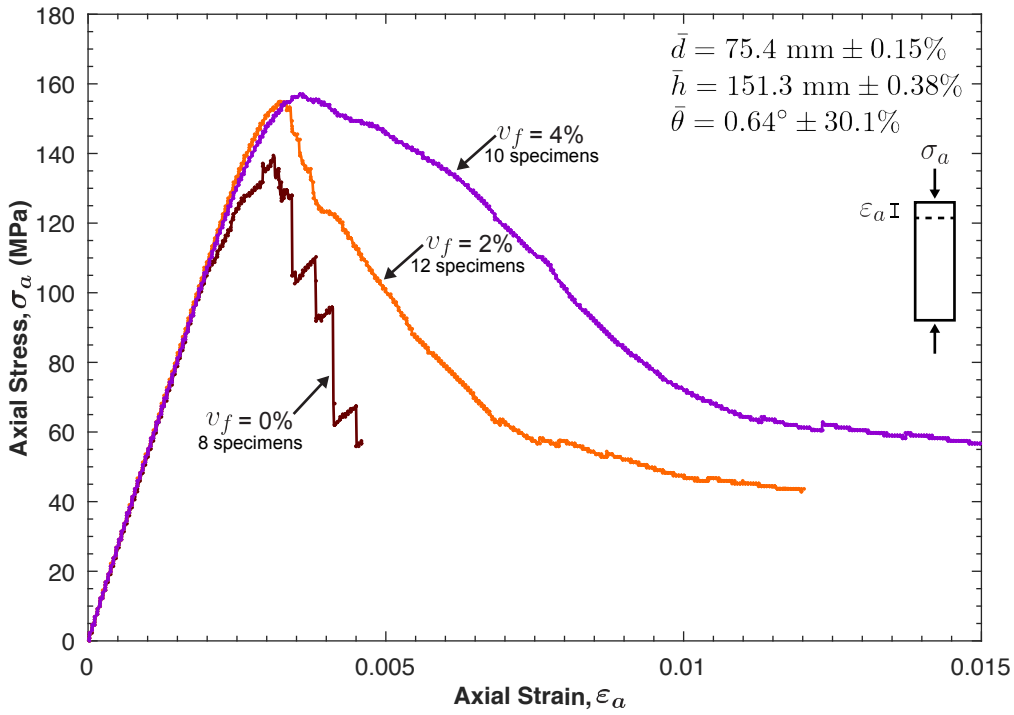

Figure 6.16: Average compression axial stress - axial strain response of UHPC with 0%, 2%, and 4% fibers by volume.

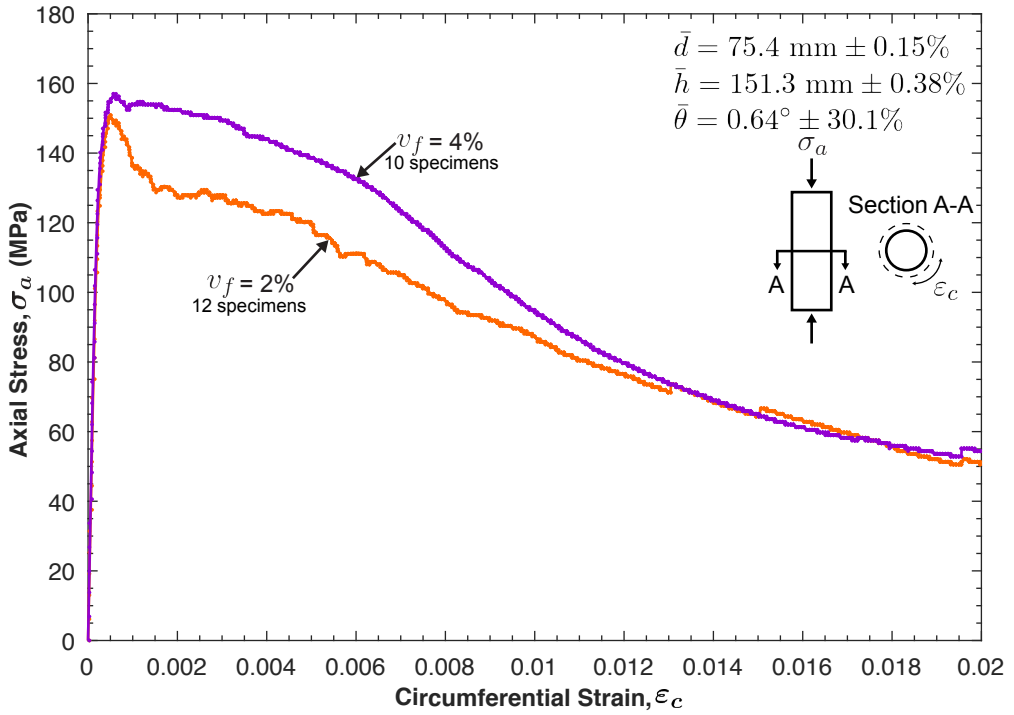

Figure 6.17: Average compression axial stress - circumferential strain response of UHPC with 0%, 2%, and 4% fibers by volume.

6.4.3 Poisson's Ratio

A summary of UHPC compression properties, including the modulus of elasticity, Poisson's ratio, compression strength, and strain at ultimate capacity, for $v_f = 0\%$, 2%, and 4% are shown in Table 6.2. The average Poisson's ratio values are calculated following Eq. 6.1 for 5 individually tested cylinders for each fiber volume. As shown in Table 6.2, the Poisson's ratio results for UHPC at different fiber volumes are similar with an average value of 0.17 ± 10%. It is concluded that fibers have minimal effect on the elastic properties of UHPC as they activated and most effective when cracks initiate and starts to propagate in the material.

Table 6.2: Summary of UHPC compression properties.

v_f (%)	$\bar{E}$ (GPa)	$\bar{\nu}$	$\bar{f}_c$ (MPa)	$\bar{\varepsilon}_c$
0	53.3 ± 5%	0.16 ± 16%	122 ± 18%	0.0026 ± 21%
2	54.3 ± 3%	0.16 ± 5%	158 ± 3%	0.0033 ± 4%
4	53.3 ± 5%	0.18 ± 3%	161 ± 3%	0.0038 ± 12%
Ave	53.7 ± 4%	0.17 ± 10%		

6.4.4 Compressive strength evolution with concrete age

The UHPC compressive strength gain behavior is investigated herein by compiling the cube compressive strength data for $v_f = 0\%$, 2%, and 4% according to the concrete age after casting. Cube compression tests were performed at 4, 7, 14, and 28 days, and at the time of testing a specific UHPC property (i.e. fracture, tension, and fiber pullout). The time frame covered by cube compression tests included the period within which all the specimens listed in the overall experimental program, shown in Table 5.4, were tested.

Tables 6.3, 6.4, and 6.5, and Figs. 6.18, 6.19, and 6.20 present a compilation of the cube compression data as a function of time for $v_f = 0\%$, 2%, and 4%, respectively. The Weibull cumulative function, obtained by Graybeal (2006), to estimate the strength gain behavior for any time after 0.9 days from casting of UHPC with $v_f = 2\%$ is presented in Eq. 6.2. The function calculates the compressive strength, $f_{c,t}$, in MPa at time, t, in days after casting based on the 28-day compressive strength, $f_{c,28}$, in MPa; it is plotted, as thick solid lines,

against the experimental results obtained in this research in Fig. 6.18, 6.19, and 6.20.

$$f_{c,t} = f_{c,28}\left[1 - e^{-\left(\frac{t-0.9}{3}\right)^{0.6}}\right] \tag{6.2}$$

The cube compression results indicate that UHPC rapidly gains strength over the course of 4 days reaching approximately 75% of its 28-day compressive strength, $f_{c,28}$. The strength gain rate decreases afterwards to reach more than 90% of $f_{c,28}$ at 14 days from casting. The strength continues to slowly increase after 28 days, particularly for UHPC with $v_f = 2\%$ and 4%, reaching around 20% of $f_{c,28}$ at approximately 200 days, after which the strength appears to remain constant.

Eq. 6.2 accurately describes the strength evolution with time until about 100 days after casting, but underestimate the rate of strength gain afterwards. However, more data is needed to prove such increase in strength after 100 days as the tested specimens presented in this research were limited.

6.4.5 Specimen geometry effect on compressive strength

As mentioned previously, the compression tests on the cylinders reported in the previous sections were performed at 400 to 410 days after casting. At that time, the cylinders ultimate strength was 122 MPa ± 18%, 158 ± 3%, and 161 MPa ± 3%, for $v_f = 0\%$, 2%, and 4%, respectively. The cube strength results for approximately the same time period were respectively 124 MPa ± 12%, 174 MPa ± 7%, and 165 MPa ± 11%. These results were obtained by averaging the values reported in the last two rows of Tables 6.3, 6.4, and 6.5 for $v_f = 0\%$, 2%, and 4%, respectively.

It can be concluded that the cube compressive strength is about 2%, 9%, and 3% greater than the strength obtained by cylinders. These results are in general agreement with the observed 5% increase in cube strength reported by Graybeal (2006). This increase in strength is expected due to the cube's shorter aspect ratio, which generates larger lateral confinement caused by the machine platens.

Finally, the compression experimental program showed that performing compression testing on cylindrical specimens results in lower standard deviations. The standard deviations also decreased with the addition of fibers in the matrix. These results were expected since the geometric imperfections and the concrete heterogeneities have a more pronouced effect in smaller and unreinforced specimens.

Table 6.3: Cube compression strength as a function of time after casting for $v_f = 0\%$.

Batch ID	**Age (days)**	**Tested Specimens**	$\bar{f}_c$ **(MPa)**
I,II	4	10	101 ± 6%
I,II	7	10	124 ± 8%
I,II	14	9	121 ± 13%
II	17	3	108 ± 8%
I,II,III	28	12	137 ± 9%
III	61	4	126 ± 16%
III	63	4	112 ± 10%
III	65	3	136 ± 2%
II	235	5	103 ± 21%
II	237	5	133 ± 14%
I	243	4	146 ± 7%
I	245	5	134 ± 23%
III	316	5	119 ± 10%
II	430	4	124 ± 16%
I	434	5	123 ± 8%

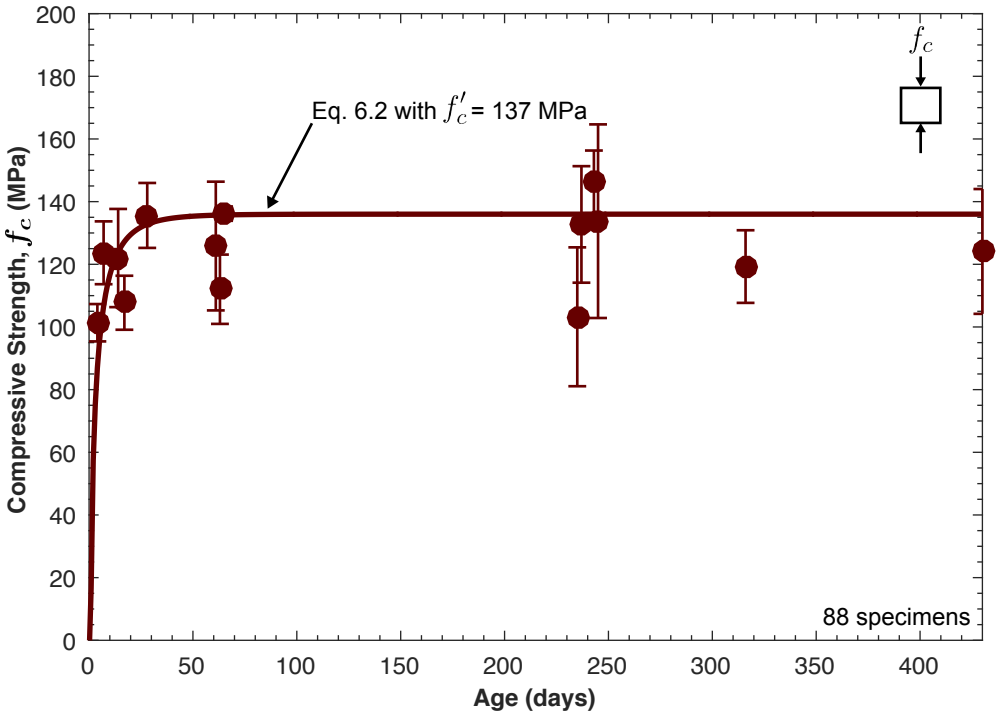

Figure 6.18: Cube compression strength as function of time after casting for $v_f = 0\%$.

Table 6.4: Cube compression strength as function of time after casting for $v_f = 2\%$

Batch ID	**Age (days)**	**Tested Specimens**	$\bar{f}_c$ **(MPa)**
IV,V	4	8	111 ± 6%
IV,V	7	9	119 ± 12%
IV,V	14	8	145 ± 7%
IV,V,VI	28	13	148 ± 7%
VII	37	5	133 ± 7%
VI	56	3	141 ± 9%
VI	57	3	145 ± 12%
VI	60	3	157 ± 4%
VI	62	4	151 ± 7%
VII	64	5	135 ± 2%
VI	66	3	146 ± 2%
V	187	4	177 ± 8%
IV	235	4	183 ± 3%
VI	269	5	158 ± 9%
IV	386	5	175 ± 7%
IV	428	5	173 ± 7%

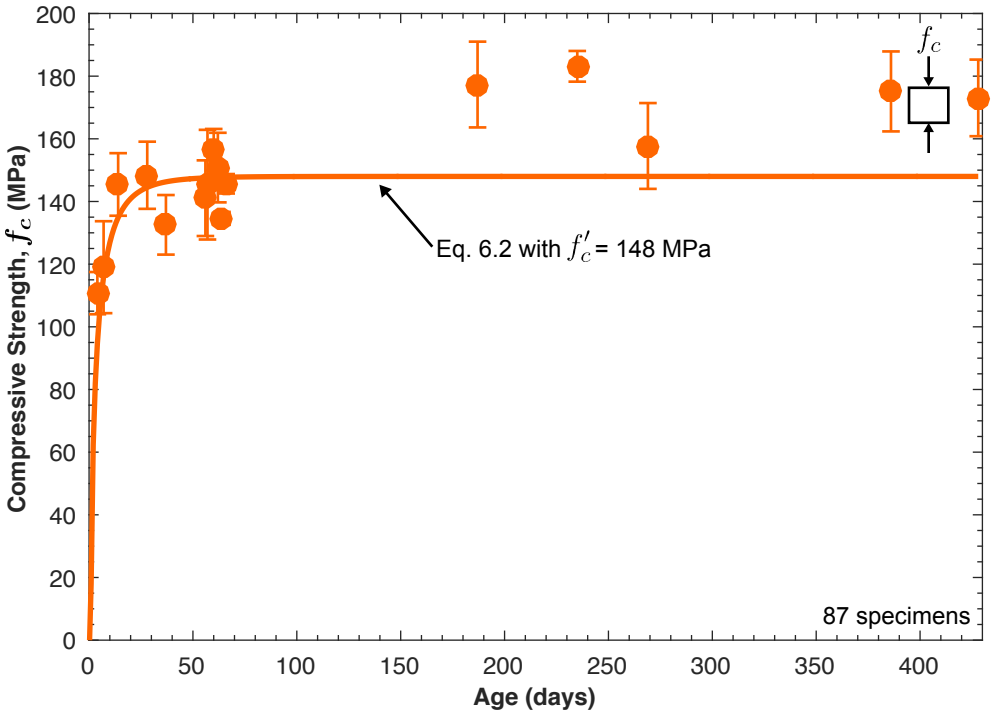

Figure 6.19: Cube compression strength as function of time after casting for $v_f = 2\%$.

Table 6.5: Cube compression strength as function of time after casting for $v_f = 4\%$.

Batch ID	**Age (days)**	**Tested Specimens**	$\bar{f}_c$ **(MPa)**
VIII,IX	4	9	112 ± 9%
VIII,IX	7	8	133 ± 7%
VIII,IX	14	8	147 ± 7%
VIII,IX,X	28	13	151 ± 15%
X	82	3	137 ± 6%
X	91	4	157 ± 10%
X	93	4	153 ± 5%
X	95	3	163 ± 7%
IX	184	4	178 ± 7%
VIII	224	4	182 ± 9%
VIII	231	4	187 ± 7%
X	290	5	138 ± 20%
IX	382	5	160 ± 8%
VIII	423	5	169 ± 14%

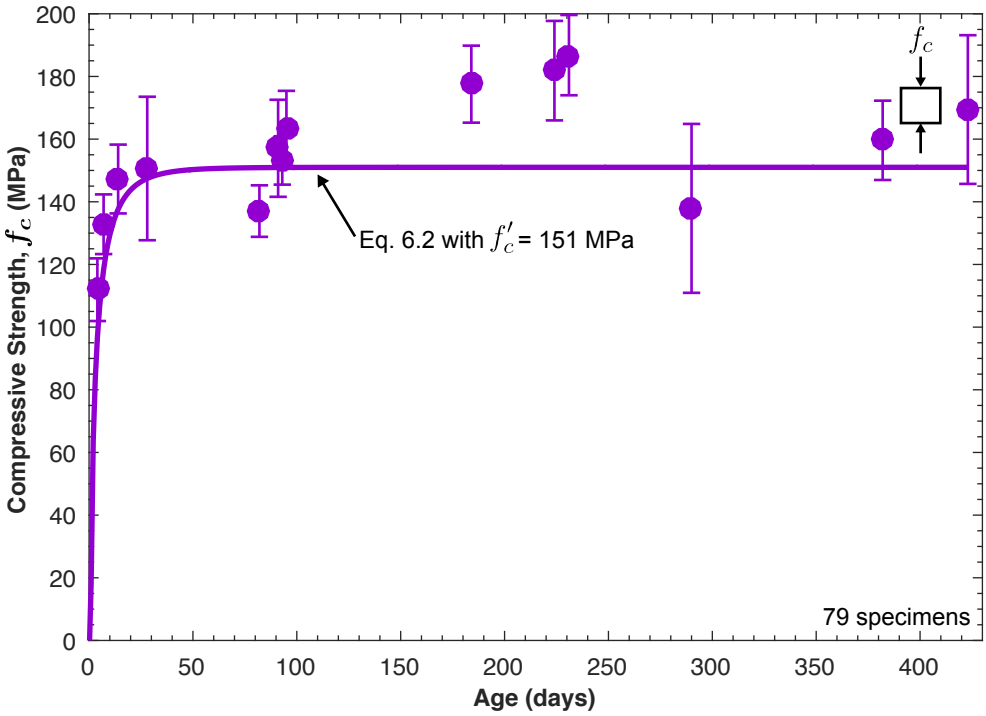

Figure 6.20: Cube compression strength as function of time after casting for $v_f = 4\%$.

Chapter 7

UHPC Fracture Behavior to Inform Computational Models

This chapter characterizes the basic behaviors of individual cracks in UHPC without and with fiber reinforcement through a set of three point bending tests performed on nothed beams. Sections 7.1 and 7.2 respectively describe the fracture toughness test matrix and the specimens' preparation procedure. Section 7.3 details the test setup, instrumentation, and procedure. Finally, section 7.4 discusses the experimental results including the effects of fiber orientation on the fracture response and crack propagation in fiber-reinforced UHPC.

7.1 Test matrix

The UHPC fracture behavior at fiber contents of 0%, 2% and 4% was characterized from 36 notched beam specimens obtained from the six UHPC batches shown in Table 7.1. The specimens were tested between 176 and 245 days after placement. The compression strength at the time of fracture testing was obtained from companion cube specimens and reported in Table 7.1.

Table 7.1: UHPC fracture behavior test matrix.

Batch ID	v_f (%)	**Tested property**	**Tested specimens**	**Age (days)**	$\bar{f}_c$ **(MPa)**
I	0	Fracture Cube strength	5 5	243	146 ± 7%
II	0	Fracture Cube strength	6 5	235	103 ± 21%
IV	2	Fracture	5	179	-
V	2	Fracture Cube strength	6 4	187	177 ± 8%
VIII	4	Fracture	8	176	-
IX	4	Fracture Cube strength	6 4	184	178 ± 7%

7.2 Specimen preparation

The fracture specimens were placed in specially designed Polyvinyl chloride (PVC) molds having an width of 51 mm, a height of 115 mm, and a length of 508 mm. The molds are made of 25 mm thick PVC to ensure rigidity of the form, to prevent deformations, and to facilitate demolding without using form oil. Since fiber orientation influences crack initiation and propagation, it was addressed by either placing fresh UHPC vertically into the molds at different locations (Fig. 7.1a,b) or from one side of the molds, allowing the material to flow to the other side as it fills the volume (Fig. 7.1c). The vertical placement technique is adopted in batches IV and VIII in an attempt to obtain a random fiber distribution. The second placement method was adopted in batches V and IX to align the fibers parallel to the specimens bottom surface (Table 7.1).

The specimens were demolded 48 hours after placement and the 51 mm side length where fresh UHPC was placed was cut using a concrete saw. The specimens were then transported by land to, and from, the nearest waterjet cutting facility (Lynchburg, VA) where the top 13 mm of the height was cut and a 5 mm wide and 25 mm high round tip notch in the middle of each specimen's length was introduced. Waterjet cutting was chosen to ensure plane and parallel beam surfaces and to reduce geometric irregularities between the tested specimens. Afterwards, the specimens were labeled, measured, and marked for equipment installation.

The following measurements were recorded for each tested specimen and reported in Appendix C: the beam width at eleven locations, beam height at ten, and beam length at four; the notch width and height were measured at two locations each. The final beams had an average width, $\bar{W}$, of 51.2 mm ± 1.7%, an average height, $\bar{H}$, of 101.0 mm ± 0.9%, and an average length of 457.9 mm ± 1.7%. The notches had an average width, $\bar{w}$, of 5.9 mm ± 9.9% and and average height, $\bar{h}$, of 25.9 mm ± 0.7%.

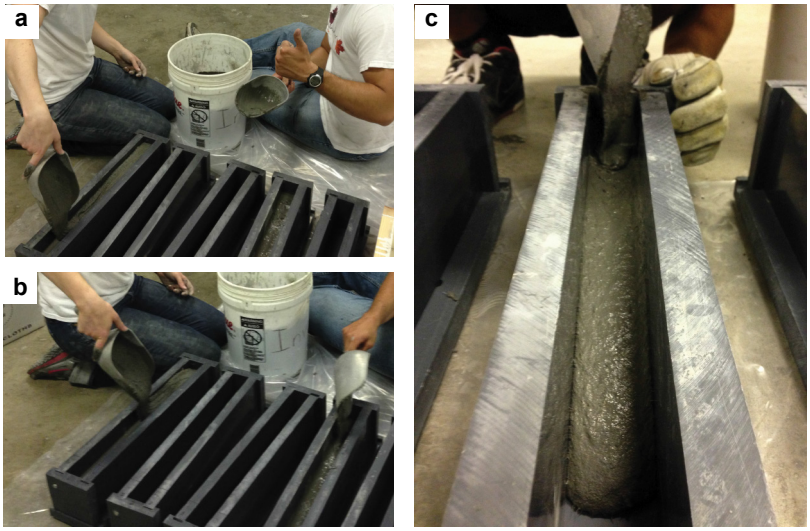

Figure 7.1: Fresh UHPC with $v_f = 2\%$ and 4% placed: a) vertically and b) from one side of the mold.

7.3 Test setup, instrumentation, and procedure

The test setup and procedure followed recommendations by Graybeal (2006), which are partially based on ASTM E1820 *Standard Test Method for Measurement of Fracture Toughness* (2015). The fracture tests were completed in an MTS 50 kN capacity compression machine, with load readings accuracy of 0.2%. The beams rested on two 51 mm diameter rigid steel rods at a span of 406 mm, and were loaded at the mid-span of the top flange as shown in Fig. 7.2. More details on the fracture test fixture design and dimensions are reported Appendix D.

A clip-on gage (Epsilon 3541), with 5 mm travel range and an accuracy of 0.2%, was mounted to two knife edges glued to the bottom flange at the notch boundaries, to measure the crack mouth opening displacement (CMOD). The axial displacement was measured using an axial extensometer (MTS 632.11B-20), with 7.6 mm travel and an accuracy of 0.2%.

The axial extensometer was attached to two smooth steel rods extending between the machine top fixture and a bottom fixed reference (Fig. 7.2). Unfortunately, this extensometer slipped during testing and its readings are not reliable. The fracture tests were displacement-controlled with a constant CMOD rate of 0.006 mm/s for the beams without fibers and 0.013 mm/s for the ones with fibers. The CMOD rate was increased by 3 to 5 times during the post-peak portion of the fiber-reinforced specimens.

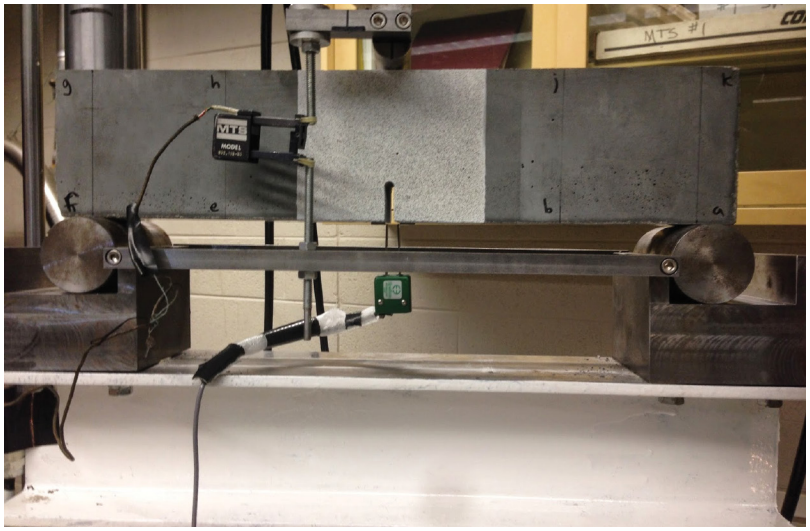

Figure 7.2: Fracture toughness test setup.

7.4 Results

7.4.1 Fracture behavior of UHPC without fibers

The individual load-CMOD trends for the fracture tests without fiber reinforcement are shown in Fig. 7.3, with the average trend plotted as a thicker solid line. The average curve is calculated from the individual load values at one value of CMOD. At the end of each test, the specimens split in two equal pieces (Fig. 7.3) at an average crack opening of 0.11 mm ± 20.2%. The load-CMOD curves are initially linear then becomes non-linear when cracks start to form and propagate. The average peak load was 2.1 kN ± 10.8%, which occurred at an average crack mouth opening of 0.021 mm ± 22.5%.

The load versus axial displacement individual trends are shown in Fig. 7.4. The displacement values in these trends are not reliable as the axial extensometer experienced slippage during the test, which resulted in mild initial pre-peak slopes and sharp decreases

in loads in the post-peak portion as shown in Fig. 7.4. However, in absence of any other approach to obtain the fracture energy, G_F, of UHPC without fibers, which is a key parameter in the computational models of concrete, G_F was estimated using the following formula: $G_F = U_o/A$, where U_o is the total area under the load vs. axial mid-span displacement curve, and $A = W(H - h)$ is the ligament area. This formula is similar to the one proposed by the RILEM technical committee 50-FMC (1985), $G_F = (U_o + mgd)/A$, but ignores the beam weight, mg, correction since the experimental axial displacement at fracture, d, cannot be used. Following this approximation, the average fracture energy was found to be $\bar{G}_F = 57.8$ N-m/m^2 $\pm$ 13.2%. This value is in line with the reported fracture energy range of 12 to 50 N-m/m^2 for similar cementitious composites (Kang and Kim, 2011; Richard and Cheyrezy, 1995).

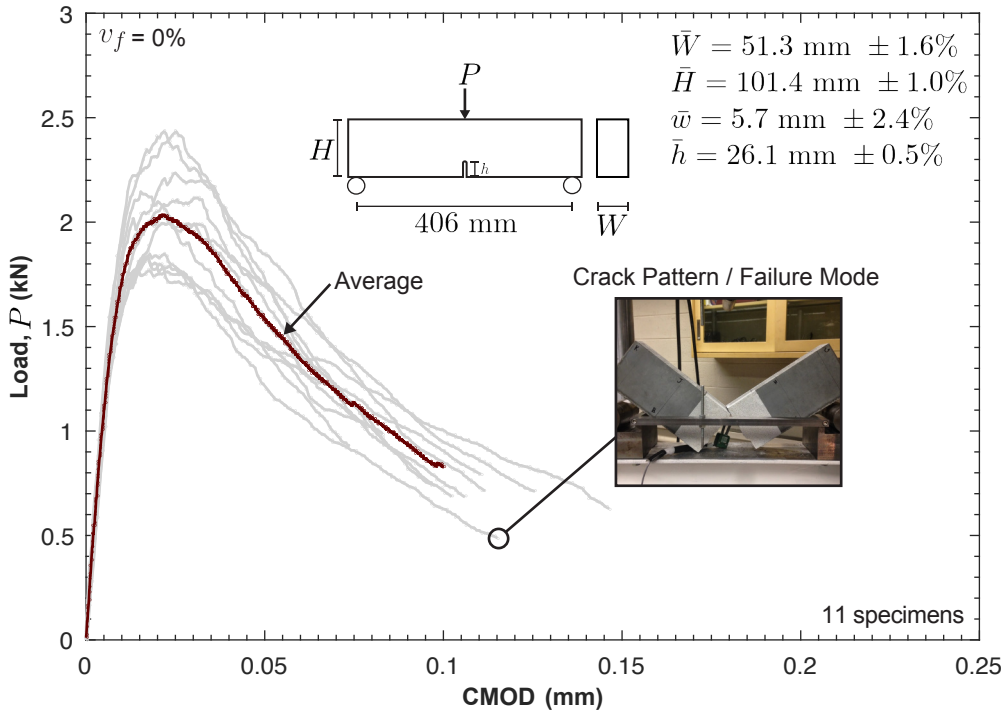

Figure 7.3: Individual and average load-CMOD trends for UHPC without fibers.

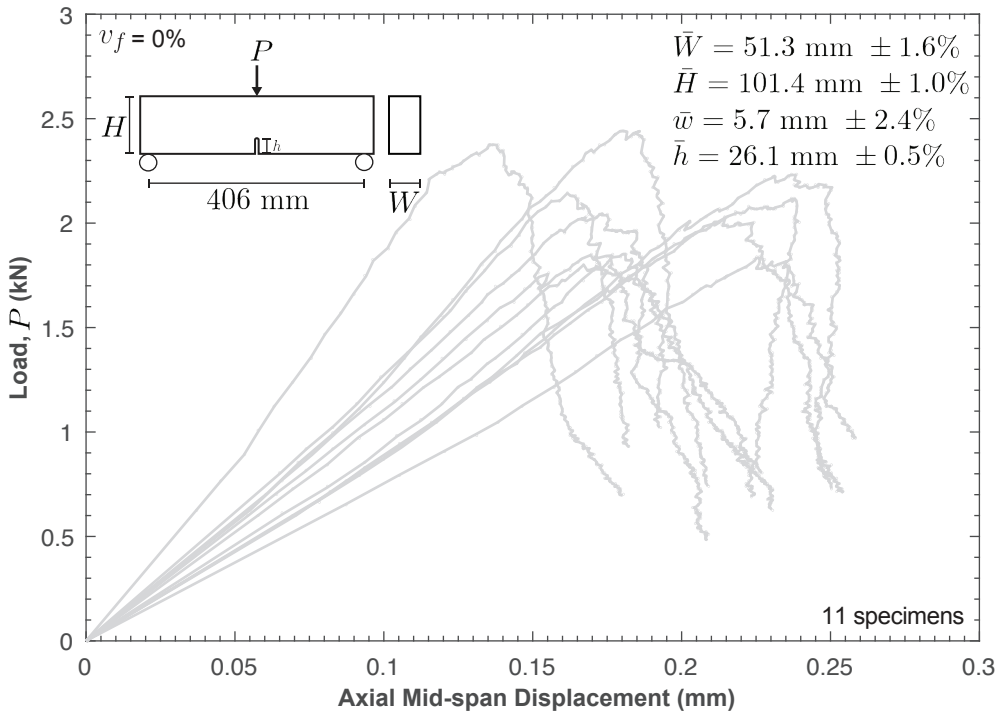

Figure 7.4: Individual load vs. axial mid-span displacement trends for UHPC without fibers.

7.4.2 Fracture behavior of UHPC with fibers

The individual load-CMOD trends for the fracture of UHPC containing 2% by volume ($v_f = 2\%$) are plotted in Figs. 7.5 and 7.6 for UHPC placed vertically and from one side of the molds, respectively. The average trends are plotted as thicker solid lines above the individual results. The fiber reinforced specimens were stopped at a CMOD of 3.5 mm without complete failure. Similarly, the individual trends for UHPC with $v_f = 4\%$ are shown in Figs. 7.7 and 7.8 for the two placement methods. The average load-CMOD trends for UHPC with $v_f = 0\%, 2\%$, and 4% are compared in Fig. 7.9.

The average peak fracture load increased from 2.1 kN ± 10.8% for the unreinforced specimens to 10.5 kN ± 13.2% when UHPC with $v_f = 2\%$ was placed vertically into the molds. This corresponds to 400% increase in the load carrying capacity when fibers are introduced into the matrix highlighting the fiber efficiency in bridging cracks and improving the fracture performance of the material. The CMOD at peak load also increased from 0.021 mm ± 22.5% for $v_f = 0\%$ to 0.49 mm ± 15.7% for UHPC placed vertically with $v_f = 2\%$. When fresh UHPC flowed from one side of the mold to the other, fibers were preferentially

aligned parallel to the bottom side of the mold and perpendicular to the cracking plane, which limited crack propagation and increased the peak load to 12.6 kN ± 8.5% (20% higher than the random placement method). The CMOD at peak load was 0.63 mm ± 31.7%.

The average peak load further increased to 17.7 kN ± 7.0% when fresh UHPC was vertically placed at $v_f = 4\%$, which resulted in a larger number of fibers bridging the cracks. The CMOD at peak load was 0.74 mm ± 25.3%. However, placing fresh UHPC at $v_f = 4\%$ from one side reduced the fracture peak load to 15.7 kN (10% decrease compared to random placement). The CMOD at peak load remained in the same range with 0.78 mm ± 14.2%. It is hypothesized that with higher fiber volume contents, chunks of fibers are formed as the concrete flows from one side of the mold to the other, which disturbs fiber alignment. This has more likely occurred because the UHPC mix adopted in this research was optimized for $v_f = 2\%$ to ensure adequate flowability of the wet mix. When adding 4% fibers by volume without changing the mix proportions of Table 5.3, it was observed that the flow of UHPC was very slow and the fibers tended to roll in chunks as the mix was flowing from one side to the other. The fiber alignment of the fracture specimens at each placement method will be approximated using the lattice discrete particle model (LDPM) in Chapter 10.

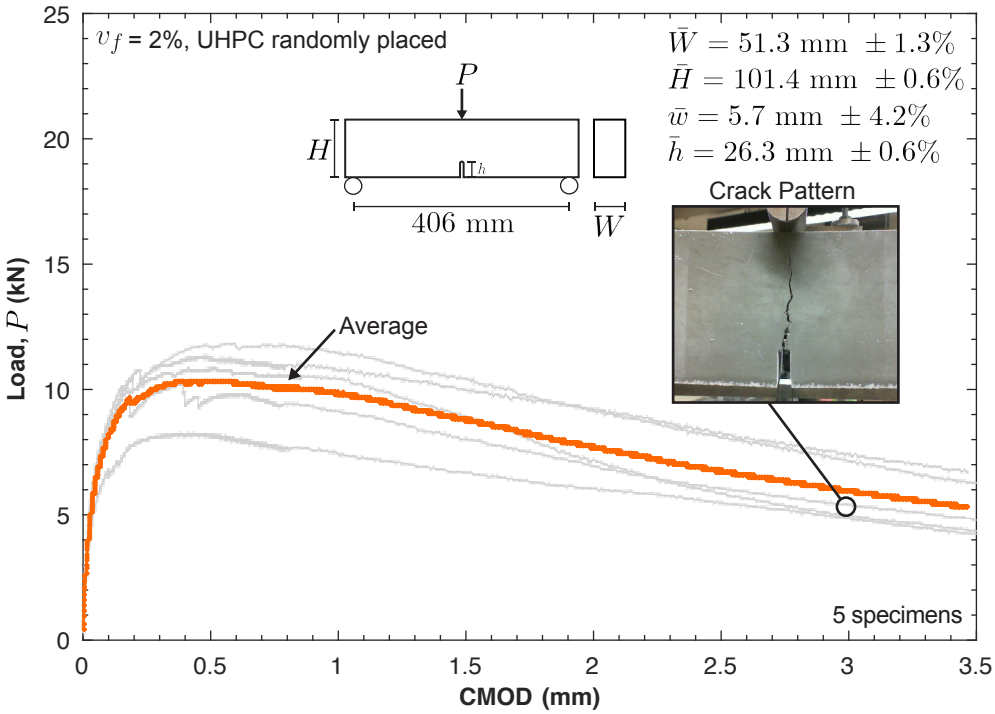

Figure 7.5: Individual and average load-CMOD trends for UHPC with $v_f = 2\%$ placed vertically into the beam molds.

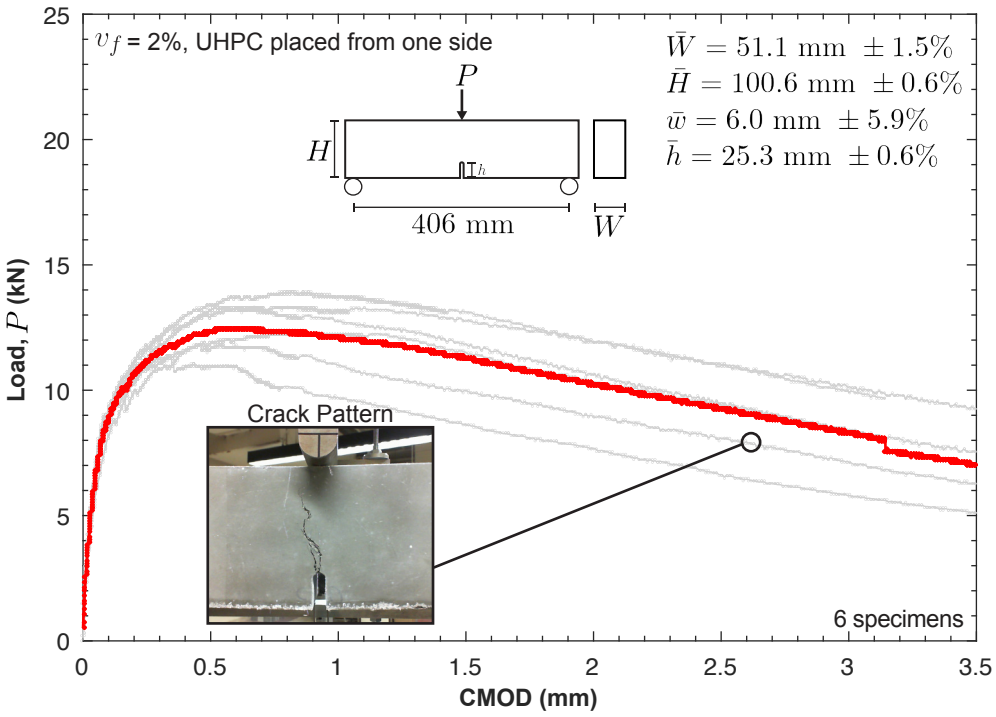

Figure 7.6: Individual and average load-CMOD trends for UHPC with $v_f = 2\%$ placed one side of the beam molds.

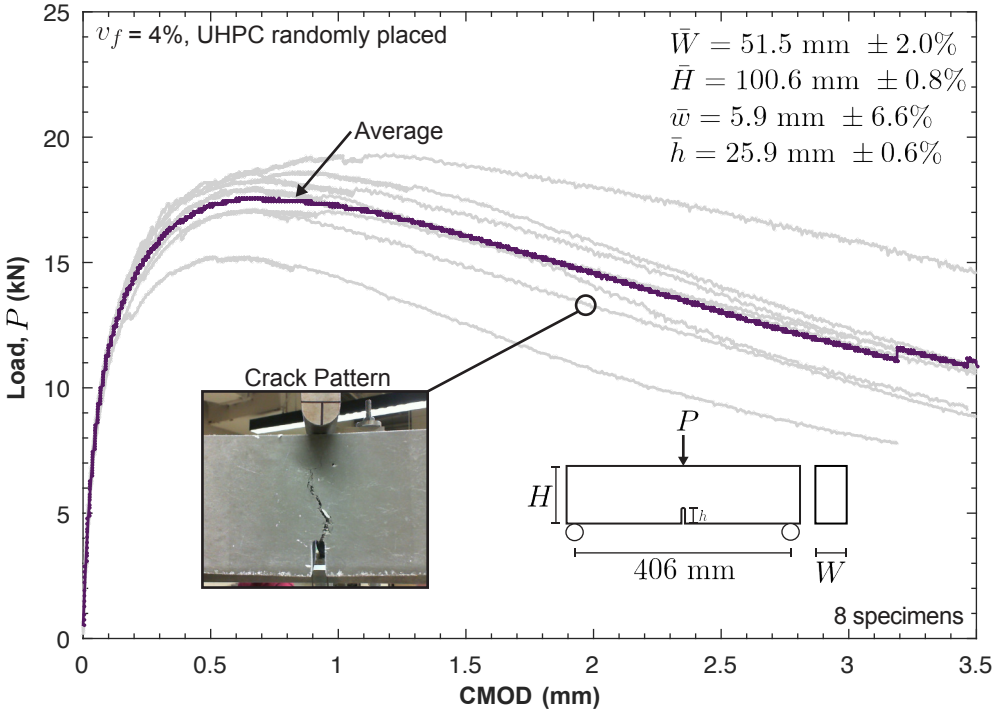

Figure 7.7: Individual and average load-CMOD trends for UHPC with $v_f = 4\%$ placed vertically into the beam molds.

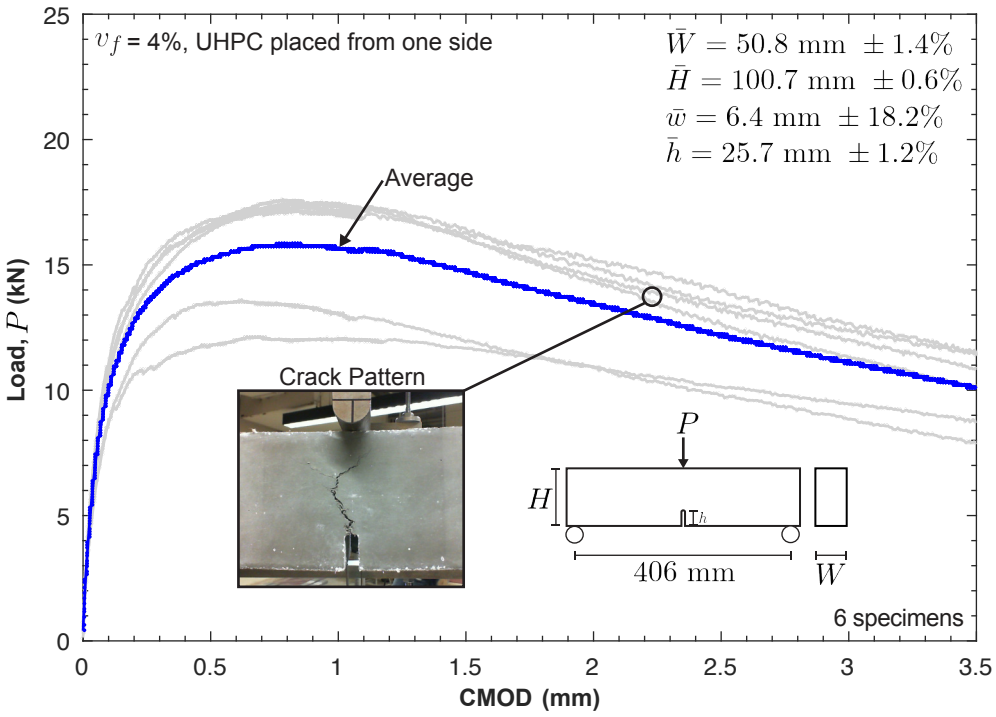

Figure 7.8: Individual and average load-CMOD trends for UHPC with $v_f = 4\%$ placed one side of the beam molds.

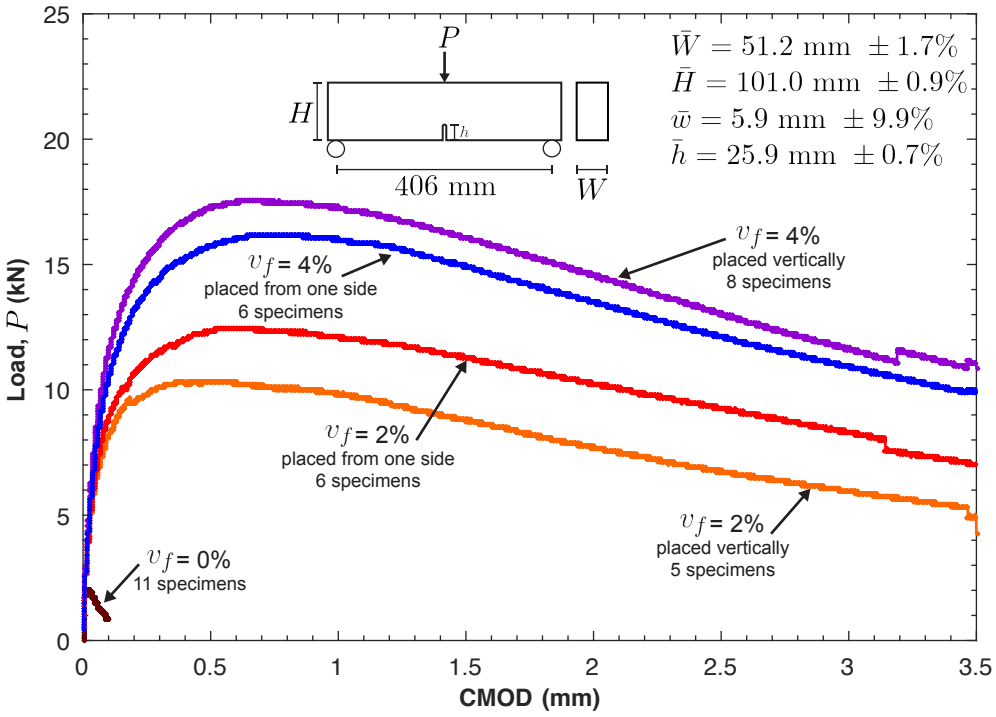

Figure 7.9: Average load-CMOD trends for UHPC at different fiber contents and placement methods.

Chapter 8

UHPC Tensile Behavior to Inform Computational Models

This chapter characterizes the ultimate tension strength of UHPC with and without fibers from two experimental investigations: mortar briquette direct tension and split cylinder tests. The test matrix, specimen preparation, and test setup, instrumentation, and procedure are outlined in sections 8.1 through 8.3, respectively. Section 8.4 discusses the ultimate tension strength results highlighting the biaxial stress state and fiber alignment effects. The direct tension tests performed by Maya Duque and Graybeal (2016) for UHPC with 2% fiber by volume are summerized in section 8.5. These tests characterized the UHPC tensile axial stress-strain trends at various fiber orientation distributions and are used in the subsequent chapters to validate the computational models' predictive capabilities.

8.1 Test Matrix

The UHPC tension strength at fiber contents of 0%, 2%, and 4% was characterized from 41 dogbone-shaped specimens tested in direct tension and 20 cylindrical specimens tested by applying a compressive line load along the cylinder's length (Table 8.1). The tests were performed between 231 and 245 days after placement. The compression strength at the time of tension testing was obtained from companion cube specimens and reported in Table 8.1.

Table 8.1: UHPC tension test matrix.

Batch ID	v_f (%)	**Tested property**	**Tested specimens**	**Age (days)**	$\bar{f}_c$ (MPa)
I	0	Direct tension	10	245	134 ± 23%
		Split cylinder	5		
		Cube compression	5		
II	0	Direct tension	9	237	133 ± 14%
		Split cylinder	5		
		Cube compression	5		
IV	2	Direct tension	12	235	183 ± 3%
		Split cylinder	5		
		Cube compression	4		
VIII	4	Direct tension	10	231	187 ± 7%
		Split cylinder	5		
		Cube compression	4		

8.2 Specimen preparation

The direct tension specimens were installed in dogbone-shaped steel molds having a height of 76 mm, a width of 25 mm mid-height, and a thickness of 25 mm. The tension specimens, described in AASHTO T132 *Standard Method of Test for Tensile Strength of Hydraulic Cement Mortars* (2009), have their smallest cross section at mid-height with an area of 625 mm^2. The specimens were vertically filled with fresh UHPC as shown in Fig. 8.1 and demolded after 48 hours. This placement method is expected to align the fibers parallel to the mold walls and perpendicular to the potential crack plane because the specimen's cross-sectional dimensions at mid-height (25 mm × 25 mm) are only twice as large as the fiber length ($L_f = 13$ mm).

Figure 8.1: Mortar briquette specimens preparation.

Similarly to the Poisson's ratio tests, the split tension tests were placed in cylindrical molds having a diameter of 102 mm and a height of 204 mm. The molds' heights were deliberately increased by approximately 10 mm using duct tape mounted around the top circumference as shown in Fig. 8.2a. The extra height was added to allow room for adequate surface preparation of hardened UHPC. The extra height was then cut using a concrete saw to remove any rough edges and to obtain a uniform height for all the cylinders (Fig. 8.2b). The following measurements were recorded for each tested cylinder and reported in Appendix E: the height at four locations and the diameter at three. The final cylinders had an average height, $\bar{h}$, of 201.1 mm $\pm$ 0.7%, and an average diameter, $\bar{d}$, of 101.8 mm $\pm$ 0.3%.

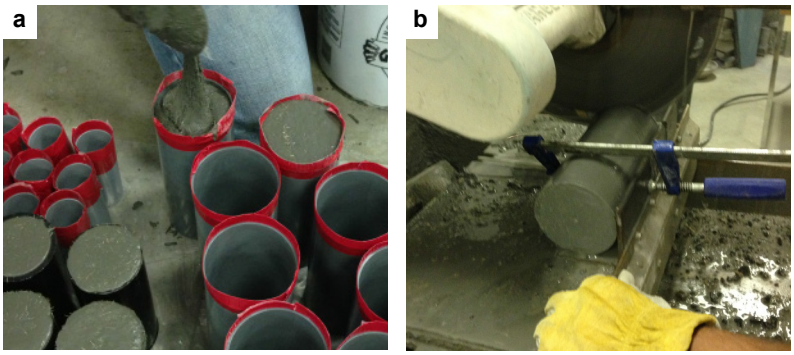

Figure 8.2: Split cylinder specimens preparation.

8.3 Test setup, instrumentation, and procedure

The mortar briquette specimens were placed in steel grip fixtures and placed in an MTS 150 kN capacity tension machine, with load readings accuracy of 0.2% (Fig. 8.3a). The displacement were measured using the crosshead LVDT, which had a travel of 250 mm

and an accuracy of 0.2%. The test setup and procedure was in accordance with AASHTO T132 (2009) with one exception: they were controlled at a constant displacement rate of 0.0085 mm/s for the unreinforced specimens and 0.025 mm/s for the specimens with fibers (Graybeal, 2006). This portion of the test was modified to gain insights on the UHPC post-peak behavior in tension.

The split cylinder test setup and procedure was in accordance with ASTM C496/C496M *Standard Test Method for Splitting Tensile Strength of Cylindrical Concrete Specimens* (2011). This test indirectly measure the tension strength of concrete by applying a line of compressive loads along the length of the cylinder. The specimens were installed in a steel jig that aligns the cylinder and bearing strips, and placed in an Forney 1,557 kN capacity, with 0.2% load reading accuracy. The cylinders were loaded in compression at a constant load rate of 3.4 MPa/sec, as suggested by Graybeal (2006), which is above the ASTM specified load rate of 1.0 MPa/sec. This rate was adopted because of the higher tension strength of UHPC compared to regular concrete for which the ASTM standard was designed for. The splitting tensile strength, $f_{t,s}$, was calculated according to the following equation:

$$f_{t,s} = \frac{2P}{\pi h d} \tag{8.1}$$

where P is load at failure, and h and d are the cylinder's height and diameter, respectively.

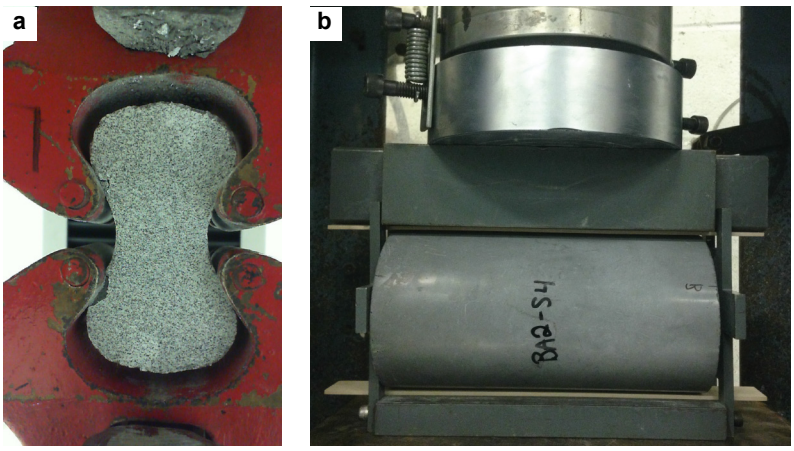

Figure 8.3: Test setups for: a) direct tension and b) split cylinder.

8.4 Results

8.4.1 Direct tension strength for UHPC without fibers

The individual axial stress-displacement trends for the direct tension tests without fiber reinforcement are shown in Fig. 8.4, with the average trend plotted as a thicker solid line. The average curve is calculated from the individual stress values at one value of displacement. The stress values are calculated by dividing the load values over the specimen's smallest cross sectional area where the failure is expected to occur. The displacement readings were not transformed into tensile strains because: (1) the specimens do not have a constant gage length where a uniform strain field can be assumed and (2) an extensometer that measure the crack opening displacement without the elastic displacements of the test setup was not installed.

The results show that the UHPC behaved linearly until reaching an average tensile strength, $\bar{f}_t$, of 8.5 MPa $\pm$ 8.9%, afterwhich the specimens split in two pieces as shown in Fig. 8.4. It was noticed that the failure plane did not always occur across the smallest cross sectional area at mid-height of the specimens. In a number of specimens, the crack initiated at the points of contact between the steel grip fixture and UHPC as shown in Fig. 8.4. It is hypothesized that this failure mode is attributed to three main reasons: (1) the gripping method practically applies the total load through four contact points creating regions of concentrated stresses, which deteriorate the concrete in those regions and initiates cracking (2) the gripping method allows partial rotation at both ends of the specimen, which creates situations of non-uniform loading conditions and stress concentrations; and (3) the existence of geometric non-linearities and imperfections in the concrete matrix, which causes premature cracking.

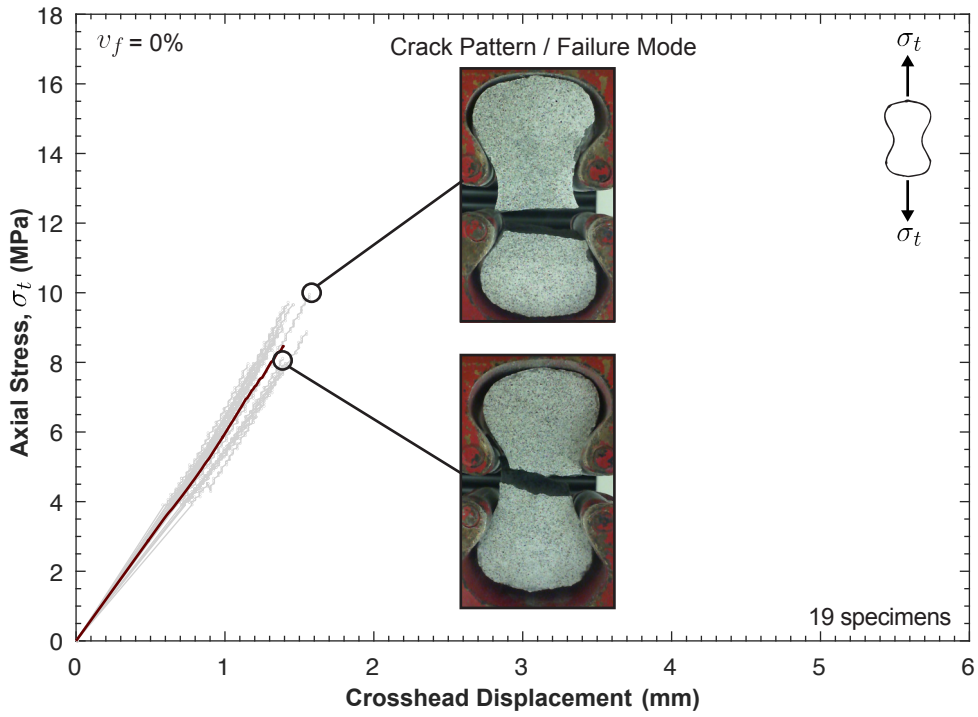

Figure 8.4: Individual and average axial stress-displacement trends for UHPC with $v_f = 0\%$.

8.4.2 Direct tension strength for UHPC with fibers

The individual tensile stress-displacement trends for UHPC containing 2% and 4% by volume are shown in Figs. 8.5 and 8.6, with the average trends plotted as thicker solid lines. The average trends at various fiber contents are compared in Fig. 8.7.

The results show that UHPC with 2% fiber volume behaved linearly until an average ultimate strength, $\bar{f}_t$, of 7.9 MPa $\pm$ 9.8% was reached. After the peak, a drop in the load occurred followed by a load increase as the fibers bridging the crack are pulled out of the matrix. The load starts to decrease again at large values of crack opening until the fibers are completely pulled out of the matrix as shown in Fig. 8.5. The tensile strength of UHPC with $v_f = 2\%$ was 7% lower that the strength of observed in UHPC without fibers. It is believed that this decrease is a size effect resulting from placing UHPC in specimens with width and thickness only twice as large as the fiber length. For instance, some fibers could have been oriented parallel to cracking plane reducing the effective matrix area and thus decreasing the ultimate strength.

The inclusion of 4% fibers by volume in UHPC resulted in 57.6% increase in the peak

strength compared to unreinforced strength. The material behavied linearly till an average ultimate capacity, $\bar{f}_t$, of 13.4 MPa $\pm$ 14.2%, after which the load starts to decrease until the fibers are completely pulled out of the matrix. All the fiber-reinforced specimens showed a significant amount of post-peak load carrying capacity which signify that the tension strength of UHPC could be considered in structural design reducing or eliminating tension steel bar reinforcement. The effect of fiber orientation on the tensile behavior of UHPC is investigated in section 8.5.

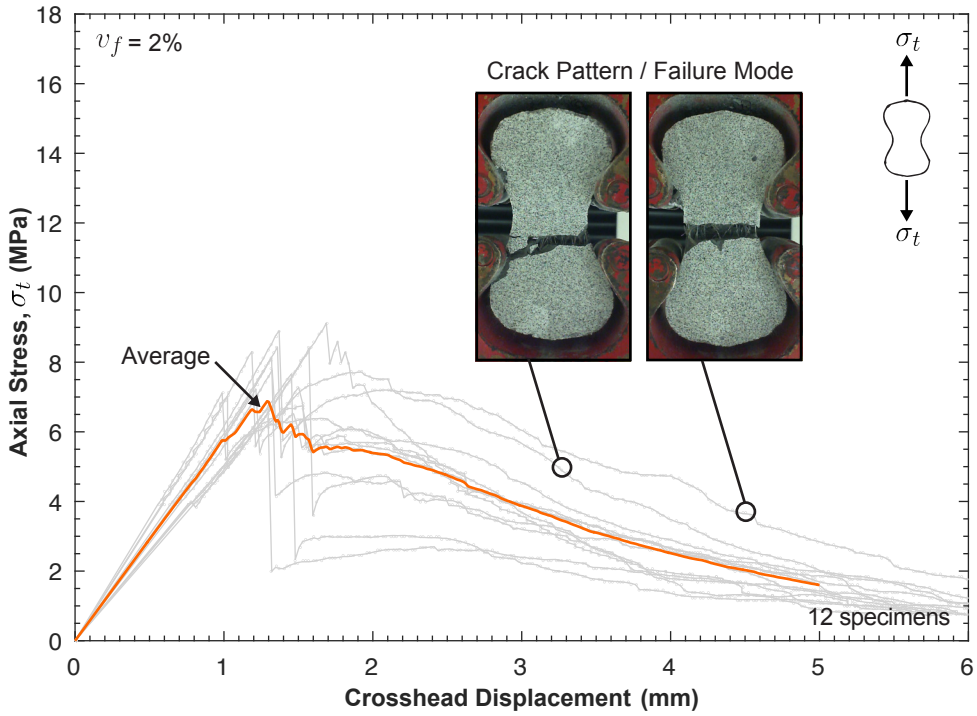

Figure 8.5: Individual and average axial stress-displacement trends for UHPC with $v_f = 2\%$.

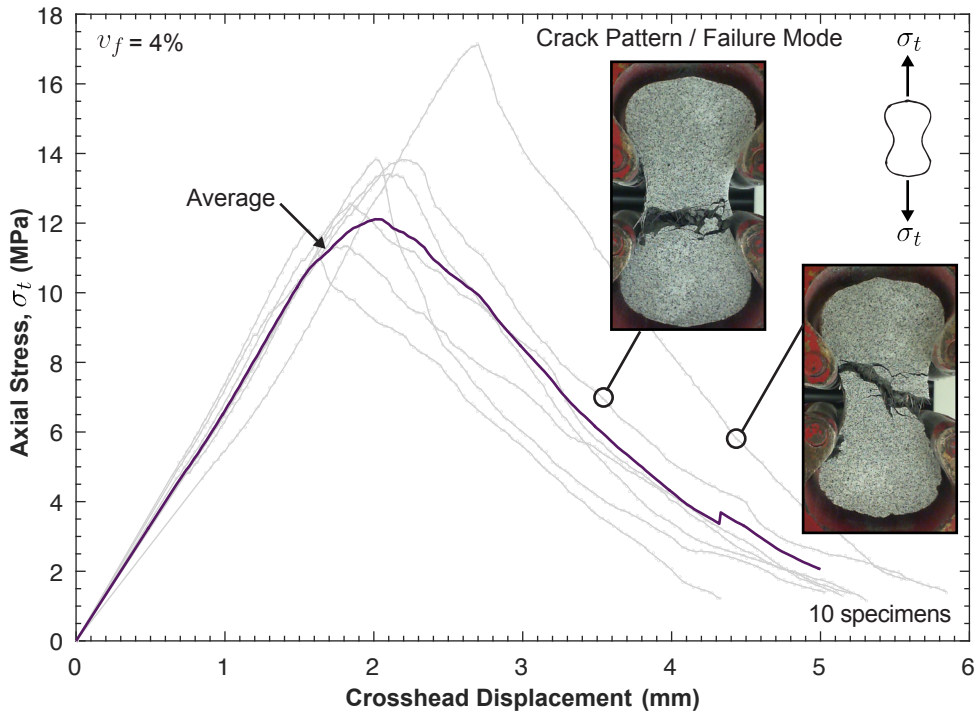

Figure 8.6: Individual and average axial stress-displacement trends for UHPC with $v_f = 4\%$.

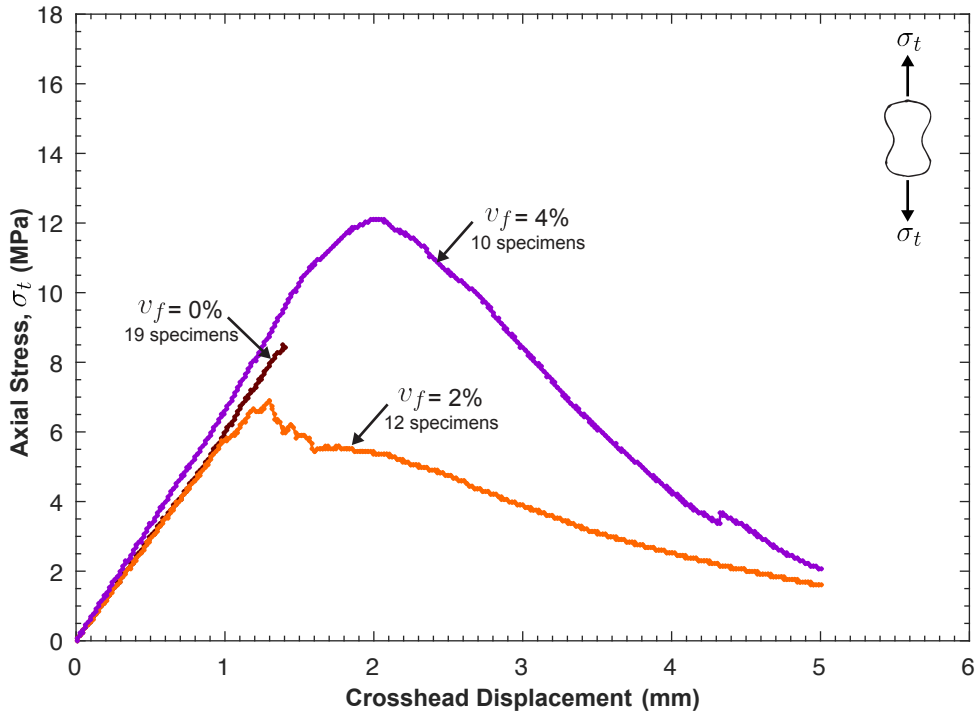

Figure 8.7: Average axial stress-displacement trends for $v_f = 0\%$, 2%, and 4%.

8.4.3 Splitting tension strength of UHPC with and without fibers

A summary of the tensile strength results for UHPC with and without fiber reinforcement is presented in Table 8.2. The average splitting strength values, $\bar{f}_{t,s}$, are calculated following Eq. 8.1 for 10, 5, and 5 individually tested cylinders with $v_f = 0\%$, 2%, and 4%, respectively.

Table 8.2: UHPC tension strength at various fiber contents.

v_f (%)	Direct tension $\bar{f}_t$ (MPa)	Splitting tension $\bar{f}_{t,s}$ (MPa)
0	8.6 ± 8.9%	7.2 ± 23.1%
2	7.9 ± 9.8%	21.2 ± 8.6%
4	13.4 ± 14.2%	30.6 ± 8.3%

At the end of each test, the unreinforced specimens split into two equal pieces as shown in Fig. 8.8a. When fibers were introduced in the matrix, the specimens did not fail at first crack and the ultimate capacity increased by 194% and 325% for $v_f = 2\%$ and 4%, respectively. A typical failure mode for the fiber-reinforced specimens is shown in Fig. 8.8b.

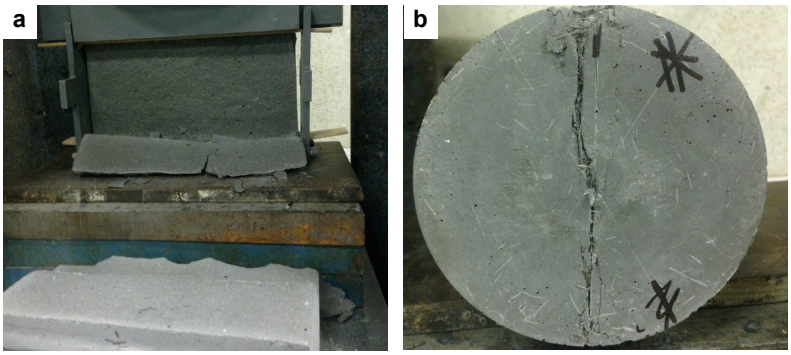

Figure 8.8: Typical failure modes for the split cylinders without and with fiber reinforcement.

As shown in Table 8.2, the calculated direct and splitting tension capacities for UHPC without fibers are in the same range as expected. However, the splitting tension capacities for UHPC with 2% and 4% fibers by volume are 168% and 128% higher than their corresponding uniaxial tension values, respectively. Although the fiber orientation distributions between the two specimens are certainly different, it is unlikely that fiber orientation is the sole cause of such high difference in capacities. In fact, based on the placement methods

followed, a random fiber distribution in the split cylinder specimens and a preferential orientation perpendicular to the crack plane in the dogbone-shaped specimens could be assumed. These orientations, if true, would result in lower splitting tension capacities. Based on this observation, it is concluded that the split cylinder tests do not determine the uniaxial tension capacities of UHPC with fiber reinforcement. In fact, the loading configuration creates a state of biaxial stresses inside the cylinder and along the cracking plane.

The stress field at the onset of cracking in a UHPC split cylinder can be approximated utilizing the closed-form solution of an elastic disk derived by Liu (2009). For planar deformations, either plane strain or plane stress, and in a Cartesian coordinate system (x, y) with origin, O, located at the cylinder's center, Liu (2009) expressed the stresses in the cylinder's cross section as follows:

$$\sigma_x = -\frac{2P}{\pi h}\left[\frac{x^2(r-y)}{(r^2+x^2-2ry+y^2)^2}+\frac{x^2(r+y)}{(r^2+x^2+2ry+y^2)^2}\right]+\frac{P}{\pi hr} \tag{8.2}$$

$$\sigma_y = -\frac{2P}{\pi h}\left[\frac{(r-y)^3}{(R^2+x^2-2ry+y^2)^2}+\frac{(r+y)^3}{(r^2+x^2+2ry+y^2)^2}\right]+\frac{P}{\pi hr} \tag{8.3}$$

$$\tau_{xy} = -\frac{2P}{\pi h}\left[\frac{4rxy(r^2-y^2-x^2)(r^2-y^2+x^2)}{(r^2+x^2-2ry+y^2)^2+(r^2+x^2+2ry+y^2)^2}\right] \tag{8.4}$$

where σ_x, σ_y, and τ_{xy} are the axial and shear stresses, P is the total load applied along the cylinder height, h, and $r = d/2$ is the radius of the cylinder.

The longitudinal and transverse stress fields along the crack plane ($x = 0$) for UHPC without fibers at the onset of failure are plotted in Fig. 8.9. In this plane, the tension field, σ_x, is uniform and can be calculated following Eq. 8.2, which reduces to Eq. 8.1 as suggested in ASTM C496/C496M: $\sigma_x = \bar{f}_{t,c} = 2P/\pi hd = 7.2$ MPa. In the longitudinal direction, a compression field, σ_y, is created, with a minimum value of 21.6 MPa located at the center of the cylinder. The stress rapidly increases when moving away from the center reaching a value of 62.2 MPa at the middle 75% of the diameter, after which it continues to increase at a slower rate as it approaches the points of load application at $y = \pm r$.

In the fiber-reinforced cylinders, the splitting crack is bridged by the fibers at various locations along the diameter. The fibers, being pulled out of the matrix due to the tension field, are subject to significant confining compressive stresses orthogonal to the fiber pullout direction. It is hypothesized that these confining stresses improve the bond and frictional stresses of the fiber-matrix interface, providing additional tension resistance to the split

cylinder tests compared to the uniaxial tension. This hypothesis is validated in the following chapter by pulling a single fiber out of a UHPC prism while applying active confinement stresses to the prism's external surface.

Finally, based on the above investigations, it is concluded that the use of the splitting tensile test to characterize the tensile behavior of UHPC should be highly discouraged as it does not provide a valid characterization of the uniaxial tensile strength. In addition, the equation suggested by ASTM C496/C496M (Eq. 8.1) to determine the split tensile strength should not be used for fiber-reinforced UHPC. In these concretes, failure of the material do not occur when the first crack is formed which signify that the elastic approximation at the onset of failure upon which Eq. 8.1 was derived is no longer valid.

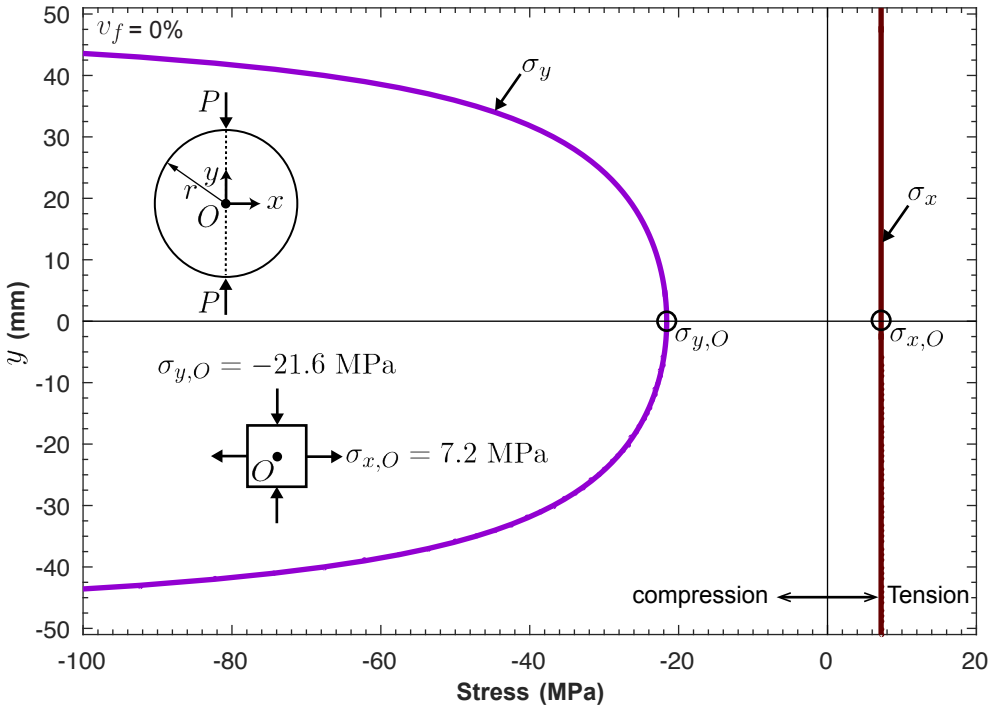

Figure 8.9: Transverse and longitudinal stress fields along the cylinder's diameter for UHPC without fibers at onset of cracking.

8.5 Uniaxial tension tests by Maya Duque and Graybeal

To overcome the hurdles encountered when utilizing existing standard methods to characterize the tensile behavior of fiber-reinforced UHPC, Graybeal and Baby (2013) developed a uniaxial tension test method that resembles the methods used in the mechanical testing of metals. The test method suggest using a prismatic shape specimen having a length of 431.8 mm and a square cross section of 50.8 mm on each side as shown in Fig. 8.10. Tapered aluminum plates are mounted to two sides at the end of each specimen and clamped in the hydraulic wedge grips of the testing frame. The aluminum plates were used to minimize stress disturbance in the test specimen. This gripping method eliminates the relative rotation at the specimen ends creating a uniform strain field which minimizes strain localization within individual cracks and eludes the fiber confinement effects on the tensile behavior. The tests are controlled with a constant displacement rate of 0.00254 mm/s. The displacement is measured with four LVDTs mounted over a gage length of 101.6 mm. The approach is validated to properly captures the uniaxial tensile mechanical response of UHPC including the elastic behavior, multiple cracking, crack straining, and strain localization into a single crack. More information about the test setup and procedure can be found in Graybeal and Baby (2013).

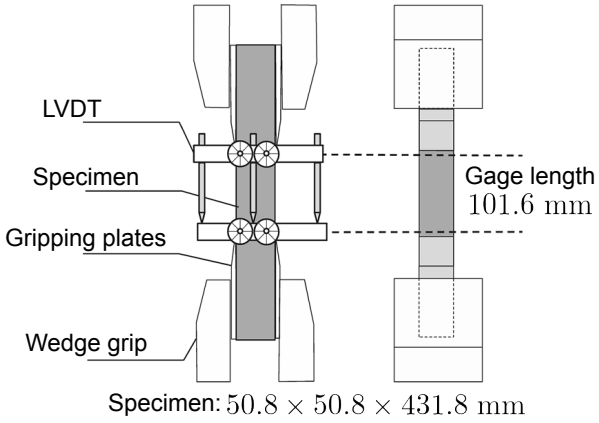

Figure 8.10: Uniaxial tension test setup by Graybeal and Baby (2013). Under fair use 2016.

Maya Duque and Graybeal (2016) utilized the uniaxial test method described above to obtain the uniaxial tensile stress-strain response for UHPC at various fiber orientation distributions. The UHPC used in these tests is the same proprietary product described in Chapter

5 with 2% fibers by volume. Therefore, these results obtained from these tests will be used in the subsequent chapters to calibrate or validate the computational models described in Chapters 3 and 4. A summary of the experimental procedure and results is briefly discussed below.

In order to mimic the casting process of structural components, Duque and Graybeal (2016) extracted the tension specimens from 50 mm thick slabs where UHPC flowed from one side of the slab to the other at it fills the slab molds volume. After curing at ambient tempreture for over 180 days, prismatic specimens (50.8 mm × 50.8 mm × 431.8 mm) were cut from the slabs at three inclinations with respect to the flow direction during casting: parallel, perpendicular, and at 45° with respect to the flow direction as shown in Fig. 8.11. Companion specimens were also placed in individual molds with the same specimen dimensions, in which the UHPC flowed from one side of the mold to the other. The companion beams were added to investigate the difference in tensile behavior between specimens placed in laboratory or field conditions.

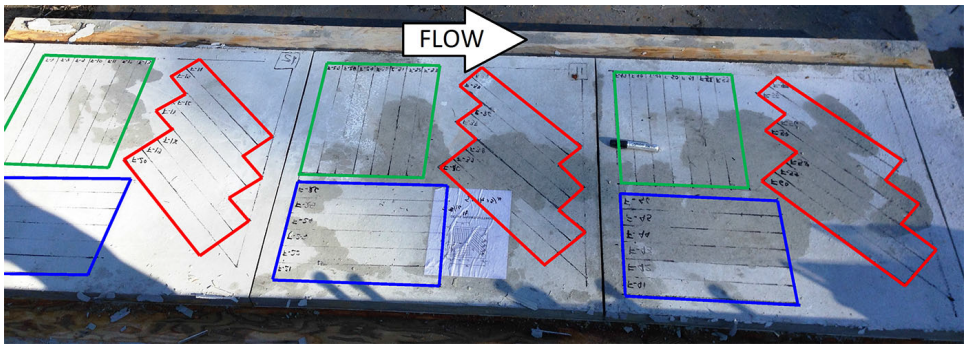

Figure 8.11: Specimen layout cut from UHPC slabs with $v_f = 2\%$ (Maya Duque and Graybeal, 2016). Under fair use 2016.

After completion of the tension tests, image analysis was performed the cross sections of three tested specimens for each casting method. In each of these specimens, high resolution pictures were taken for the sections located at a distance of 1.5 times the fiber length ($L_f = 13$ mm) from the main crack. The number of fibers bridging the cut plane and the dimensions of the fiber cross-sectional footprints were then measured and recorded. Maya Duque and Graybeal then calculated the fiber orientation factor for each specimen according to the following equation (Markovic, 2006; Wille et al., 2013; Karihaloo and Kulasegaram, 2015):

$$\mu = \frac{1}{N}\sum_{i=1}^{N}\cos\theta_i = \frac{1}{N}\sum_{i=1}^{N}\frac{b_i}{a_i} \tag{8.5}$$

where N is the total number of fibers captured in the cut section, θ_i is the angle between the fiber axis and the vector normal to the cut plane, a_i is the major axis of the fiber elliptical footprint on the cut plane, and b_i is the minor axis of the footprint and is equal to the fiber diameter, d_f, as shown in Fig. 8.12.

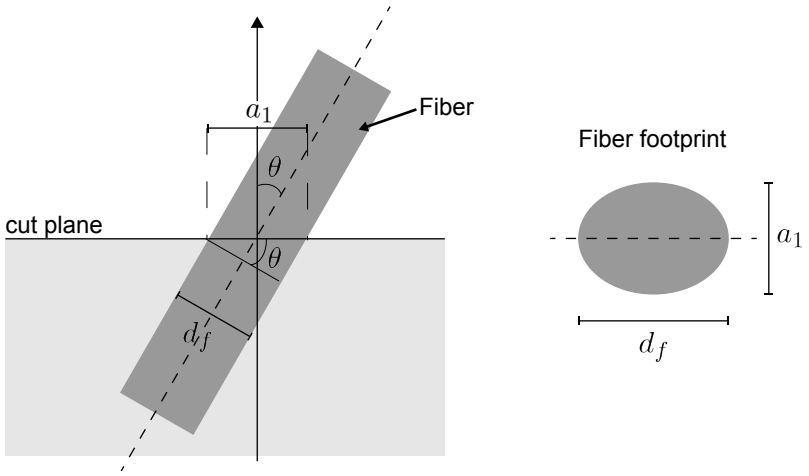

Figure 8.12: Fiber footprint on cut plane.

The tensile mechanical response for the tests by Maya Duque and Graybeal (2016) at the calculated orientation factors pertaining to the four casting methods are reported in Table 8.3. $\bar{\varepsilon}_u$ is the average strain at the onset of strain localization. The individual tensile axial stress-strain trends for each casting method are shown in Figs. 8.13 to 8.16 and the average trends, plotted as thicker solid lines, are compared in Fig. 8.17.

Table 8.3: Tensile results at various orientation factors (Maya Duque and Graybeal, 2016).

Casting method	$\bar{N}$	$\bar{\mu}$	$\bar{f}_t$ **(MPa)**	$\bar{\varepsilon}_u$
perpendicular to flow direction	555 ± 12.5%	0.65 ± 8.4%	6.6 ± 9.4%	0.0033 ± 20.4%
45° inclination from flow direction	852 ± 9.5%	0.74 ± 4.9%	7.9 ± 20.1%	0.0036 ± 47.9%
parallel to flow direction	1103 ± 5.7%	0.83 ± 3.6%	13.0 ± 6.3%	0.0061 ± 32.7%
Mold casted from one side	1047 ± 3.9%	0.85 ± 0.7%	9.73 ± 9.7%	0.0034 ± 29.9%

The tensile results highlight the strong influence of fiber orientation distributions on the tensile behavior of UHPC including first cracking, multi-cracking stress, strain domains, and strain at localization (Maya Duque and Graybeal, 2016). The average tensile strength, $\bar{f}_t$, in the direction of flow increased by 97% when the fibers were preferentially oriented in that direction ($\mu = 0.83 \pm 3.6\%$) compared to when the fibers were perpendicular to it ($\mu = 0.65 \pm 8.4\%$). The first cracking stress was also increased with fiber orientation as shown in Fig. 8.17.

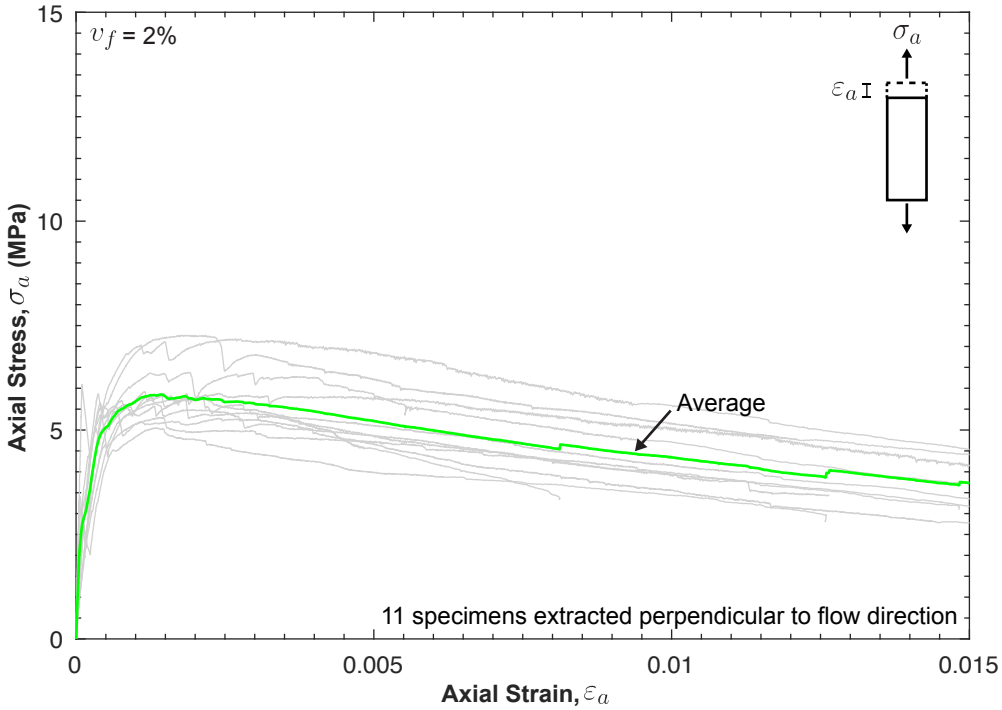

Figure 8.13: Uniaxial tensile stress-strain response for specimens extracted perpendicular to flow direction (Maya Duque and Graybeal, 2016).

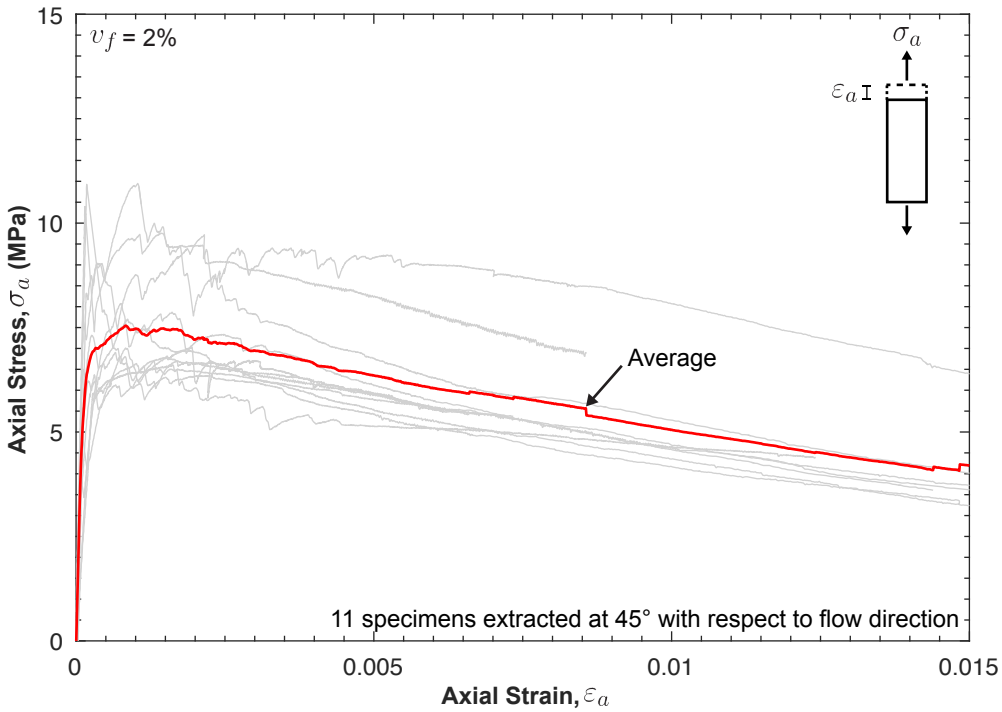

Figure 8.14: Uniaxial tensile stress-strain response for specimens extracted at 45° with respect to flow direction (Maya Duque and Graybeal, 2016).

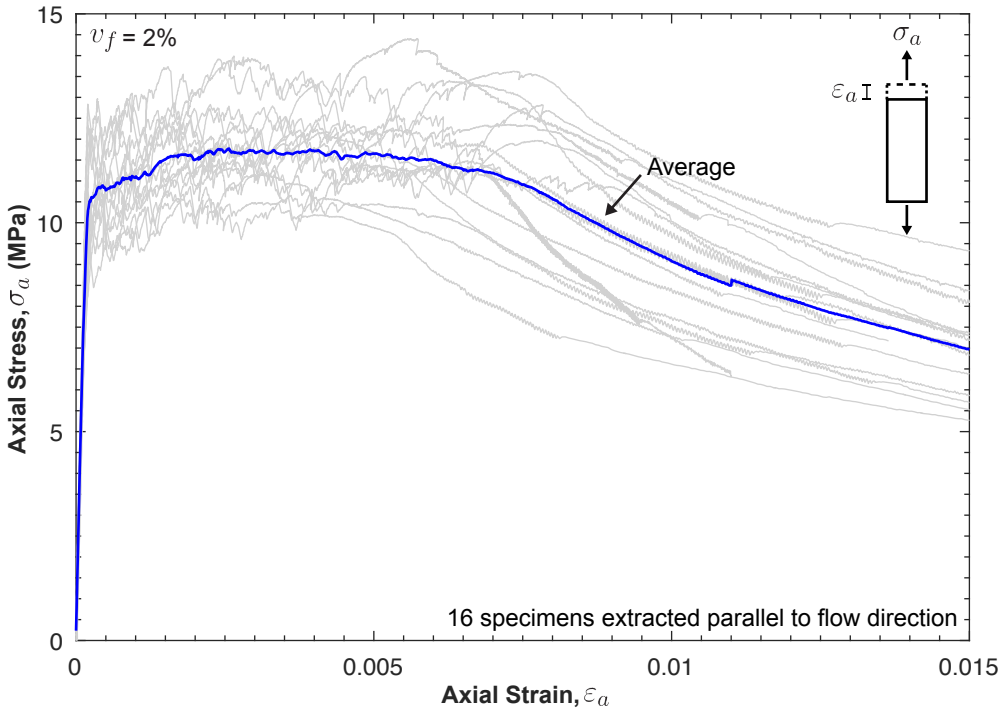

Figure 8.15: Uniaxial tensile stress-strain response for specimens extracted parallel to flow direction (Maya Duque and Graybeal, 2016).

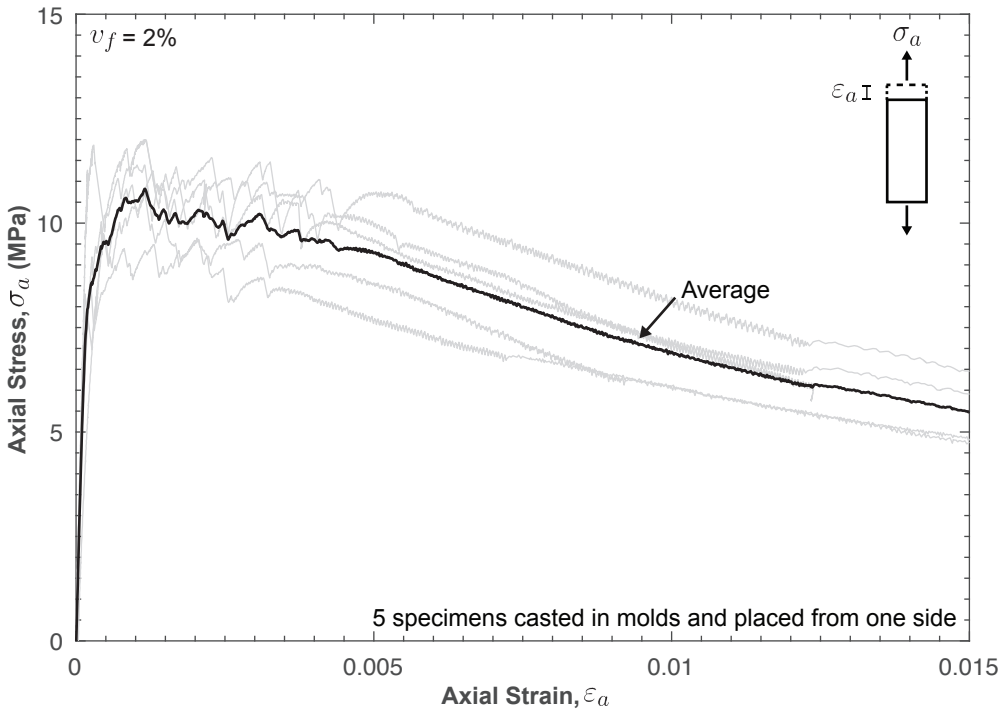

Figure 8.16: Uniaxial tensile stress-strain response for the mold casted specimens placed from one side (Maya Duque and Graybeal, 2016).

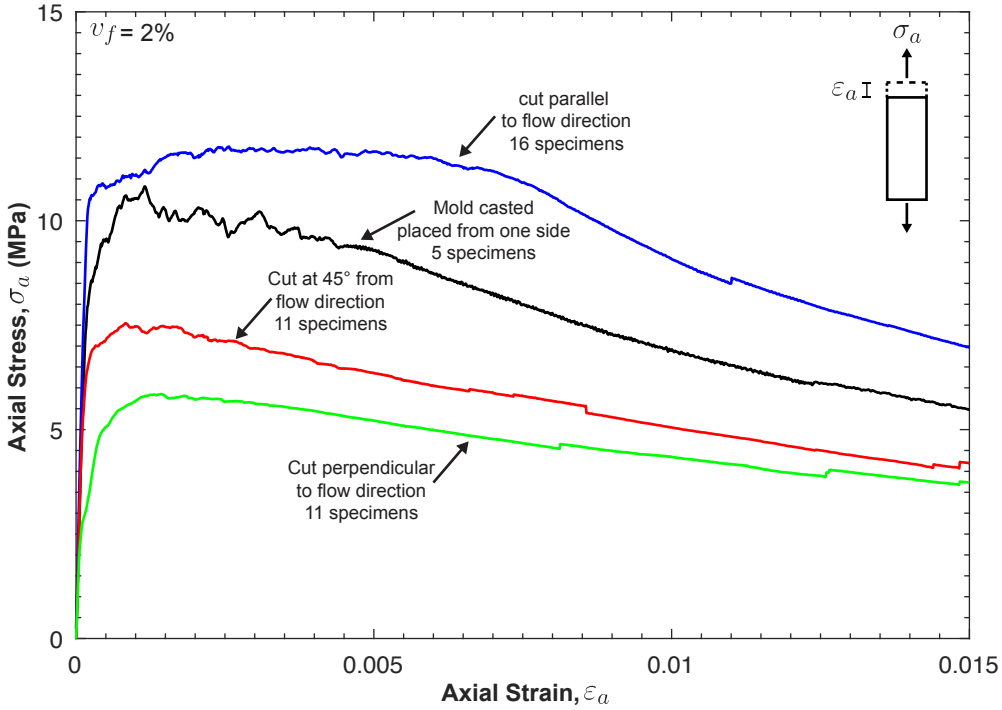

Figure 8.17: Average uniaxial tensile stress-strain response for specimens at different casting methods (Maya Duque and Graybeal, 2016).

In summary, this chapter investigated the ultimate tensile strength of UHPC without and with fiber reinforcement utilizing existing standard experimental procedures, which are typically used for regular concrete without fiber reinforcement. The shortcomings of these methods to properly evaluate the uniaxial tensile strength of UHPC were highlighted and discussed. To overcome these hurdles and to obtain a representative stress-strain response of UHPC with fibers at various orientation factors, the uniaxial tension tests by Maya Duque and Graybeal (2016) were briefly discussed. The experimental results reported in this chapter are utilized in the Chapters 10 and 11 to inform the tension parameters of the computational tools and validate their predictive capabilities.

Chapter 9

UHPC Fiber-Matrix Interfacial Properties to Inform Computational Models

This chapter characterizes the interfacial properties between fibers and the surrounding UHPC matrix through a set of single fiber pullout experiments. In these tests, one fiber is pulled out of the UHPC matrix at a constant displacement rate corresponding to the fiber slip relative to the concrete surface along the application of load. The results are used to provide a fiber load-slip response that could be programmed into computational models to account for the effect of fiber reinforcement on the structural behavior of UHPC. The details of the experimental program, including the test matrix, specimen preparation, and test setup, instrumentation, and procedure are presented in sections 9.1, 9.2, and 9.3, respectively. The experimental results including the effects of fiber embedment length and confinement stresses on the fiber-matrix load-slip relationship are discussed in section 9.4. Finally, a uniaxial interaction law for simulating UHPC fiber-matrix interface behavior is presented and evaluated in section 9.5.

9.1 Test matrix

The single fiber pullout response was evaluated from 1,307 tests in UHPC without fibers ($v_f = 0\%$) and with fibers ($v_f = 2\%$, 4%). The fibers are Dramix® OL 13/.20 smooth high carbon steel fiber, with length, L_f, and diameter, d_f, of 13 mm and 0.2 mm, respectively. A key parameter for fiber pullout resistance is the fiber embedment length and this was varied as $L_e = 4.0$, 5.0, 6.5, and 7.5 mm in the test matrix (Figs. 9.1a-b). The influence of fiber proximity to a free edge, $e = 3.2$, 12.7, and 25.4 mm (Fig. 9.1c), and to each other was also considered, $d = 3.2$ and 12.7 mm (Fig. 9.1a).

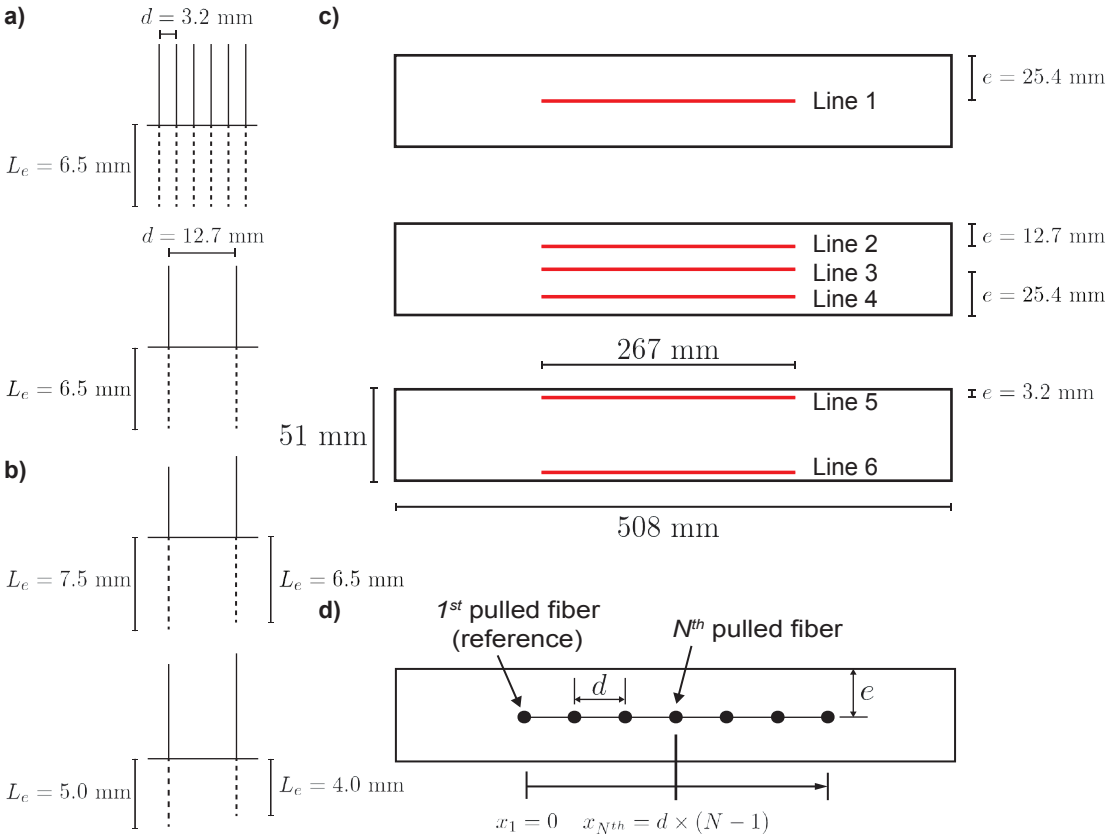

Figure 9.1: a) Fiber details for batches III, VI, & X; b) fiber layout for batch VII; c) specimen layouts; d) typical fiber line.

A multi-axial stress state is common at the structural scale which influences the fiber pullout response. A subset of experiments considering a compressive confinement stress orthogonal to the fiber pullout direction are considered where $\sigma_c = 17$, 35, and 53 MPa. Fibers were received in two shipments from the UHPC manufacturer and so this is also

treated as a variable in Table 9.1. The fibers pertaining to a certain set of parameters were pulled in five different time spans, denoted as test groups 1-5, as shown in Table 9.1.

Test group	**Batch ID**	v_f (%)	**Fiber shipment**	**Tested parameters**	**Tested fibers**
1	III	0	A	e, d	196
2	VI	2	A	e, d	239
3	X	4	A	e, d	235
4	VI	2	A	σ_c	334
5	VII	2	A, B	L_e	303

Table 9.1: Single fiber pullout tests matrix.

The compressive strength within each fiber testing group was obtained from companion cube specimens, performed on several days within each time span. The average compression strength values, $\overline{f}_c$, and the concrete age for each test group are reported in Table 9.2.

Test group	**Batch ID**	v_f (%)	**Age (days)**	$\bar{f}_c$ **(MPa)**
1	III	0	60 - 75	124 ± 13.2%
2	VI	2	55 - 70	148 ± 7.4%
3	X	4	70 - 95	153 ± 9.0%
4	VI	2	260 - 320	157 ± 8.7%
5	VII	2	35 - 64	134 ± 4.9%

Table 9.2: Cube compressive strength, $\overline{f}_c$, at time of testing.

The average compressive strengths at the time of fiber pullout testing are consistent across test groups 2, 3, and 4. Test group 1 strength is approximately 20% lower because fibers resist principal tension stresses and provide some degree of confinement. Test group 5 is approximately 9% lower than test groups 2 and 4 because it was performed at earlier ages. However, since all tests were completed when UHPC is in its hardened state ($\geq$ 28 days), it can be concluded that the difference in compressive capacities is mostly related to the fiber volume content, v_f; and therefore, the compressive strength, f_c, is not considered an independent parameter when discussing the fiber pullout results.

9.2 Specimen preparation

The fibers were installed in rectangular specimens having a length of 508 mm, width of 51 mm, and height of 90 mm, with specimen layouts shown in Fig. 9.1c. The fibers were placed on strong tape, with the free length ($L_f - L_e$) exposed from the top of the tape, at a pre-measured spacing between fibers, d (Fig. 9.2a). The tape was mounted on the side of a plastic fixture, with the exposed portion of the fiber protruding from the surface. The plastic fixtures were then placed into the rectangular molds, with fibers extending upwards, allowing for UHPC to be placed over the top as shown in Fig. 9.2b. The location of each tested fiber in a line with reference to the first pulled fiber, $x_1 = 0$, was tracked and denoted by x_N, where, N is the number of fibers pulled in a line (Fig. 9.1d). More information on the specimen preparation can be found in Black (2014).

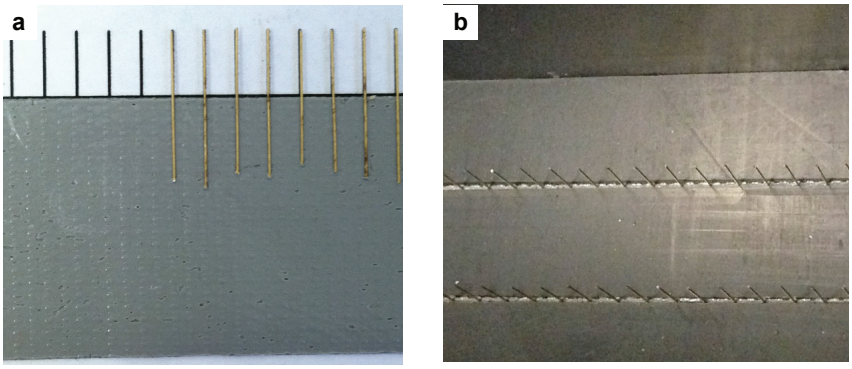

Figure 9.2: Fiber installation process.

9.3 Test setup and procedure

The pullout tests were performed in a 45 kN load capacity Instron 4204 machine with a 1,000 N load cell and an internal 254 mm LVDT to measure crosshead movement, with an measurment accuracy of 0.2%. The fiber specimens were centered on the frame platform, aligning the fiber being tested under a Starrett® 162A pin vise. A metal clamp was fastened to the platform, and then tightened to restrain the specimen from moving (Fig. 9.3a).

After installing the specimen, the actuator was lowered to grip the exposed fiber length without touching the specimen concrete surface. Care was taken to ensure that the fibers were aligned inside the pin vise grip and then the grip was tightened around the fiber using

pliers. A single arm extensometer, with a stroke ± 4 mm and an accuracy of 0.2%, was attached to the grip to measure fiber slip. The fibers were pulled out at a displacement rate of 0.018 mm/s based on the actuator crosshead displacement.

For tests with an external confinement stress applied, the specimens were centered in an engineer's bench vise where the top 25 mm of the specimen's height was in contact with the vise's movable jaws at a width of 50 mm (Fig. 9.3b). Two 44 kN button load cells with an accuracy of 0.2% were used to read the confinement load as the vise was manually tightened using the lever arm. The confinement stress at the level of the fiber embedded region, σ_c, was calculated as the applied force from the load cell divided by the vice jaw contact area of 1290 mm^2 and confirmed with a linear finite element analysis of the test setup (Appendix F).

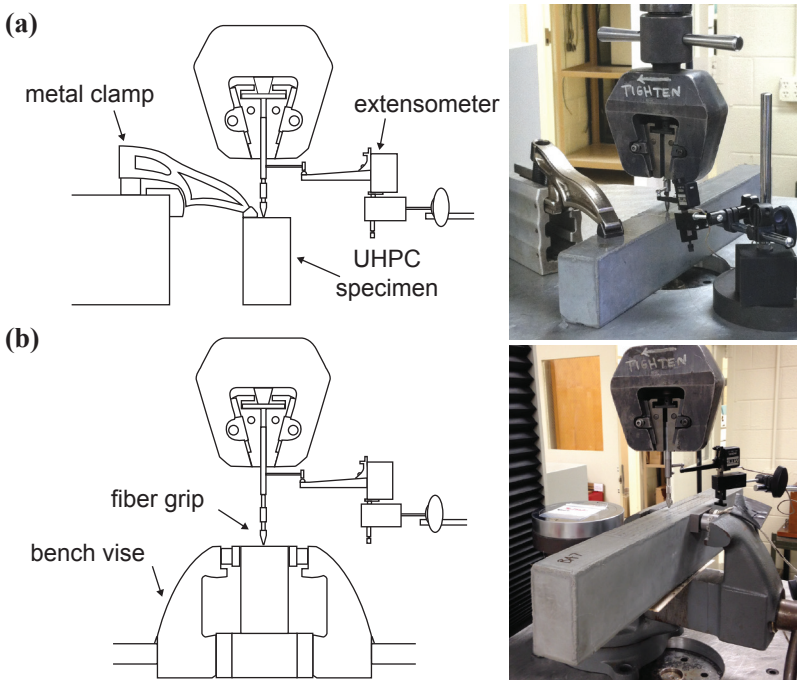

Figure 9.3: Configuration of the single fiber pullout test: a) no external pressure; b) with external pressure.

9.4 Fiber pullout results

Fiber pullout influences to adjacent fibers, d, edge distance, e, matrix fiber volume, v_f, confinement stress, σ_c, embedment length, L_e, and fiber origin are explored in this sec-

tion with the goal of identifying general parameter trends for the uniaxial fiber pullout law discussed later in this chapter. The pullout behavior is quantified in terms of the load-slip response curves ($P-v$), the maximum pullout load, P_{max}, and the pullout work, W , defined as the area beneath the $P-v$ curve which represents energy dissipated through fiber-matrix friction. The study for the effects of parameters d, e, and v_f on the fiber-pullout response was done in collaboration of Valerie Black as part of her Master's thesis work at Virginia Tech (Black, 2014); A brief discussion of these findings is summarized herein.

9.4.1 General fiber pullout response trends

Representative single fiber pullout load-slip response curves ($P-v$) are presented in Figs. 9.4, 9.5, & 9.6 for UHPC fiber matrix volumes of $v_f = 0\%$, 2%, and 4%, respectively. The gray $P-v$ curves represent individual fiber tests along one line (Figure 9.1), with the average and one standard deviation trends plotted as heavier solid and dashed lines, respectively, which are calculated from the ranges of P at one value of slip, v.

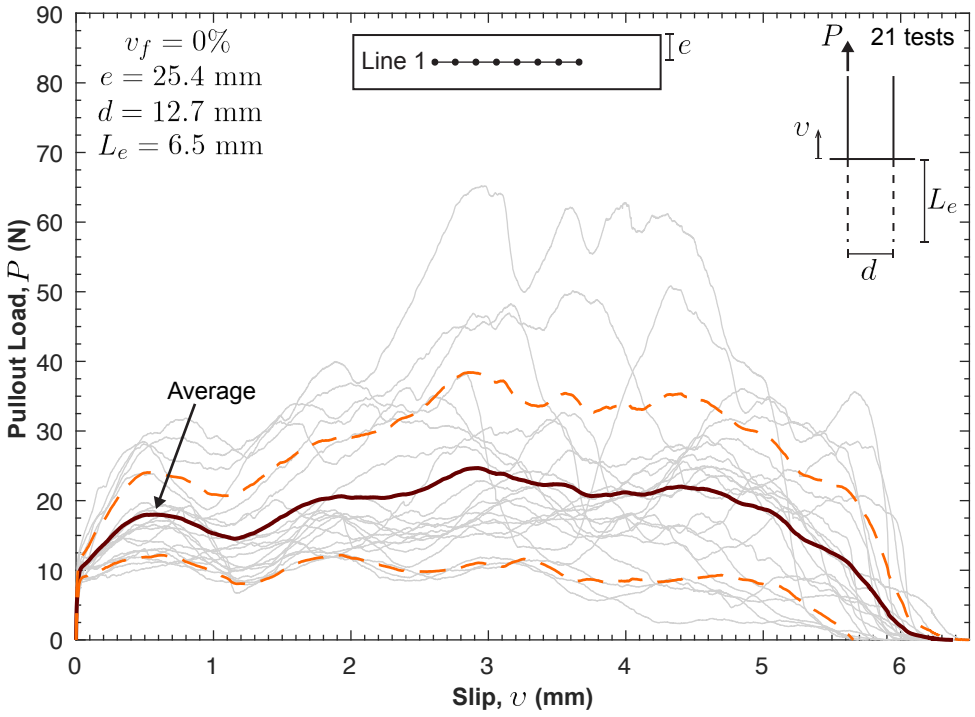

Figure 9.4: Examples of individual and average load-slip response curves for a line of fibers in UHPC without fibers.

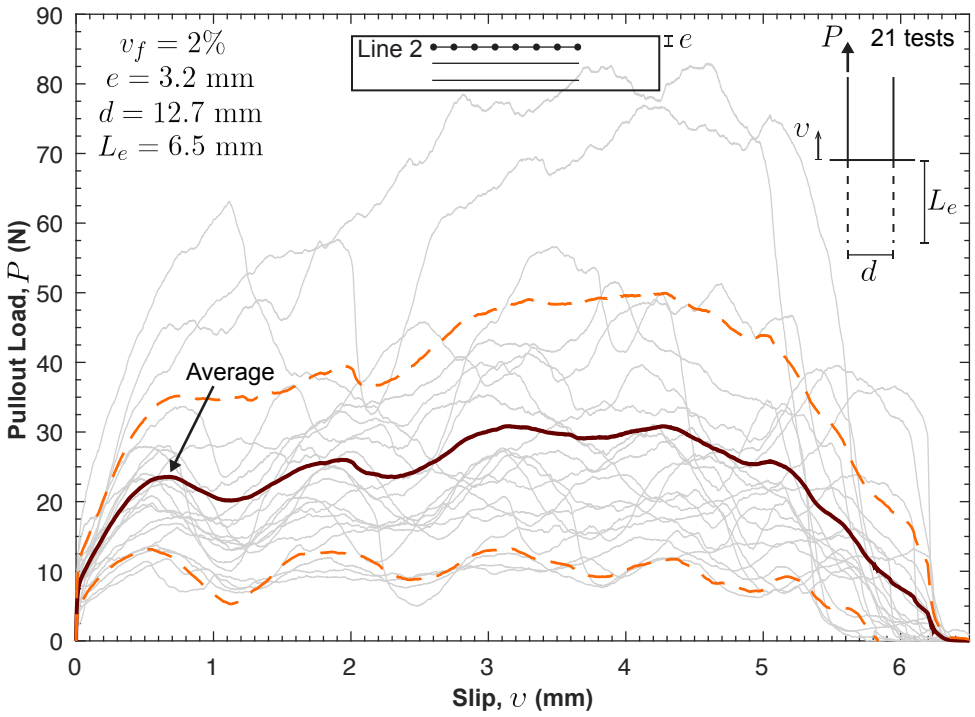

Figure 9.5: Examples of individual and average load-slip response curves for a line of fibers in UHPC with $v_f = 2\%$.

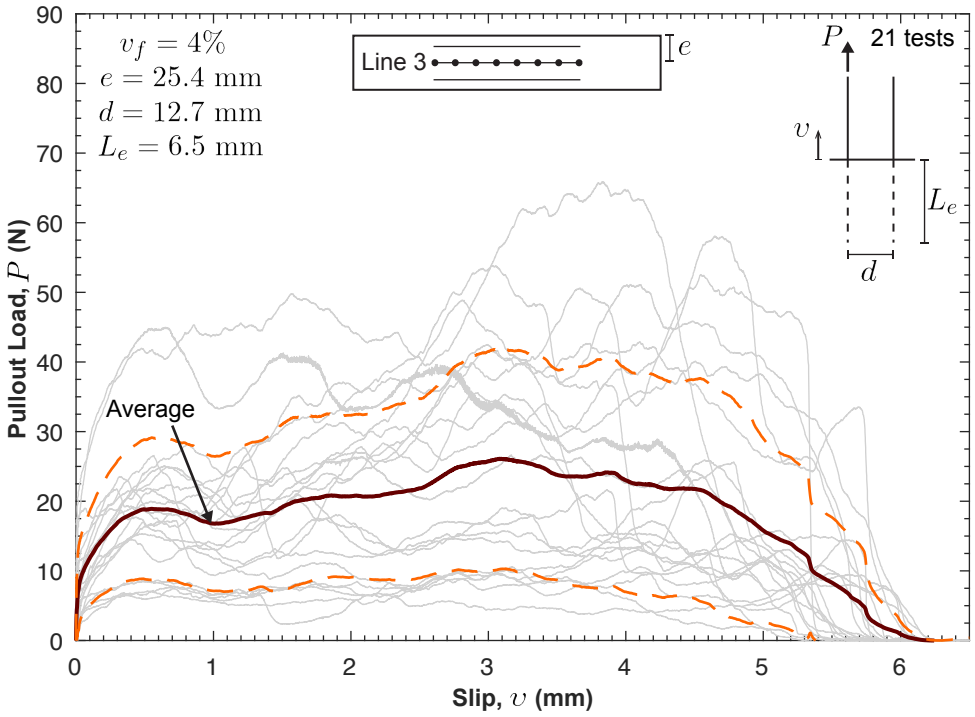

Figure 9.6: Examples of individual and average load-slip response curves for a line of fibers in UHPC with $v_f = 4\%$.

The fiber load-slip stiffness before debonding is high, approximately 500 N/mm at $v \backslash L_e \lesssim 0.01$, and then it begins to degrade as the initial static frictional bond is overcome. As the fiber starts pulling out of the matrix ($v \backslash L_e > 0.01$), it rolls over the matrix particles creating clamping frictional forces, which increase the pullout load until the maximum load, P_{max}, beyond which the fiber-matrix interface loses strength and the load decreases to zero. It is hypothesized that the clamping forces are due to three underlying mechanisms governing the frictional pullout response: 1) the matrix particles adhering to the fiber surface create a wedge effect; 2) the fiber-end deformation, generated during the manufacturing process of cutting the fiber to length, create a local anchorage point at the fiber tip; and 3) the scratching of fiber brass-coated surface create additional friction during pullout (Wille and Naaman, 2012). The last two effects are confirmed for this study in the microscopic pictures of Fig. 9.7 showing the fiber-end deformation before fiber installation (Fig. 9.7a), and the fiber damage abrasion and the flattening of the fiber tip after pullout (Fig. 9.7b). Finally, the load-slip variability within the frictional zone ($v/L_e \gtrsim 0.1$) is caused by local stress interlock and release resulting from compaction and crushing of the matrix particles surrounding the fiber.

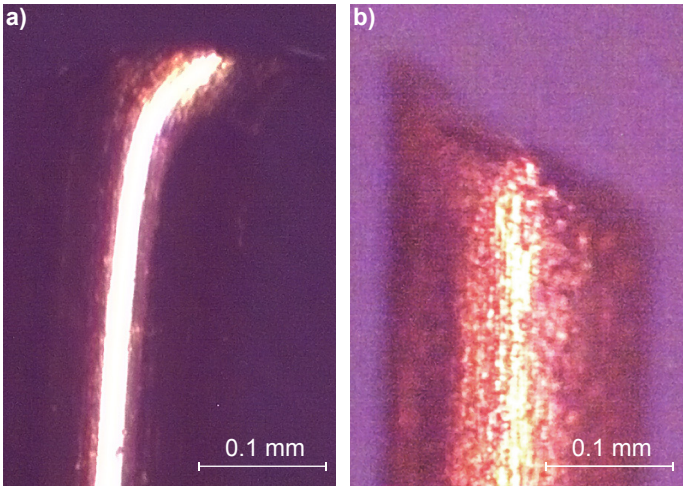

Figure 9.7: Microscopic pictures showing: a) fiber-end deformation before fiber installation; and b) fiber surface damage abrasion and tip flattening after pullout.

9.4.2 Test variability and ANOVA statistical procedures

The data set size and variability highlighted in Figs. 9.4, 9.5, & 9.6 support the need for formal statistical analysis to identify the influence of tested parameters on fiber load-slip response. The variability of the fiber pullout tests can be attributed to a number of

parameters including: 1) the concrete having weaker spots at the level of fibers leading to weaker bond between fiber and matrix (i.e. not fully hydrated cement particles, air voids, cluster of fibers, etc.); 2) the number of fibers in the concrete matrix in contact with the pulled fiber, fiber distribution, and fiber orientation being different at the level of embedment of each fiber; 3) variability in fiber geometric properties (i.e. diameter, curvature, end deformations, etc.); and 4) variability in the test setup (i.e. vice alignment, gripping angle, etc.).

Analysis of variance (ANOVA) is implemented as a statistical hypothesis test that decides if a variable effect is statistically significant or unlikely to have occurred by chance (Montgomery et al., 2012). If the probability of interaction (p-value) is less than the threshold value (or confidence level), the influence of the variable on the response of the model is statistically significant. An important assumption in ANOVA models is that the distribution of the residuals (error between the linear regression model predicted and observed responses) follows a Gaussian distribution. The normality of the residual distribution is confirmed by Black (2014).

ANOVA compares differences among variable means resulting in a p-value that is used to determine the influence of the tested variables on the pullout response. There is a high probability of interaction if the p-value is greater than the significance level. A commonly accepted significance level of 0.05 is adopted for the p-value corresponding to a 95% confidence interval that the test variable has a statistically significant influence on the response.

9.4.3 Influence of fiber proximity on load-slip response

It is hypothesized that a single fiber pullout test is independent from adjacent pullout tests in a specimen line, i.e., performing one pullout test does not influence the results of the next pullout test (Fig. 9.1d). Denoting the location of each fiber in a line relative to the first fiber as, $x = d \times (N - 1)$, the Pearson product-moment correlation coefficient, $\rho_{a,b}$, can be calculated with the goal of quantifying how much two random variables, in this case W or P_{max} and x, influence each other. If there is no correlation between the two variables, $\rho_{a,b} = 0$. If correlation exists, $\rho_{a,b}$ will be between -1 and +1, with, +1 being perfect positive correlation (increase or decrease in one variable always predicts the same directional change for the second variable) and -1 meaning perfect negative correlation (increase or decrease in one variable always predicts the opposite directional change for the second variable). This graphical variations of P_{max} and W with respect to x for a tested line of fibers (Line 1 of

Fig. 9.1c) are shown in Fig. 9.8.

Correlation coefficients for each fiber line tested sequence are reported in Black (2014), with means of $\overline{\rho}_{x,W} = -0.04$ and $\overline{\rho}_{x,P_{max}} = -0.04$ and a coefficient of variation (COV) of 0.20. It follows that relationships between W or P_{max} and fiber location x is unlikely, indicating that the distance between fibers, d, has no effect on the fiber-pullout response in UHPC without and with fibers. This is supported by the ANOVA statistical significance with confidence levels $< 95\%$ at 17%, 1%, and 34% for P_{max}, and 63%, 88%, and 39% for W, when $v_f = 0\%$, 2%, and 4% respectively. The load-slip response comparison shown in Fig. 9.9 also confirms this hypothesis, in which the average load-slip responses for $d = 3.2$ and 12.7 mm are similar. For the remainder of this chapter, fibers within a line are considered as one group pertaining to a set of geometric parameters, for example edge distance, e, and embedment length, L_e.

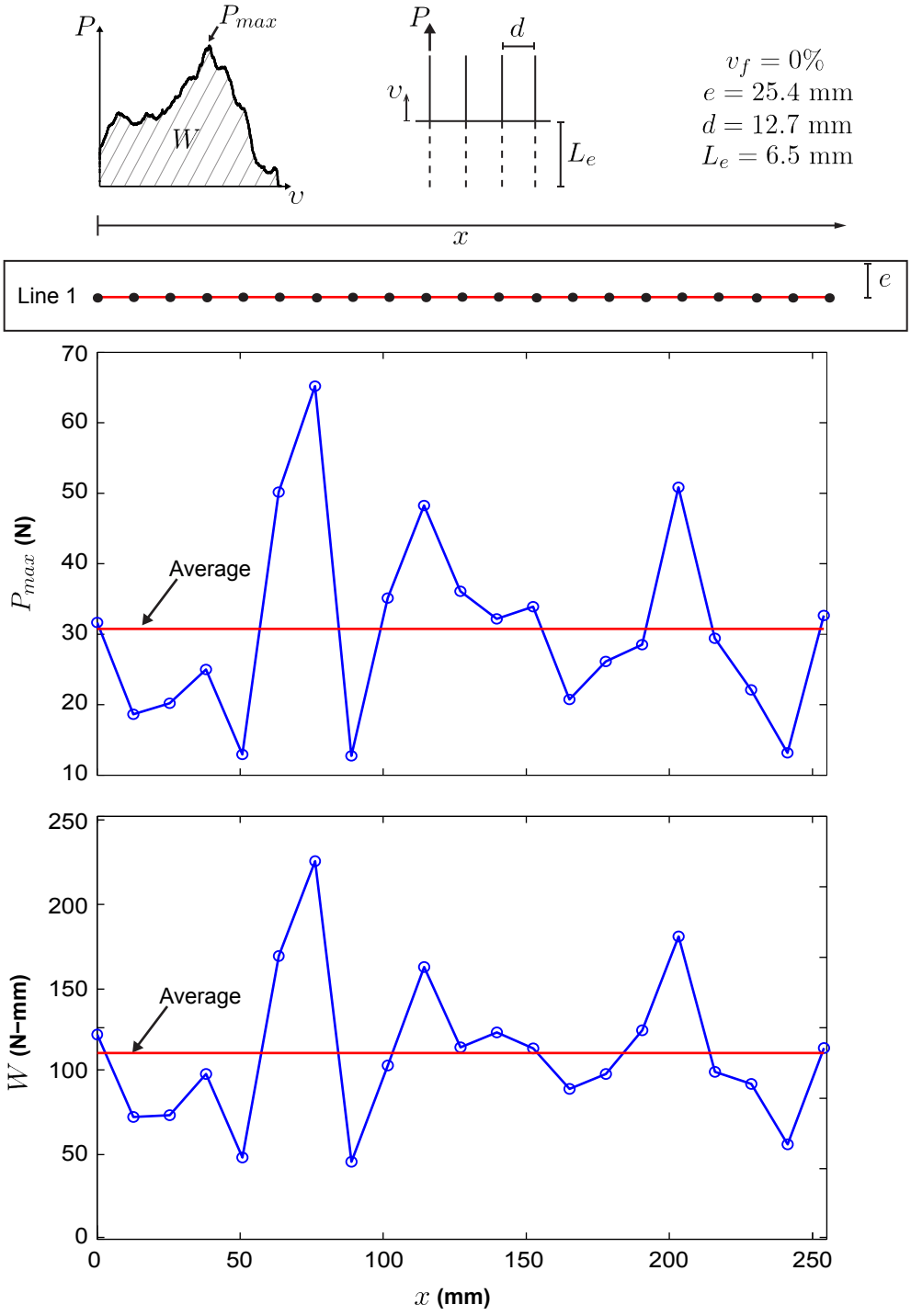

Figure 9.8: Example of individual fiber pullout maximum load and work for a line of fibers in UHPC without fibers.

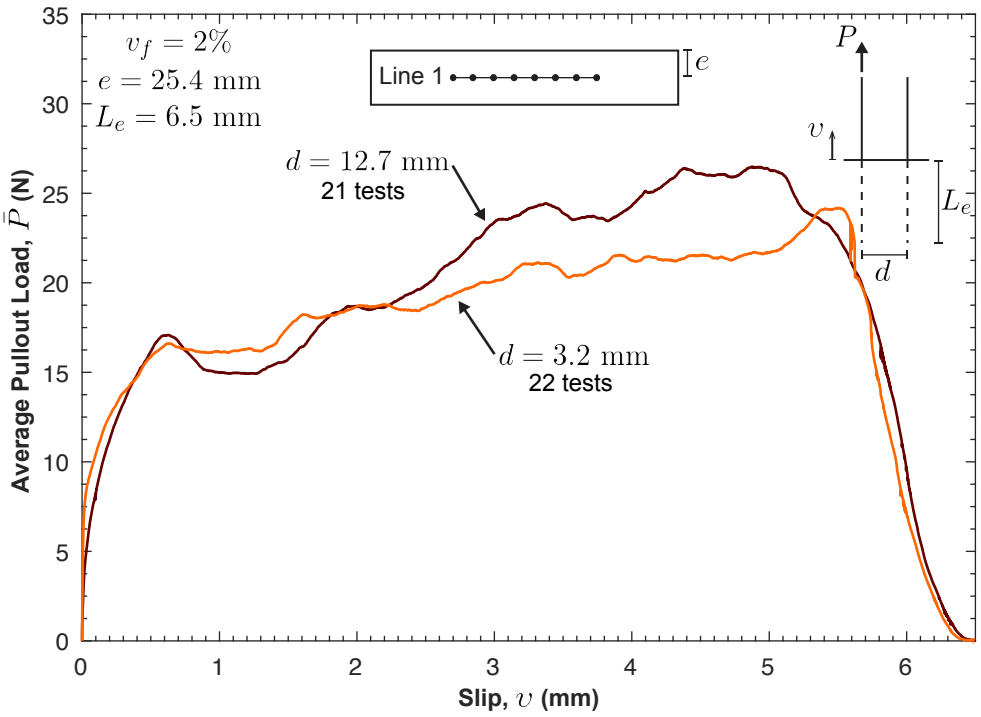

Figure 9.9: Example of average load-slip response curves showing no effect of fiber proximity parameter in UHPC with $v_f = 2\%$.

9.4.4 Influence of edge distance on fiber pullout response

It is assumed that fiber-matrix interface bond weakens close to a free edge because there is less concrete confining the pullout zone. These observations are confirmed for this study in Fig. 9.10, where the average $\overline{P}_{max}$ for $e = 3.2$ mm is approximately 20% lower than $e = 12.7$ and 25.4 mm. The ANOVA statistical significance show a confidence level of 100% ($> 95\%$) that e influences the results of P_{max} and W supporting the hypothesis for v_f =0%. The influence of edge distance diminishes when adding fibers into the matrix with confidence levels ($< 95\%$) of 89% and 54% for P_{max} and to 78% and 50% for W at $v_f = 2\%$ and 4%, respectively. The introduction of fibers in the matrix bridge microcracks maintaining confinement at the free edge resulting in consistent pullout responses independent of e as shown in Figs. 9.11 and 9.12, for $v_f = 2\%$ and 4%, respectively.

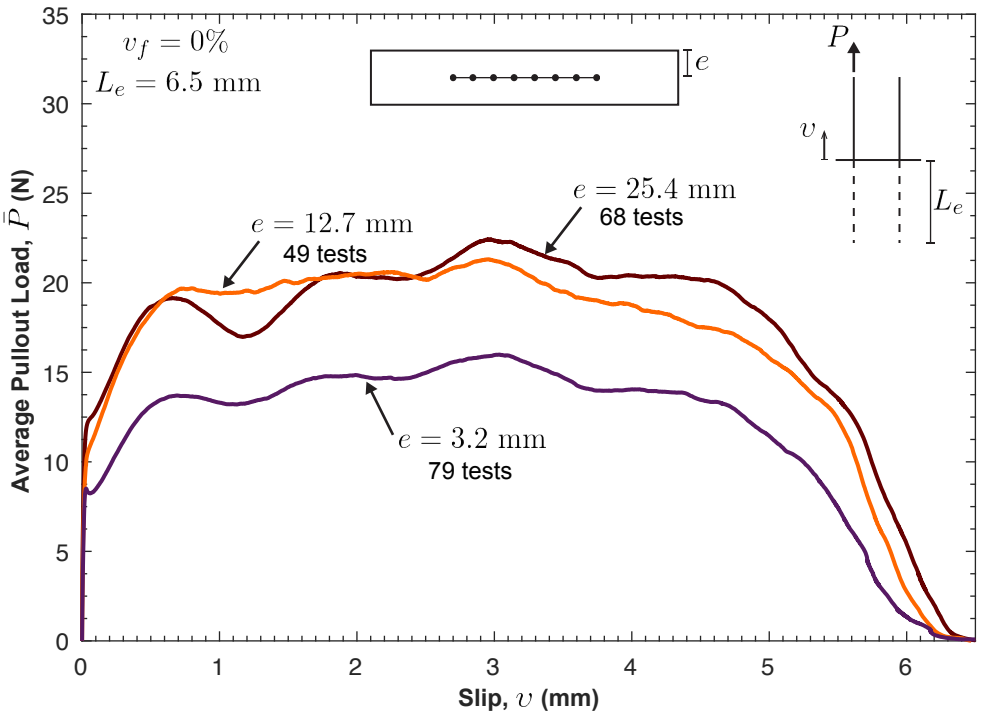

Figure 9.10: Average load-slip response curves showing the effect of fiber edge distance in UHPC without fibers.

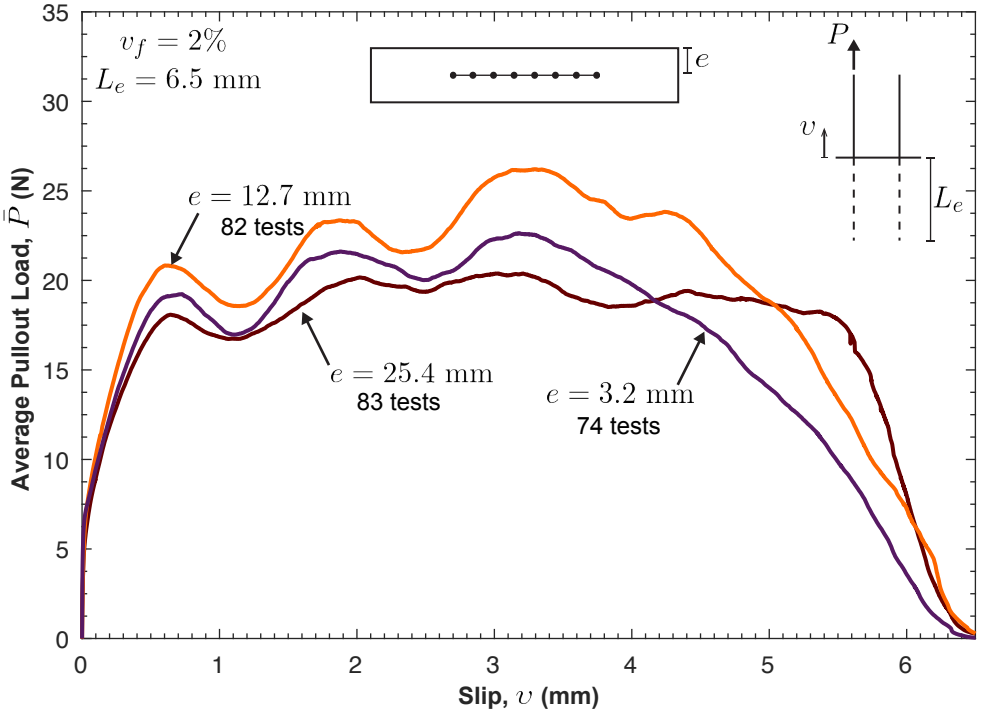

Figure 9.11: Average load-slip response curves showing no effect of the fiber edge distance in UHPC with $v_f = 2\%$.

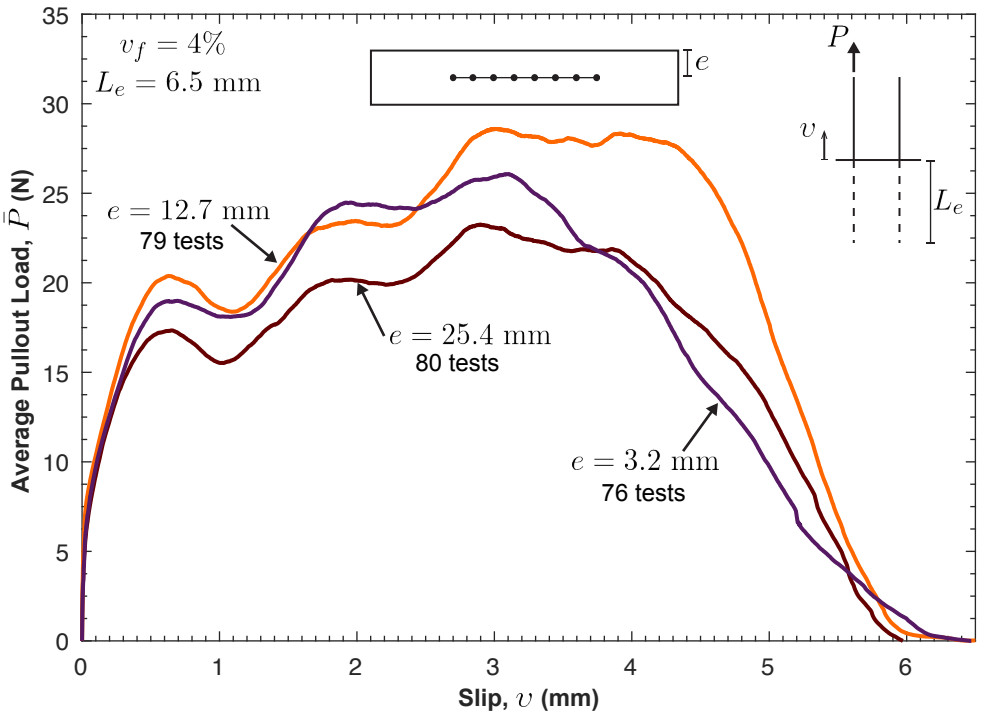

Figure 9.12: Average load-slip response curves showing no effect of the fiber edge distance in UHPC with $v_f = 4\%$.

9.4.5 Influence of fiber volume content on fiber pullout response

It is expected that when fibers experience uniaxial tension in a UHPC matrix, the fiber-matrix bond is improved with an increasing volume of matrix fiber reinforcement, v_f. In the vicinity of a macroscopic crack, fibers surrounding the fiber embedded region limit cracking around the fiber, maintaining confinement that supports friction resistance. Fibers in the matrix may also be in contact with the fiber in tension across a crack, which increases mechanical friction as the fiber debonds and pulls out. The fiber pullout results shown in Table 9.3 confirm this hypothesis, with the average peak strength $\overline{P}_{max}$ approximately 10% and 18% higher for matrix fiber volumes $v_f = 2\%$ and 4% compared to UHPC without fibers ($v_f = 0\%$ and with $e \geq 12.7$ mm).

The average pullout energy, $\bar{W}$, is minimally affected with 3% and 1% increase for v_f = 2% and 4% respectively. The load-slip responses with varying fiber volumes are shown in Fig. 9.13 highlighting similar results for UHPC with and without fibers before the first pullout peak load at $\upsilon/L_e \approx 0.1$. Adding more fibers to the matrix improves the fiber-matrix

interface strength beyond the first peak pullout load as fibers control the concrete damage surrounding the fiber.

Test group	v_f (%)	e (mm)	**Tested fibers**	$\overline{W}$ (N-mm)	$\overline{P}_{max}$ (N)
1	0	≥ 12.7	117	109.1 ± 46.2%	28.7 ± 44.9%
		3.2	79	77.8 ± 44.1%	22.0 ± 44.1%
2	2	All	239	112.7 ± 59.9%	31.5 ± 54.9%
3	4	All	235	109.7 ± 62.2%	33.8 ± 57.4%

Table 9.3: Summary of fiber pullout averaged results for showing the effect of fiber volume content in UHPC.

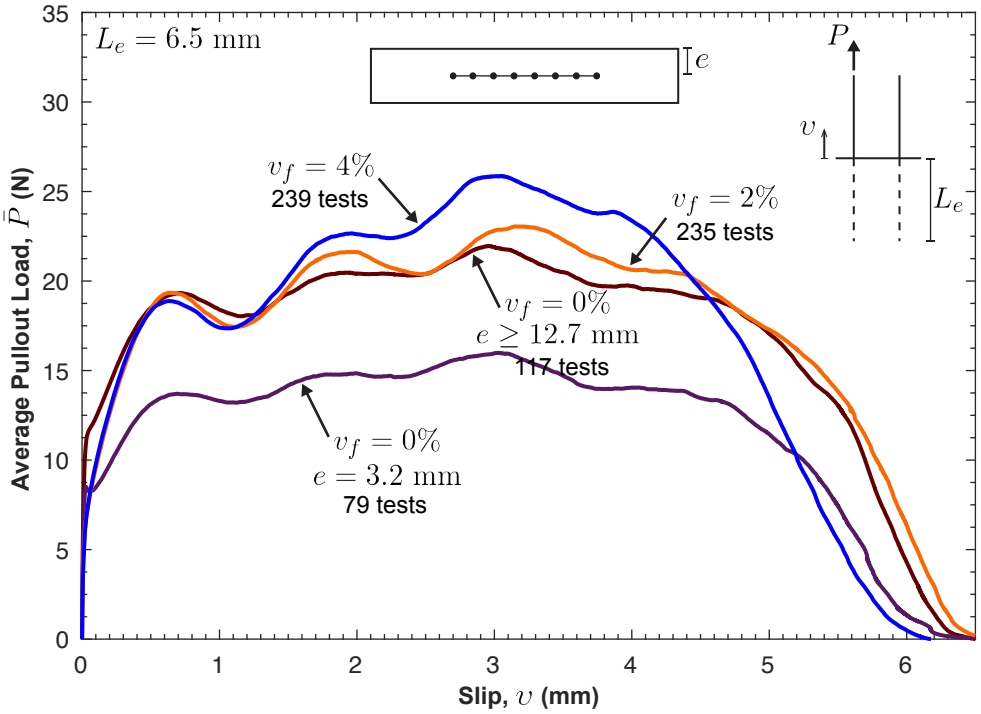

Figure 9.13: Average load-slip response curves showing the effect of fiber volume content in UHPC.

9.4.6 Influence of an external confinement stress on fiber pullout response

Compression stresses orthogonal to the fiber pullout direction improve the fiber-matrix interface bond by increasing confinement and reducing cracks near a fiber. These multi-axial

stress states, where principal tensile and compressive stresses intersect at a crack, is common at the structural scale, for example, in a shear wall where compressive gravity loads from the building combine with lateral shear.

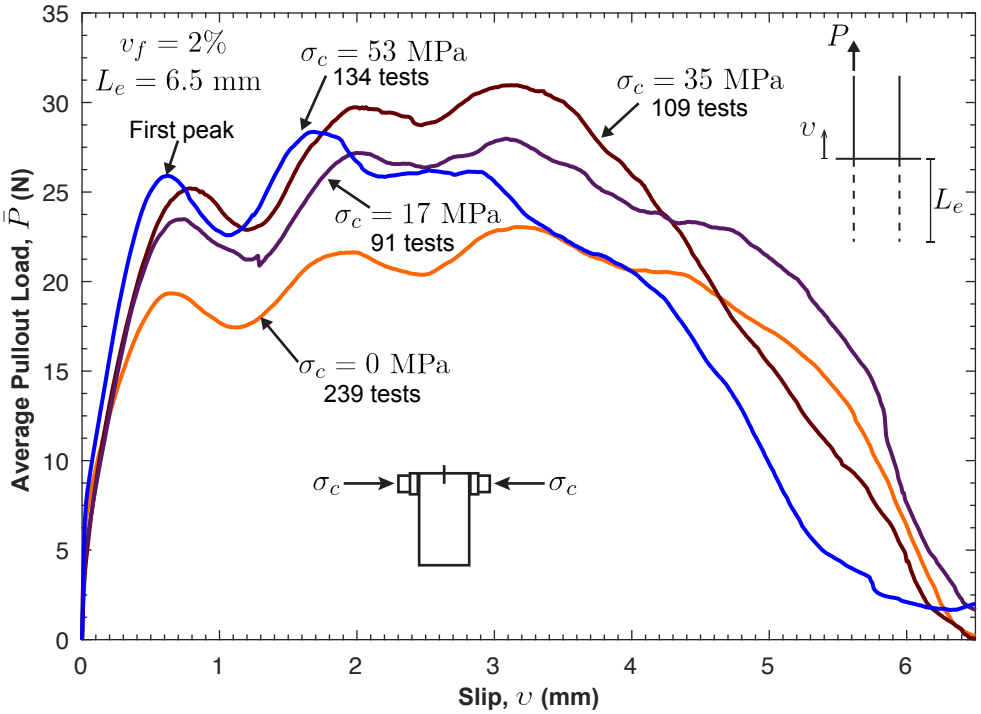

Figure 9.14: Average load-slip response curves showing the effect confinement stress, σ_c, in UHPC with $v_f = 2\%$.

The load-slip response comparison in Fig. 9.14 highlights the benefit of confinement, with the first pullout peak load increasing by 21% to 34% as lateral confinement grows from 17 MPa to 53 MPa (approximately 11% to 35% of UHPC compressive strength, f_c). Confinement stresses also increase the initial bond stiffness at ($\upsilon/L_e \lesssim 0.1$). The average maximum pullout load $\bar{P}_{max}$, summarized in Table 9.4, also increases, however at the highest confining stress the benefits decrease (compare a 21% increase in $\overline{P}_{max}$ at $\sigma_c = 17$ MPa to 14% increase at $\sigma_c = 53$ MPa). Increased confinement stress also corresponds to decreasing post peak ductility as the pullout energy is rapidly dissipated (compare post-peak curves at $\sigma_c = 17$ MPa to $\sigma_c = 53$ MPa in Figure 9.14). This decrease in confinement efficiency and post-peak ductility is due to the formation of a tensile stress field, σ_t, of $0.11\sigma_c$, in the longitudinal direction of the specimen (see Appendix F), which reduces friction and creates micro-cracks in concrete surrounding the fiber (σ_t increases from 1.9 to 5.8 MPa when σ_c grows from 17 MPa to 53 MPa). Confining the embedded region in both transverse and longitudinal

directions would delay micro-cracking and maintain confinement efficiency.

Test group	v_f (%)	σ_c **(MPa)**	**Tested fibers**	$\overline{W}$ **(N-mm)**	$\overline{P}_{max}$ **(N)**
2	2	0	239	112.7 ± 59.9	31.5 ± 54.9
		17	91	136.8 ± 58.7	37.8 ± 48.2
4	2	35	109	136.0 ± 62.0	38.8 ± 52.4
		53	134	116.4 ± 49.5	35.9 ± 40.2

Table 9.4: Summary of fiber pullout averaged results for showing the effect of confinement stress, σ_c, for $v_f = 2\%$.

9.4.7 Influence of fiber source on fiber pullout response

It was observed during the experimental program that fiber batches from two different UHPC shipments were producing slightly varied results when embedded within the same concrete block. To explore this trend, load-slip response from the two different fiber shipments are compared in this section. Fibers from the first shipment (shipment A) were packed in cardboard boxes of 20 Kg and had an average diameter, d_f, of 0.23 mm ± 14.7% (obtained from a random sample size of 30 fibers). Fibers from the second shipment were packed in bags of the same weight (shipment B) and had an average diameter of 0.22 mm ± 0.84%.

The fiber average load-slip curves from both shipment are similar in their initial slopes for slip values less than 0.5 mm ($\upsilon/L_e \lesssim 0.08$) and in their frictional behavior before complete pullout at slip values greater than 3.5 mm ($\upsilon/L_e \gtrsim 0.54$) as shown in Fig. 9.15. However, fibers from shipment B had a stronger fiber-matrix interface friction resulting in approximately 20% increase in maximum pullout load $\overline{P}_{max}$ compared to fibers from shipment A as shown in Fig. 9.15 and Table 9.5. It is hypothesized that this increase in pullout friction is due to variations in raw materials and manufacturing processes followed to produce the two fibers, including brass coating material, surface roughness, and fiber end-deformations. This hypothesis is supported by the similarities between $\overline{P} - \nu$ curves of shipment A tested in groups 2 and 5, which verifies that the difference in the behavior is due to the fiber origin and not the UHPC matrix.

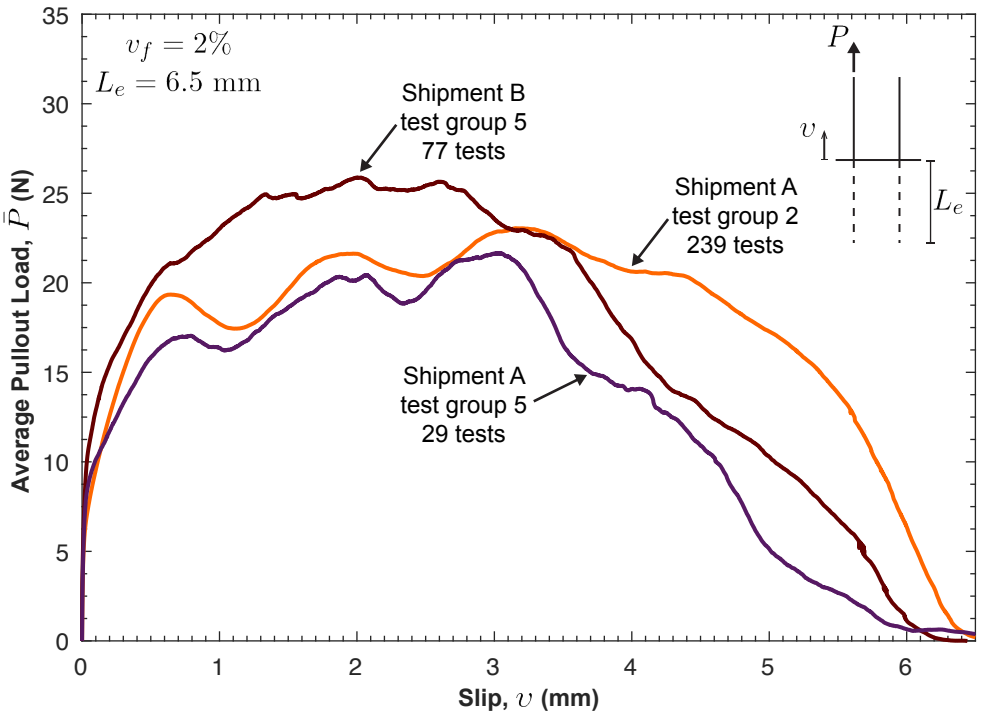

Figure 9.15: Average load-slip response curves showing the effect of fiber origin in UHPC with $v_f = 2\%$.

9.4.8 Influence of fiber embedment length on fiber pullout response

When fibers are embedded in UHPC, cracks can initiate at any location along the fiber length resulting in varying embedded lengths between the two crack faces. To study this effect, load-slip response for fibers with L_e = 4.0, 5.0, 6.5, and 7.5 mm was obtained, and presented in Fig. 9.16. As expected, decreasing L_e results in lower pullout loads (40% to 63% decreases in $\bar{P}_{max}$ as shown in Table 9.5) because the fiber surface area in contact with the matrix is smaller. The observations and trends are incorporated into a uniaxial load-slip fiber law presented in the next section.

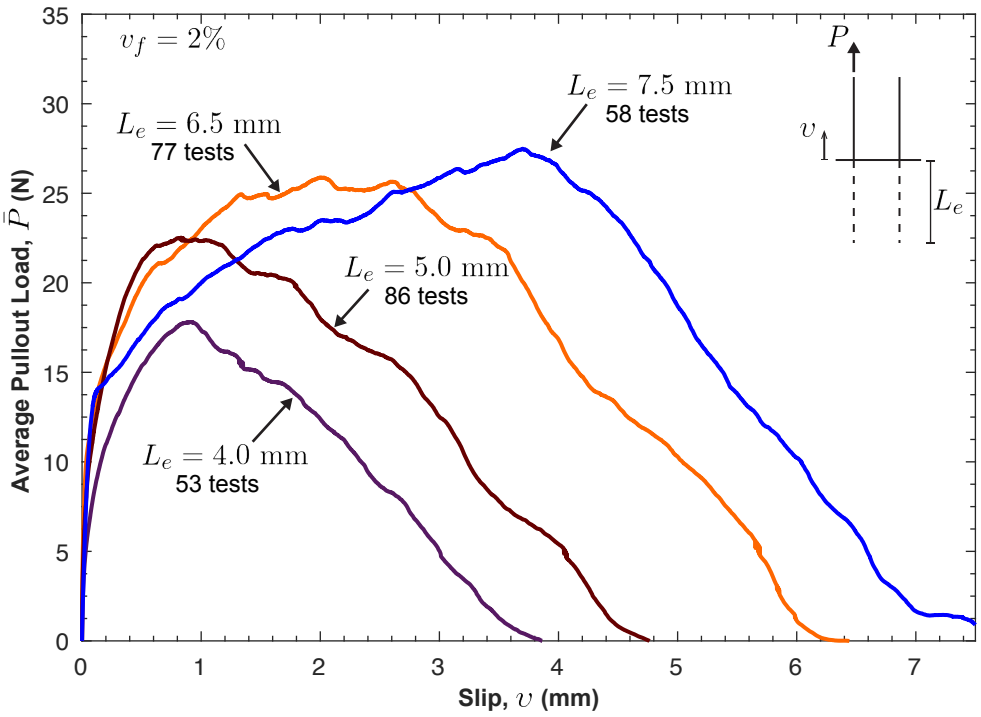

Figure 9.16: Average load-slip response curves showing the effect of embedment Length, L_e, in UHPC with $v_f = 2\%$.

Test group	v_f (%)	fiber shipment	L_e (mm)	Tested fibers	$\overline{W}$ (N-mm)	$\overline{P}_{max}$ (N)
2	2	A	6.5	239	112.7 ± 59.9	31.5 ± 54.9
5	2	A	6.5	29	83.64 ± 76.0	26.6 ± 61.9
		B	7.5	58	126.2 ± 81.3	31.5 ± 56.8
			6.5	77	108.1 ± 71.9	32.0 ± 57.6
			5.0	86	65.1 ± 68.1	28.7 ± 62.1
			4.0	53	39.6 ± 79.4	21.5 ± 76.0

Table 9.5: Summary of fiber pullout averaged results showing the effect of embedment length, L_e, for $v = 2\%$.

9.5 Fiber pullout model parameters

Fiber model parameters necessary to simulate the fiber-matrix interaction of single straight steel fibers embedded in UHPC are derived in this section considering fiber embedment length and confinement stress. The uniaxial fiber law utilized herein is derived by Lin et al. (1999)

and described in detail in Chapter 3. Fig. 3.5, which illustrates the model typical results, is reproduced below for convenience. The fiber pullout load-slip response curve is defined initially by a gradual debonding governed by the bond fracture energy, G_d, and a constant value of frictional stress, τ_0. Once the fiber completely debonds from the surrounding matrix, the resistance is purely frictional and controlled by the post-peak frictional parameter, β, which could be positive or negative in the case of slip-hardening or slip-softening.

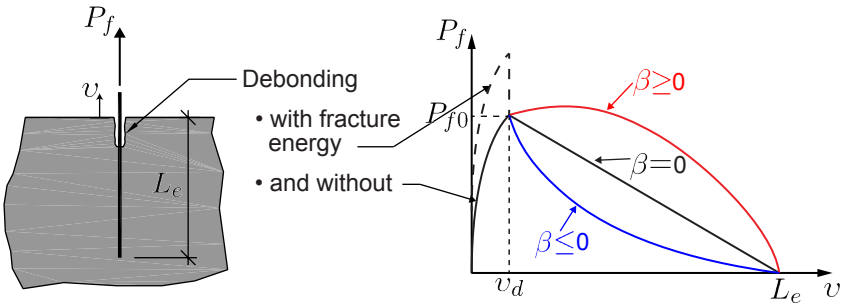

Figure 3.5: Typical pullout load versus slippage ($P_f - \upsilon$) relationship (Schauffert and Cusatis, 2012). Under fair use 2016. (repeated from page 25)

9.5.1 Derivation of uniaxial fiber load-slip parameters

The initial slopes of the experimental load-slip curves of Fig. 9.16 at varying embedment length values are similar, approximately 500 N/mm, then they begin to degrade as the load increases beyond 5 N. The post-peak portions of the response are consistent with parallel straight lines and a constant load decay rate of approximately 6.3 N/mm. These two observations are typical fiber pullout responses for steel fibers embedded in concrete and suggest a constant single value of the model frictional stress, τ_0, a negligible value of debonding fracture energy, G_d, and a frictional post-peak parameter, β, value of 0. However, the experimental data show inconsistencies in the pre-peak load-slip relationships with increasing values of fiber embedment. For instance, lower load values are observed within the pre-peak portions of the curves in Fig. 9.16 when the embdement length is increased from 5.0 mm to 6.5 and 7.5 mm, respectively (compare a pullout load of 21.2 N at a slip, υ, of 0.5 mm for $L_e = 5.0$ mm to 19.9 and 17.0 N, at the same slip value, for $L_e = 6.5$ and 7.5 mm). To overcome this issue, the post-peak portion of the shortest embedment length, $L_e = 4.0$ mm, is solely fitted to identify the only free parameter of the model, namely the frictional bond stress, τ_0. The pre-peak portion of the behavior, instead, is predicted through the model fracture mechanics formulation (Eqs. 3.21 and 3.22). A frictional stress value of $\tau_0 = 10$ MPa is

found to properly capture the post-peak response of the load-slip curve at $L_e = 4.0$ mm, which is similar to the average bond strength values calculated based on maximum pullout loads reported by other researchers for the same fibers embedded in similar UHPC mixes (Wille and Naaman, 2013). Afterwards, by only changing the embedment length, the fiber law was able to predict the post-peak portions of the curves at $L_e = 5.0$, 6.5, and 7.5 mm as shown in Fig. 9.18. The model ability to predict the fiber pullout behavior at different embedment length values is key to structural-level computational modeling as cracks can initiate along any location within the fiber length.

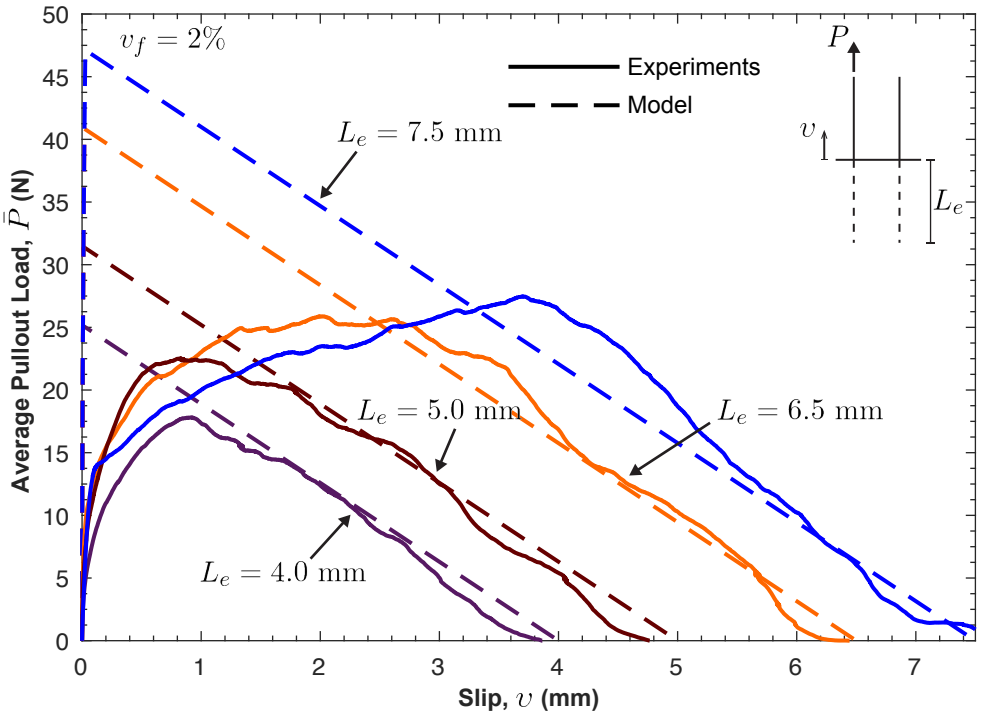

Figure 9.18: Fiber model vs. experimental load-slip response curves at different values of fiber embedment length.

The Lin et. al (1999) model, with $G_d = 0$, $\tau_0 = 10$ MPa, and $\beta = 0$, assume an initial static friction between the fiber and the surrounding matrix which is gradually overcome as the load increases to $P(\upsilon_d) = P_{max}$. At the critical debonding slip, υ_d, the fiber is completely debonded and starts to slip relative to the concrete surface along the application of load. The model results of Fig. 9.18 have steeper dedonding pre-peak slopes (approximately 20,000 N/mm) and higher peak loads (i.e. $P_{max} = 47.1$ N at $\upsilon_d = 0.027$ mm for $L_e = 7.5$ mm) compared to the experimental data (with 500 N/mm initial slopes and P_{max} of 27.4 N occuring at $\upsilon = 3.68$ mm for $L_e = 7.5$ mm). This discrepancy suggest negligible fiber-matrix

interface bond in the single fiber pullout tests, in which the fibers, having no initial static friction, directly starts to slip out of the matrix when tension loads are applied at the fiber tip. To investigate this hypothesis, the state of stresses in the concrete around of the fiber is examined by a three dimensional finite element model (FEM) of the fiber-matrix interaction. A quarter portion of the middle section of the UHPC specimen, where the fibers are installed, was modeled as solid elements assuming a linearly elastic material with modulus of elasticity of 55 GPa and a Poisson's ratio of 0.16 as shown in Fig. 9.19. The fiber was modeled with a truss element at an embedment length of 7.5 mm and a perfect bond with the UHPC was assumed. The boundary conditions were assigned to the concrete FEM nodes on the bottom and cut planes of the quarter model as shown in Fig. 9.19. A prescribed displacement is applied to the fiber tip and the load, P, and slip, v, at the exit point between the fiber and concrete surface were recorded. The simulations were carried out with the Finite Element Analysis Program (FEAP) (Taylor, 2014).

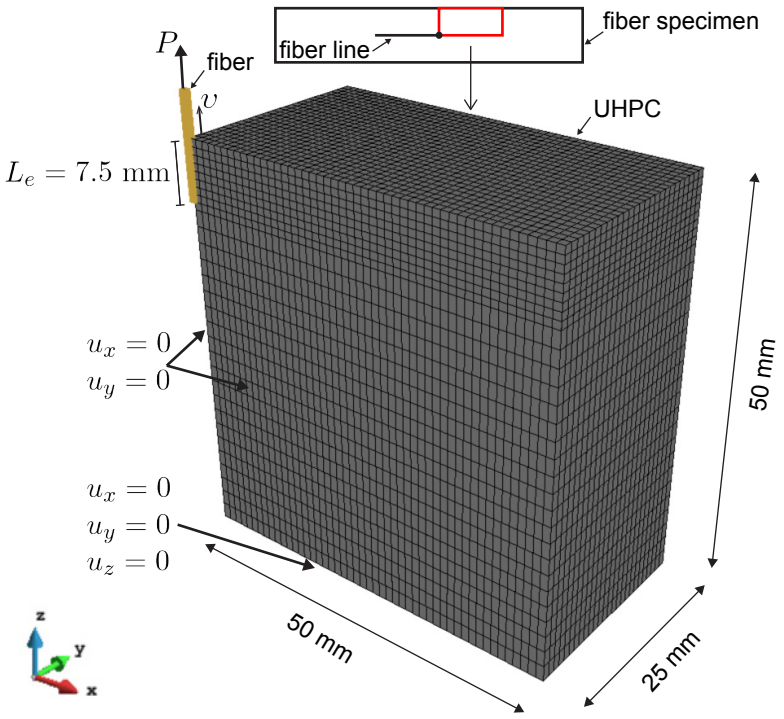

Figure 9.19: Geometry and boundary conditions of the a linearly elastic FEM of the fiber pullout test assuming perfect bond.

The load-slip results of the FEM model are compared to the Lin et al. (1999) model results and experimental data in Fig. 9.20. If the fiber is fully bonded to the UHPC, the initial load-slip behavior is similar to the linear FEM model results (with a slope of 37,000

N/mm) until a pullout load of 9.1 N, beyond which the maximum principal tension stress exceeds the tension strength of UHPC ($f_t = 8.6$ MPa) creating micro-cracks in the concrete surrounding the fiber and reducing the bond stiffness (Fig. 9.21). If the interface is initially governed by static friction, the load-slip curve is expected to have an initial slope, closer in value to the elastic fully bonded case, which starts degrading with increasing fiber loads (since the local static frictional stress is gradually overcome over the embedded fiber region). This phenomenon is governed by the first part of the Lin et al. (1999) model curve describing gradual debonding at a maximum frictional stress, τ_0, of 10 MPa as shown in Fig. 9.20. The experimental average load-slip curve have a significantly lower initial slope (approximately 500 N/mm) than both models, which indicates that the initial frictional bond is negligible in the experiments and therefore, the fiber can only gain strength by sliding out of the specimen and rolling the matrix particle creating clamping frictional forces.

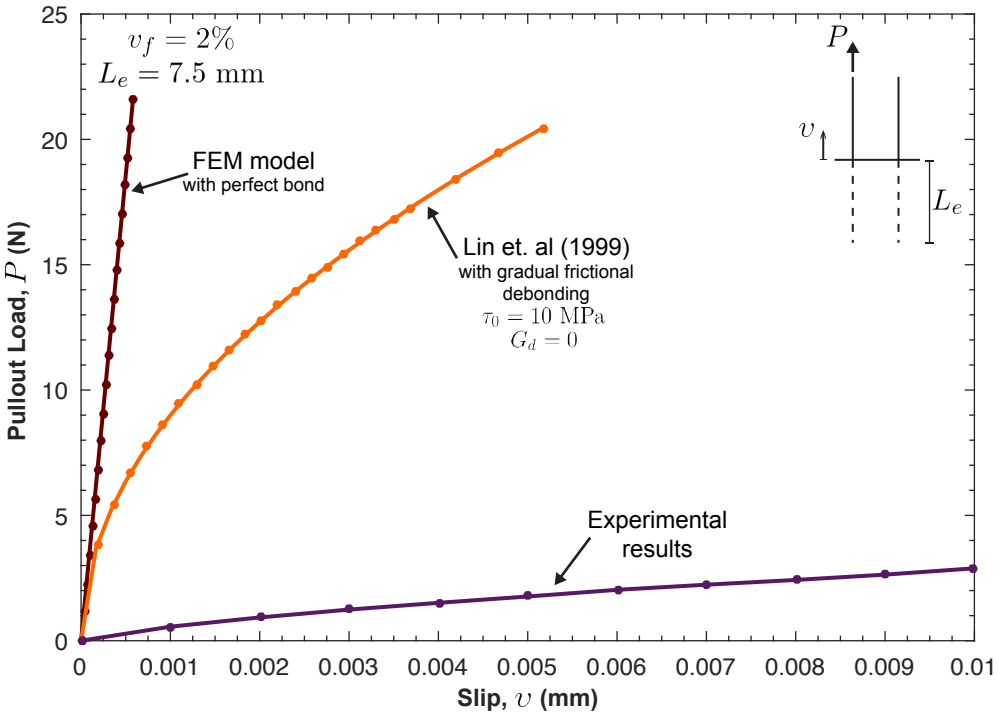

Figure 9.20: Effect of fiber-matrix bond properties on the initial load-slip response curve.

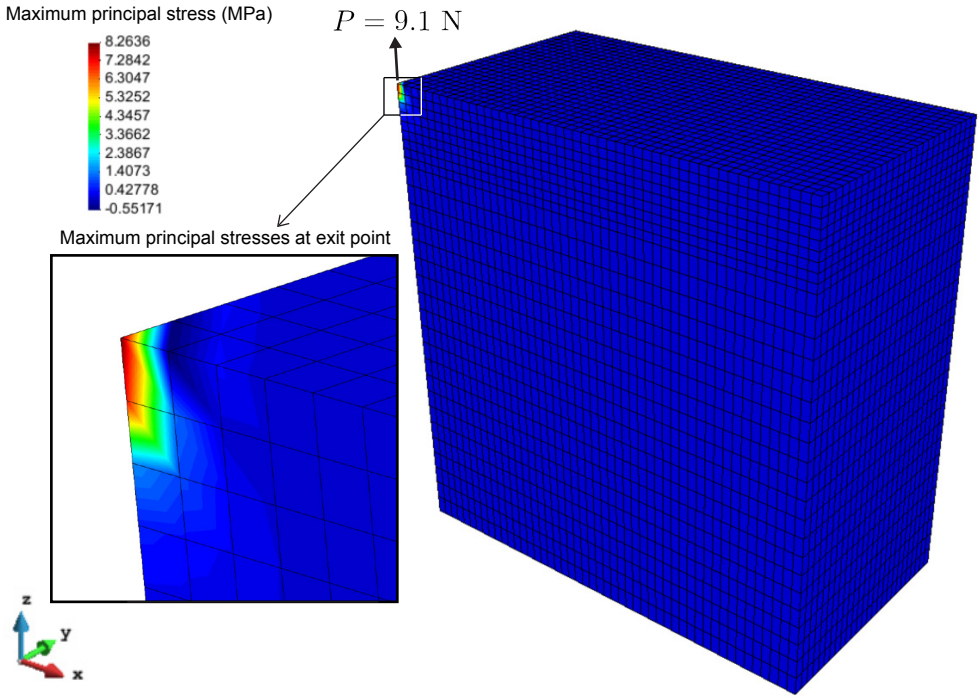

Figure 9.21: Maximum principal stress contours at the exit point between the fiber and matrix at the onset of cracking.

Steel fibers embedded in UHPC are known to have an initial bonding frictional stress that is activated on the structural level at the onset of cracking. The sensitivity of the fiber bridging force to small values of crack opening (or slip) improves the material response and increase the strength and ductility of the composites. Therefore, it can be concluded that the initial frictional bond observed in the single fiber pullout tests is broken before the start of the tests which is different than when the fibers are bridging cracks in a composite. The loss of initial bond in the experiments can be attributed to the a number of reasons including: 1) matrix fibers in contact with the embedded portion of the tested fibers weakens the bond between the fiber and matrix; 2) the initial bond could have been disturbed while demolding the fiber specimens and pulling the strong tape to expose the fibers free ends (Fig. 9.2); and 3) test setup variability and vice alignment generated a compression pre-load which could have disturbed the initial bond.

For the remainder of this document, the Lin et. al (1999) model with $G_d = 0$, $\tau_0 = 10$ MPa, and $\beta = 0$ will be used to simulate the fiber-matrix interface of fibers embedded in UHPC (Fig. 9.18). Research is ongoing to design a new experimental testing method that quantifies the interfacial bond properties at the early stages of the load-slip response ($\upsilon \leq 1$

mm), which controls the fiber efficiency in UHPC structural components and systems.

9.5.2 Influence of confinement stress on model parameters

External confinement stresses increased the first peak load values and the initial stiffness slopes of the average load-slip response curves as shown in Fig. 9.14. This behavior is reflected in the model parameters through an increase in the frictional stress values, τ_0, as confinement stress increases. The increase in the friction coefficient, $\tau_0(0)/\tau_0(\sigma_c)$, is derived, based on the first peak values of Fig. 9.14, as a function of confinement stress, σ_c, which can be conveniently embedded in model formulations with a polynomial interpolation shown in Fig. 9.22 (dashed curves) and represented as

$$\frac{\tau_0(\sigma_c)}{\tau_0(0)} = (-1.44\sigma_c^2 + 14.15\sigma_c) \times 10^{-3} \ (0 \leq \sigma_c \leq 53 \text{ MPa}). \tag{9.1}$$

Eq. 9.1 should be used with caution as it was derived from the experimental data in which the concrete specimen was confined along its thickness but not in its longitudinal direction. In fact, the confining procedure created a tension field of $0.11\sigma_c$ in the longitudinal direction as discussed in Appendix F. More data points are needed to predict the increase in the frictional stress for values above 53 MPa.

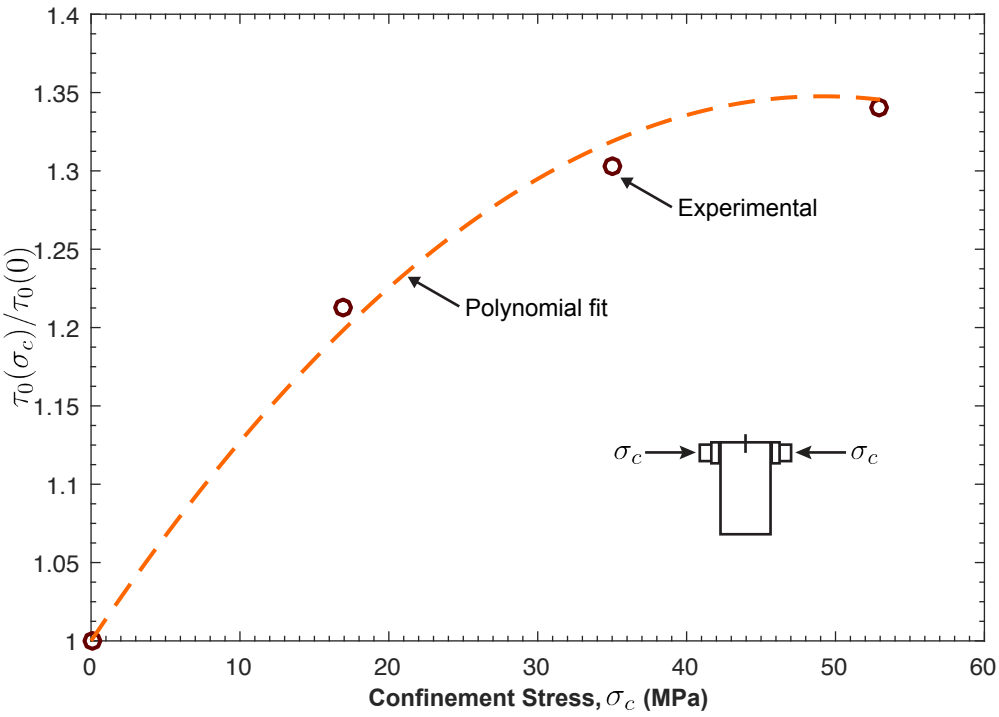

Figure 9.22: Maximum principal stress contours at the exit point between the fiber and matrix at the onset of cracking.

Chapter 10

Lattice Discrete Particle Model for UHPC Structural Behavior

This chapter describes the numerical modeling of UHPC in tension, fracture, and compression with the Lattice Discrete Particle Model (LDPM) and the Lattice Discrete Particle Model for fiber-reinforced concrete (LDPM-F). The LDPM input parameters are identified in section 10.1 by fitting the model results for UHPC without fibers to the experimental data. Fibers are then explicitly generated and assigned the fiber-matrix interaction model parameters obtained in Chapter 9. LDPM-F prediction simulations are carried out in section 10.2 without any further changes in the identified parameters, and their results are compared to the experimental data for fiber-reinforced UHPC that were not utilized during the calibration phase.

10.1 LDPM parameter identification for UHPC

The LDPM constitutive equations, formulated by Cusatis and coworkers (Cusatis et al., 2011a) and summarized in Chapter 3, are governed by a number of parameters that are calibrated from material tests. The parameter identification for UHPC without fibers is carried out herein by building the simulation models for tension, fracture, and compression to mimic the experimental conditions including mix design, internal structure, dimensions, loading, and boundary conditions. The numerical simulations were performed with the Modeling and Analysis of the Response of Structures (MARS) software (Pelessone, 2016),

which is a multi-purpose computational code for the explicit dynamic simulation of structural performance. MARS is installed on the Advanced Research Computing (ARC) NewRiver system at Virginia Tech, which has two 2.5 GHz Intel Xeon E5-2680 Haswell processors on its login and compute nodes, each with 12 cores, for a total of 24 cores per node, and with 128 GB of 2133 MHz memory on each node.

10.1.1 LDPM meso-structure parameters

The LDPM simulates concrete's internal structure at the mesoscale, where the material is viewed as a two phase composite in which hard or stiff particles are held together by a weaker or softer binder matrix. This step requires the identification of the UHPC mix proportions and particle size parameters which were determined based on a typical Ductal© UHPC mix composition, estimated by Graybeal (2006) and shown in Table 5.1. In constructing the LDPM meso-structure, the fine sand and ground quartz particles were both treated as 'aggregate', a, and the portland cement and silica fume were considered as 'binder', b. Therefore, the cement content parameter, c, was set equal to b at 943 Kg/m^3, and the water-to-binder and aggregate-to-binder ratios were set equal to $w/b = 0.138$ and $a/b = 1.305$, respectively.

UHPC is characterized with a maximum aggregate size of 0.6 mm, which if set as the maximum aggregate size of the model, d_a, would lead to very large number of particles generated for a given volume and substantially increases the computational cost of UHPC simulations. To overcome this hurdle, the coarce grained approximation, recommended by Smith et al. (2014) and summarized in section 3.2, is adopted herein, and thus, the simulated maximum aggregate size, d_a, is increased to 4 mm. The coarsened system of particles was shown to provide accurate results with significant reduction in computational cost. The minimum aggregate size is assumed to be $d_0 = d_a/2 = 2$ mm with a Fuller curve exponent $n_F = 0.5$. These parameters simulate about 30% of the aggregate mass which is an adequate resolution for the concrete's internal structure (Cusatis et al., 2011b) since it generates a representative mesoscale facet network, where cracks could initiate and propagate. A complete list of LDPM meso-structure parameters is provided in Table 10.1. To account for the variations in the internal structure that are possible in the experiments, three mesh generations of the LDPM meso-structure were analyzed and their averaged numerical results are reported.

Table 10.1: LDPM meso-structure parameters for UHPC.

LDPM parameter	**Calibrated value**
Binder content, b	943 Kg/m^3
Water-to-binder ratio, w/b	0.138
Aggregate-to-binder ratio, a/b	1.305
Minimum aggregate size, d_0	2 mm
Maximum aggregate size, d_a	4 mm
Fuller exponent, n_F	0.5

For the remainder of this chapter, the LDPM input parameters governing the mechanical behavior of UHPC were identified and validated for the coarsened system of particles, which is governed by the meso-structure parameters of Table 10.1. These parameters (i.e. minimum and maximum particle size) should not be varied without a complete reassessment of their effect on the LDPM macroscopic results, specifically the model's strain softening response and damage localization as described in Section 3.2.

10.1.2 LDPM elastic and tension parameters

The model elastic parameters, namely the effective normal modulus, $E_0 = 90$ GPa, and the shear-normal coupling parameter, $\alpha = 0.292$, are obtained by best fitting the average experimental modulus of elasticity, $\bar{E} = 53.7$ GPa, and Poisson's ratio, $\bar{\nu} = 0.17$. The values for E_0 and α are first estimated utilizing the macro-to-meso formulas (Eqs. 3.8 and 3.9), then refined by graphically matching the numerical stress-strain curve to the experimental results. The experimental data from both UHPC with and without fibers were used in the identification of the elastic parameters because LDPM neglects the contribution of fibers before matrix cracking. This approximation is proven to be valid in the elastic regime as discussed in Section 6.4.3 where it was shown that fibers, 2-4% by volume, have minimal impact on the elastic properties of UHPC.

Next, the identification of the LDPM tension parameters, namely the facet tensile strength, σ_t, and the tensile characteristic length, l_t, is performed by matching the model results for UHPC without fibers to the experimental data obtained from three tests: (1) the mortar briquette direct tension tests; (2) the splitting tensile tests; and (3) the fracture toughness

tests. The model's geometry, loading scheme, and fixities mimic the experimental conditions and are detailed hereafter for each test.

The middle 48 mm of the mortar briquette specimens, where failure is expected to occur, is only reproduced with LDPM. Similarly to the specimen geometry, the model is dogbone-shaped with the smallest cross-section occurring at mid-length and having a width and thickness of 25 mm as shown in Fig. 10.1a. Two rigid steel plates are defined at the top and bottom ends of the model to impose the boundary conditions. The plates are modeled with hexahedron solid elements, having triangular mesh surfaces, and are tied to the LDPM surface nodes through master and slave constraints. All translational degrees of freedom (u_x, u_y, u_z) are restrained excluding the vertical translation (u_y) at the top of the specimen where a uniform constant displacement is imposed (Figs. 10.1a,b). The plates are allowed free rotation around the transverse axes (r_x, r_z) with restricted rotation around the vertical direction (r_y) to mimic the support conditions of the experimental setup. Next, the software generates the zero-diameter edge and surface nodes (Fig. 10.1b) and positions the LDPM particles, which diameters and locations are governed by the mix design parameters specified in the previous section, as shown in Fig. 10.1c. The lattice system is then defined by a Delaunay tetrahedralization that connects the particle centers creating three-dimensional tetrahedra that fill the specimen's volume. The tetrahedralization is followed by a domain tessellation which defines the facets pertaining to each particle and forms a potential crack network. Each mortar briquette simulation utilized 1 node with 16 cores and is characterized by a run time of 12 minutes.

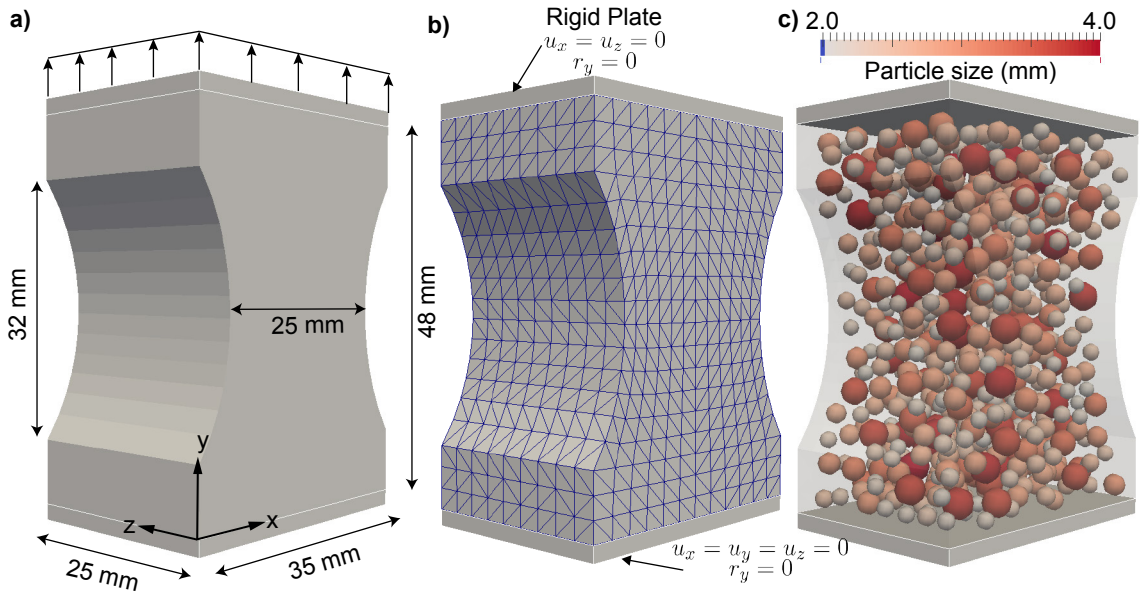

Figure 10.1: Mortar briquette simulation model showing: a) the specimen geometry and loading scheme; b) boundary conditions and surface nodes; and c) particle size distribution.

The splitting tension cylindrical specimens, with a nominal diameter of 102 mm and a length of 205 mm, were modeled as prisms having the same length and a square cross section with sides equal to the cylinder's diameter as shown in Fig. 10.2a. This change in the outside geometry was done to minimize the stress localization, induced when a nodal load is applied at the tip of a circular cross section, and to prevent early cracking of concrete around the supports. Two rigid steel plates, having a width of 5 mm and a length of 204 mm, are defined at mid-width of the top and bottom ends of the model to impose boundary conditions as shown in Fig. 10.2b. The plates are modeled with triangular shell elements and are tied to the LDPM surface nodes through master and slave constraints. All transnational (u_x, u_y, u_z) and rotational degrees (r_x, r_y, r_z) of freedom are restrained excluding the vertical translation (u_y) at the top of the specimen where a uniform downward displacement is imposed (Fig. 10.2a,b). Fig. 10.2c shows the LDPM generated particles for the splitting tension model. Each simulation utilized 1 node with 16 cores and is characterized by a run time of approximately 5 hours.

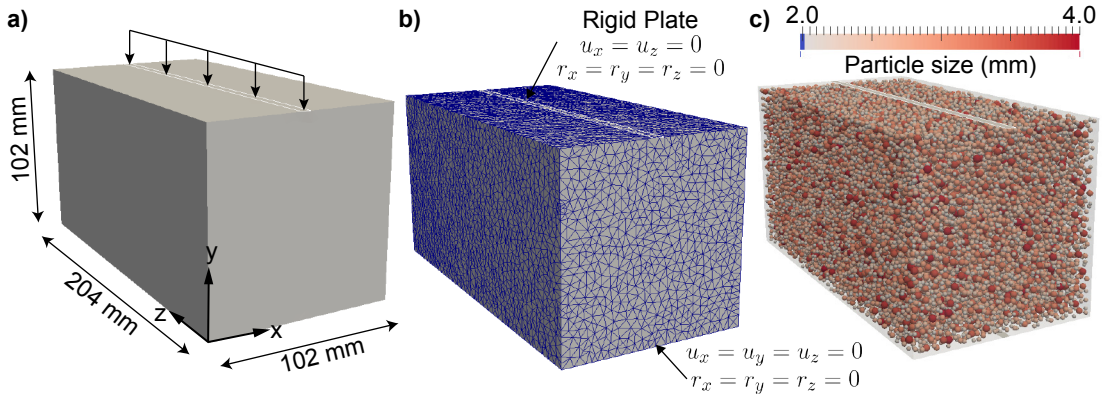

Figure 10.2: Splitting tension simulation model showing: a) the specimen geometry and loading scheme; b) boundary conditions and surface nodes; and c) particle size distribution.

Similarly to the experiments, the fracture toughness models are performed on 3-point bending prisms having a span of 407 mm, a nominal width of 51 mm, a nominal height of 102 mm, and nominal notch dimensions of 5 mm width and 25 mm height with a round tip, introduced at mid-span of the bottom flange as shown in Fig. 10.3a. A rigid steel plate, having a width of 2 mm and a length of 51 mm, is defined at mid-span of the top flange of the beam to impose boundary conditions. The plate is modeled with triangular shell elements and is tied to the LDPM surface nodes through master and slave constraints. The transnational degrees of freedom in the transverse directions (u_x, u_z) and all rotational degrees (r_x, r_y, r_z) of freedom are restrained as shown in Fig. 10.3b. A uniform downward displacement is imposed on the plate to mimic the loading protocol of the experiments (Fig. 10.2a). The boundary conditions at the supports are imposed directly to the LDPM nodes to reflect roller supports at both beam ends as shown in Fig. 10.2b. The middle 115 mm of the beam span, where the failure is expected to occur, is only reproduced with LDPM to save on computational cost (Fig. 10.2c). The remaining two 146 mm side pieces of the beam are modeled with elastic hexahedron elements and tied to the LDPM surface nodes with penalty constraints. Each simulation utilized 1 node with 16 cores and is characterized by a run time of approximately 20 hours.

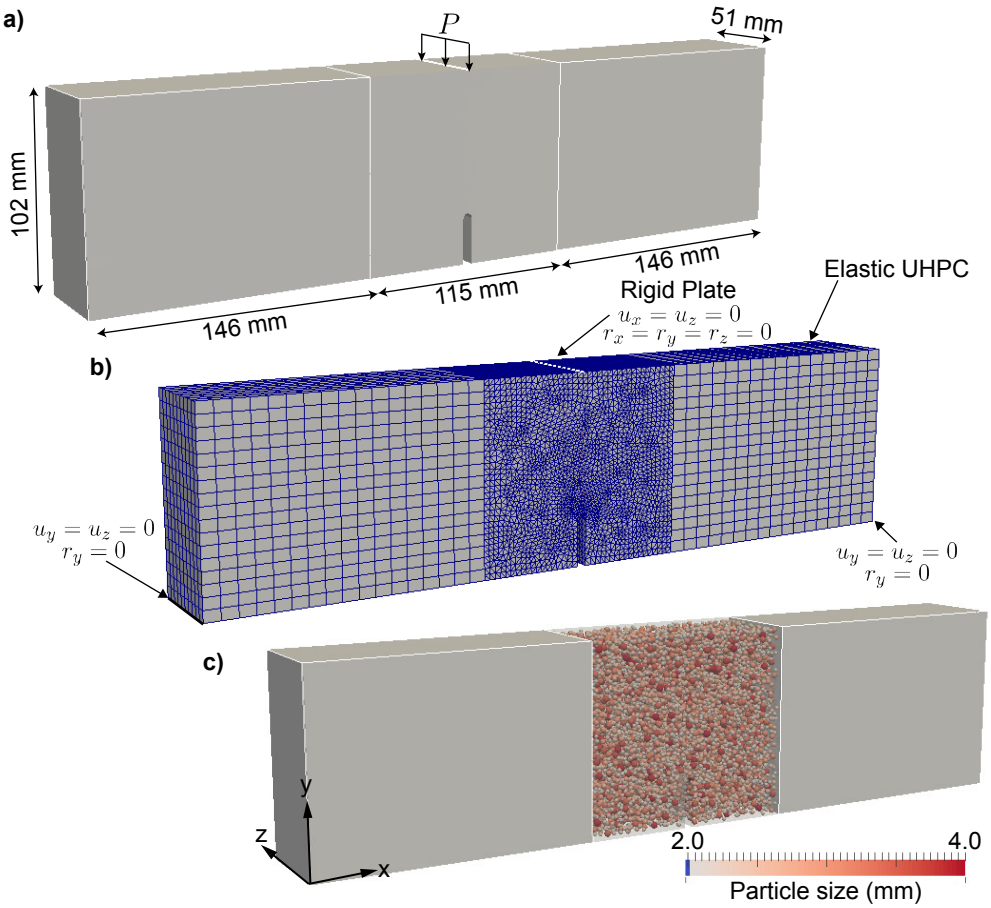

Figure 10.3: Fracture toughness simulation model showing: a) the specimen geometry and loading scheme; b) boundary conditions and surface nodes; and c) particle size distribution.

After building the model geometry and generating the LDPM meso-structure, the tension parameters, $\sigma_t = 7.5$ MPa and $l_t = 50$ mm, which governs the facet tensile strength and softening behavior, are identified by a trial and error procedure to best fit the average experimental results taking into account a number of observations discussed hereafter.

The average tension strength, $\bar{f}_t = 8.6$ MPa $\pm$ 8.9%, obtained from the mortar briquette specimens is used with caution since the test setup allows rotations at both ends of the dogbone-shaped specimens creating a non uniform tensile stress field. In many cases, the failure did not occur at the vicinity of the minimum cross section, as discussed in Section 8.4.1, which suggest that the obtained tensile strength could be higher than the actual value. To obtain an estimation of the direct tension strength of UHPC without fibers while eluding the effects non uniform strain fields, the tension strength, $\bar{f}_t \approx 7.75$ MPa $\pm$ 3.2%, obtained by Maya Duque et. al. (2016) from pull-off tests on the same UHPC is used herein for

reference. In these tests, a concrete core, with a diameter of 51 mm, is partially drilled, at a depth of 25 mm, perpendicular to the top surface of a UHPC slab without fibers. The bottom end of the core cylinder was kept attached. A steel disc was then glued to the top surface of the core and pulled vertically at a constant stress rate of 35 ± 15 kPa/sec until failure (Maya et al., 2016). The simulated macroscopic tensile strength of UHPC without fibers is 7.7 MPa which is in good agreement with the experimental data. Fig. 10.4 show the simulated axial stress stress-displacement curve of the mortar briquette specimen, with the crack pattern at peak and two post-peak points illustrated in Fig. 10.5. The simulated crack pattern consists of an an individual crack forming at the mid-length when the load approaches its peak value then starts to propagates through the specimen and widen as the displacement is increased until failure (Fig. 10.5).

The experimental average splitting tensile strength, $\bar{f}_{t,s} = 7.2$ MPa ± 23.1%, is characterized by high variability with a standard deviation of 1.7 MPa. This variability is attributed to the nature of the test setup and loading procedure which creates regions of stress concentration at the vicinity of the supports inducing local imperfections and triggering the brittle failure of the material. The simulated macroscopic splitting strength of UHPC without fibers is 6.6 MPa which is deemed satisfactory as it lies in scatter of the experimental results. Fig. 10.6 show the simulated splitting tensile stress plotted as function of top displacement, with the crack pattern at peak and two post-peak points illustrated in Fig. 10.7. Similarly to the experiments, the simulated crack pattern consist of an individual crack forming at the mid-width vertical plane when the load approaches its peak value. The crack then starts to propagates through the specimen and widens as the downward displacement is increased until failure (Fig. 10.5).

The simulated fracture toughness load-CMOD curve is plotted against the experimental scatter in Fig. 10.8. This curve was obtained by calibrating the value of the tensile characteristic length parameter, $l_t = 50$ mm, which governs the tensile softening behavior, to match the experimental average fracture energy, $\bar{G}_F$, of 53.8 J/mm^2 ± 13.2%. The simulated load vs. axial mid-span deflection is plotted in Fig. 10.9 but was not compared to the experimental results due to the axial extensometer slippage observed during the tests (for more information, see Section 7.4.1). Similarly to the experiments, the simulated crack pattern consist of an individual crack strating at the notch when the load is applied and propagates to the top beam flange as the downward displacement is increased until failure as shown Fig. 10.10. It is hypothesized that the simulated maximum fracture load, $P_s = 3.3$ kN,

was higher than the experimental peak average load, $P = 2.1$ kN $\pm$ 10.8% for two possible reasons: (1) the adopted coarse graining approximation changes the accuracy of the stress concentration at the notch tip, which in turn influences the shape of the load-CMOD curve at the peak load, and (2) transporting the specimens to the waterjet cutting facility, where the notch was introduced, and the cutting process itself might have produced imperfections and micro-cracks around the notch tip (given the brittle nature of UHPC without fibers) and resulted in lower values of peak fracture loads (for more information on the specimen preparation, see Section 7.2). This limitation is not crucial for the current study as it does not have a significant effect on the fiber-reinforced model results, where the fiber content and orientation have a greater impact on the behavior.

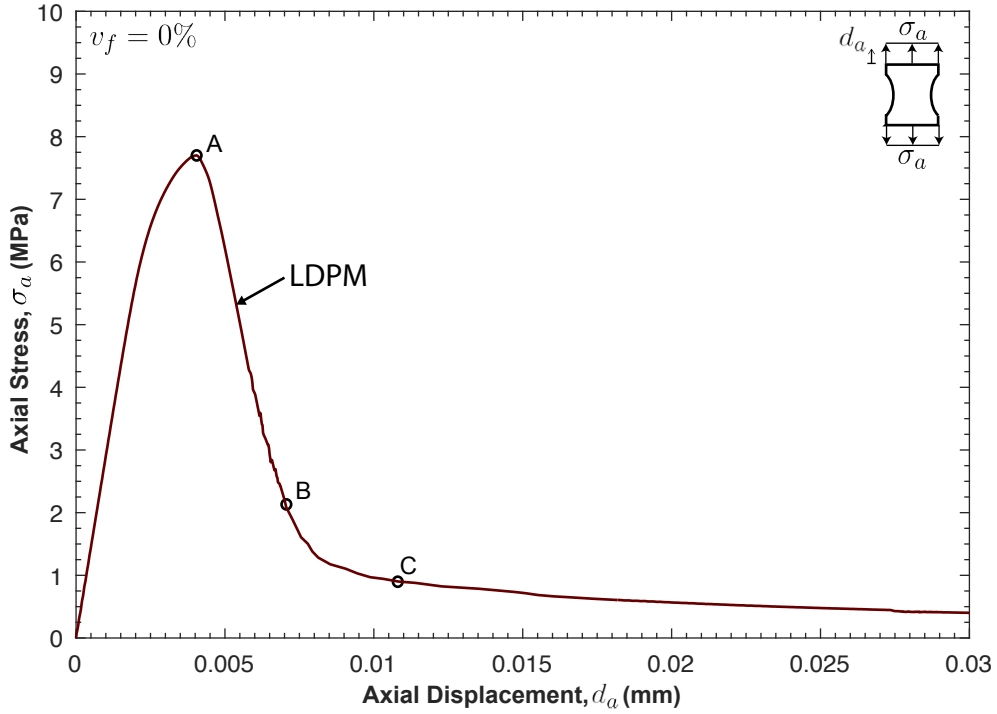

Figure 10.4: Mortar briquette direct tension simulation results for the LDPM tension parameters identification for UHPC without fibers.

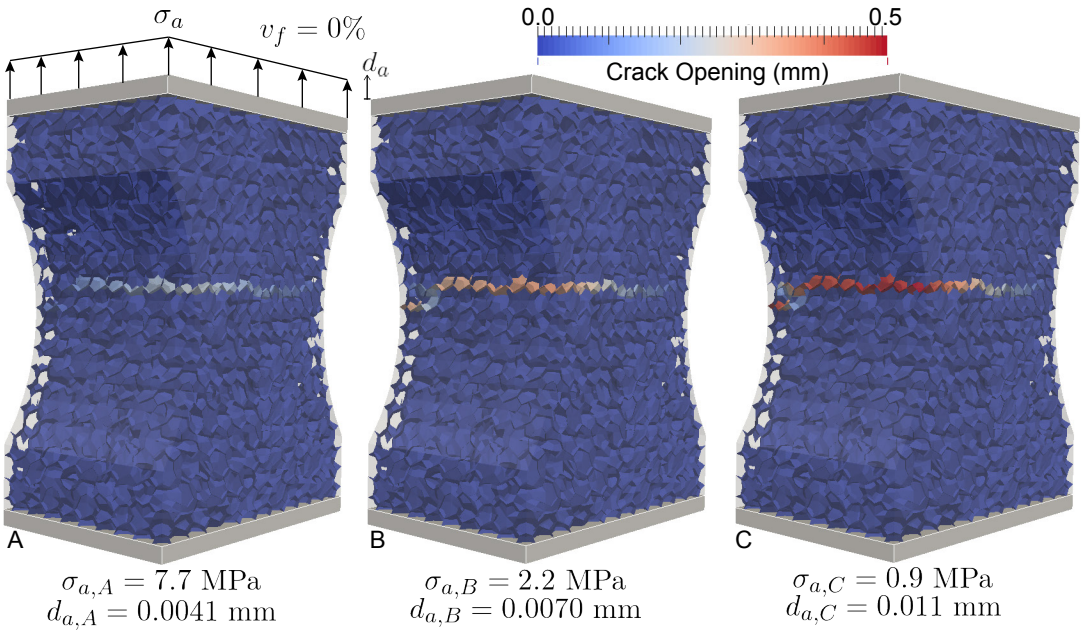

Figure 10.5: Simulated crack evolution and failure mode for the mortar briquette direct tension specimens at the locations depicted in Fig. 10.4 for UHPC without fibers.

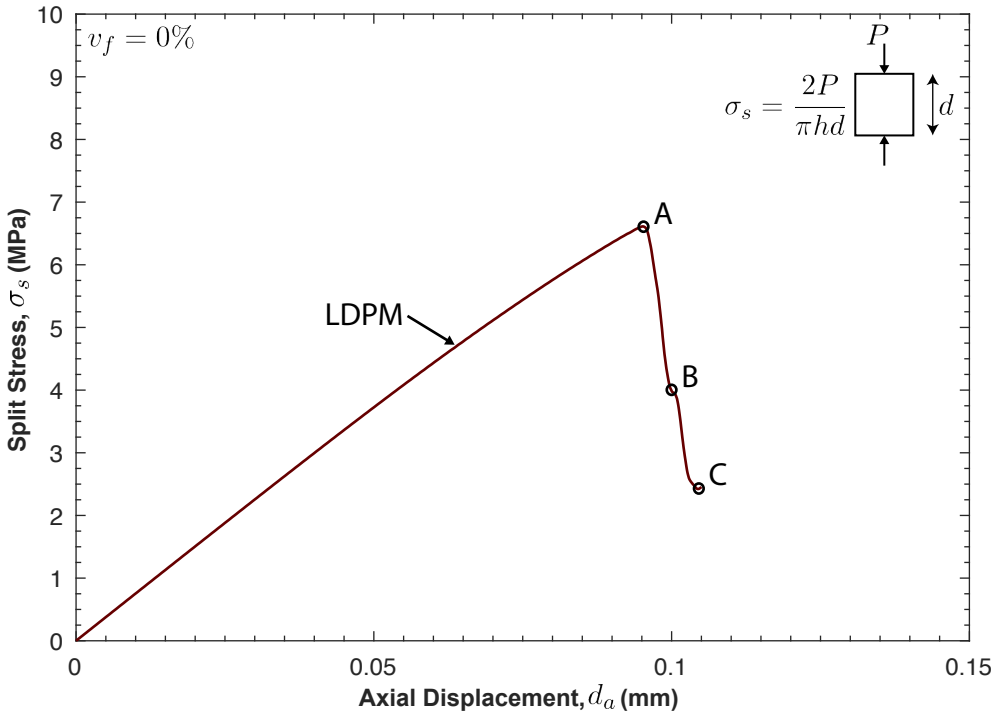

Figure 10.6: Splitting tensile simulation results for the LDPM tension parameters identification for UHPC without fibers.

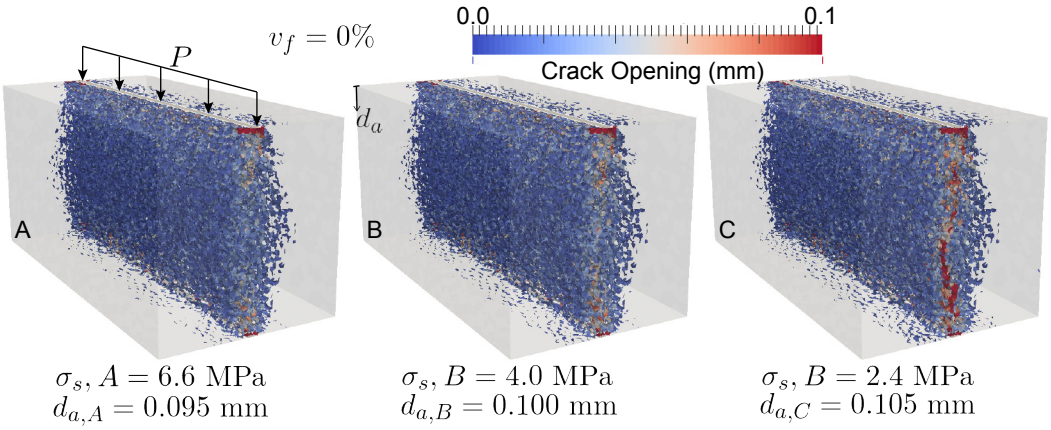

Figure 10.7: Simulated crack evolution and failure mode for the splitting tension specimens at the locations depicted in Fig. 10.6 for UHPC without fibers.

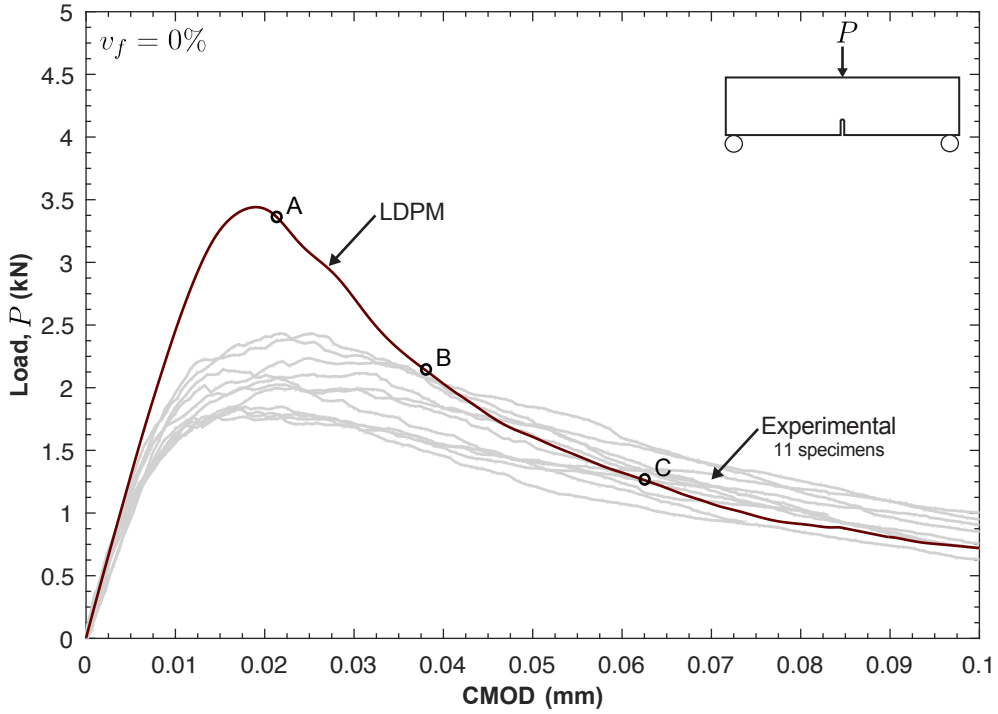

Figure 10.8: Fracture toughness simulated load-CMOD curve for the LDPM tension parameters identification for UHPC without fibers.

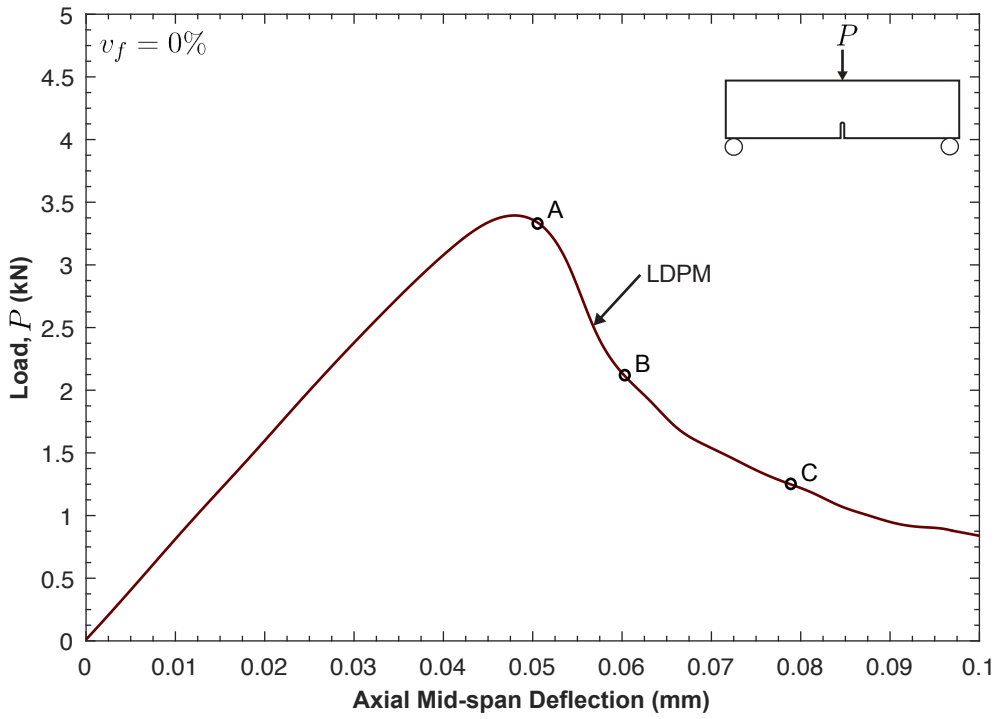

Figure 10.9: Predicted axial load-deflection curve for UHPC without fibers.

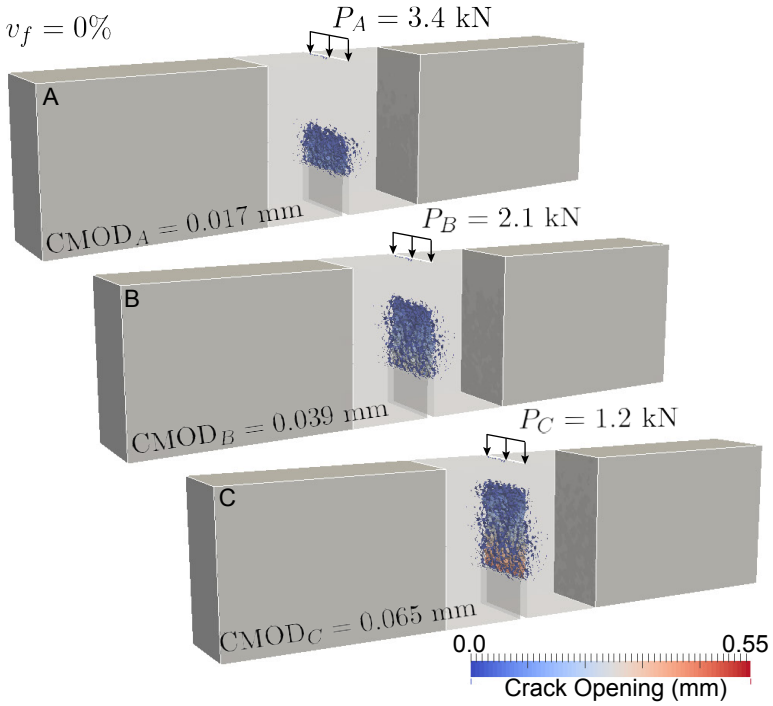

Figure 10.10: Simulated crack evolution and failure mode for the fracture toughness specimens at the locations depicted in Figs. 10.6 and 10.9 for UHPC without fibers.

10.1.3 LDPM unconfined compression parameters

The facet shear strength ratio, σ_s/σ_t, softening exponent, n_t, and initial friction, μ_0, parameters govern the LDPM behavior in the nonlinear and post-peak portions of the uniaxial unconfined compression, and are identified by matching the model results to the experimental data.

The uniaxial unconfined compression model mimic the experimental specimen geometry, with a nominal diameter of 76 mm and a height of 152 mm, as shown in Fig. 10.11a. Two rigid steel plates, 100 mm in diameter, are defined at the top and bottom ends of the model to impose the boundary conditions. The plates are modeled with shell triangular elements, and tied to the LDPM surface nodes through sliding friction nodal constraints with a kinematic friction factor, $f_k = 0.0084$, a static friction factor, $f_s = 0.03$, and a characteristic length, $A = 0,0195$ mm. The plates' translational (u_x, u_y, u_z) and rotational (r_x, r_y, r_z) degrees of freedom are restrained, excluding the vertical translation, u_y, at the top of the specimen, where a constant downward displacement is imposed as shown in Figs. 10.11a,b. Fig. 10.11c shows the LDPM generated particles for the unconfined compression cylindrical specimen. Each simulation utilized 1 node with 16 cores and is characterized by a run time of approximately 10 hours.

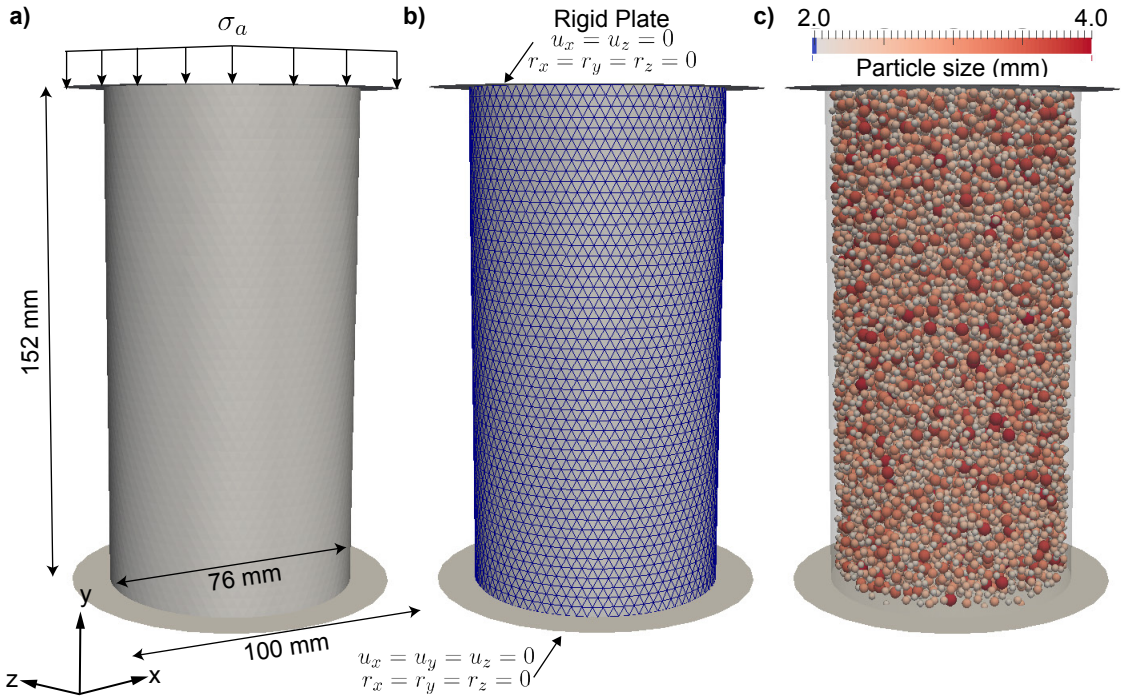

Figure 10.11: Unconfined compression cylinder simulation model showing: a) the specimen geometry and loading scheme; b) boundary conditions and surface nodes; and c) particle size distribution.

The nonlinear portion of the compressive axial stress-strain curve, shown in Fig. 10.12, was captured by setting the shear strength ratio, σ_s/σ_t, at 8.5, and initial friction, μ_0, at 0.15. The softening exponent, $n_t = 0.2$, was found to properly simulate the post-peak response. Fig. 10.13 shows the LDPM predicted axial stress vs. circumferential strain curve. A key advantage in the LDPM simulations is the model's ability to capture the compression crack propagation and failure mode through the visualization of splitting cracks as the compressive displacement is increased until failure, as shown in Fig. 10.14.

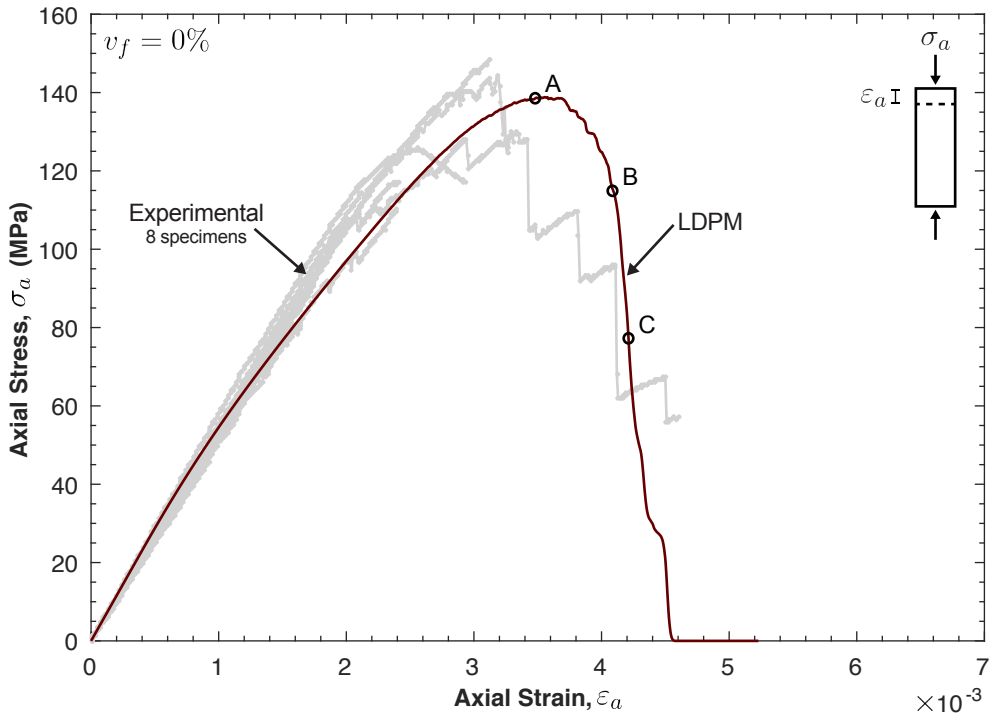

Figure 10.12: Unconfined compression simulated axial stress-strain curve for the LDPM compression parameters identification for UHPC without fibers.

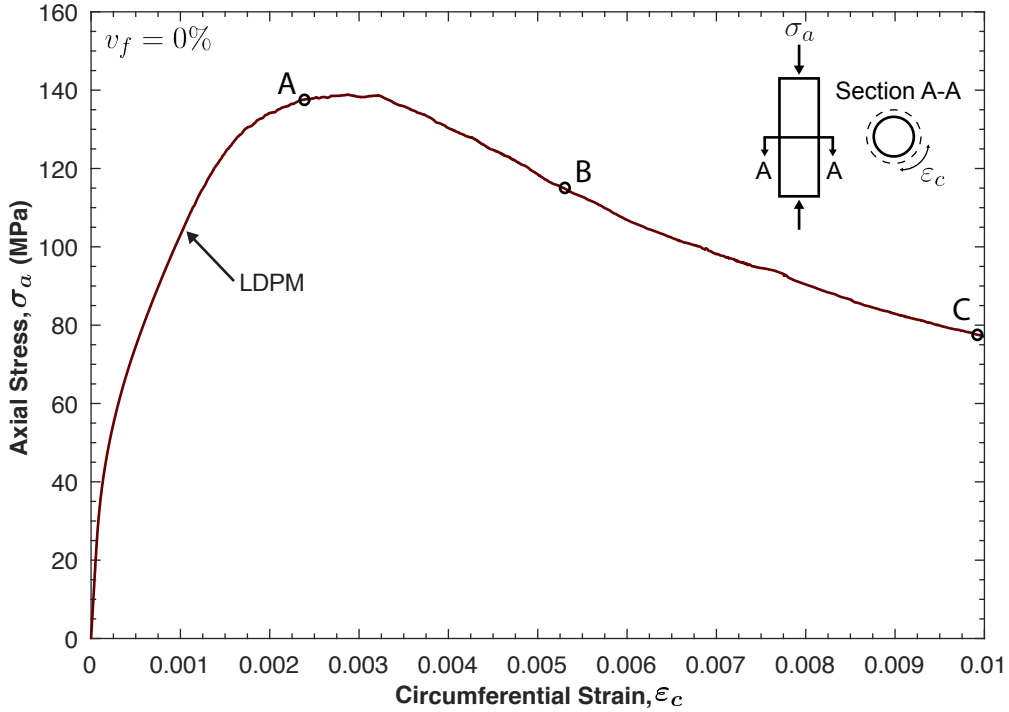

Figure 10.13: Predicted compression axial stress vs. circumferential strain curve for UHPC without fibers.

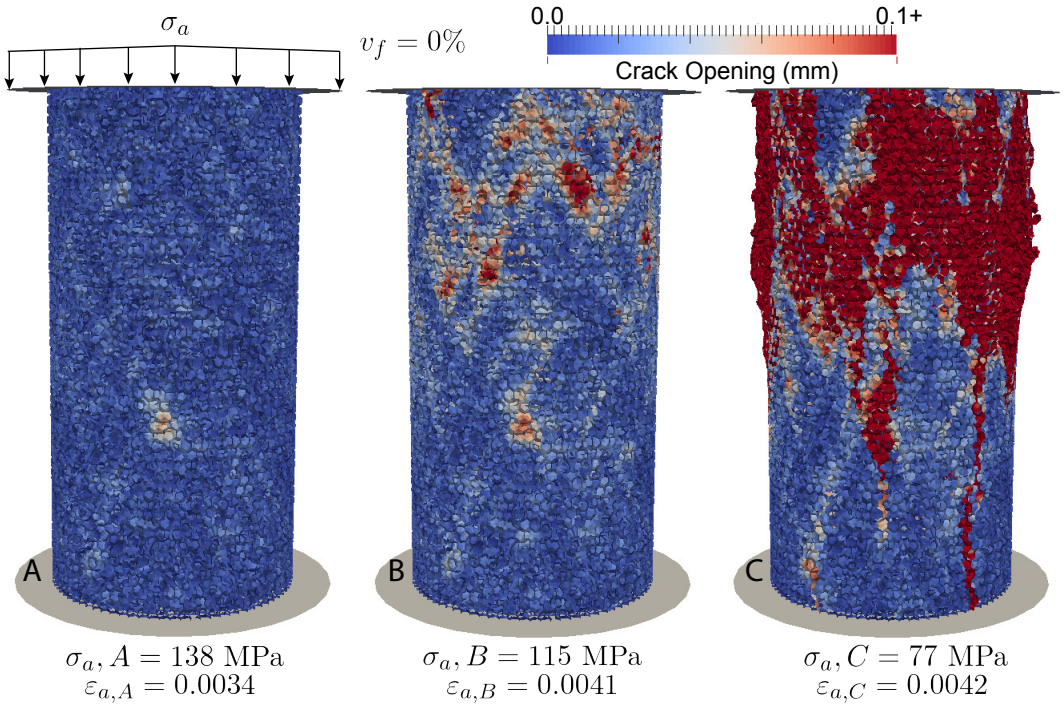

Figure 10.14: Simulated crack evolution and failure mode for the unconfined compression cylinderical specimens at the locations depicted in Figs. 10.12 and 10.13 for UHPC without fibers.

The compression parameters are validated by modeling the cube compression specimens, having 51 mm sides, without changing any further parameter and comparing the results with the experimental data. The same modeling procedure followed in simulating the cylindrical specimens is followed herein for the cube compression models as shown in Fig. 10.15. Each cube compression simulation utilized 1 node with 16 cores and is characterized by a run time of approximately 35 minutes.

The predicted tension strength, $f_c = 135.2$ MPa, is in excellent agreement with the 28-day experimental strength, $f_{c,28} = 137$ MPa, obtained from the cube specimens and reported in Table 6.3. Fig. 10.16 show the predicted axial stress stress-strain curve obtained from the cube compression model, with the crack pattern at peak and two post-peak points illustrated in Fig. 10.17. Finally, the calibrated LDPM parameters for UHPC without fibers are summarized in Table 10.2.

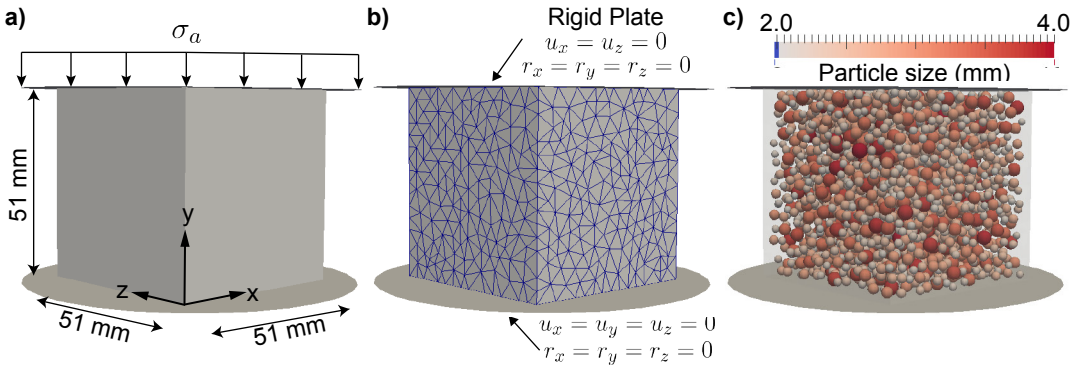

Figure 10.15: Unconfined compression cube simulation model showing: a) the specimen geometry and loading scheme; b) boundary conditions and surface nodes; and c) particle size distribution.

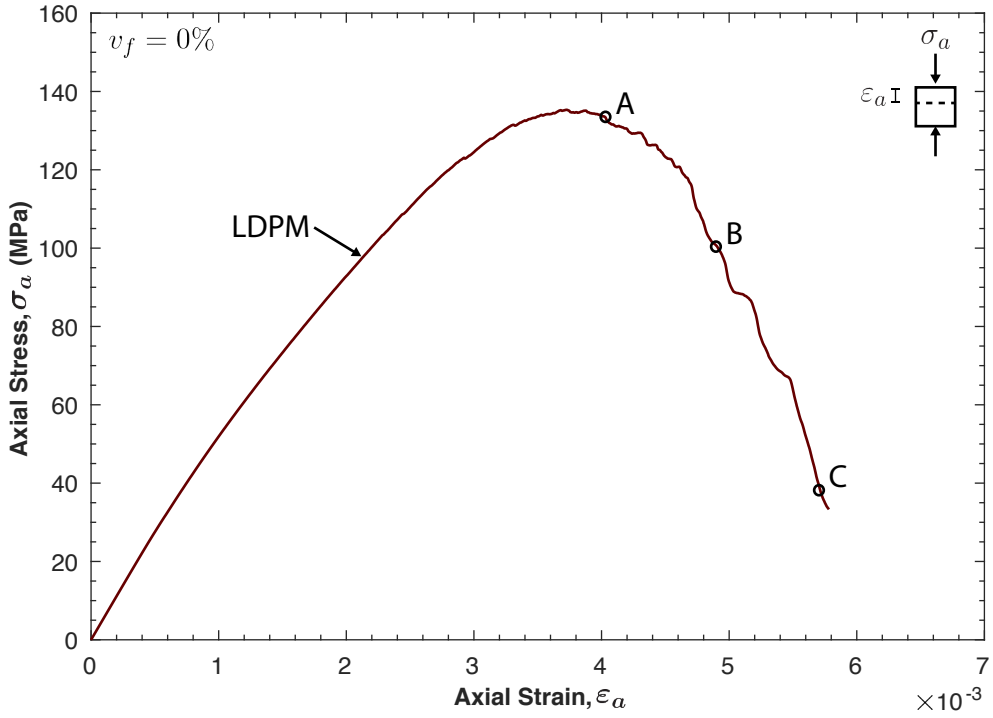

Figure 10.16: Predicted cube compressive axial stress-strain curve for UHPC without fibers.

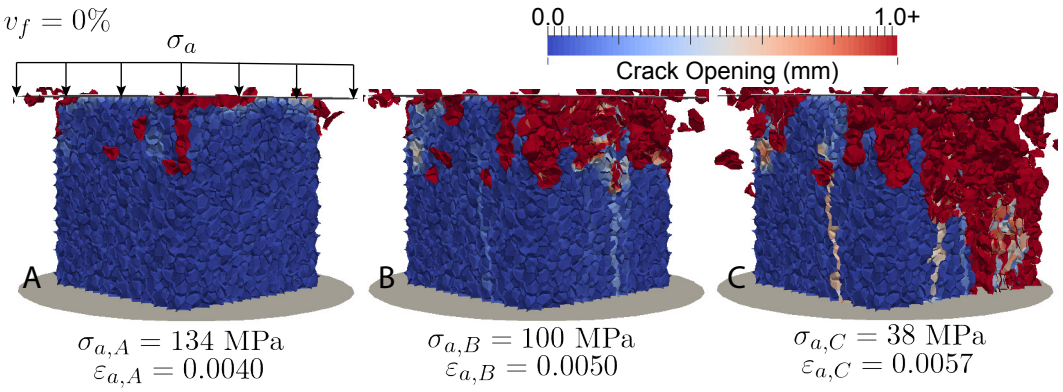

Figure 10.17: Simulated crack evolution and failure mode for the unconfined compression cubical specimens at the locations depicted in Fig. 10.16 for UHPC without fibers.

Table 10.2: Test performed for calibration and value of LDPM parameters in simulations for UHPC without fibers.

Test performed	**LDPM parameter**	**Calibrated value**
Direct tension	Tensile strength, σ_t	7.5 MPa
Fracture toughness test	Tensile characteristic length, l_t	50 mm
Uniaxial unconfined compression	Effective normal modulus, E_0	90 GPa
	Shear-normal coupling parameter, α	0.292
	Shear strength ratio, σ_s/σ_t	8.5
	Softening exponent, n_t	0.2
	Initial friction, μ_0	0.15

10.2 LDPM-F prediction simulations for fiber-reinforced UHPC

The calibration of the LDPM-F requires the identification of the model parameters governing the interface behavior between the fiber and its surrounding matrix. Since the fiber-matrix interaction problem occurs at a scale smaller than the meso-scale adoped in LDPM, it is analyzed utilizing the semi-empirical formulation of Yang et al. (2008), which adopts the Lin et al. (1999) formulation to generate a representative fiber pullout load-slip relationship (for more information, see Section 3.1.3). The fiber pullout model parameters derived

in Section 9.5.1 are adopted herein, with a frictional stress, $\tau_0 = 10$ MPa, a bond fracture energy, $G_d = 0$ J/m^2, and a slip hardening/softening parameter, $\beta = 0$. The fiber material and geometrical parameters are then inputted in the model, namely a fiber modulus of elasticity, $E_f = 205$ GPa, tensile strength, $\sigma_{u,f} = 2,500$ MPa, length, $L_f = 13$ mm, and cross sectional area, $A_f = 0.0314$ mm^2. Other failure mechanisms include fiber rupture with inclined pulling, matrix micro-spalling, and fiber snubbing (described in detail in Schauffert and Cusatis (2012) and summarized in Section 3.1.3), whose parameters, in absence of experimental data, are assumed on the basis of Schauffert et al. (2012) and Smith et al. (2014). A complete list of LDPM-F calibrated parameters is provided in Table 10.3.

Table 10.3: LDPM-F calibration parameters for UHPC with fibers

LDPM parameter	**Calibrated value**
Fiber length, L_f	13 mm
Fiber sectional area, A_F	0.0314 mm^2
Fiber elastic modulus, E_f	205 GPa
Fiber strength, $\sigma_{f,s}$	2,500 MPa
Frictional stress, τ_0	10 MPa
Debonding fracture energy, G_d	0.0 J/m^2
Frictional parameter, β	0.0
Spalling parameter, k_{sp}	0.6
Snubbing parameter, k_{sn}	0.0
Fiber strength decay, k_{rup}	0.0
Plastic parameter, γ_u	1.0

The LDPM-F explicitly models all straight smooth fibers contained in a volume at given fiber content, v_f, as single discrete segments, and mimics the fiber distributions in real structural components. A preferential orientation scale parameter, S_i, where $i = x, y, z$, defines how likely a fiber is to be oriented in a specific direction compared to the directions orthogonal to it. If $S_x = 5$, then a fiber is five times more likely to be oriented in direction x than directions, y, and z. The spacial distribution of the fibers depends on the geometric parameter, entitled 'chopped', in MARS. If the this parameter is activated, the control volume for fiber generation is increased and the fibers intersecting the specimen boundaries are chopped or cut. This results in shorter length fibers inside the specimen at the vicinity of the external surfaces which is the case for cored, machined, or extracted specimens. If the specimens are placed in molds, the 'chopped' parameter is deactivated and the fiber location and orientation are affected by the specimen's boundaries. Similarly to the models without

fibers, the average results of three numerical simulations is reported to reproduce the effects of fiber spacial distributions.

For the remainder of this chapter, no further changes are made to the LDPM and LDPM-F parameters listed in Tables 10.1, 10.2, and 10.3. The model validation is carried out hereafter by comparing the predicted mechanical responses of UHPC at different fiber volume contents and orientations to the experimental data, that were not utilized during the parameter identification phase.

10.2.1 Uniaxial direct tension

The direct tension tests, performed by Maya Duque and Graybeal (2016) and summarized in section 8.5, are modeled in this section with LDPM and LDPM-F to validate the model predictive capabilities in direct tension. These tests were chosen for the model validation for a number of reasons: (1) they eliminate the relative rotations of the tension specimens, creating a uniform uniaxial tensile stress field and minimizing premature strain localization in individual cracks; (2) they include a 102 mm gauge length allowing the generation of multi-cracks as expected in real fiber-reinforced UHPC structural components; and (3) they are characterized by a quantitative measure of the fiber preferential orientation, which is linked to a specific placement method.

The direct tension tests were modeled as dogbone-shaped specimens with a middle gauge length of 102 mm having a constant square cross section of 51 mm sides as shown in Fig. 10.18a. Two rigid steel plates are defined at the top and bottom ends of the model to impose the boundary conditions. The plates are modeled with hexahedron solid elements, having triangular mesh surfaces, and tied to the LDPM surface nodes through master and slave constraints. All translational (u_x, u_y, u_z) and rotational (r_x, r_y, r_z) degrees of freedom are restrained excluding the vertical translation (u_y) at the top of the specimen where a uniform constant displacement is imposed (Figs. 10.18a,b). Fig. 10.18c shows the LDPM meso-structure for the direct tension model.

The fibers are then generated by assigning a fiber volume content, $v_f = 2\%$, and the fiber system is then overlapped with the particle system as shown in Fig. 10.19.

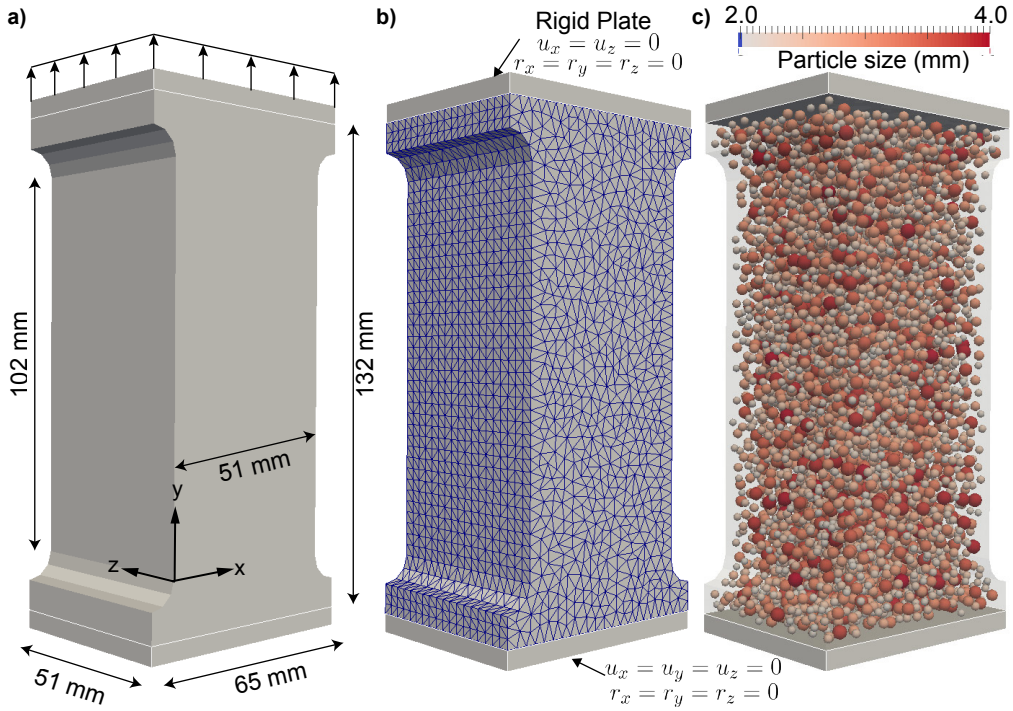

Figure 10.18: Uniaxial direct tension simulation model showing: a) the specimen geometry and loading scheme; b) boundary conditions and surface nodes; and c) particle size distribution.

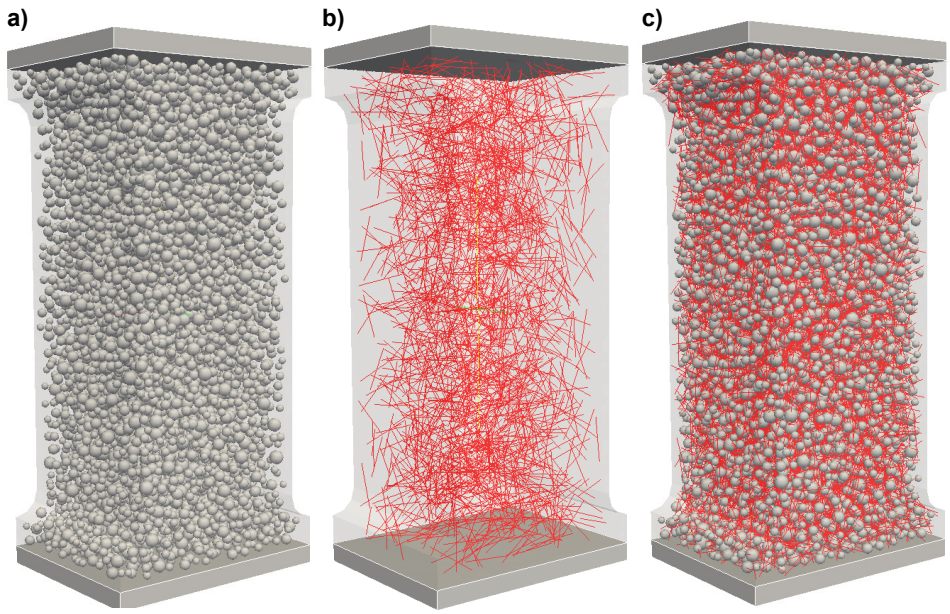

Figure 10.19: Uniaxial direct tension fiber model showing: a) the LDPM particles; b) the generated fiber segments at fiber volume content, $v_f = 2\%$, with random orientations (1/10 of fibers are shown); and c) the fiber system overlapped with the particle system with $v_f = 2\%$.

The direct tension test with $v_f = 0\%$ is first analyzed to obtain a benchmark for investigating the effect of fiber reinforcement on the tensile stress-strain response and crack patterns. Each simulation utilized 1 node with 16 cores and is characterized by a run time of approximately 3.5 hours. Fig. 10.20 shows the simulated uniaxial tensile stress-strain curve, with the crack pattern at peak and two post-peak points depicted in Fig. 10.21. As expected, the simulated failure mode consist of an individual crack forming inside the gauge length when the stress approaches its peak value. The crack then starts to propagates through the specimen and widens as the tensile displacement is increased until failure (Fig. 10.21). The predicted ultimate tension strength for these specimens is $f_t = 7.4$ MPa which is similar to the experimental tension strength of UHPC without fibers as discussed in the previous section.

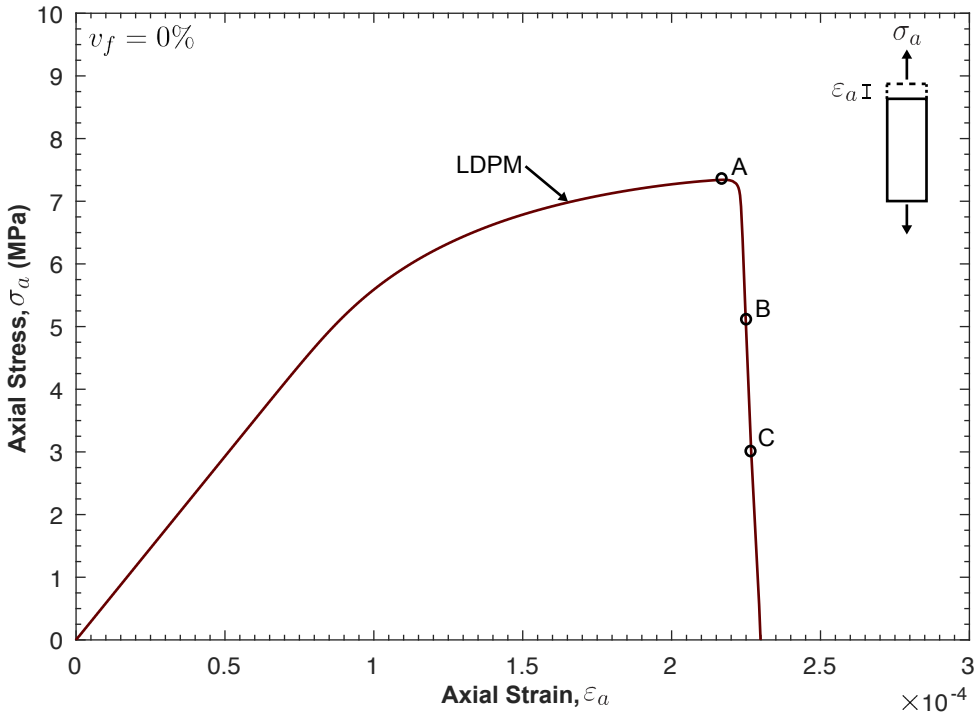

Figure 10.20: Predicted uniaxial stress-strain curve for UHPC without fibers.

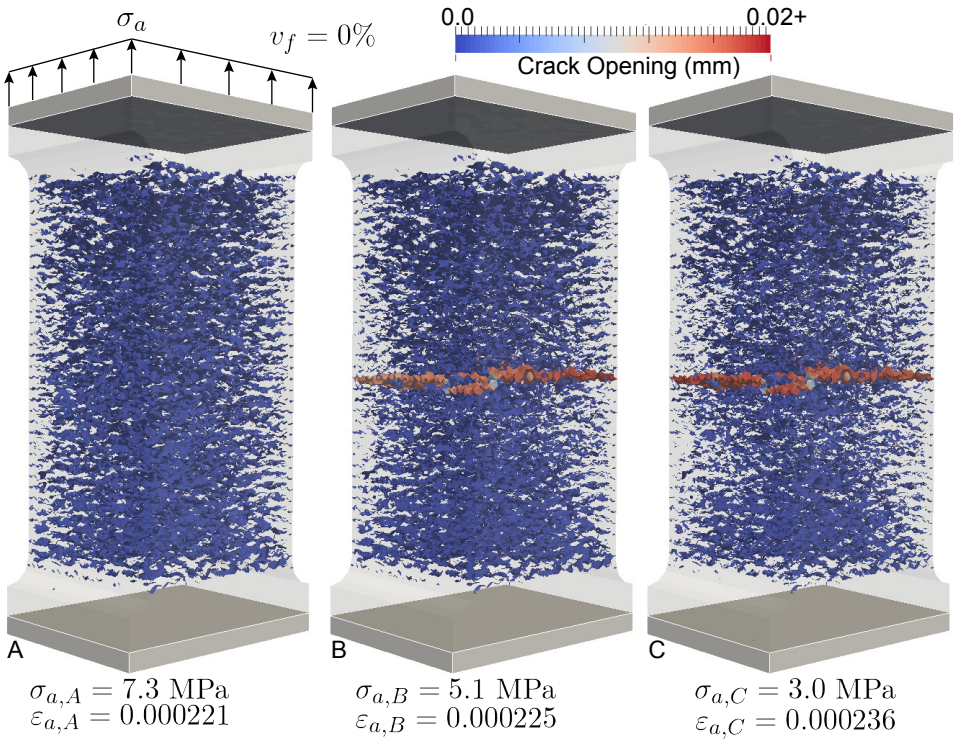

Figure 10.21: Simulated crack evolution and failure mode for the uniaxial direct tension specimens at the locations depicted in Fig. 10.20 for UHPC without fibers.

For the first set of the fiber-reinforced simulations, the 'chopped' parameter in MARS is deactivated because the numerical results are compared to the experimental data for the specimens casted in molds. Maya Duque and Graybeal (2016) calculated an average orientation factor obtained from three tested specimens pertaining to the four placement methods. The orientation factor is obtained as follows: $\mu = 1/N \sum_{i=1}^{N} \cos\theta_i = 1/N \sum_{i=1}^{N} b_i/a_i$, where N is the total number of fibers captured, by image analysis, in a cross-section cut at distance of $1.5L_f = 19.5$ mm from the main crack after testing, θ_i is the angle between the fiber axis and the vector normal to the cut plane, a_i is the major axis of the fiber elliptical footprint on the cut plane, and b_i is the minor axis of the footprint and is equal to the fiber diameter, $d_f = 0.2$ mm (for more information, see Section 8.5). Although analyzed for one section along the gauge length, it is assumed that the calculated orientation factor value is representative across all sections of the specimen. In LDPM-F, the fiber distribution mimics the real spacial distribution found in the experiments through a trial and error procedure to find the preferential alignment scale value along the application of load, S_y, that matches the experimental orientation factor in the same direction. Since the model explicitly generates all fibers in a volume, the simulated orientation factor in each trial is calculated by the same

equation: $\mu_i = 1/N \sum_{i=1}^{N} \cos\theta_i$, in which N is the total number of fibers generated in the specimen volume. A preferential orientation scale, $S_y = 5$, is found to match the experimental orientation factor, $\bar{\mu}_y = 0.85 \pm 0.7\%$, for the specimens casted in mold, in which fresh UHPC was placed from one side of the mold. The histogram of the simulated fiber distribution is shown in Fig. 10.22, in which θ_y is the angle between the fiber axis and the vertical direction, y.

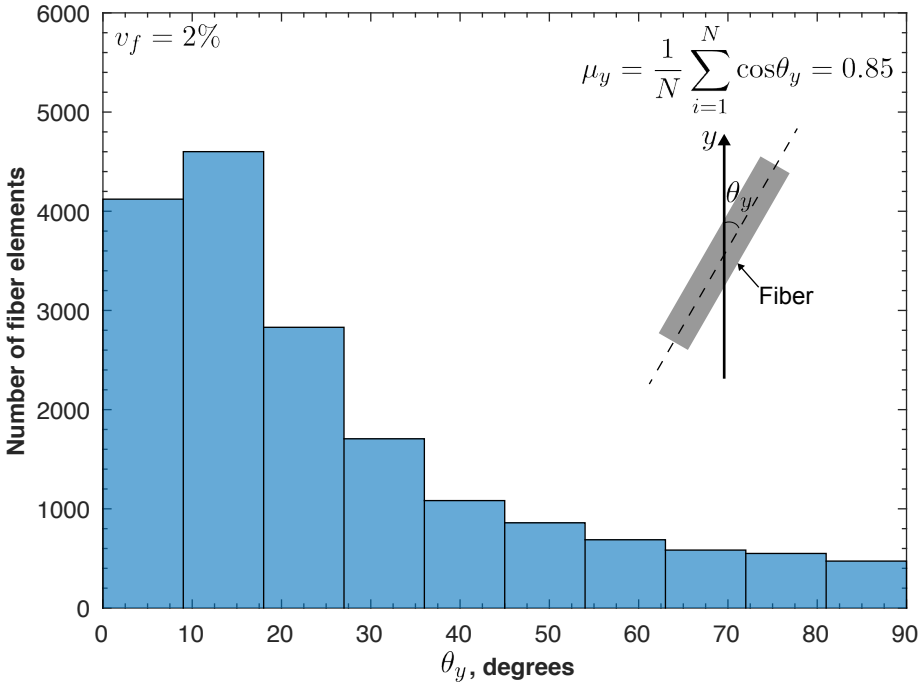

Figure 10.22: Simulated histogram of fiber orientation in the vertical direction, y, for the mold casted direct tension specimens.

The simulations for the mold-casted fiber-reinforced direct tension specimens with $v_f = 2\%$ utilized 1 node with 16 cores on NewRiver and are characterized by a run time of approximately 9 hours. The predicted stress-strain curve with $v_f = 2\%$ and $\mu_y = 0.85$ is compared to its corresponding experimental scatter in Fig. 10.23. The crack patterns at the peak load (point A), at the onset of strain localization (point B), and during the strain softening regime (point C) are depicted in Fig. 10.24. The LDPM-F captured well the tensile behavior of UHPC including: (1) the first peak strength where macroscopic cracks starts to appear, with a simulated strength, $f_t = 9.0$ MPa, compared to an average experimental value, $\bar{f}_t$, of $9.7 \pm 9.7\%$; (2) the multiple cracking behavior and the pseudo stress plateau until the strain localizes into a single crack at $\varepsilon_a = 0.004$ (point B), compared to an experimental average localization strain of $\bar{\varepsilon}_u = 0.0034 \pm 29.9\%$; and (3) the strain softening behavior,

where the strain is localized into a single or multiple closely spaced macroscopic cracks (compare crack pattern of point B to point C in Fig. 10.24). The observation must be made that these numerical simulations were based on the fiber pullout model parameter identification approach of section 9.5.1, supporting the hypothesis of initial bond breakage during the fiber pullout tests, which is not the case in actual UHPC specimens.

The second test group of the experimental tests consisted of specimens extracted from a UHPC slab and cut parallel (at 0°) to the flow direction during placement (Maya Duque and Graybeal, 2016). The average experimental orientation factor was found to be similar to the casted specimens, at the studied section, with $\bar{\mu}_y = 0.83 \pm 3.6\%$. However, the experimental results show a stronger tensile strength and more ductile response than the mold casted specimens with the same orientation factor (compare the experimental average of both tests in Fig. 8.17). It is hypothesized that when UHPC flows over a longer span in the slabs, compared to the individual molds, more fibers tend to be oriented parallel to the flow direction. It follows that a larger number of fibers is preferentially oriented parallel to the flow at various locations throughout the specimen's length, and therefore, a larger overall orientation factor than the one obtained form only one cut section, is expected. This is reflected in the model by aligning all the simulated fibers parallel to the vertical direction, $\mu_y = 1.0$, which generates the maximum possible simulated response for comparison purposes. Fig. 10.25 shows the predicted stress-strain curve with $v_f = 2\%$ and $\mu_y = 1$, which is compared to simulated curve with $\mu_y = 0.85$ and plotted against experimental scatter from the extracted and mold casted specimens, with $\mu_y = 0.85$.

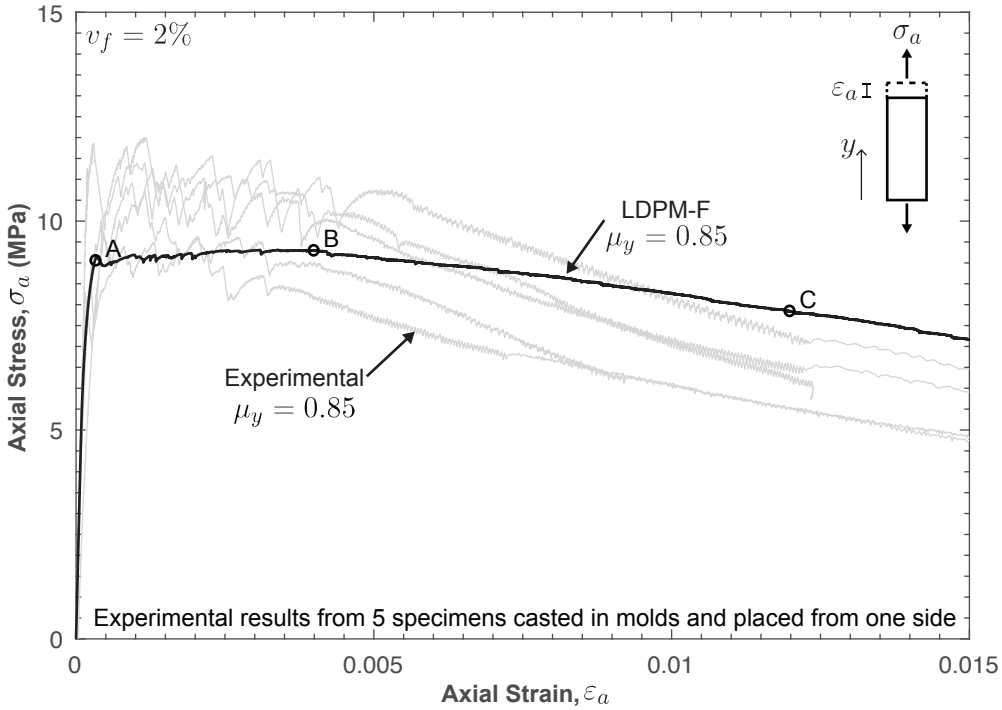

Figure 10.23: LDPM-F predicted and experimental stress-strain responses for the direct tension tests with 2% fiber content and an orientation factor of 0.85.

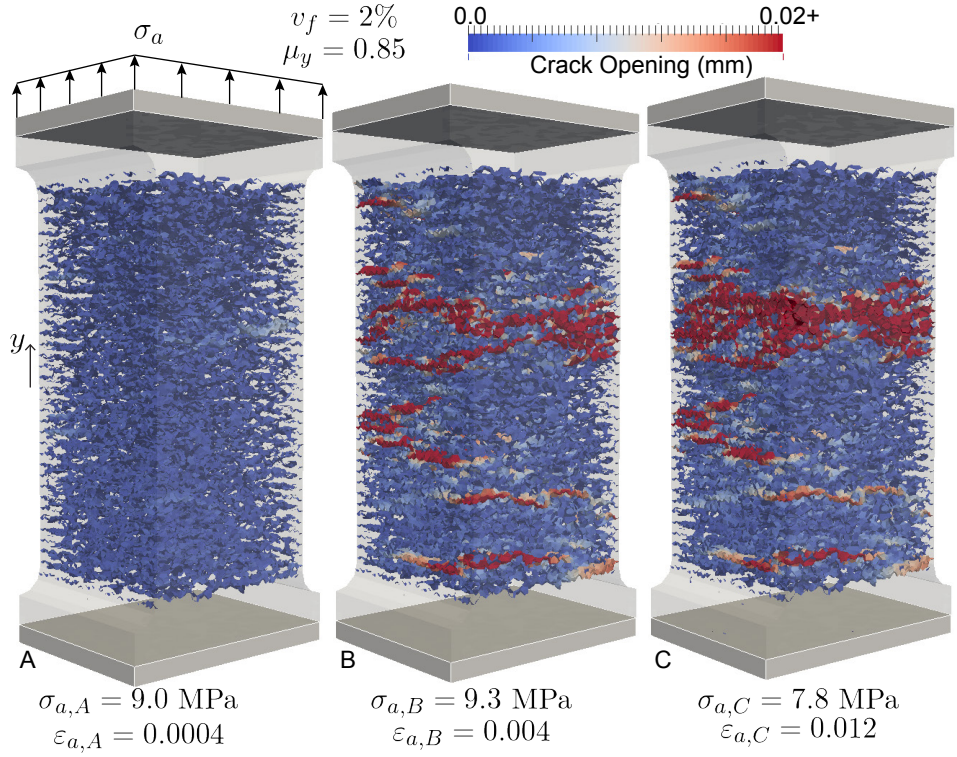

Figure 10.24: Simulated crack evolution in direct tension at the locations depicted in Fig. 10.23 for 2% fiber content and an orientation factor of 0.85.

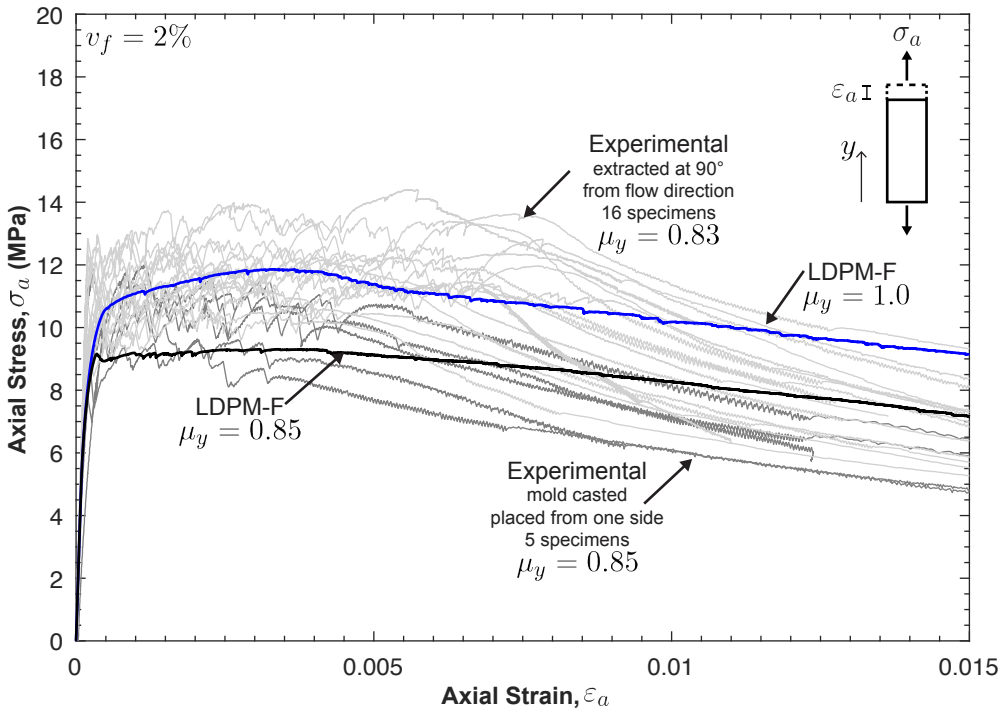

Figure 10.25: Predicted stress-strain responses at orientation factors of 0.85 and 1.0 and experimental results for the extracted and mold casted specimens.

Following the same procedure, the model predicted stress-strain curves for the extracted specimens at $\mu_y = 0.74$ and 0.65 are compared to their respective experimental scatter in Figs. 10.26 and 10.27. In these simulations, the 'chopped' parameter in MARS is activated because the specimens were cut from casted slabs. The preferential orientation scale values, S_y, matching the experimental orientation factors, μ_y, of 0.74 and 0.65 were found to be 3.2 and 1.8, respectively. Once again, the LDPM-F predicted results are in good agreement with the experimental data for $\mu_y = 0.74$ (specimens extracted at 45° from flow direction) and for the post-peak response at $\mu_y = 0.65$ (specimens extracted at 90° from flow direction). However, the model over-estimated the peak strength at $\mu_y = 0.65$ as expected, because the ultimate strength of these specimens ($\bar{f}_t = 6.6$ MPa $\pm$ 9.4%) was lower than the unreinforced specimens tensile strength ($f_t = 7.4$ MPa). In its current formulation, the LDPM-F assumes the matrix strength to be independent of the presence of fibers.

The effect of increasing the fiber volume content, v_f, on the stress-strain response including the increases in ultimate strength and ductility are predicted with LDPM-F in Fig. 10.28. In these simulations, the orientation factor, μ_y, is fixed at a value of 0.85. The crack patterns at

a axial strain of 0.012 for $v_f = 2\%$, 3%, and 4% are compared in Fig. 10.29. As expected, the crack network is characterized by a more distributed crack pattern with significant increase in the cracked zone, as the fiber content is increased from 2% to 4%.

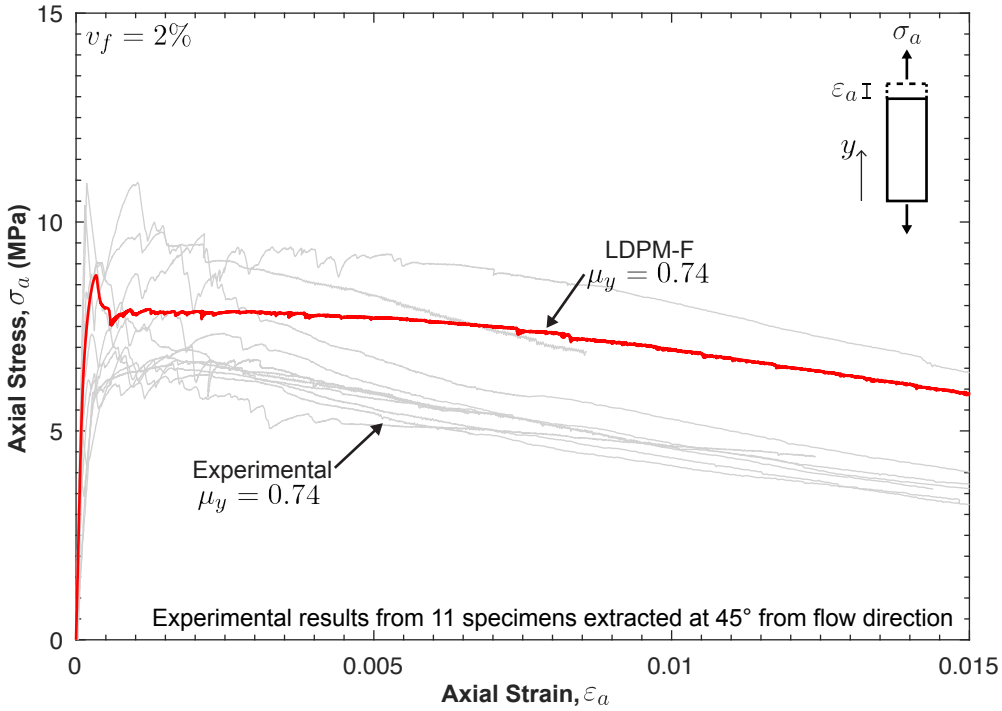

Figure 10.26: LDPM-F predicted and experimental stress-strain responses for the direct tension tests with 2% fiber content and an orientation factor of 0.74.

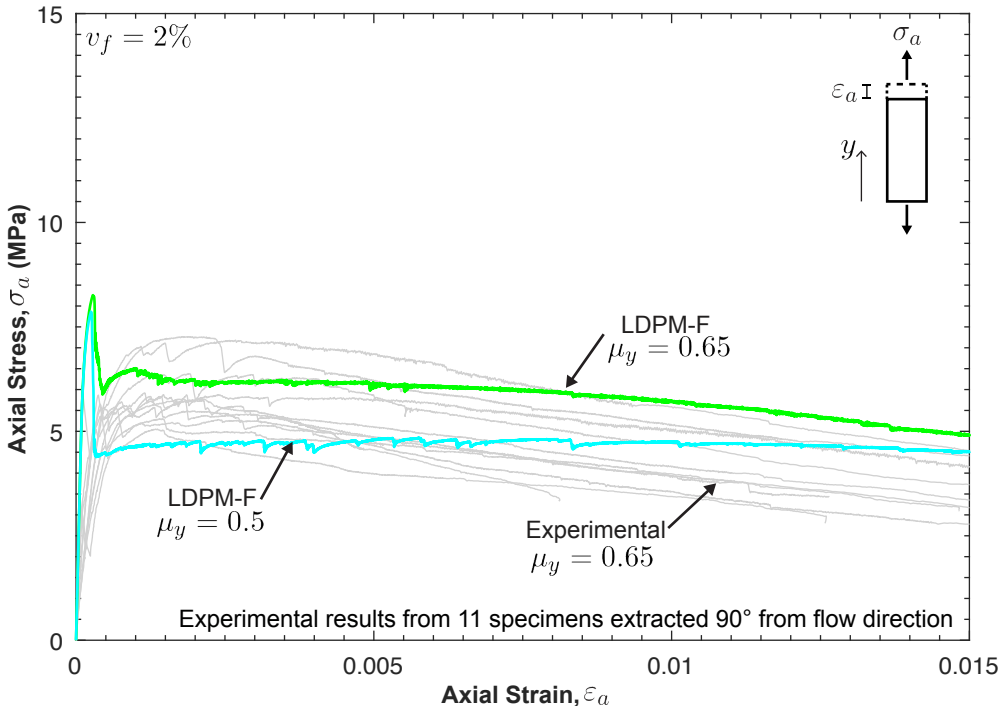

Figure 10.27: LDPM-F predicted stress-strain responses for the direct tension tests with 2% fiber content and an orientation factor, μ_y, of 0.65 and 0.50 plotted against the experimental results at $\mu_y = 0.65$.

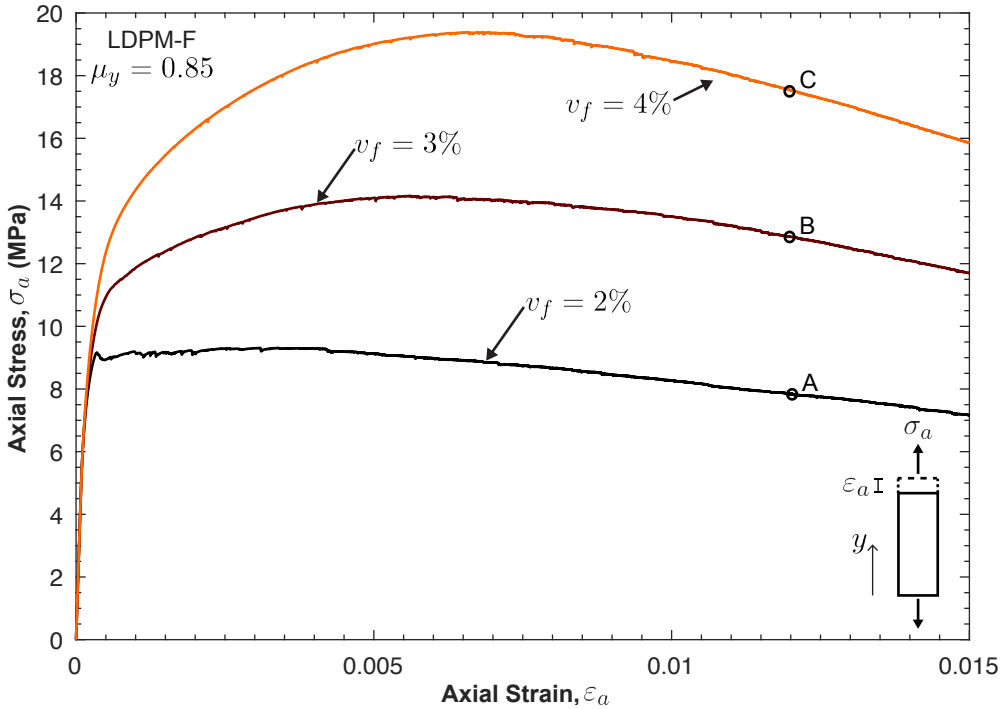

Figure 10.28: Predicted stress-strain responses at different fiber contents with and orientation factor of 0.85.

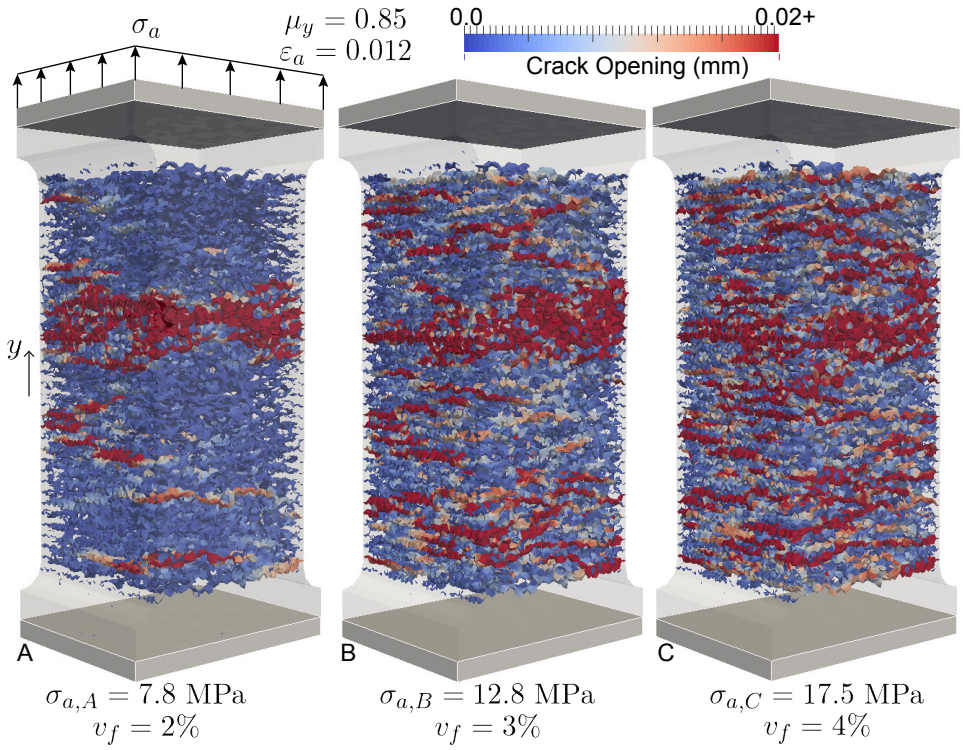

Figure 10.29: Simulated crack networks in direct tension at the locations depicted in Fig. 10.28 for 2%, 3%, and 4% fiber contents and at an orientation factor of 0.85.

10.2.2 Fracture toughness

The fracture toughness tests, described in Chapter 7, are modeled in this section with LDPM-F. The same three point bending notched beam model used in the parameter identification phase (Fig. 10.3) is also used for the fiber-reinforced simulations, with a fiber volume ratio, $v_f = 2\%$. In these tests, fresh UHPC was placed either vertically into the molds or from one side, allowing the material to flow to the other side of the specimen as it fills the volume. No qualitative assessment of the real fiber distribution was performed. However, the placement method, where the UHPC is placed from one side of the mold, is similar to the one followed by Maya Duque and Graybeal (2016) for the mold casted specimens, which had the same width as the beam specimens. Therefore, it is reasonable to assume that the orientation factor in the flow direction is similar for both specimens with $\mu_x = 0.85$. The fiber generation with $v_f = 2\%$ is then carried out, with geometric parameter, 'chopped', activated because the notch at mid-length of the bottom flange was introduced after the UHPC has hardened. A preferential orientation scale, S_x, of 5.5 matched an orientation factor of

0.85 calculated following the same procedure described in the previous section for the direct tension specimens. Each fracture toughness simulation utilized 2 nodes on NewRiver, with 16 cores each, and is characterized by a simulation time of approximately 24 hours.

The numerical results with $v_f = 2\%$ and $\mu_x = 0.85$ are compared to the experimental data in Fig. 10.30, in which the concrete was placed from one side. The simulated results are in general agreement with the experimental results, which indicates that the estimated orientation factor ($\mu_x = 0.85$) is indeed representative of the real fiber distribution at the vicinity of the beam notch. The simulated crack evolution is depicted in Fig. 10.31 at the three locations marked on the load-CMOD curve of Fig. 10.30. Unlike the unreinforced specimens, the fiber addition produced distributed crack patterns with significant increases the fracture zone.

The simulated load-CMOD curve is in excellent agreement with the experimental data until a CMOD of approximately 1.2 mm, beyond which the curve show a milder softening behavior than the experimental data; the fracture softening in the model does not start until a CMOD of 2 mm compared to a CMOD of approximately 1.2 mm in the experiments. This difference between the model results and the experiments is attributed to the micro-spalling formulation in LDPM. That is, when an inclined fiber is pulled out of the matrix, localized fracture and fragmentation reduces the embedded portion of the fiber length by: $s_f = P_{fN}\sin(\theta/2)/(k_{sp}\sigma_t d_f \cos^2(\theta/2))$, where P_{fN} is the normal component of the crack-bridging force, θ is the angle between the deflection angle between the fiber embedded segment and the facet normal vector, σ_t is the meso-scale tensile strength, and k_{sp} is the spalling parameter (for more information, see LDPM-F formulation summary in section 3.1.3 as developed by Schauffert and Cusatis (2012)). This spalling equation is empirical, was developed for regular concrete Yang et al. (2008), and thus, it needs to be updated for UHPC. Based on the fracture test results of Fig. 10.30, the formulation should to induce higher values of s_f (more micro-spalling) at larger values of crack openings than currently estimated by the formula. However, this issue is not considered important for quasi-static structural simulations as it is not expected to influence the results until high values of strains in the post-peak regime are reached.

The model simulations are then reproduced at orientation factors, μ_x, of 0.75, 0.65, and 0.5, in order to link a placement method to an orientation factor. The load-CMOD simulation results are plotted in Fig. 10.32 against the experimental data for both placement methods (vertical placement and from one side). It can be concluded from Fig. 10.32 that both

placement methods somewhat oriented the fibers parallel to the bottom of the longitudinal direction of the molds; because the initial part of the simulated curve with a perfect random distribution ($\mu_x = 0.5$) did not reach the experimental scatter. Placing UHPC vertically in the molds oriented the fibers in the longitudinal direction with orientation factors between 0.65 to 0.75. Placing the specimens from one side increased the number of aligned fibers with orientation factors between 0.75 and 0.85 as shown in Fig. 10.32. Moreover, the predicted fracture load is plotted against the axial mid-span deflection in Fig. 10.33. Finally, the effect of fiber orientation on the crack patterns is depicted in Fig. 10.34 at a crack mouth opening of 2.69 mm. As expected, the crack network is characterized by an increase in the damaged zone when more fibers are preferentially aligned perpendicular to the crack planes.

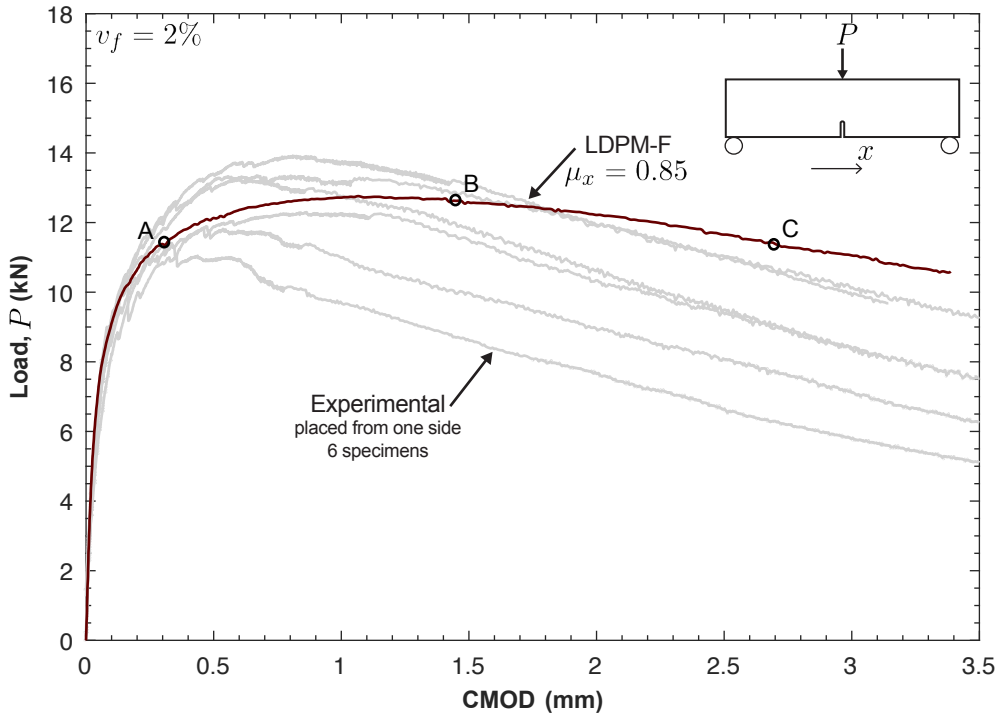

Figure 10.30: Predicted load-CMOD response for 2% fiber content and an orientation factor of 0.85 plotted on top of the experimental scatter where UHPC was placed from one side of the molds.

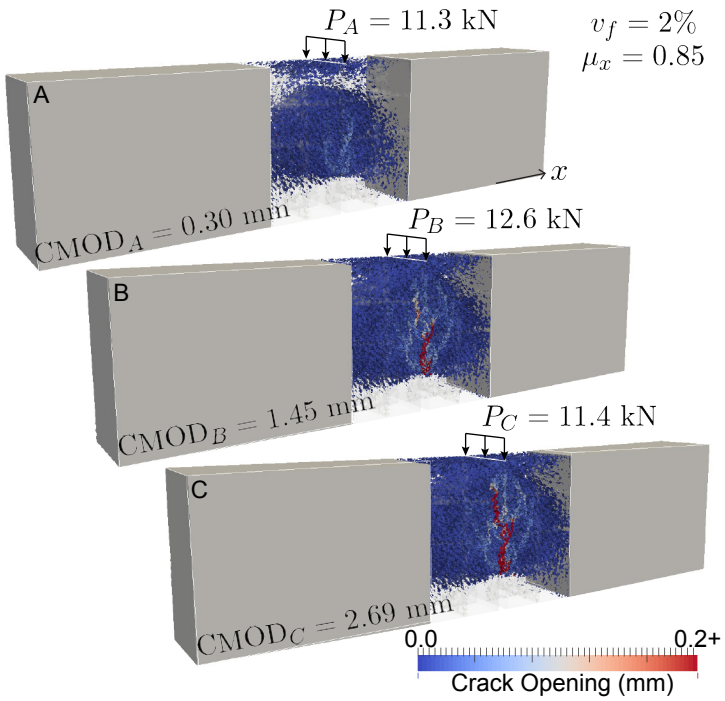

Figure 10.31: Simulated fracture evolution at the locations depicted in Fig. 10.30 for 2% fiber content and an orientation factor of 0.85.

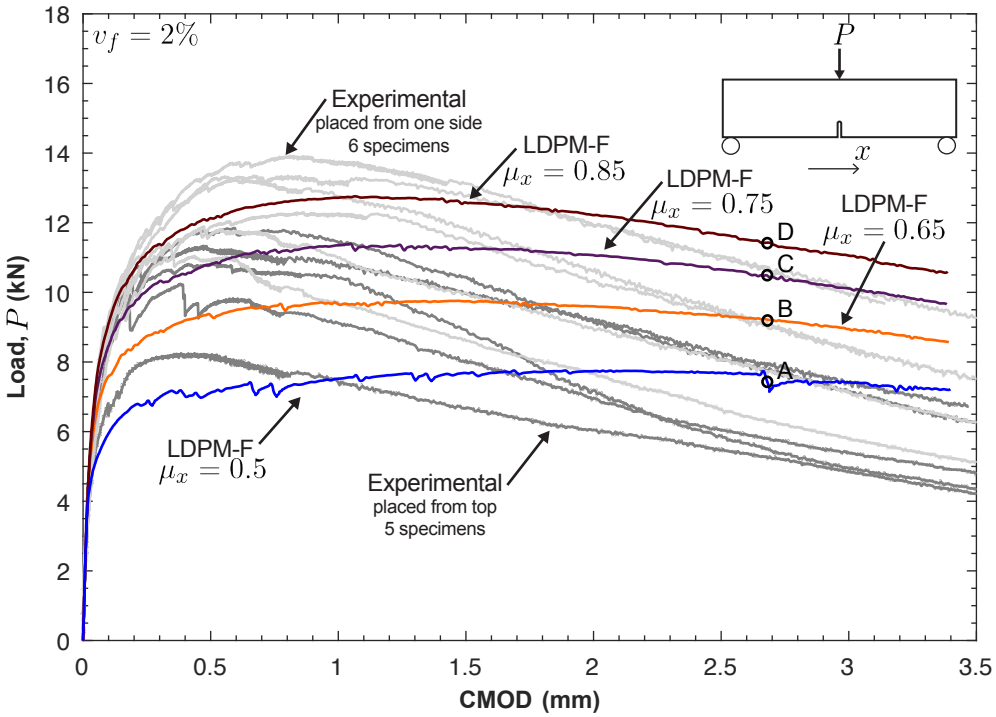

Figure 10.32: Predicted load-CMOD response for UHPC with 2% fiber content at different orientation factors plotted on top of the experimental scatter.

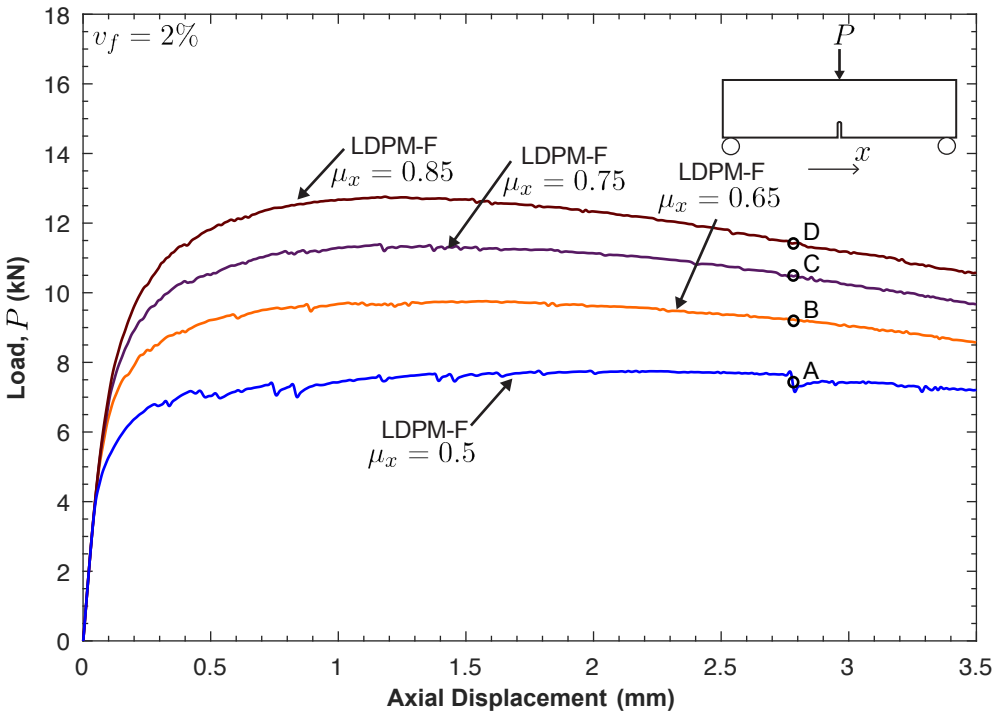

Figure 10.33: Predicted fracture load vs. axial mid-span deflection UHPC with 2% fiber content at different orientation factors.

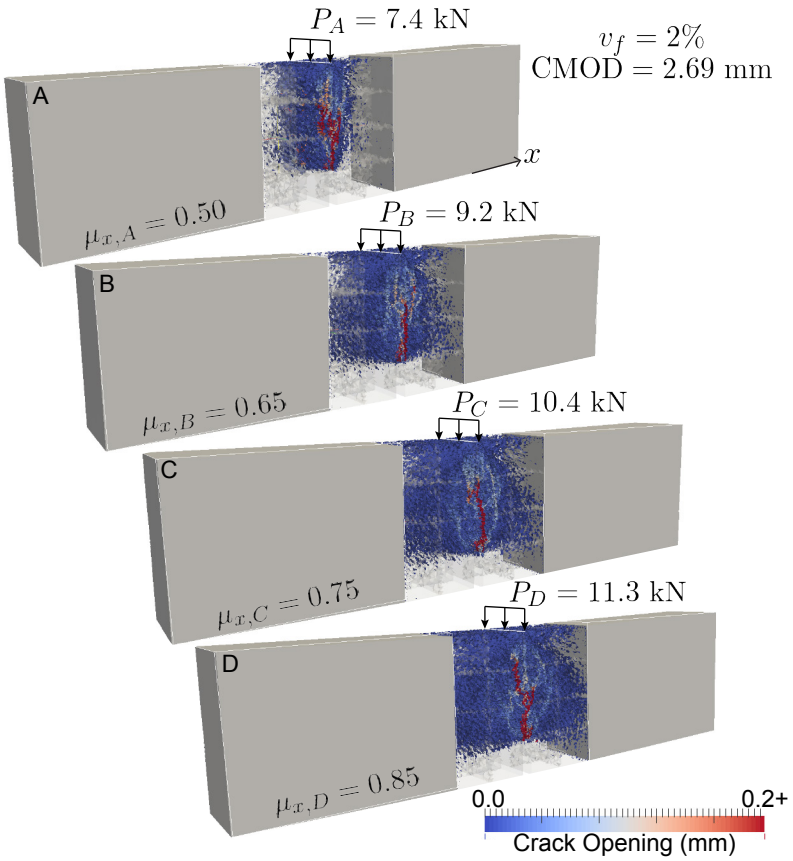

Figure 10.34: Simulated fracture crack patterns at the locations depicted in Figs. 10.32 and 10.33 with different orientation factors.

10.2.3 Splitting tension

The splitting tension specimens, described in Section 8.4.3, are modeled in this section with LDPM-F. The same model used in the parameter identification phase is also used for the fiber-reinforced simulations, with a fiber volume ratio, $v_f = 2\%$. Fig. 10.35 show the numerical split tensile load plotted as a function of the axial displacement with perfectly random and aligned fiber distributions; the splitting crack propagation is illustrated in Fig. 10.36 at the three locations depicted in Fig. 10.35.

The numerical peak load obtained when fibers are randomly oriented in the specimen ($\mu_x = 0.5$) was 370.4 kN. When all the generated fiber segments are aligned perpendicular to the expected crack plane ($\mu_x = 1.0$), the numerical peak increased to 537.8 MPa. The average experimental splitting strength for the experimental data is significantly higher than

both numerical values with 692.9 kN ± 8.6%. In fact, this discrepancy in the results is expected because the LDPM-F fiber-matrix interaction formulation does not depend on the confining stress acting transversely to the fiber axis, which was discussed in Section 8.4.3. The confinement effect is proven to increase the fiber-matrix interfacial bond in Section 9.4.6. A quantitative initial estimate of this increase is empirically derived in Section 9.5.2, and could be conveniently embedded in the model formulation with a polynomial interpolation to improve the model predictions in similar biaxial stress states occurring in real structural components. However, more experimental data is needed to obtain the behavior of the fiber frictional stress outside the tested ranges of active confinement stresses.

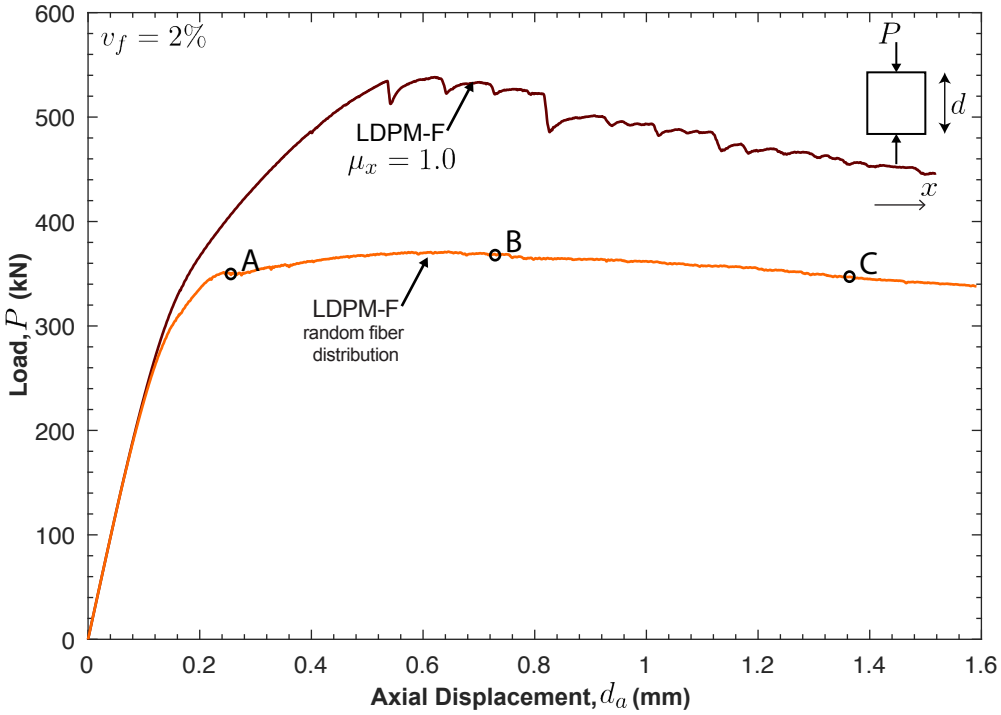

Figure 10.35: Numerical split tensile stress plotted as a function of the axial displacement with perfectly random and aligned fiber distributions at 2% fiber volume content.

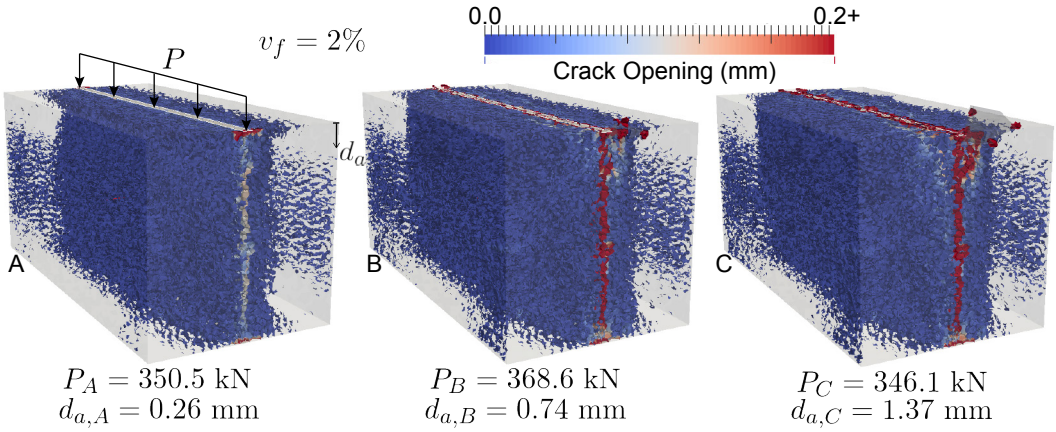

Figure 10.36: Simulated fracture crack patterns at the locations depicted in Fig. 10.35 for 2% fibers by volume randomly distributed in the specimen's volume.

10.2.4 Uniaxial unconfined compression

The unconfined compression specimens, described Chapter 6, are modeled in this section with LDPM-F. The same model used in the parameter identification phase is also used for the fiber-reinforced simulations, with a fiber volume ratio, $v_f = 2\%$. Fig. 10.37 show the numerical results for uniaxial compressive stress-strain response, with perfectly random distribution, plotted on top of the experimental scatter. It is concluded that the peak strength and ductility in uniaxial compression is over-estimated in the numerical simulations because the model does not properly capture the matrix micro-spalling behavior in the case of fractures undergoing severe shearing, which is an open issue and is subject of future research studies.

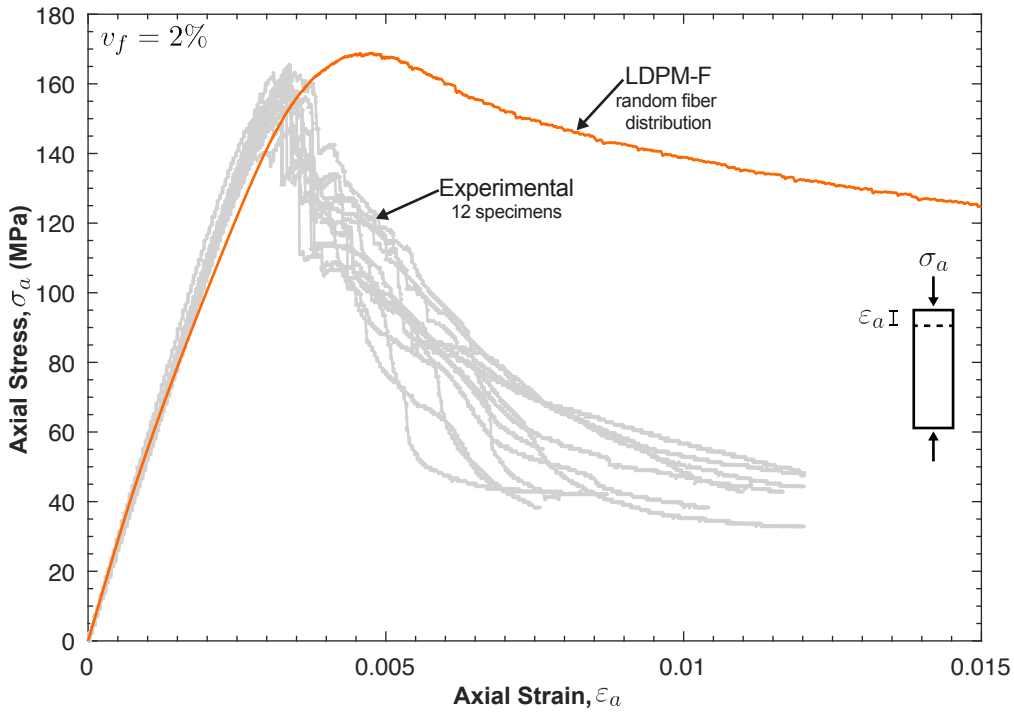

Figure 10.37: Experimental and numerical uniaxial unconfined compression stress-strain responses at 2% fiber volume content.

Chapter 11

Triaxial Smeared-Crack Continuum Model for UHPC Structural Behavior

This chapter presents the numerical modeling of UHPC with the new macroscopic smeared-crack continuum formulation for fiber reinforcement (described in Section 4.2). The continuum model parameters for UHPC without fibers are identified first, following the procedure recommended for the parent model, formulated by Moharrami and Koutromanos (2016). The new parameters governing the fiber-concrete interaction are obtained afterwards in Section 11.1. Prediction simulations are carried out in Section 11.2 to validate the behavior of the continuum model behavior at various fiber reinforcement ratios and distributions.

11.1 Continuum model parameter identification for UHPC

The continuum model constitutive equations are governed by a number of parameters that are calibrated from material tests. The parameter identification for UHPC without and with fiber reinforcement is carried out herein by single element analysis, to evaluate the model behavior in tension and compression. The numerical simulations are conducted with the Finite Element Analysis Program FEAP (Taylor, 2014) which uses an implicit integration scheme.

11.1.1 Model parameters for UHPC without fibers

The model elastic parameters, namely the modulus of elasticity, $E = 53.7$ GPa and Poisson's ratio, $\nu = 0.17$, are directly informed from the average experimental values reported in Chapter 6. The data from both UHPC with and without fibers were used because the model neglects the contribution of fibers before matrix cracking. As previously discussed, the approximation is valid in the elastic regime as shown in Section 6.4.3 where fibers, 2-4% by volume, had minimal impact of the elastic properties.

Next, the identification of the tension and crack opening behavior parameters, namely the macroscopic tension strength, $\sigma_t = 7.5$ MPa, and tension (Mode-I) fracture energy, $G_t = 60$ J/m^2, is performed by setting these values equal to the experimental macroscopic tension strength and fracture energy for UHPC without fibers, as discussed in Chapters 7, 8, and 11. The residual tension ratio, M is assumed to be 1% of the ultimate tension strength. Fig. 11.1 shows the uniaxial tension stress-strain response obtained from a single element analysis for UHPC without fibers.

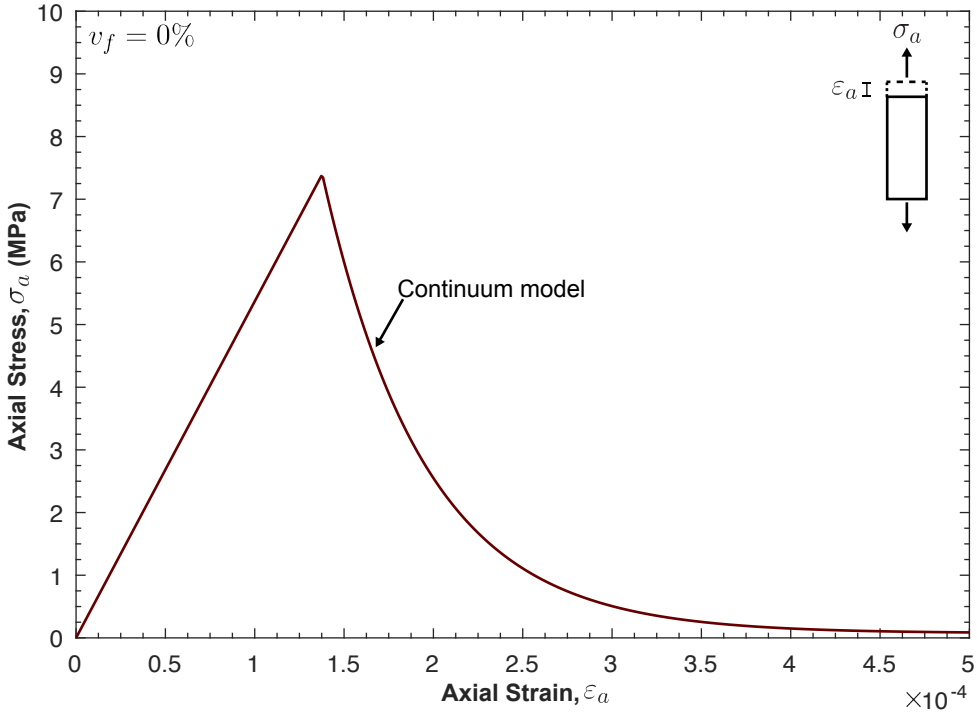

Figure 11.1: Single element uniaxial tension stress-strain curve for UHPC without fibers.

The unconfined compression strength, $f_c = 140$ MPa, strain at peak compressive strength,

$\varepsilon_o = 0.0031$, the compressive stress at which the plastic behavior starts, $f_o = 80$ MPa, the residual compressive strength ratio, $f_{res}/f_c = 0.1$, and the compressive fracture energy, $G_c = 70,000$ J/m^2 govern the model behavior in the nonlinear and post-peak portions of the uniaxial unconfined compression behavior, and are identified by matching the model results to the experimental data. Fig. 11.2 shows the uniaxial unconfined compression stress-strain response obtained from a single element analysis for UHPC without fibers, plotted on top of the experimental scatter.

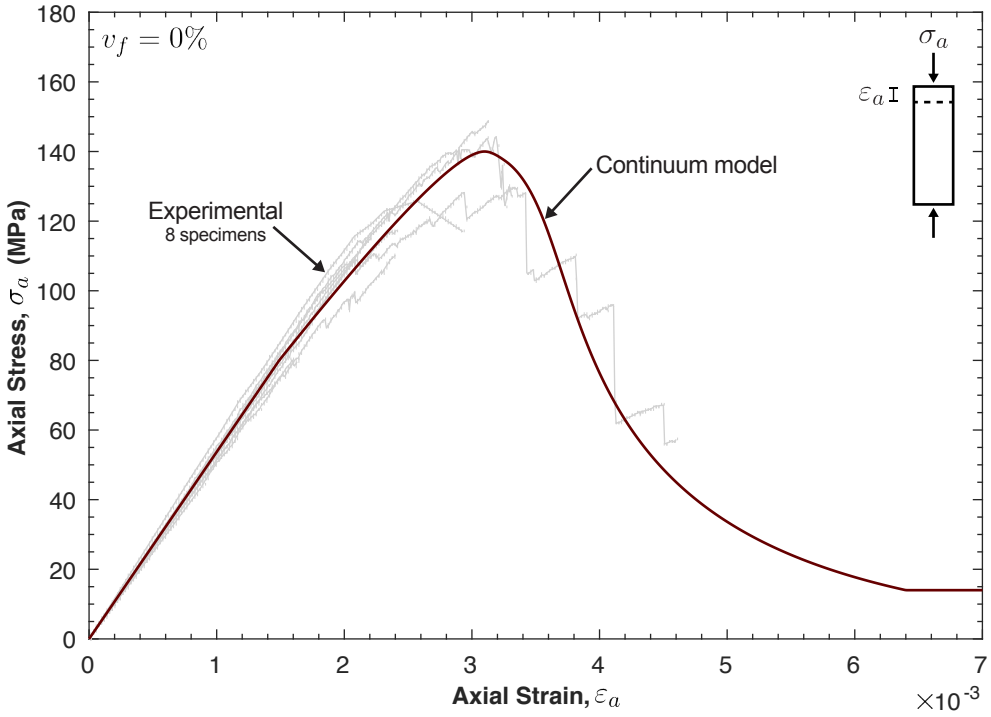

Figure 11.2: Single element uniaxial stress-strain curve for the compression parameter identification for UHPC without fibers.

11.1.2 Model parameters for UHPC with fibers

The calibration of the smeared-cracked model for fiber-reinforced UHPC requires the identification fiber-matrix interface behavior and the strain adjustment function that accounts for the development of multiple cracking when the composite is subject to tensile forces. Similarly to LDPM, the continuum model utilizes the Lin et al. (1999) formulation to generate a representative load-slip relationship for the fibers bridging a crack surface. The fiber pullout derived in Section 9.5.1 are also adopted herein, with a frictional stress, $\tau_0 = 10$

MPa, a bond fracture energy, $G_d = 0$ J/m^2, and a slip hardening/softening parameter, $\beta = 0$. The fiber material and geometrical parameters are then inputted in the model, namely the fiber modulus of elasticity, $E_f = 205$ GPa, length, $L_f = 13$ mm, and diameter, $d_f = 0.2$ mm.

The strain adjustment function parameters, described in Fig. 4.8, are identified next utilizing the mold-casted direct tension tests performed by Maya Duque and Graybeal (2016), which had 2% fibers by volume and a fiber orientation factor in the direction of load, μ_y, of 0.85 (based on Eq. 8.5). In the spirit of the continuum formulation, the model averages the overall fiber contribution in a given volume over three mutually orthogonal directions (x, y, z) and requires the fiber volume content, $v_f = 2\%$, and the orientation factors in the three directions (μ_x, μ_y, μ_z) as inputs. The model then automatically calculates the fiber orientation weight factor in each direction, $a_i = \mu_i/(\mu_x + \mu_y + \mu_z)$, which is used in the fiber stress computations. This is enforced in the formulation to insure that the simulated amount of fibers in a volume always corresponds to v_f (for more information, see Section 4.2.3).

To obtain the orientation factors in all three mutually orthogonal directions given the factor in one direction, and assuming that the factors in the other two directions are equal, the spacial distribution algorithm of MARS, described in Section 11.2, is utilized. MARS explicitly simulates all fibers contained in a volume at a given fiber content, v_f. A preferential orientation scale parameter governs how likely each simulated fiber is to be oriented in a specific direction compared to the two direction orthogonal to it. Utilizing this function, several fiber distributions were generated with MARS at different preferential orientation scales and their corresponding orientation factors in three directions are calculated per Eq. 8.5: $\mu_i = 1/N \sum_{i=1}^{N} \cos\theta_i$, in which N is set to be equal to the total number of fibers generated in the specimen volume, and θ_i is the angle between the fiber axis and the principal direction ($i = x, y, z$). The results of this investigation for a control volume, mimicking the geometry of the direct tension specimens with 51 mm square cross section and a height of 102 mm, are presented in Fig. 11.3. This relationship, although developed for the direct tension specimen, could be used for different geometries to estimate the relationship between orientation factors in orthogonal directions. For an orientation factor, $\mu_y = 0.85$, the orientation factors in the other two principal directions are estimated, from Fig. 11.3, to be $\mu_x = \mu_z = 0.25$.

The identifications of the parameters defining the strain adjustment function of Fig. 4.8 are carried out next by matching the results of a single element, having a size $h_y = 102$ mm, to experimental data as illustrated in Fig. 11.4. The first required input parameter,

$\varepsilon_{cr,a} = \varepsilon_a - \varepsilon_{ini} = 0.0005$, is the cracking strain at the start of the pseudo stress plateau phase (at first major crack). ε_a is the element total strain depicted in Fig. 11.4 and $\varepsilon_{ini} = f_t/E$ is the unreinforced matrix cracking strain. To ensure mesh objectivity, the second parameter, $d_b = 0.35$ mm, is given in terms of the total displacement, with $d_b = (\varepsilon_b - \varepsilon_{ini}) \times h_y$, where ε_b is the strain at which the softening behavior is initiated (see Fig. 11.4). The post-peak parameters, $d_c = (\varepsilon_b - \varepsilon_{ini}) \times h_y = 0.7$ mm, and adjusted crack opening, $d_e = 0.03$ mm, account for the transition from strain concentration in several cracks to the localization in one single crack, and are calibrated by matching the initial softening portion of the stress-strain curve as shown in Fig. 11.4. The last parameter, $d_d = 3.8$ mm, represent complete pullout of the fibers and the total loss of tensile capacity in the material.

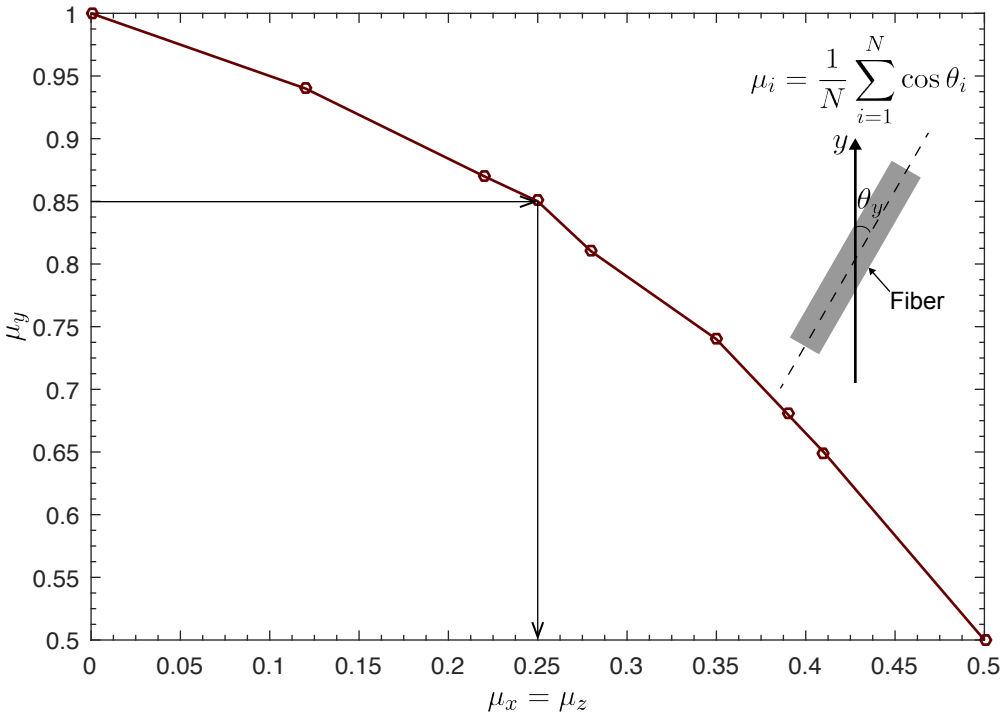

Figure 11.3: Relation between orientation factors in three mutually orthogonal direction (x, y, z).

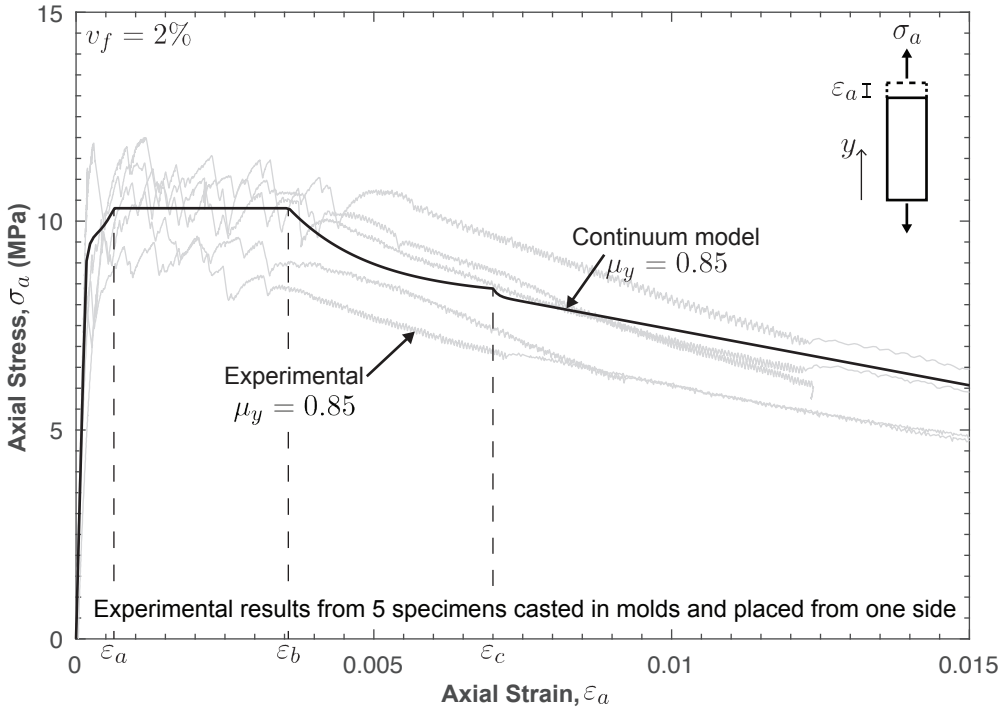

Figure 11.4: Simulated uniaxial tensile stress-strain response for UHPC with 2% fiber content and orientation factor of 0.85 for the identification of the strain adjustment function parameters.

After identifying the calibration parameters governing the tension behavior of the fiber-concrete interaction, the model mesh objectivity is demonstrated by discretizing the single element, with $h_y = 102$ mm into four equal elements, each with $h_y = 25.5$ mm. The cross sectional dimension of both models is kept the same with equal width and length of 25 mm. Fig. 11.5 shows the simulated results for both models with one and 4 elements. As expected the results of both models are similar and characterized by equal element strains during the hardening regime until the macroscopic strain, ε_a, localizes at point A of Fig. 11.5. Beyond point A, the model enters into the crack straining and softening regimes, and the damage in the 4 elements model is localized into one element, as shown in point B of Fig. 11.5.

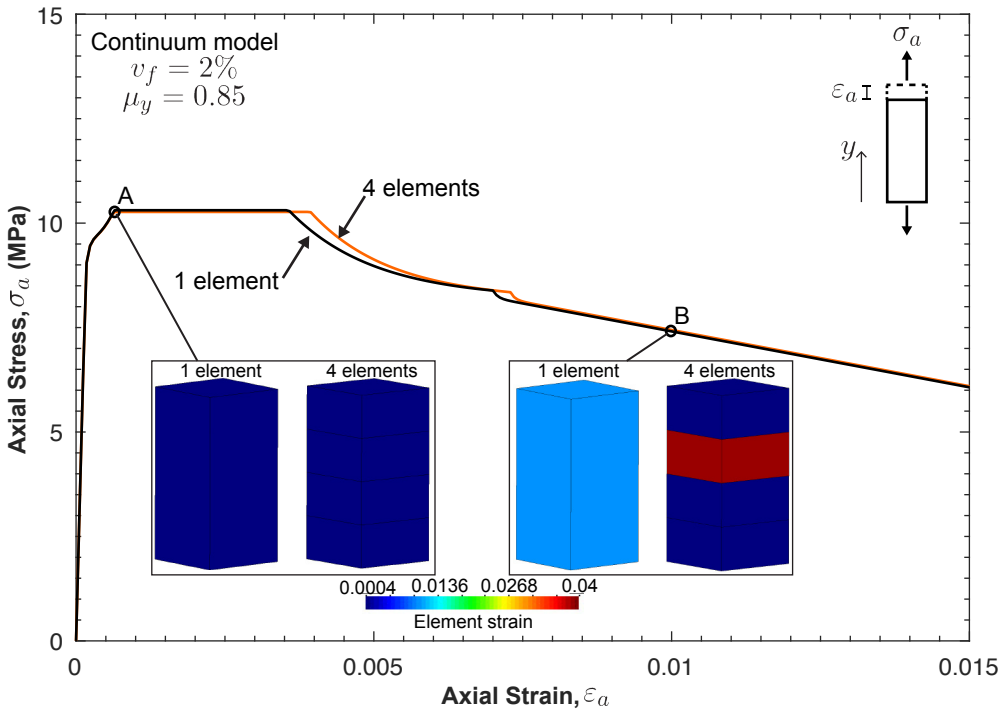

Figure 11.5: Simulated uniaxial tensile stress-strain response with one and four elements for UHPC at 2% fiber content and an orientation factor of 0.85.

Finally, the unreinforced matrix parameters governing the confined concrete behavior are calibrated, namely, parameter, a, influencing the confined concrete ultimate strength, the dilatancy parameter, α_p, controlling the volumetric expansion due to inelastic behavior, and parameter, d, reflecting the effect of pressure on the hardening variable evolution. Although typically derived from triaxial compression tests, these parameters, in the current study, are obtained by matching the fiber-reinforced model compression stress-strain curve results to the experimental data assuming a random fiber distribution in the compression specimens. When loading the concrete in uniaxial compression, the specimen expands in the transverse directions and a tension field is created triggering splitting cracks until failure. In the fiber-reinforced specimens, the fibers bridge the aforementioned splitting cracks providing a level of local confinement, which improves the strength and ductility of the material. This phenomenon is similar to the behavior of confined concrete and thus, an inverse analysis to determine the confined parameters is applicable given that the fiber contribution to crack bridging is now calibrated. Fig. 11.6 shows the model calibrated compression stress-strain curve plotted on top of the experimental data for UHPC with 2% fiber volume content and assuming a random fiber distribution ($\mu_x = \mu_y = \mu_z = 1$) in the compression specimens.

This curve was obtained by setting: $a = 0.4$, $\alpha_p = 0.2$, and $d = 11$. A complete list of the continuum model calibrated parameters for UHPC without and with fibers is provided in Table 11.1.

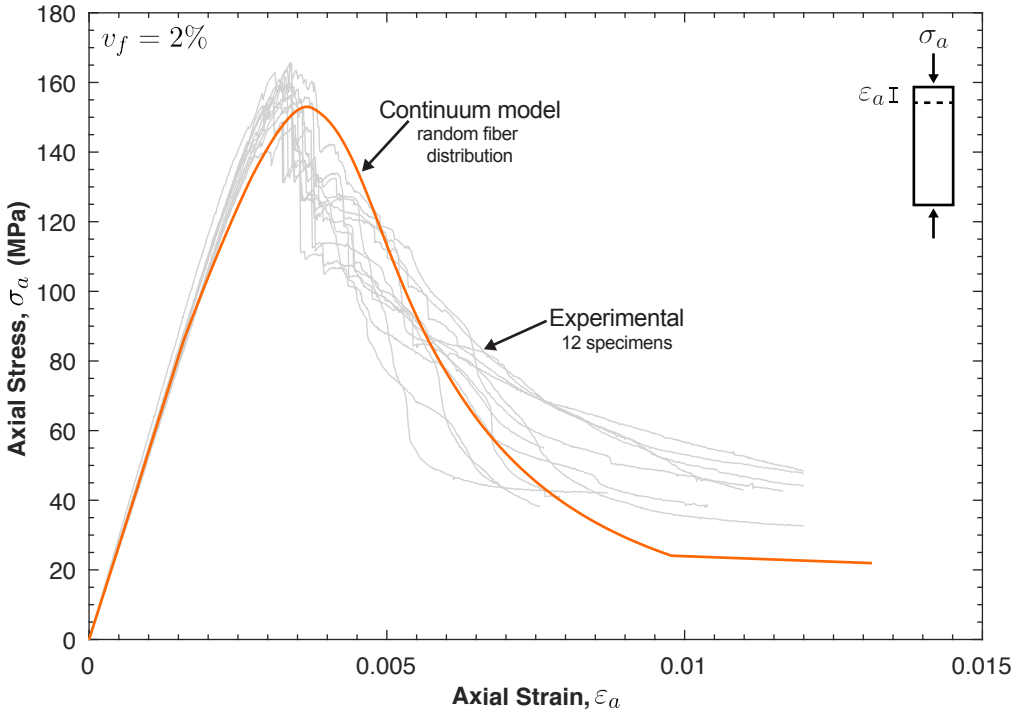

Figure 11.6: Simulated uniaxial tensile stress-strain response for UHPC with 2% fiber content for the identification of the confined matrix parameters.

Table 11.1: Calibrated smeared-crack continuum parameters for UHPC without and with fibers.

Material	**Model parameter**	**Calibrated value**
UHPC without fibers	Modulus of elasticity, E	53.7 GPa
	Poisson's ratio, ν	0.17
	Tension strength, f_t	7.5 MPa
	Mode-I fracture energy, G_t	60 J/m^2
	Residual tension ratio, M	0.01
	Compression strength, f_c	140 MPa
	Compression stress, f_o	80 MPa
	Compression residual ratio, f_{res}/f_o	0.1
	Compression fracture energy, G_c	70,000 J/m^2
	Parameter, a	0.40
	Parameter, α_p	0.20
	Parameter, d	11
UHPC with fibers	Fiber modulus of elasticity, E_f	205 GPa
	Fiber length, L_f	13 mm
	Fiber diameter, d	0.2 mm
	Frictional stress, τ_0	11 MPa
	Debonding fracture energy, G_d	0.0 J/m^2
	Frictional parameter, β	0.0
	Cracking strain at localization, $\varepsilon_{cr,a}$	0.0005
	Crack opening, d_b	0.35 mm
	Crack opening, d_c	0.70 mm
	Crack opening, d_d	3.80 mm
	Adjusted crack opening, d_e	0.03 mm

11.2 Model prediction simulations for fiber-reinforced UHPC

In this section, the model validation is carried out without further changes to the continuum model calibrated parameters of Table 11.1. The predicted mechanical responses of UHPC at different orientations and fiber contents are compared to the available experimental data, that were not utilized during the parameter identification phase.

11.2.1 Uniaxial direct tension

The direct tension tests, by Maya Duque and Graybeal (2016), that were not used in the parameter identification phase are compared to the model simulations in this section, with $v_f = 2\%$, by only changing the fiber orientation factors to match the reported experimental values. As discussed in section 10.2.1, the specimens extracted from a UHPC slab and cut parallel (at 0°) to the flow direction during placement had an average experimental orientation factor similar to one for the mold casted specimens but showed a stronger tensile strength and more ductile response (compare the experimental average of both tests in Fig. 8.17). It is hypothesized that more fibers are aligned in these specimens, which were not captured by the experimental method followed to calculate orientation factor; since it was only calculated for one single section along the gage length (for more information, see section 10.2.1). For comparison purposes, the model orientation factors are increased and compared to the experimental scatter. Fig. 11.7 shows the predicted stress-strain curves with $v_f = 2\%$, for $\mu_y = 0.94$, and $\mu_y = 1$, which is compared to simulated curve with $\mu_y = 0.85$ and plotted against experimental scatter from the extracted and mold casted specimens, with $\mu_y = 0.85$. The orientation factors in the transverse directions (μ_x and μ_z) are obtained from Fig. 11.3 with $\mu_x = \mu_z = 0.12$ for $\mu_y = 0.94$ and $\mu_x = \mu_z = 0$ for $\mu_y = 1$.

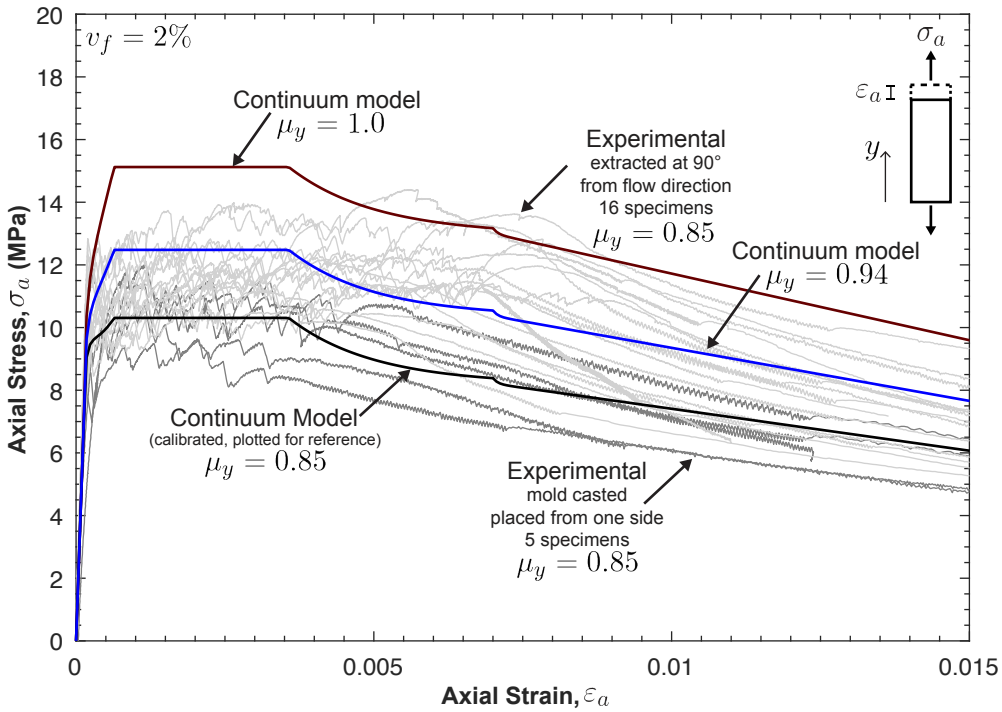

Figure 11.7: Continuum model predicted stress-strain responses at orientation factors of 0.94 and 1.0 and experimental results for the extracted and mold casted specimens.

Following the same procedure, the model predicted stress-strain curves for the extracted specimens at $\mu_y = 0.74$ and 0.65 are compared to their respective experimental scatter in Figs. 11.8 and 11.8. The transverse orientation factors matching the reported one in the vertical directions are found from Fig. 11.3 with $\mu_x = \mu_z = 0.35$ and 0.41 for $\mu_y = 0.74$ and 0.65, respectively. The model results are in good agreement with the experimental data for $\mu_y = 0.74$ (specimens extracted at 45° from flow direction) and for the post-peak response at $\mu_y = 0.65$ (specimens extracted at 90° from flow direction). However, the model over-estimated the peak strength at $\mu_y = 0.65$ as expected, because the ultimate strength of these specimens ($\bar{f}_t = 6.6$ MPa $\pm$ 9.4%) was lower than the unreinforced tensile strength ($f_t = 7.5$ MPa). In its current formulation, the model assumes the matrix strength to be independent of the presence of fibers. The model simulation with random fiber distribution ($\mu_x = \mu_y = \mu_z = 0.5$) is plotted in Fig. 11.9 for reference.

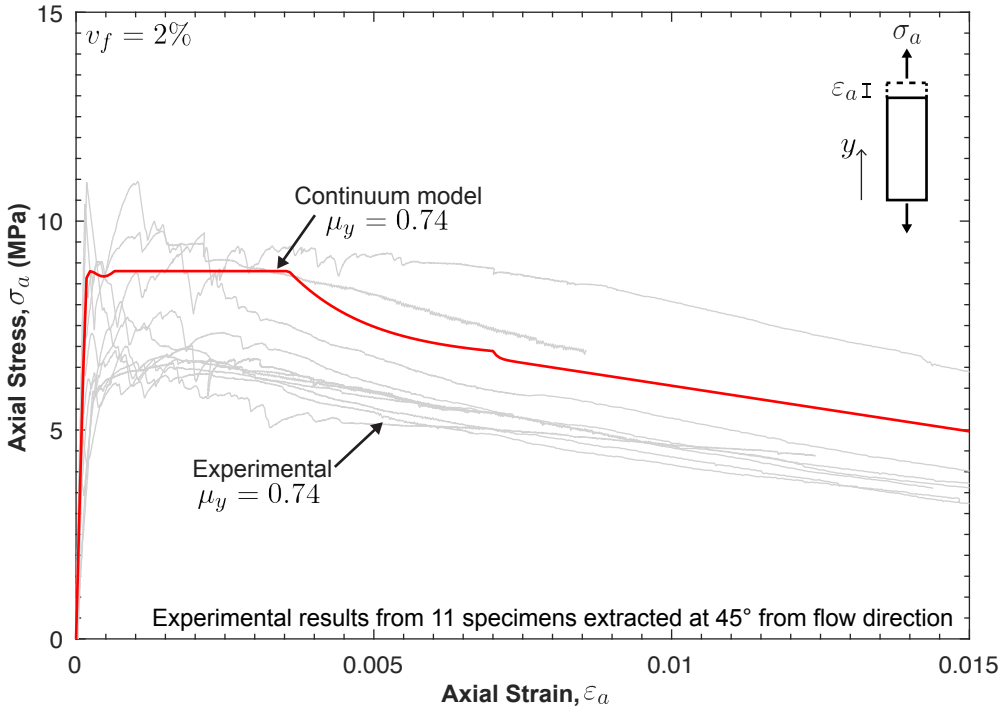

Figure 11.8: Continuum model predicted and experimental stress-strain responses for the direct tension tests with 2% fiber content and an orientation factor of 0.74.

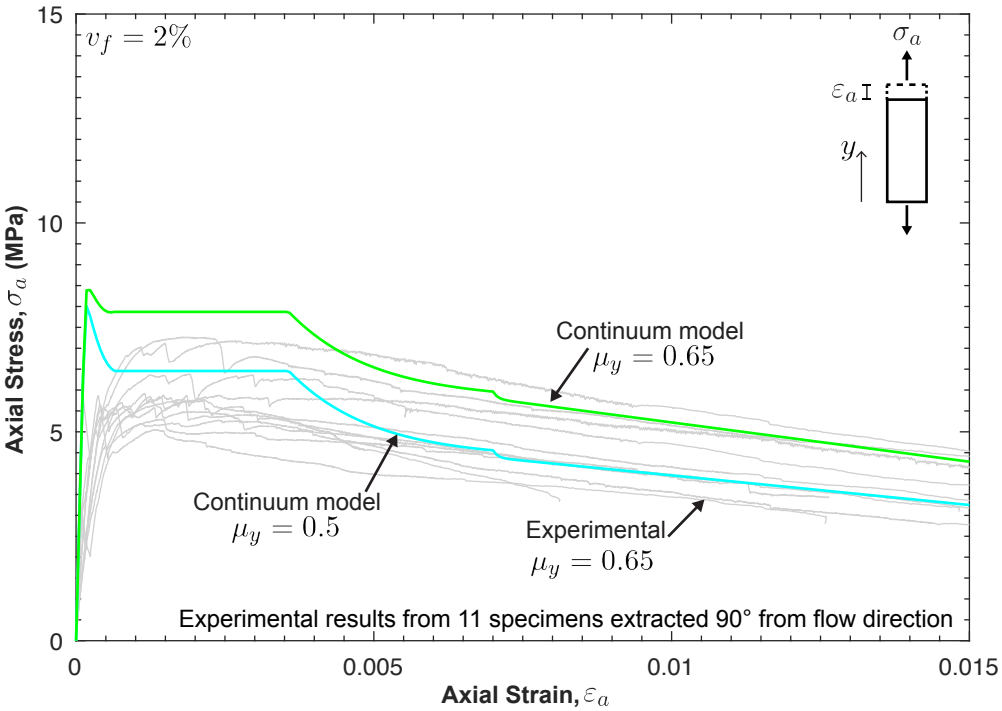

Figure 11.9: Continuum model predicted stress-strain responses for the direct tension tests with 2% fiber content and an orientation factor, μ_y, of 0.65 and 0.50 plotted against the experimental results at $\mu_y = 0.65$.

11.2.2 Uniaxial unconfined compression

The unconfined compression specimens, described in Chapter 6, for $v_f = 4\%$ are modeled in this section with the newly formulated continuum model. The same single element model used in the parameter identification phase, with $v_f = 0\%$ and 2%, is used herein by only changing the fiber ratio to $v_f = 4\%$. Fig. 11.10 shows the numerical results for the uniaxial compressive stress-strain, assuming a random fiber distribution ($\mu_x = \mu_y = \mu_z = 0.5$), plotted on top of the corresponding experimental scatter. The predicted results are in excellent agreement with the experimental data, validating the model predictions at different fiber volume ratios in compression.

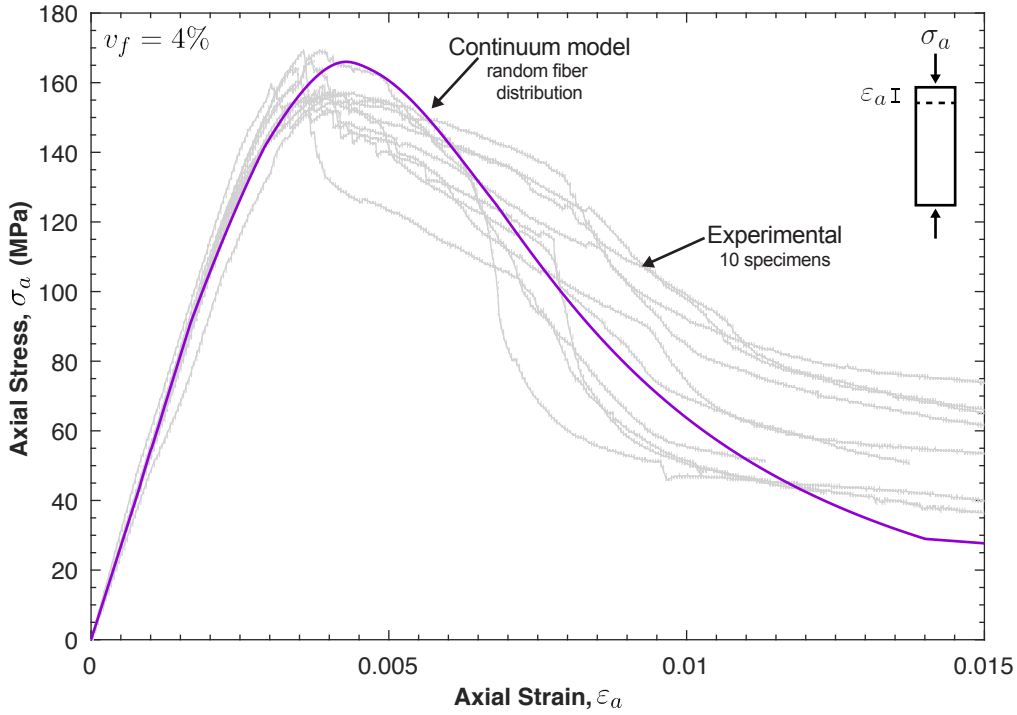

Figure 11.10: Continuum model predicted and experimental stress-strain responses for the compression tests with 4% fiber content.

Chapter 12

Conclusions and Future Work

12.1 Conclusions

A computational framework for the analysis and design of structural components and systems made Ultra-High Performance Concrete (UHPC) was introduced. The modeling strategy utilized the Lattice Discrete Particle Model (LDPM) to represent UHPC material and structural member response, and extended a structural-level triaxial continuum constitutive law to account for the addition of discrete fibers.

Predictive computational tools rely on extensive material characterization that can capture all aspects of material response, and therefore, a large portion of this work focused on evaluating and implementing material testing protocols to characterize compression, fracture, tension, and fiber-matrix interaction of UHPC without fibers and with fibers added as a percentage of total matrix volume (2% and 4%). The experimental program highlighted the effect of fibers on bridging structural cracks and improving the post-peak performance and ductility of the material. The compression testing protocol captured the full axial stress vs. axial and circumferential strain curves including post-peak behavior, by maintaining a constant circumferential displacement rate as the specimen is compressed. The orientation of fibers was considered as a test variable for the fracture toughness tests by placing UHPC randomly or from one side of prismatic beam molds. The three-point bending notched beam fracture test highlighted the effect of fiber orientation in controlling crack propagation showing 20% increase in the peak load when a portion of the fibers, 2% by volume, were

preferentially oriented perpendicular to crack directions. The tension tests consisted of direct and splitting (indirect) tension tests and showed the impact of fiber orientations on the tension behavior. This investigation also highlighted an enhanced fiber resistance when fibers are subject to lateral confining stresses, generated when a compressive load is applied along the length of a split cylinder specimen. These findings were further investigated in single fiber pullout tests where fibers are embedded in UHPC and subjected to active confining stresses. The fiber pullout investigation also quantified the bond-slip properties of straight steel fiber embedded, at various embedment length values, in UHPC for use in structural analysis and modeling.

The LDPM parameter identification was performed utilizing the experimental results in tension, fracture, and compression for UHPC without fibers. Fibers were explicitly generated in a volume and assigned the fiber-matrix interaction parameters informed from the fiber pullout tests. The validation of LDPM for fiber reinforced UHPC (LDPM-F) was carried out by comparing the numerical simulations to the experimental data that were not used in the parameter identification phase. The model was able to reproduce with great accuracy the uniaxial tension and fracture experimental data at different fiber distributions. Moreover, LDPM-F remarkably reproduced the effect of fiber content and orientation on the crack network and failure mode of the specimens. It was identified that the LDPM-F prediction could be enhanced by incorporating a number of findings from this research. First, the experimental data suggested a dependence of the fiber orientation on the unreinforced matrix tension strength of the model, since the experimental strength at low orientation factors was smaller than the strength of the unreinforced specimens. This phenomenon is recommended to be reflected in LDPM-F to improve the model predictions at vicinity of the first crack at low orientation factors. Second, the fiber confinement effect on the increase in bond strength of the fiber-matrix interaction should be considered to properly capture the macroscopic behavior under biaxial stress states. Finally, more research is needed to update the matrix micro-spalling approach in LDPM-F especially for the cases of fractures undergoing severe shearing.

In the realm of continuum smeared-crack modeling, a novel constitutive law to account for the effect of fiber reinforcement was formulated, as an extension of an existing triaxial model for concrete under cyclic loading (Moharrami and Koutromanos, 2016). The matrix model parameters are obtained from the experimental results in direct tension and compression for UHPC without fibers. The fibers contribution is smeared into three mutually orthogonal

directions based on the fiber volume ratio and the corresponding orientation factors. The fiber-matrix interaction and the multi-cracking behavior are identified from single fiber pull-out tests and from fiber-reinforced direct tension tests. The model was validated to capture UHPC intrinsic properties and material behavior at various fiber contents and orientations by comparing the numerical simulations to the experimental data in tension and compression, that was not used in the calibration phase. The continuum model is computationally efficient and could be used to assess the performance of large scale structural systems made with UHPC.

12.2 Future Work

In the course of developing this document, several research needs were identified to push forward ongoing standardization efforts to develop UHPC material testing protocols and establish design models for use in structural analysis. These research needs are summarized below.

12.2.1 Material characterization

Assessing UHPC material behavior requires more detailed approaches than regular concrete due to its intrinsic capability to maintain strength beyond the matrix cracking limit. Fibers in the matrix transmit forces between crack surfaces limiting crack propagation and providing resistance to tensile stresses. Therefore, it is critical that material characterization standards address not only the elastic behavior and peak strength of UHPC but also its post-cracking performance in tension, fracture, and compression. Fiber content, placement method, dispersion, and orientation are important when assessing the material mechanical response. UHPC interface with different materials, such as steel rebars and regular concrete, is also essential for composite construction and retrofit of aging infrastructure. Standardizing these methods minimize variations in material data and establishes appropriate design models for finding the structural characteristics of UHPC members in flexure, shear, compression, and ductility. The specific needs are summarized as follows:

- Material characterization tests that obtains the cyclic properties of UHPC including the fiber-matrix interaction and fiber pullout.

- Material characterization of the interface between UHPC and other construction materials such as steel, regular concrete, etc.
- Material characterization tests that describes the UHPC behavior without fibers, especially in direct tension and fracture toughness.
- Standardized uniaxial direct tension procedure that creates a uniform tension field in the tested specimen eliminating the effect of support rotations and biaxial stresses.
- Standardized unconfined compression test method that captures the overall behavior of the material including the post-cracking regime.
- Unified approach to characterize the fiber distribution in real specimens, by linking the placement method of fresh UHPC to representative and clearly defined orientation factors in the three mutually orthogonal principal directions.
- Fiber pullout testing method and experimental procedure that characterize the initial frictional bond between the fiber and the matrix.
- Fiber pullout experiments where a fiber is pulled at an inclined angle to characterize fiber efficiency and matrix micro-spalling.

12.2.2 Design applications and structural behavior

If evaluated solely based on cost, the unit price of UHPC is significantly higher than conventional concrete. However, many advantages and exceptional performance levels for implementing UHPC in new construction and retrofit of aging infrastructure have been documented around the world, including: strength, ductility, toughness, impact resistance, flexibility, stability, increased useful life, impermeability, corrosion resistance, abrasion, and freeze/thaw, severe environment and chemical resistance. When these enhanced properties are combined with innovative design concepts, structural members made with UHPC use less material, eliminate/decrease the need congested reinforcement, and require less maintenance compared to their concrete counterpart, which justifies the increased initial cost over the extended life of the structure. To fully take advantage of key performance, sustainability, and resilient characteristics of UHPC, applications in structural systems should optimize its use and incorporate it in areas that are most susceptible to environmental and structural damage. Such applications include bridge columns in contact with soil, water, and other

corrosive environments, bridge decks especially in cold regions where the structure is subject to freezing and thawing, connections, load bearing members in earthquake prone regions, etc. To develop methodologies for the design and retrofit with UHPC, material models for finding member characteristics in flexure, shear, and compression need to be coupled with validated computational tools to accelerate the implementation of innovative design concepts. Introducing reliable computational tools that can capture material response on both the material and structural level can serve as a proof-of-concept tool to evaluate UHPC innovative structural applications through virtual experiments covering a large number of parameters that are difficult to produce experimentally. Such strategy offers a mechanics-based shortcut to UHPC design and analysis that can strategically support design concepts development and ongoing UHPC material.

12.2.3 Computational models

This research has validated the two modeling approaches that could be used to simulate UHPC material, component, and system behavior. However more research is needed in the following areas:

- Develop an LDPM micro-spalling approach to accurately represent the spalling effect on the macroscopic response in dense cementitious composites like UHPC.
- Identify the fiber-matrix interaction under severe fracture shearing.
- Develop constitutive laws for the behavior of UHPC structural components under cyclic loads.
- Validate the models to capture the behavior of structural components and systems

12.2.4 Structural scale experimental validation

Prototype experimental testing of different UHPC structural applications are needed as they constitute a fundamental step to ensure performance, integrity, and safety of the built environment. Large scale tests build experience with UHPC placement, establish best construction practices, evaluate predicted cracking patterns and limit states, and verify the design approaches and computational tools in predicting the load-deformation response and failure modes.

Bibliography

AASHTO T132 (2009). "Standard Method of Test for Tensile Strength of Hydraulic Cement Mortars." *Standard Specifications for Transportation Materials and Methods of Sampling and Testing*, American Association of State Highway and Transportation Officials, Washington, DC.

Alnaggar, M. and Cusatis, G. (2012). "Automatic Parameter Identification of Discrete Mesoscale Models with Application to the Coarse-Grained Simulation of Reinforced Concrete Structures." *20th Analysis Computation Specialty Conference*, Chicago, IL, American Society of Civil Engineers, 406–417 (July).

Arslan, A., Ince, R., and Karihaloo, B. L. (2002). "Improved Lattice Model for Concrete Fracture." *Journal of Engineering Mechanics*, 128(1), 57–65.

ASTM C230/C230M (2014). "Standard Specification for Flow Table for Use in Tests of Hydraulic Cement." *ASTM International*, West Conshohocken, PA.

ASTM C39/C39M (2015). "Standard Test Method for Compressive Strength of Cylindrical Concrete Specimens." *ASTM International*, West Conshohocken, PA.

ASTM C469/469M (2014). "Standard Test Method for Static Modulus of Elasticity and Poisson's Ratio of Concrete in Compression." *ASTM International*, West Conshohocken, PA.

ASTM C496/C496M (2011). "Standard Test Method for Splitting Tensile Strength of Cylindrical Concrete Specimens." *ASTM International*, West Conshohocken, PA.

ASTM C496/C496M (2013). "Standard Test Method for Compressive Strength of Hydraulic Cement Mortars (Using 2-in. or [50-mm] Cube Specimens)." *ASTM International*, West Conshohocken, PA.

ASTM E1820 (2015). "Standard Test Method for Measurement of Fracture Toughness." *ASTM International*, West Conshohocken, PA.

Barber, C. B., Dobkin, D. P., and Huhdanpaa, H. (1996). "The quickhull algorithm for convex hulls." *ACM Transactions on Mathematical Software (TOMS)*, 22(4), 469–483.

Bastien-Masse, M., Denarié, E., and Brühwiler, E. (2016). "Effect of fiber orientation on the in-plane tensile response of UHPFRC reinforcement layers." *Cement and Concrete Composites*, 67, 111–125.

Bažant, Z. P. (1990). "Justification and improvement of Kienzler and Herrmann's estimate of stress intensity factors of cracked beam." *Engineering Fracture Mechanics*, 36(3), 523–525.

Bažant, Z. P., Caner, F. C., Carol, I., Adley, M. D., and Akers, S. A. (2000). "Microplane Model M4 for Concrete. I: Formulation with Work-Conjugate Deviatoric Stress." *Journal of Engineering Mechanics*, 126(9), 944–953.

Bažant, Z. P. and Oh, B. H. (1983). "Crack band theory for fracture of concrete." *Matériaux et Construction*, 16(3), 155–177.

Bažant, Z. P. and Planas, J. (1997). "Fracture and Size Effect in Concrete and Other Quasibrittle Materials.

Bažant, Z. P., Tabbara, M. R., Kazemi, M. T., and Cabot, G. P. (1990). "Random Particle Model for Fracture of Aggregate or Fiber Composites." *Journal of Engineering Mechanics*, 116(8), 1686–1705.

Beghini, A., Bažant, Z. P., Zhou, Y., Gouirand, O., and Caner, F. C. (2007). "Microplane Model M5f for Multiaxial Behavior and Fracture of Fiber-Reinforced Concrete." *Journal of Engineering Mechanics*, 133(1), 66–75.

Belletti, B., Cerioni, R., Meda, A., and Plizzari, G. (2008). "Design Aspects on Steel Fiber-Reinforced Concrete Pavements." *Journal of Materials in Civil Engineering*, 20(9), 599–607.

Belytschko, T., Liu, W. K., Moran, B., and Elkhodary, K. (2014). *Nonlinear Finite Elements for Continua and Structures, 2nd Edition*. John Wiley & Sons, second edition (January).

Bencardino, F., Rizzuti, L., Spadea, G., and Swamy, R. N. (2010). "Experimental evaluation of fiber reinforced concrete fracture properties." *Composites Part B: Engineering*, 41(1), 17–24.

Bićanić, N. and Pearce, C. J. (1996). "Computational aspects of a softening plasticity model for plain concrete." *Mechanics of Cohesive-frictional Materials*, 1(1), 75–94.

Black, V. M. (2014). "Single Straight Steel Fiber Pullout Characterization in Ultra-High Performance Concrete." M.S. thesis, Virginia Tech, Virginia Tech (July).

Bolander, J. E., Choi, S., and Duddukuri, S. R. (2009). "Fracture of fiber-reinforced cement composites: effects of fiber dispersion." *International Journal of Fracture*, 154(1-2), 73–86.

Bolander Jr., J. E. and Saito, S. (1998). "Fracture analyses using spring networks with random geometry." *Engineering Fracture Mechanics*, 61(5-6), 569–591.

Bolander Jr., J. E., Shiraishi, T., and Isogawa, Y. (1996). "An adaptive procedure for fracture simulation in extensive lattice networks." *Engineering Fracture Mechanics*, 54(3), 325–334.

Borst, R. d., Remmers, J. J. C., Needleman, A., and Abellan, M. A. (2004). "Discrete vs smeared crack models for concrete fracture: bridging the gap." *International Journal for Numerical and Analytical Methods in Geomechanics*, 28(7-8), 583–607.

Caballero, A., Carol, I., and López, C. M. (2006). "A meso-level approach to the 3D numerical analysis of cracking and fracture of concrete materials." *Fatigue & Fracture of Engineering Materials & Structures*, 29(12), 979–991.

Caner, F. C. and Bažant, Z. P. (2013). "Microplane Model M7 for Plain Concrete. I: Formulation." *Journal of Engineering Mechanics*, 139(12), 1714–1723.

Cedolin, L. and Bažant, Z. P. (1980). "Effect of finite element choice in blunt crack band analysis." *Computer Methods in Applied Mechanics and Engineering*, 24(3), 305–316.

Comi, C. and Perego, U. (2001). "Fracture energy based bi-dissipative damage model for concrete." *International Journal of Solids and Structures*, 38(36-37), 6427–6454.

Cundall, P. A. (1971). "Computer model for simulating progressive, large-scale movements in blocky rock systems." *Proceedings of Symposium of International Society of Rock Mechanics*, International Society for Rock Mechanics, Nancy, France, 129–136 (October).

Cundall, P. A. and Strack, O. D. L. (1979). "A discrete numerical model for granular assemblies." *Géotechnique*, 29(1), 47–65.

Cunha, V. M. C. F., Barros, J. A. O., and Sena-Cruz, J. M. (2009). "Pullout Behavior of Steel Fibers in Self-Compacting Concrete." *Journal of Materials in Civil Engineering*, 22(1), 1–9.

Cunha, V. M. C. F., Barros, J. A. O., and Sena-Cruz, J. M. (2011). "An integrated approach for modelling the tensile behaviour of steel fibre reinforced self-compacting concrete." *Cement and Concrete Research*, 41(1), 64–76.

Cusatis, G., Bažant, Z. P., and Cedolin, L. (2003a). "Confinement-Shear Lattice Model for Concrete Damage in Tension and Compression: I. Theory." *Journal of Engineering Mechanics*, 129(12), 1439–1448.

Cusatis, G., Bažant, Z. P., and Cedolin, L. (2003b). "Confinement-Shear Lattice Model for Concrete Damage in Tension and Compression: II. Computation and Validation." *Journal of Engineering Mechanics*, 129(12), 1449–1458.

Cusatis, G., Bažant, Z. P., and Cedolin, L. (2006). "Confinement-shear lattice CSL model for fracture propagation in concrete." *Computer Methods in Applied Mechanics and Engineering*, 195(52), 7154–7171.

Cusatis, G. and Nakamura, H. (2011). "Discrete modeling of concrete materials and structures." *Cement and Concrete Composites*, 33(9), 865–866.

Cusatis, G., Rezakhani, R., Alnaggar, M., Zhou, X., and Pelessone, D. (2014). "Multiscale computational models for the simulation of concrete materials and structures." *Computational Modelling of Concrete Structures*, CRC Press, 23–38.

Cusatis, G., Pelessone, D., and Mencarelli, A. (2011a). "Lattice Discrete Particle Model (LDPM) for failure behavior of concrete. I: Theory." *Cement and Concrete Composites*, 33(9), 881–890.

Cusatis, G., Mencarelli, A., Pelessone, D., and Baylot, J. (2011b). "Lattice Discrete Particle Model (LDPM) for failure behavior of concrete. II: Calibration and validation." *Cement and Concrete Composites*, 33(9), 891–905.

De Borst, R., Sluys, L. J., Muhlhaus, H. B., and Pamin, J. (1993). "Fundamental issues in finite element analyses of localization of deformation." *Engineering Computations*, 10(2), 99–121.

Delaunay, B. (1934). "Sur la sphere vide." *Izv Akad Nauk SSSR*.

Di Luzio, G. and Cusatis, G. (2013). "Solidification–microprestress–microplane (SMM) theory for concrete at early age: Theory, validation and application." *International Journal of Solids and Structures*, 50(6), 957–975.

Drucker, D. C. and Prager, W. (1952). "Soil Mechanics and Plastic Analysis or Limit Design." *Quarterly of applied mathematics*, 10(2), 157–165.

Grassl, P. and Jirásek, M. (2006). "Damage-plastic model for concrete failure." *International Journal of Solids and Structures*, 43(22-23), 7166–7196.

Graybeal, B. (2014). "Design and Construction of Field-Cast UHPC Connections." *Report No. FHWA-HRT-14-084*, Federal Highway Administration (October).

Graybeal, B. A. (2006). "Material Property Characterization of Ultra-High Performance Concrete." *Report No. FHWA-HRT-06-103*, Federal Highway Administration (August).

Graybeal, B. A. and Baby, F. (2013). "Development of Direct Tension Test Method for Ultra-High- Performance Fiber-Reinforced Concrete." *Materials Journal*, 110(2), 177–186.

Herrmann, H. J. (1990). "Fracture patterns and scaling laws." *Physica A: Statistical Mechanics and its Applications*, 163(1), 359–372.

Herrmann, H. J., Hansen, A., and Roux, S. (1989). "Fracture of disordered, elastic lattices in two dimensions." *Physical Review B*, 39(1), 637–648.

Hillerborg, A., Modéer, M., and Petersson, P. E. (1976). "Analysis of crack formation and crack growth in concrete by means of fracture mechanics and finite elements." *Cement and Concrete Research*, 6(6), 773–781.

Hrennikoff, A. (1941). "Solution of problems of elasticity by the framework method." *Journal of applied mechanics*, 8(4), 169–175.

Huespe, A. E. and Oliver, J. (2011). "Crack Models with Embedded Discontinuities." *Numerical Modeling of Concrete Cracking*, Springer Vienna, Vienna, 99–159.

Jirásek, M. (2011). "Damage and Smeared Crack Models." *Numerical Modeling of Concrete Cracking*, Springer Vienna, Vienna, 1–49.

Jirásek, M. and Bažant, Z. P. (1994a). "Localization Analysis of Nonlocal Model Based on Crack Interactions." *Journal of Engineering Mechanics*, 120(7), 1521–1542.

Jirásek, M. and Bažant, Z. P. (1994b). "Macroscopic fracture characteristics of random particle systems." *International Journal of Fracture*, 69(3), 201–228.

Kabele, P. (2007). "Multiscale framework for modeling of fracture in high performance fiber reinforced cementitious composites." *Engineering Fracture Mechanics*, 74(1-2), 194–209.

Kanda, T. and Li, V. C. (1998). "Interface Property and Apparent Strength of a High Strength Hydrophilic Fiber in Cement Matrix." *Journal of Materials in Civil Engineering*, 10(1), 5–13.

Kang, S.-T. and Kim, J.-K. (2011). "The relation between fiber orientation and tensile behavior in an Ultra High Performance Fiber Reinforced Cementitious Composites (UHPFRCC)." *Cement and Concrete Research*, 41(10), 1001–1014.

Karihaloo, B. and Kulasegaram, S. (2015). "Determination of fibre orientation factor in high and ultra-high- performance fibre-reinforced self-compacting concrete." *High Performance Fiber Reinforced Cement Composites (HPFRCC7)*, Stuttgart, Germany, Fraunhofer IRB Verlag, 137–144.

Kim, D. J., El-Tawil, S., and Naaman, A. E. (2008). "Loading Rate Effect on Pullout Behavior of Deformed Steel Fibers." *Materials Journal*, 105(6), 576–584.

Lee, J. and Fenves, G. L. (1998). "Plastic-Damage Model for Cyclic Loading of Concrete Structures." *Journal of Engineering Mechanics*, 124(8), 892–900.

Lepech, M. D. and Li, V. C. (2009). "Water permeability of engineered cementitious composites." *Cement and Concrete Composites*, 31(10), 744–753.

Lewis-Smith, J. (2014). "Characterization of Ultra-High Performance Concrete for Impact Resistant Structures.

Li, V. C. (2003). "On Engineered Cementitious Composites (ECC)." *Journal of advanced concrete technology*, 1(3), 215–230.

Li, V. C., Wang, Y., and Backer, S. (1990). "Effect of inclining angle, bundling and surface treatment on synthetic fibre pull-out from a cement matrix." *Composites*, 21(2), 132–140.

Li, Z., Li, F., Chang, T. Y. P., and Mai, Y.-W. (1998). "Uniaxial Tensile Behavior of Concrete Reinforced with Randomly Distributed Short Fibers." *Materials Journal*, 95(5), 564–574.

Lin, Z., Kanda, T., and Li, V. C. (1999). "On interface property characterization and performance of fiber-reinforced cementitious composites." *Concrete Science and ...*.

Lin, Z. and Li, V. C. (1997). "Crack bridging in fiber reinforced cementitious composites with slip-hardening interfaces." *Journal of the Mechanics and Physics of Solids*, 45(5), 763–787.

Liu, C. (2009). "Elastic Constants Determination and Deformation Observation Using Brazilian Disk Geometry." *Experimental Mechanics*, 50(7), 1025–1039.

Lubliner, J., Oliver, J., Oller, S., and Oñate, E. (1989). "A plastic-damage model for concrete." *International Journal of Solids and Structures*, 25(3), 299–326.

Luzio, G. D. (2007). "A symmetric over-nonlocal microplane model M4 for fracture in concrete." *International Journal of Solids and Structures*, 44(13), 4418–4441.

Markovic, I. (2006). "High-performance hybrid-fibre Concrete: Development and utilization." Ph.D. thesis, Delft University of Technology.

Maya, L. F., De la Varga, I., and Graybeal, B. (2016). "Fiber reinforcement influence on the tensile response of UHPFRC Fiber Reinforcement Influence on the Tensile Response of UHPFRC." *First International Interactive Symposium on UHPC*.

Maya Duque, L. F. and Graybeal, B. (2016). "Fiber orientation distribution and tensile mechanical response in UHPFRC." *Materials and structures*, 50(1), 55.

Mazars, J. and Pijaudier Cabot, G. (1989). "Continuum Damage Theory—Application to Concrete." *Journal of Engineering Mechanics*, 115(2), 345–365.

Moharrami, M. and Koutromanos, I. (2016). "Triaxial Constitutive Model for Concrete under Cyclic Loading." *Journal of Structural Engineering*, 04016039–15.

Moharrami Gargari, M. (2016). "Development of Novel Computational Simulation Tools to Capture the Hysteretic Response and Failure of Reinforced Concrete Structures under Seismic Loads." Ph.D. thesis, Virginia Polytechnique Institute and State University, Blacksburg, VA (July).

Montgomery, D. C., Peck, E. A., and Vining, G. G. (2012). *Introduction to Linear Regression Analysis*. John Wiley & Sons, 5 edition (April).

Naaman, A. (1972). "A statistical theory of strength for fiber reinforced concrete,." Ph.D. thesis, Massachusetts Institute of Technology, Massachusetts Institute of Technology.

Naaman, A. E. and Najm, H. (1991). "Bond-Slip Mechanisms of Steel Fibers in Concrete." *Materials Journal*, 88(2), 135–145.

Oliver, J., Huespe, A. E., and Sánchez, P. J. (2006). "A comparative study on finite elements for capturing strong discontinuities: E-FEM vs X-FEM." *Computer Methods in Applied Mechanics and Engineering*, 195(37-40), 4732–4752.

Orange, G., Acker, P., and Vernet, C. (1999). "A new generation of UHP concrete: Ductal®. Damage resistance and micromechanical analysis." *Third international workshop on high performance fiber reinforced cement composites (HPFRCC3), Mainz, Germany*, 101–111.

Ortiz, M., Leroy, Y., and Needleman, A. (1987). "A finite element method for localized failure analysis." *Computer Methods in Applied Mechanics and Engineering*, 61(2), 189–214.

Ožbolt, J., Li, Y., and Kožar, I. (2001). "Microplane model for concrete with relaxed kinematic constraint." *International Journal of Solids and Structures*, 38(16), 2683–2711.

Pelessone, D. (2016). *Modeling and Analysis of the Response of Structures (MARS), user's manual*. ES3, San Diego, CA.

Radtke, F. K. F., Simone, A., and Sluys, L. J. (2010). "A computational model for failure analysis of fibre reinforced concrete with discrete treatment of fibres." *Engineering Fracture Mechanics*, 77(4), 597–620.

Rashid, Y. R. (1968). "Ultimate strength analysis of prestressed concrete pressure vessels." *Nuclear Engineering and Design*, 7(4), 334–344.

Richard, P. and Cheyrezy, M. (1995). "Composition of reactive powder concretes." *Cement and Concrete Research*, 25(7), 1501–1511.

RILEM technical committee 50-FMC (1985). "Determination of the fracture energy of mortar and concrete by means of three-point bend tests on notched beams." *Materials and structures*, 18(4), 287–290.

Robins, P., Austin, S., and Jones, P. (2002). "Pull-out behaviour of hooked steel fibres." *Materials and structures*, 35(7), 434–442.

Sancho, J. M., Planas, J., Cendón, D. A., Reyes, E., and Gálvez, J. C. (2007). "An embedded crack model for finite element analysis of concrete fracture." *Engineering Fracture Mechanics*, 74(1-2), 75–86.

Schauffert, E. A. and Cusatis, G. (2012). "Lattice Discrete Particle Model for Fiber-Reinforced Concrete. I: Theory." *Journal of Engineering Mechanics*, 138(7), 826–833.

Schauffert, E. A., Cusatis, G., Pelessone, D., O'Daniel, J. L., and Baylot, J. T. (2012). "Lattice Discrete Particle Model for Fiber-Reinforced Concrete. II: Tensile Fracture and Multiaxial Loading Behavior." *Journal of Engineering Mechanics*, 138(7), 834–841.

Schlangen, E. and Garboczi, E. J. (1997). "Fracture simulations of concrete using lattice models: Computational aspects." *Engineering Fracture Mechanics*, 57(2-3), 319–332.

Schlangen, E. and van Mier, J. G. M. (1992). "Experimental and numerical analysis of micromechanisms of fracture of cement-based composites." *Cement and Concrete Composites*, 14(2), 105–118.

Smith, J., Cusatis, G., Pelessone, D., Landis, E., O'Daniel, J., and Baylot, J. (2014). "Discrete modeling of ultra-high-performance concrete with application to projectile penetration." *International Journal of Impact Engineering*, 65, 13–32.

Stengel, T. (2009). "Effect of Surface Roughness on the Steel Fibre Bonding in Ultra High Performance Concrete (UHPC)." *Nanotechnology in Construction 3*, Springer Berlin Heidelberg, Berlin, Heidelberg, 371–376.

Stroeven, P. (2000). "A stereological approach to roughness of fracture surfaces and tortuosity of transport paths in concrete." *Cement and Concrete Composites*, 22(5), 331–341.

Sugama, T., Carciello, N., Kukacka, L. E., and Gray, G. (1992). "Interface between zinc phosphate-deposited steel fibres and cement paste." *Journal of Materials Science*, 27(11), 2863–2872.

Sujivorakul, C. (2002). "Development of high performance fiber reinforced cement composites using twisted polygonal steel fibers." Ph.D. thesis, University of Michigan, University of Michigan.

Taylor, R. L. (2014). "FEAP - Finite Element Analysis Program.

Tregger, N., Corr, D., Graham-Brady, L., and Shah, S. (2006). "Modeling the effect of mesoscale randomness on concrete fracture." *Probabilistic Engineering Mechanics*, 21(3), 217–225.

Wille, K., Kim, D. J., and Naaman, A. E. (2010). "Strain-hardening UHP-FRC with low fiber contents." *Materials and structures*, 44(3), 583–598.

Wille, K. and Naaman, A. E. (2012). "Pullout Behavior of High-Strength Steel Fibers Embedded in Ultra-High-Performance Concrete." *Materials Journal*, 109(4), 479–488.

Wille, K. and Naaman, A. E. (2013). "Effect of Ultra-High-Performance Concrete on Pullout Behavior of High-Strength Brass-Coated Straight Steel Fibers." *Materials Journal*, 110(4), 451–462.

Wille, K., Tue, N. V., and Parra-Montesinos, G. J. (2013). "Fiber distribution and orientation in UHP-FRC beams and their effect on backward analysis." *Materials and structures*, 47(11), 1825–1838.

Yang, E.-H., Wang, S., Yang, Y., and Li, V. C. (2008). "Fiber-Bridging Constitutive Law of Engineered Cementitious Composites." *Journal of advanced concrete technology*, 6(1), 181–193.

Yip, M., Li, Z., Liao, B.-S., and Bolander, J. E. (2006). "Irregular lattice models of fracture of multiphase particulate materials." *International Journal of Fracture*, 140(1-4), 113–124.

Zubelewicz, A. and Bažant, Z. P. (1987). "Interface Element Modeling of Fracture in Aggregate Composites." *Journal of Engineering Mechanics*, 113(11), 1619–1630.

Appendix A

Ductal® UHPC Mix Proportions Experimental Data Sheets

UHPC Mix Data Sheet

Mix Date & Start Time: 7/18/13 11:37 AM
Demold Date & Time: 7/20/2013 10:00:00 AM
Mix ID: BA - I

Mix Design:

Volume of Mix: 2.10 ft^3

Material	Target Amt. (lb)	Measured (lb)
Premix	287.78	287.78
Water	17.04	17.04
Premia 150	3.94	3.94
Steel Fibers (2%)	20.45	0

Mix History:

Event	Target Duration (min)	Description	End Time (00m:00s)	Duration (00m:00s)
Mix Premix	2	Disperse any large pack-set clumps	2:05	2:05
Add Water + Premia 150	~ 1	Mix water and Premia 150 first	3:37	1:32
Mix until Wet	~	Mix until consistency of bread dough	6:22	2:45
	~	Stop and scrape sides	14:20	7:58
	~	Stop and scrape sides	19:05	4:45
	~	Stop and scrape sides	22:32	3:27
	~	Finished mixing	24:30	1:58
		Total:		

Flow Test:

Slightly dampen the flow table and brass ring
Place brass ring at center, fill, and remove slowly.
Scape any residual sample from inside the cone and deposit it onto sample
Wait 2 min, and measure
Apply 20 shocks to the sample, wait 2 min, and measure

Event	1 - Dia. (in.)	2 - Dia. (in.)	3 - Dia. (in.)	Avg. (in.)
Static Flow	**9.6**	**10**	**9.75**	**9.783**
Dynamic Flow	-	-	-	-

Notes:

Used big green mixer which is slower than the small mixer in the materials room.
Flow test spilled from one side
Increased the amount needed initially, then didn't have enough to fill all specimens

UHPC Mix Data Sheet

Mix Date & Start Time: 7/22/13 11:02 AM
Demold Date & Time: 7/24/2013 10:00 AM
Mix ID: BA - II

Mix Design:

Volume of Mix: 2.75 ft^3

Material	Target Amt. (lb)	Measured (lb)
Premix	376.85	376.86
Water	22.32	22.32
Premia 150	5.15	5.15
Steel Fibers (2%)	26.78	0

Mix History:

Event	Target Duration (min)	Description	End Time (00m:00s)	Duration (00m:00s)
Mix Premix	2	Disperse any large pack-set clumps	3:00	3:00
Add Water + Premia 150	~ 1	Mix water and Premia 150 first	5:25	2:25
Mix until Wet	~	Mix until consistency of bread dough	8:40	3:15
	~	Stop and scrape sides	23:59	15:19
	~	Stop and scrape sides	-	-
	~	Stop and scrape sides	-	-
	~	Finished mixing	29:24	5:25
		Total:		

Flow Test:

Slightly dampen the flow table and brass ring
Place brass ring at center, fill, and remove slowly.
Scape any residual sample from inside the cone and deposit it onto sample
Wait 2 min, and measure
Apply 20 shocks to the sample, wait 2 min, and measure

Event	1 - Dia. (in.)	2 - Dia. (in.)	3 - Dia. (in.)	Avg. (in.)
Static Flow	**10**	**9.5**	**9.5**	**9.667**
Dynamic Flow	-	-	-	-

Notes: Used big green mixer which is slower than the small mixer in the materials room.
Flow test spilled from one side

UHPC Mix Data Sheet

Mix Date & Start Time: 11/13/13 3:57
Demold Date & Time: 11/15/13
Mix ID: BA - III

Mix Design:

Volume of Mix: 2.20 ft^3

Material	Target Amt. (lb)	Measured (lb)
Premix	301.48	301.48
Water	17.85	17.86
Premia 150	4.12	4.12
Steel Fibers (0%)		

Mix History:

Event	Target Duration (min)	Description	End Time (00m:00s)	Duration (00m:00s)
Mix Premix	2	Disperse any large pack-set clumps		
Add Water + Premia 150	~ 1	Mix water and Premia 150 first	2:06	2:06
Mix until Wet	~	Mix until consistency of bread dough	8:30	6:24
Stop and scrape	~	Be quick	13:24	4:54
Mix until flowable	~	Make sure nothing is sticking on the sides	24:30	11:06

Flow Test:

Slightly dampen the flow table and brass ring
Place brass ring at center, fill, and remove slowly.
Scape any residual sample from inside the cone and deposit it onto sample
Wait 2 min, and measure
Apply 20 shocks to the sample, wait 2 min, and measure

Event	1 - Dia. (in.)	2 - Dia. (in.)	3 - Dia. (in.)	Avg. (in.)
Static Flow	9.75	9.5	9.85	9.70
Dynamic Flow				

Notes: Used big green mixer

Specimen Labels:

UHPC Mix Data Sheet

Mix Date & Start Time: 7/29/13 10:30
Demold Date & Time:
Mix ID: BA - IV

Mix Design:

Volume of Mix: 3.00 ft^3

Material	Target Amt. (lb)	Measured (lb)
Premix	411.11	411.12
Water	24.34	24.34
Premia 150	5.62	5.62
Steel Fibers (2%)	29.21	29.22

Mix History:

Event	Target Duration (min)	Description	End Time (00m:00s)	Duration (00m:00s)
Mix Premix	2	Disperse any large pack-set clumps	2:30	2:30
Add Water + Premia 150	~ 1	Mix water and Premia 150 first	4:43	2:13
Mix until Wet	~	Mix until consistency of bread dough	20:28	15:45
Stop and scrape	~	Be quick		
Mix until flowable	~	Make sure nothing is sticking on the sides	23:00	2:32
Add Fibers	1-2	Avoid adding fibers in clumps and balls	25:00	2:00
Mix	1-2	Mix until fibers are evenly distributed	27:10	2:10

Flow Test:

Slightly dampen the flow table and brass ring
Place brass ring at center, fill, and remove slowly.
Scape any residual sample from inside the cone and deposit it onto sample
Wait 2 min, and measure
Apply 20 shocks to the sample, wait 2 min, and measure

Event	1 - Dia. (in.)	2 - Dia. (in.)	3 - Dia. (in.)	Avg. (in.)
Static Flow	10	9.5	9.8	9.77
Dynamic Flow				

Notes: Used big green mixer

Specimen Labels:

UHPC Mix Data Sheet

Mix Date & Start Time: 9/5/13 11:13
Demold Date & Time:
Mix ID: BA - V

Mix Design:

Volume of Mix: 2.25 ft^3

Material	Target Amt. (lb)	Measured (lb)
Premix	308.33	308.34
Water	18.26	18.26
Premia 150	4.22	4.22
Steel Fibers (2%)	21.91	21.92

Mix History:

Event	Target Duration (min)	Description	End Time (00m:00s)	Duration (00m:00s)
Mix Premix	2	Disperse any large pack-set clumps	19:39	19:39
Add Water + Premia 150	~ 1	Mix water and Premia 150 first	21:15	1:36
Mix until Wet	~	Mix until consistency of bread dough	36:02	14:47
Stop and scrape	~	Be quick	41:39	5:37
Mix until flowable	~	Make sure nothing is sticking on the sides	55:06	13:27
Add Fibers	1-2	Avoid adding fibers in clumps and balls	58:00	2:54
Mix	1-2	Mix until fibers are evenly distributed	64:03	6:03

Flow Test:

Slightly dampen the flow table and brass ring
Place brass ring at center, fill, and remove slowly.
Scape any residual sample from inside the cone and deposit it onto sample
Wait 2 min, and measure
Apply 20 shocks to the sample, wait 2 min, and measure

Event	1 - Dia. (in.)	2 - Dia. (in.)	3 - Dia. (in.)	Avg. (in.)
Static Flow	9.25	9.75	9.5	9.50
Dynamic Flow	9.85	9.85	10	9.90

Notes: Used big green mixer

Specimen Labels:

UHPC Mix Data Sheet

Mix Date & Start Time: 11/22/13
Demold Date & Time:
Mix ID: BA - VI

Mix Design:

Volume of Mix: 2.20 ft^3

Material	Target Amt. (lb)	Measured (lb)
Premix	301.48	301.48
Water	17.85	17.86
Premia 150	4.12	4.12
Steel Fibers (2%)	21.42	21.42

Mix History:

Event	Target Duration (min)	Description	End Time (00m:00s)	Duration (00m:00s)
Mix Premix	2	Disperse any large pack-set clumps		
Add Water + Premia 150	~ 1	Mix water and Premia 150 first	2:07	2:07
Mix until Wet	~	Mix until consistency of bread dough		5:19
Stop and scrape	~	Be quick		4:34
Mix until flowable	~	Make sure nothing is sticking on the sides		5:37
Add Fibers	1-2	Avoid adding fibers in clumps and balls		1:41
Mix	1-2	Mix until fibers are evenly distributed	25:43	

Flow Test:

Slightly dampen the flow table and brass ring
Place brass ring at center, fill, and remove slowly.
Scape any residual sample from inside the cone and deposit it onto sample
Wait 2 min, and measure
Apply 20 shocks to the sample, wait 2 min, and measure

Event	1 - Dia. (in.)	2 - Dia. (in.)	3 - Dia. (in.)	Avg. (in.)
Static Flow	9.75	9.75	9.75	9.75
Dynamic Flow				

Notes: Used big green mixer

Specimen Labels:

UHPC Mix Data Sheet

Mix Date & Start Time: 12/16/14 9:00
Demold Date & Time:
Mix ID: BA - VII

Mix Design:

Volume of Mix: 3.00 ft^3

Material	Target Amt. (lb)	Measured (lb)
Premix	411.11	411.11
Water	24.34	24.36
Premia 150	5.62	5.64
Steel Fibers (4%)	58.42	29.22

Mix History:

Event	Target Duration (min)	Description	End Time (00m:00s)	Duration (00m:00s)
Mix Premix	2	Disperse any large pack-set clumps	2:40	
Add Water + Premia 150	~ 1	Mix water and Premia 150 first	3:50	
Mix until Wet	~	Mix until consistency of bread dough	30:50	
Stop and scrape	~	Be quick	38:20	
Mix until flowable	~	Make sure nothing is sticking on the sides	45:43	
Add Fibers	1-2	Avoid adding fibers in clumps and balls	50:32	
Mix	1-2	Mix until fibers are evenly distributed	53:15	

Flow Test:

Slightly dampen the flow table and brass ring
Place brass ring at center, fill, and remove slowly.
Scape any residual sample from inside the cone and deposit it onto sample
Wait 2 min, and measure
Apply 20 shocks to the sample, wait 2 min, and measure

Event	1 - Dia. (in.)	2 - Dia. (in.)	3 - Dia. (in.)	Avg. (in.)
Static Flow	9.5	9.25	9.5	9.42
Dynamic Flow				

Notes: Used big green mixer

Specimen Labels:

UHPC Mix Data Sheet

Mix Date & Start Time: 7/29/13 9:22
Demold Date & Time:
Mix ID: BA - VIII

Mix Design:

Volume of Mix: 3.00 ft^3

Material	Target Amt. (lb)	Measured (lb)
Premix	411.11	411.12
Water	24.34	24.34
Premia 150	5.62	5.62
Steel Fibers (4%)	58.42	58.42

Mix History:

Event	Target Duration (min)	Description	End Time (00m:00s)	Duration (00m:00s)
Mix Premix	2	Disperse any large pack-set clumps	5:50	5:50
Add Water + Premia 150	~ 1	Mix water and Premia 150 first	8:07	2:17
Mix until Wet	~	Mix until consistency of bread dough	21:03	12:56
Stop and scrape	~	Be quick	26:55	5:52
Mix until flowable	~	Make sure nothing is sticking on the sides	33:07	6:12
Add Fibers	1-2	Avoid adding fibers in clumps and balls	36:41	3:34
Mix	1-2	Mix until fibers are evenly distributed	41:08	4:27

Flow Test:

Slightly dampen the flow table and brass ring
Place brass ring at center, fill, and remove slowly.
Scape any residual sample from inside the cone and deposit it onto sample
Wait 2 min, and measure
Apply 20 shocks to the sample, wait 2 min, and measure

Event	1 - Dia. (in.)	2 - Dia. (in.)	3 - Dia. (in.)	Avg. (in.)
Static Flow	8.25	9.25	9	8.83
Dynamic Flow	8.75	9.75	9.5	9.33

Notes: Used big green mixer

Specimen Labels:

UHPC Mix Data Sheet

Mix Date & Start Time: 9/10/13 11:30
Demold Date & Time:
Mix ID: BA - IX

Mix Design:

Volume of Mix: 2.54 ft^3

Material	Target Amt. (lb)	Measured (lb)
Premix	348.07	348.07
Water	20.61	20.62
Premia 150	4.76	4.76
Steel Fibers (4%)	49.46	49.48

Mix History:

Event	Target Duration (min)	Description	End Time (00m:00s)	Duration (00m:00s)
Mix Premix	2	Disperse any large pack-set clumps	2:22	2:22
Add Water + Premia 150	~ 1	Mix water and Premia 150 first	4:20	1:58
Mix until Wet	~	Mix until consistency of bread dough	24:12	19:52
Stop and scrape	~	Be quick	32:02	7:50
Mix until flowable	~	Make sure nothing is sticking on the sides	37:20	5:18
Add Fibers	1-2	Avoid adding fibers in clumps and balls	40:32	3:12
Mix	1-2	Mix until fibers are evenly distributed	45:26	4:54

Flow Test:

Slightly dampen the flow table and brass ring
Place brass ring at center, fill, and remove slowly.
Scape any residual sample from inside the cone and deposit it onto sample
Wait 2 min, and measure
Apply 20 shocks to the sample, wait 2 min, and measure

Event	1 - Dia. (in.)	2 - Dia. (in.)	3 - Dia. (in.)	Avg. (in.)
Static Flow	8.75	8.75	8.5	8.67
Dynamic Flow	9.4	9.25	9	9.22

Notes: Used big green mixer
Not very flowable

Specimen Labels:

UHPC Mix Data Sheet

Mix Date & Start Time: 12/9/13
Demold Date & Time:
Mix ID: BA - X

Mix Design:

Volume of Mix: 2.50 ft^3

Material	Target Amt. (lb)	Measured (lb)
Premix	342.59	342.59
Water	20.29	20.30
Premia 150	4.69	4.70
Steel Fibers (4%)	48.69	48.70

Mix History:

Event	Target Duration (min)	Description	End Time (00m:00s)	Duration (00m:00s)
Mix Premix	2	Disperse any large pack-set clumps		
Add Water + Premia 150	~ 1	Mix water and Premia 150 first	2:08	2:08
Mix until Wet	~	Mix until consistency of bread dough		5:18
Stop and scrape	~	Be quick		6:15
Mix until flowable	~	Make sure nothing is sticking on the sides		5:19
Add Fibers	1-2	Avoid adding fibers in clumps and balls		3:36
Mix	1-2	Mix until fibers are evenly distributed	27:55	

Flow Test:

Slightly dampen the flow table and brass ring
Place brass ring at center, fill, and remove slowly.
Scape any residual sample from inside the cone and deposit it onto sample
Wait 2 min, and measure
Apply 20 shocks to the sample, wait 2 min, and measure

Event	1 - Dia. (in.)	2 - Dia. (in.)	3 - Dia. (in.)	Avg. (in.)
Static Flow	9	8.5	8.75	
Dynamic Flow	9.25	9.75	10	

Notes: Used big green mixer
Dropped from one side in dynamic flow test

Specimen Labels:

Appendix B

UHPC Compression Cylinders Experimental Data Sheets

Cylinder Compression Response Test Protocol

BAI	**Batch**	**Specimen ID**	U3

Geometry & Weight:

Name: Tommy

Date: 2/10/14 Time: 3:24

Nominal Dimensions: 76 × 152 (2 × 6) mm (in) **Weight:** 1.64 Kg

Out-of-Plane Angle:

Dial gage reading at a:	0.4613	in		
Dial gage reading at ℓ:	0.4195	in		
Top distance aℓ:	2.9920	in		
Distance a - ℓ:	0.0418	in	Angle θ	0.800 °

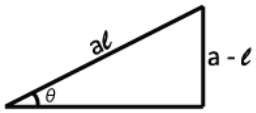

Actual Dimensions:

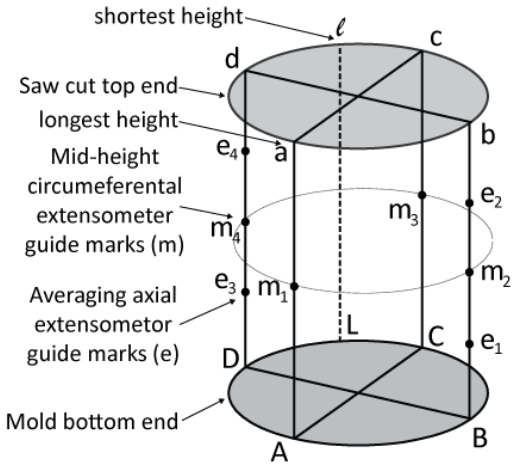

Height Aa:	152.73	mm
Height Bb:	151.95	mm
Height Cc:	151.75	mm
Height Dd:	152.13	mm
Height Lℓ:	151.67	mm
Diam. ac:	75.76	mm
Diam. m_1m_3:	75.68	mm
Diam. AC:	75.63	mm
Diam. bd:	75.65	mm
Diam. m_2m_4:	75.66	mm
Diam. BD:	75.63	mm

Guide Marks

1- Mark points e_1 & e_3 at a distance of 51 mm (2 in) from bottom of cylinder

2- Mark points m_1, m_2, m_3, m_4 at the a distance of 76 mm (3 in) from bottom of cylinder

3- Mark points e_2 & e_4 at a diatance of 102 mm (4 in) from bottom of cylinder

Geometric Comments:

Cylinder Compression Response Test Protocol

BAI	**Batch**	**Specimen ID**	U4

Geometry & Weight:

Name: Tommy

Date: 2/10/14 Time: 3:24

Nominal Dimensions: 76 × 152 (2 × 6) mm (in) **Weight:** 1.63 Kg

Out-of-Plane Angle:

Dial gage reading at a:	0.4138	in		
Dial gage reading at ℓ:	0.3956	in		
Top distance aℓ:	2.8340	in		
Distance a - ℓ:	0.0182	in	Angle θ	0.368 °

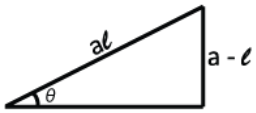

Actual Dimensions:

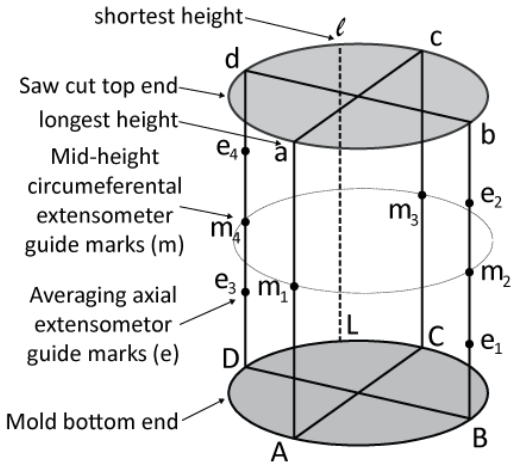

Height Aa:	152.15	mm
Height Bb:	151.92	mm
Height Cc:	151.83	mm
Height Dd:	151.88	mm
Height Lℓ:	151.80	mm
Diam. ac:	75.39	mm
Diam. m_1m_3:	75.39	mm
Diam. AC:	75.39	mm
Diam. bd:	75.38	mm
Diam. m_2m_4:	75.45	mm
Diam. BD:	75.40	mm

Guide Marks

1- Mark points e_1 & e_3 at a distance of 51 mm (2 in) from bottom of cylinder

2- Mark points m_1, m_2, m_3, m_4 at the a distance of 76 mm (3 in) from bottom of cylinder

3- Mark points e_2 & e_4 at a diatance of 102 mm (4 in) from bottom of cylinder

Geometric Comments:

Cylinder Compression Response Test Protocol

BAI	**Batch**	**Specimen ID**	U5

Geometry & Weight:

Name: Tommy

Date: 2/10/14 Time: 3:24

Nominal Dimensions: 76 × 152 (2 × 6) mm (in) **Weight:** 1.62 Kg

Out-of-Plane Angle:

Dial gage reading at a:	0.4622	in		
Dial gage reading at ℓ:	0.4215	in		
Top distance aℓ:	2.9470	in		
Distance a - ℓ:	0.0407	in	Angle θ	0.791 °

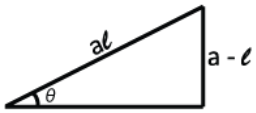

Actual Dimensions:

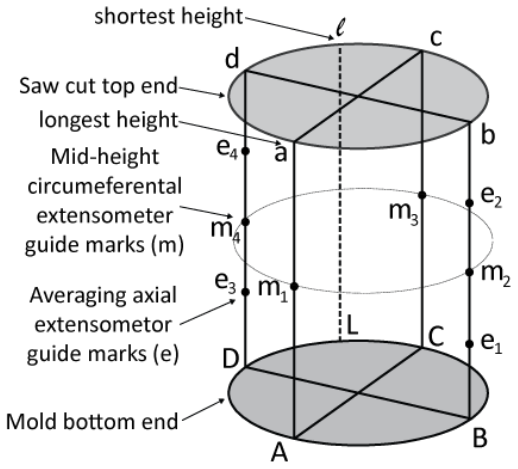

Height Aa:	152.95	mm
Height Bb:	152.20	mm
Height Cc:	151.88	mm
Height Dd:	152.53	mm
Height Lℓ:	151.92	mm
Diam. ac:	75.40	mm
Diam. m_1m_3:	75.32	mm
Diam. AC:	75.31	mm
Diam. bd:	75.32	mm
Diam. m_2m_4:	75.34	mm
Diam. BD:	75.35	mm

Guide Marks

1- Mark points e_1 & e_3 at a distance of 51 mm (2 in) from bottom of cylinder

2- Mark points m_1, m_2, m_3, m_4 at the a distance of 76 mm (3 in) from bottom of cylinder

3- Mark points e_2 & e_4 at a diatance of 102 mm (4 in) from bottom of cylinder

Geometric Comments:

Cylinder Compression Response Test Protocol

BAI	**Batch**	**Specimen ID**	U6

Geometry & Weight:

Name: Tommy

Date: 2/10/14 Time: 3:24

Nominal Dimensions: 76 × 152 (2 × 6) mm (in) **Weight:** 1.62 Kg

Out-of-Plane Angle:

Dial gage reading at a:	0.4060	in		
Dial gage reading at ℓ:	0.3991	in		
Top distance aℓ:	2.9500	in		
Distance a - ℓ:	0.0069	in	Angle θ	0.134 °

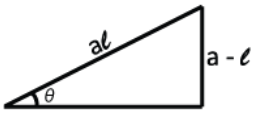

Actual Dimensions:

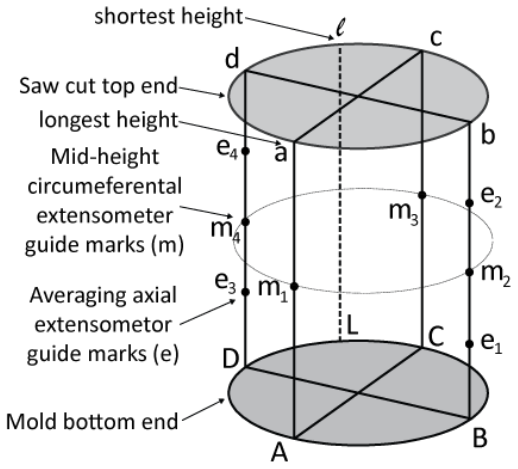

Height Aa:	151.90	mm
Height Bb:	151.82	mm
Height Cc:	151.78	mm
Height Dd:	151.85	mm
Height Lℓ:	151.75	mm
Diam. ac:	75.40	mm
Diam. m_1m_3:	75.43	mm
Diam. AC:	75.34	mm
Diam. bd:	75.41	mm
Diam. m_2m_4:	75.52	mm
Diam. BD:	75.33	mm

Guide Marks

1- Mark points e_1 & e_3 at a distance of 51 mm (2 in) from bottom of cylinder

2- Mark points m_1, m_2, m_3, m_4 at the a distance of 76 mm (3 in) from bottom of cylinder

3- Mark points e_2 & e_4 at a diatance of 102 mm (4 in) from bottom of cylinder

Geometric Comments:

Cylinder Compression Response Test Protocol

BAII	**Batch**	**Specimen ID**	U1

Geometry & Weight:

Name: Tommy

Date: 2/10/14 Time: 3:07

Nominal Dimensions: 76 × 152 (2 × 6) mm (in) **Weight:** 1.63 Kg

Out-of-Plane Angle:

Dial gage reading at a:	0.3843	in
Dial gage reading at ℓ:	0.3747	in
Top distance aℓ:	2.3860	in
Distance a - ℓ:	0.0096	in

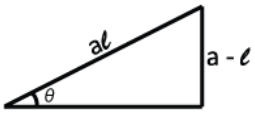

Angle θ 0.231 °

Actual Dimensions:

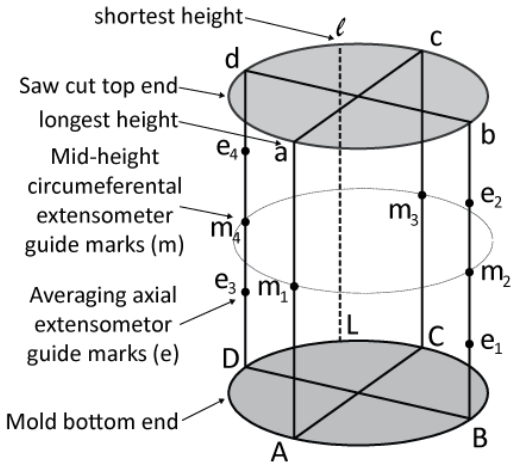

Height Aa:	151.50	mm
Height Bb:	151.47	mm
Height Cc:	151.44	mm
Height Dd:	151.44	mm
Height Lℓ:	151.25	mm
Diam. ac:	75.46	mm
Diam. m_1m_3:	75.49	mm
Diam. AC:	75.44	mm
Diam. bd:	75.49	mm
Diam. m_2m_4:	75.43	mm
Diam. BD:	75.41	mm

Guide Marks

1- Mark points e_1 & e_3 at a distance of 51 mm (2 in) from bottom of cylinder

2- Mark points m_1, m_2, m_3, m_4 at the a distance of 76 mm (3 in) from bottom of cylinder

3- Mark points e_2 & e_4 at a diatance of 102 mm (4 in) from bottom of cylinder

Geometric Comments:

Cylinder Compression Response Test Protocol

BAII	**Batch**	**Specimen ID**	U2

Geometry & Weight:

Name: Tommy

Date: 2/10/14 Time: 3:14

Nominal Dimensions: 76 × 152 (2 × 6) mm (in) **Weight:** 1.63 Kg

Out-of-Plane Angle:

Dial gage reading at a:	0.4074	in		
Dial gage reading at ℓ:	0.3722	in		
Top distance aℓ:	2.9480	in		
Distance a - ℓ:	0.0352	in	Angle θ	0.684 °

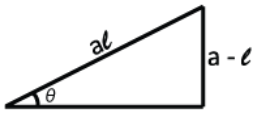

Actual Dimensions:

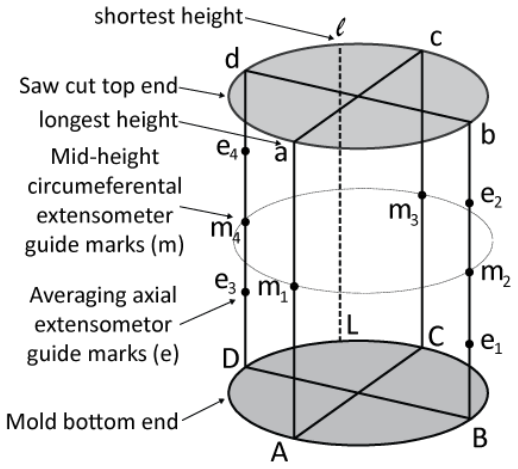

Height Aa:	151.80	mm
Height Bb:	151.46	mm
Height Cc:	151.10	mm
Height Dd:	151.51	mm
Height Lℓ:	151.13	mm
Diam. ac:	75.41	mm
Diam. m_1m_3:	75.42	mm
Diam. AC:	75.38	mm
Diam. bd:	75.38	mm
Diam. m_2m_4:	75.42	mm
Diam. BD:	75.39	mm

Guide Marks

1- Mark points e_1 & e_3 at a distance of 51 mm (2 in) from bottom of cylinder

2- Mark points m_1, m_2, m_3, m_4 at the a distance of 76 mm (3 in) from bottom of cylinder

3- Mark points e_2 & e_4 at a diatance of 102 mm (4 in) from bottom of cylinder

Geometric Comments:

Cylinder Compression Response Test Protocol

BAII	**Batch**	**Specimen ID**	U3

Geometry & Weight:

Name: Tommy

Date: 2/10/14 Time: 3:14

Nominal Dimensions: 76 × 152 (2 × 6) mm (in) **Weight:** 1.62 Kg

Out-of-Plane Angle:

Dial gage reading at a:	0.4062	in
Dial gage reading at ℓ:	0.3737	in
Top distance aℓ:	2.9320	in
Distance a - ℓ:	0.0325	in

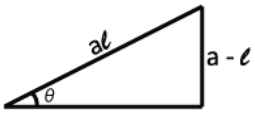

Angle θ 0.635 °

Actual Dimensions:

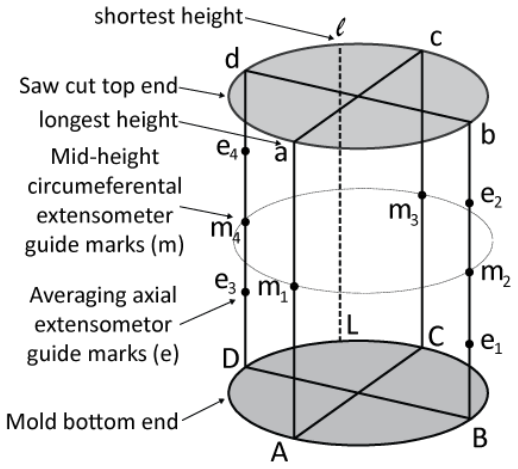

Height Aa:	152.03	mm
Height Bb:	151.55	mm
Height Cc:	151.38	mm
Height Dd:	151.77	mm
Height Lℓ:	151.33	mm
Diam. ac:	75.31	mm
Diam. m_1m_3:	75.36	mm
Diam. AC:	75.33	mm
Diam. bd:	75.30	mm
Diam. m_2m_4:	75.31	mm
Diam. BD:	75.34	mm

Guide Marks

1- Mark points e_1 & e_3 at a distance of 51 mm (2 in) from bottom of cylinder

2- Mark points m_1, m_2, m_3, m_4 at the a distance of 76 mm (3 in) from bottom of cylinder

3- Mark points e_2 & e_4 at a diatance of 102 mm (4 in) from bottom of cylinder

Geometric Comments:

Cylinder Compression Response Test Protocol

BAII	**Batch**	**Specimen ID**	U4

Geometry & Weight:

Name: Tommy

Date: 2/10/14 Time: 3:14

Nominal Dimensions: 76 × 152 (2 × 6) mm (in) **Weight:** 1.63 Kg

Out-of-Plane Angle:

Dial gage reading at a:	0.4109	in		
Dial gage reading at ℓ:	0.3782	in		
Top distance aℓ:	2.9050	in		
Distance a - ℓ:	0.0327	in	Angle θ	0.645 °

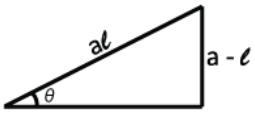

Actual Dimensions:

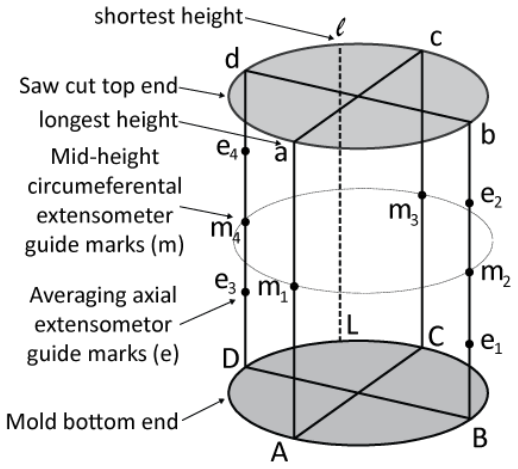

Height Aa:	152.13	mm
Height Bb:	151.81	mm
Height Cc:	151.33	mm
Height Dd:	151.78	mm
Height Lℓ:	151.28	mm
Diam. ac:	75.31	mm
Diam. m_1m_3:	75.36	mm
Diam. AC:	75.38	mm
Diam. bd:	75.31	mm
Diam. m_2m_4:	75.36	mm
Diam. BD:	75.36	mm

Guide Marks

1- Mark points e_1 & e_3 at a distance of 51 mm (2 in) from bottom of cylinder

2- Mark points m_1, m_2, m_3, m_4 at the a distance of 76 mm (3 in) from bottom of cylinder

3- Mark points e_2 & e_4 at a diatance of 102 mm (4 in) from bottom of cylinder

Geometric Comments:

Cylinder Compression Response Test Protocol

BAIV	**Batch**	**Specimen ID**	U1

Geometry & Weight:

Name: Tommy

Date: 2/10/14 Time: 3:35

Nominal Dimensions: 76 × 152 (3 × 6) mm (in) **Weight:** 1.71 Kg

Out-of-Plane Angle:

Dial gage reading at a:	0.4084	in
Dial gage reading at ℓ:	0.3952	in
Top distance aℓ:	2.6220	in
Distance a - ℓ:	0.0132	in

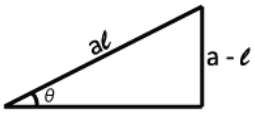

Angle θ 0.288 °

Actual Dimensions:

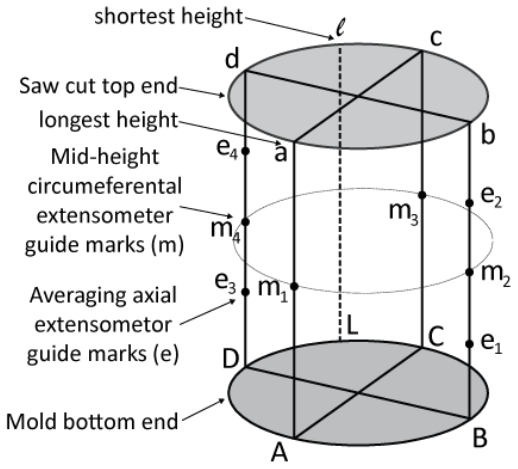

Height Aa:	151.81	mm
Height Bb:	151.71	mm
Height Cc:	151.53	mm
Height Dd:	151.62	mm
Height Lℓ:	151.46	mm
Diam. ac:	75.30	mm
Diam. m_1m_3:	75.38	mm
Diam. AC:	75.33	mm
Diam. bd:	75.27	mm
Diam. m_2m_4:	75.32	mm
Diam. BD:	75.36	mm

Guide Marks

1- Mark points e_1 & e_3 at a distance of 51 mm (2 in) from bottom of cylinder

2- Mark points m_1, m_2, m_3, m_4 at the a distance of 76 mm (3 in) from bottom of cylinder

3- Mark points e_2 & e_4 at a diatance of 102 mm (4 in) from bottom of cylinder

Geometric Comments:

Cylinder Compression Response Test Protocol

BAIV	**Batch**	**Specimen ID**	U2

Geometry & Weight:

Name: Tommy

Date: 2:10 Time: 3:35

Nominal Dimensions: 76 × 152 (3 × 6) mm (in) **Weight:** 1.71 Kg

Out-of-Plane Angle:

Dial gage reading at a:	0.4062	in
Dial gage reading at ℓ:	0.3802	in
Top distance aℓ:	2.8690	in
Distance a - ℓ:	0.0260	in

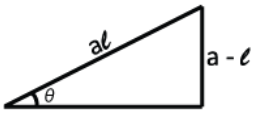

Angle θ 0.519 °

Actual Dimensions:

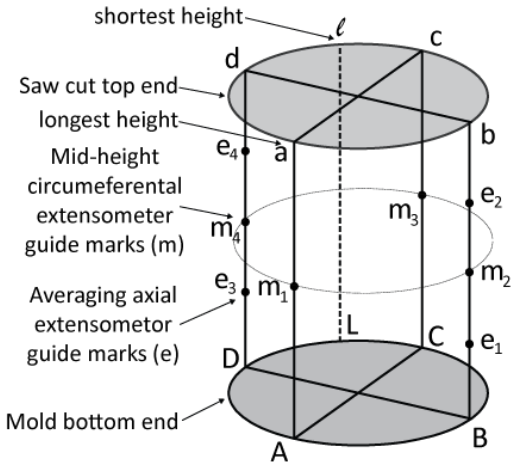

Height Aa:	151.71	mm
Height Bb:	151.30	mm
Height Cc:	151.13	mm
Height Dd:	151.53	mm
Height Lℓ:	151.09	mm
Diam. ac:	75.28	mm
Diam. m_1m_3:	75.26	mm
Diam. AC:	75.30	mm
Diam. bd:	75.25	mm
Diam. m_2m_4:	75.24	mm
Diam. BD:	75.32	mm

Guide Marks

1- Mark points e_1 & e_3 at a distance of 51 mm (2 in) from bottom of cylinder

2- Mark points m_1, m_2, m_3, m_4 at the a distance of 76 mm (3 in) from bottom of cylinder

3- Mark points e_2 & e_4 at a diatance of 102 mm (4 in) from bottom of cylinder

Geometric Comments:

Cylinder Compression Response Test Protocol

BAIV	**Batch**	**Specimen ID**	U3

Geometry & Weight:

Name: Tommy

Date: 2/10/14 Time: 3:35

Nominal Dimensions: 76 × 152 (3 × 6) mm (in) **Weight:** 1.71 Kg

Out-of-Plane Angle:

Dial gage reading at a:	0.4013	in
Dial gage reading at ℓ:	0.3693	in
Top distance aℓ:	2.9660	in
Distance a - ℓ:	0.0320	in

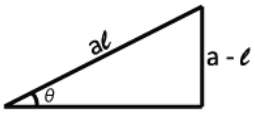

Angle θ 0.618 °

Actual Dimensions:

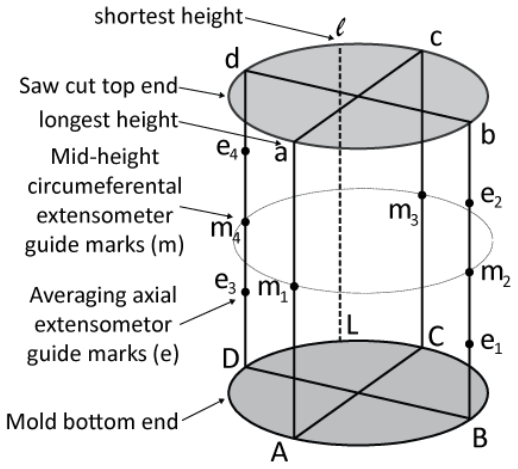

Height Aa:	151.82	mm
Height Bb:	151.35	mm
Height Cc:	150.99	mm
Height Dd:	151.56	mm
Height Lℓ:	150.95	mm
Diam. ac:	75.46	mm
Diam. m_1m_3:	75.38	mm
Diam. AC:	75.40	mm
Diam. bd:	75.43	mm
Diam. m_2m_4:	75.42	mm
Diam. BD:	75.39	mm

Guide Marks

1- Mark points e_1 & e_3 at a distance of 51 mm (2 in) from bottom of cylinder

2- Mark points m_1, m_2, m_3, m_4 at the a distance of 76 mm (3 in) from bottom of cylinder

3- Mark points e_2 & e_4 at a diatance of 102 mm (4 in) from bottom of cylinder

Geometric Comments:

Cylinder Compression Response Test Protocol

BAIV	**Batch**	**Specimen ID**	U4

Geometry & Weight:

Name: Tommy

Date: 2/10/14 Time: 3:35

Nominal Dimensions: 76 × 152 (3 × 6) mm (in) **Weight:** 1.71 Kg

Out-of-Plane Angle:

Dial gage reading at a:	0.4017	in
Dial gage reading at ℓ:	0.3678	in
Top distance aℓ:	2.9380	in
Distance a - ℓ:	0.0339	in

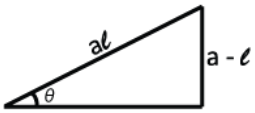

Angle θ 0.661 °

Actual Dimensions:

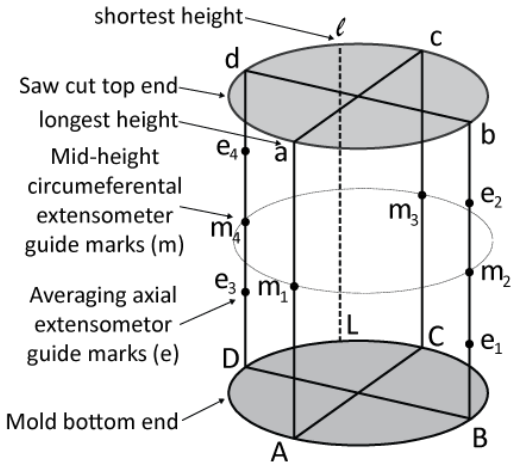

Height Aa:	151.83	mm
Height Bb:	151.29	mm
Height Cc:	151.15	mm
Height Dd:	151.59	mm
Height Lℓ:	151.00	mm
Diam. ac:	75.72	mm
Diam. m_1m_3:	75.68	mm
Diam. AC:	75.67	mm
Diam. bd:	75.71	mm
Diam. m_2m_4:	75.67	mm
Diam. BD:	75.68	mm

Guide Marks

1- Mark points e_1 & e_3 at a distance of 51 mm (2 in) from bottom of cylinder

2- Mark points m_1, m_2, m_3, m_4 at the a distance of 76 mm (3 in) from bottom of cylinder

3- Mark points e_2 & e_4 at a diatance of 102 mm (4 in) from bottom of cylinder

Geometric Comments:

Cylinder Compression Response Test Protocol

BAIV	**Batch**	**Specimen ID**	U5

Geometry & Weight:

Name: Tommy

Date: 2/10/14 Time: 3:35

Nominal Dimensions: 76 × 152 (3 × 6) mm (in) **Weight:** 1.72 Kg

Out-of-Plane Angle:

Dial gage reading at a:	0.4101	in
Dial gage reading at ℓ:	0.3797	in
Top distance aℓ:	2.7780	in
Distance a - ℓ:	0.0304	in

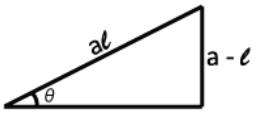

Angle θ 0.627 °

Actual Dimensions:

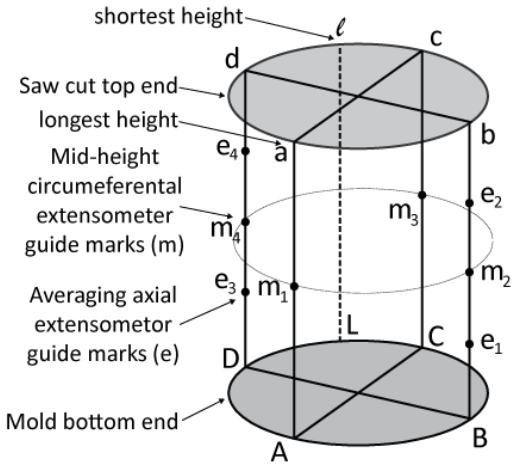

Height Aa:	151.99	mm
Height Bb:	151.83	mm
Height Cc:	151.37	mm
Height Dd:	151.59	mm
Height Lℓ:	151.33	mm
Diam. ac:	75.30	mm
Diam. m_1m_3:	75.20	mm
Diam. AC:	75.24	mm
Diam. bd:	75.28	mm
Diam. m_2m_4:	75.26	mm
Diam. BD:	75.18	mm

Guide Marks

1- Mark points e_1 & e_3 at a distance of 51 mm (2 in) from bottom of cylinder

2- Mark points m_1, m_2, m_3, m_4 at the a distance of 76 mm (3 in) from bottom of cylinder

3- Mark points e_2 & e_4 at a diatance of 102 mm (4 in) from bottom of cylinder

Geometric Comments:

Cylinder Compression Response Test Protocol

BAIV	**Batch**	**Specimen ID**	U6

Geometry & Weight:

Name: Tommy

Date: 2/10/14 Time: 3:35

Nominal Dimensions: 76 × 152 (3 × 6) mm (in) **Weight:** 1.70 Kg

Out-of-Plane Angle:

Dial gage reading at a:	0.3988	in
Dial gage reading at ℓ:	0.3616	in
Top distance aℓ:	2.9600	in
Distance a - ℓ:	0.0372	in

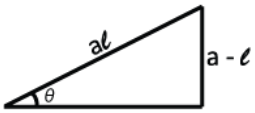

Angle θ 0.720 °

Actual Dimensions:

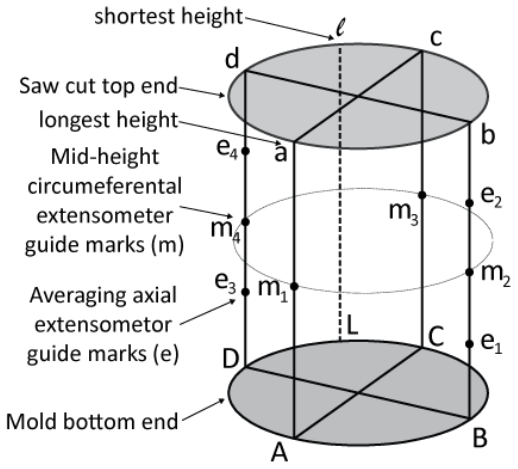

Height Aa:	151.79	mm
Height Bb:	151.37	mm
Height Cc:	150.95	mm
Height Dd:	151.57	mm
Height Lℓ:	150.87	mm
Diam. ac:	75.29	mm
Diam. m_1m_3:	75.26	mm
Diam. AC:	75.22	mm
Diam. bd:	75.27	mm
Diam. m_2m_4:	75.29	mm
Diam. BD:	75.24	mm

Guide Marks

1- Mark points e_1 & e_3 at a distance of 51 mm (2 in) from bottom of cylinder

2- Mark points m_1, m_2, m_3, m_4 at the a distance of 76 mm (3 in) from bottom of cylinder

3- Mark points e_2 & e_4 at a diatance of 102 mm (4 in) from bottom of cylinder

Geometric Comments:

Cylinder Compression Response Test Protocol

BAIV	**Batch**	**Specimen ID**	U7

Geometry & Weight:

Name: Tommy

Date: 2/10/14 Time: 3:36

Nominal Dimensions: 76 × 152 (2 × 6) mm (in) **Weight:** 1.71 Kg

Out-of-Plane Angle:

Dial gage reading at a:	0.4030	in
Dial gage reading at ℓ:	0.3678	in
Top distance aℓ:	2.8750	in
Distance a - ℓ:	0.0352	in

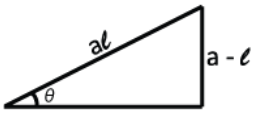

Angle θ 0.702 °

Actual Dimensions:

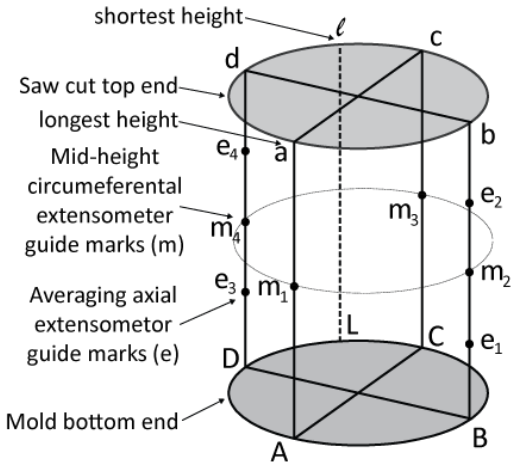

Height Aa:	151.90	mm
Height Bb:	151.30	mm
Height Cc:	151.08	mm
Height Dd:	151.57	mm
Height Lℓ:	151.07	mm
Diam. ac:	75.28	mm
Diam. m_1m_3:	75.23	mm
Diam. AC:	75.21	mm
Diam. bd:	75.36	mm
Diam. m_2m_4:	75.27	mm
Diam. BD:	75.21	mm

Guide Marks

1- Mark points e_1 & e_3 at a distance of 51 mm (2 in) from bottom of cylinder

2- Mark points m_1, m_2, m_3, m_4 at the a distance of 76 mm (3 in) from bottom of cylinder

3- Mark points e_2 & e_4 at a diatance of 102 mm (4 in) from bottom of cylinder

Geometric Comments:

Cylinder Compression Response Test Protocol

BAIV	**Batch**	**Specimen ID**	U8

Geometry & Weight:

Name: Tommy

Date: 2/10/14 Time: 3:36

Nominal Dimensions: 76 × 152 (2 × 6) mm (in) **Weight:** 1.71 Kg

Out-of-Plane Angle:

Dial gage reading at a:	0.4021	in
Dial gage reading at ℓ:	0.3643	in
Top distance aℓ:	2.8570	in
Distance a - ℓ:	0.0378	in

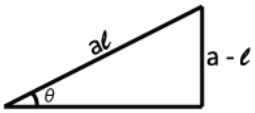

Angle θ 0.758 °

Actual Dimensions:

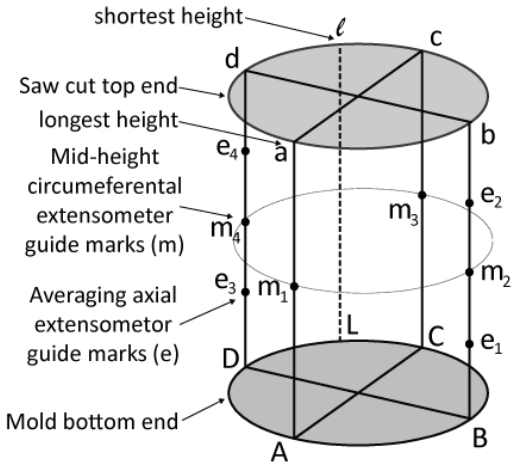

Height Aa:	151.86	mm
Height Bb:	151.30	mm
Height Cc:	150.94	mm
Height Dd:	151.52	mm
Height Lℓ:	150.85	mm
Diam. ac:	75.39	mm
Diam. m_1m_3:	75.37	mm
Diam. AC:	75.35	mm
Diam. bd:	75.42	mm
Diam. m_2m_4:	75.31	mm
Diam. BD:	75.31	mm

Guide Marks

1- Mark points e_1 & e_3 at a distance of 51 mm (2 in) from bottom of cylinder

2- Mark points m_1, m_2, m_3, m_4 at the a distance of 76 mm (3 in) from bottom of cylinder

3- Mark points e_2 & e_4 at a diatance of 102 mm (4 in) from bottom of cylinder

Geometric Comments:

Cylinder Compression Response Test Protocol

BAIV	**Batch**	**Specimen ID**	U9

Geometry & Weight:

Name: Tommy

Date: 2/10/14 Time: 3:36

Nominal Dimensions: 76 × 152 (2 × 6) mm (in) **Weight:** 1.71 Kg

Out-of-Plane Angle:

Dial gage reading at a:	0.4072	in
Dial gage reading at ℓ:	0.3733	in
Top distance aℓ:	2.9660	in
Distance a - ℓ:	0.0339	in

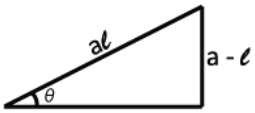

Angle θ 0.655 °

Actual Dimensions:

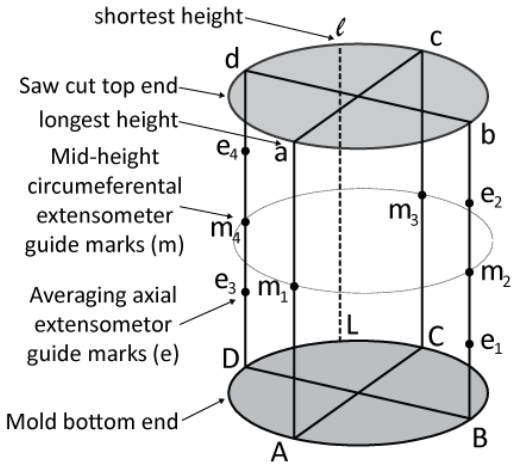

Height Aa:	151.99	mm
Height Bb:	151.53	mm
Height Cc:	151.11	mm
Height Dd:	151.69	mm
Height Lℓ:	151.11	mm
Diam. ac:	75.39	mm
Diam. m_1m_3:	75.36	mm
Diam. AC:	75.41	mm
Diam. bd:	75.36	mm
Diam. m_2m_4:	75.40	mm
Diam. BD:	75.43	mm

Guide Marks

1- Mark points e_1 & e_3 at a distance of 51 mm (2 in) from bottom of cylinder

2- Mark points m_1, m_2, m_3, m_4 at the a distance of 76 mm (3 in) from bottom of cylinder

3- Mark points e_2 & e_4 at a diatance of 102 mm (4 in) from bottom of cylinder

Geometric Comments:

Cylinder Compression Response Test Protocol

BAIV	**Batch**	**Specimen ID**	U10

Geometry & Weight:

Name: Tommy

Date: 2/10/14 Time: 3:36

Nominal Dimensions: 76 × 152 (2 × 6) mm (in) **Weight:** 1.72 Kg

Out-of-Plane Angle:

Dial gage reading at a:	0.4052	in
Dial gage reading at ℓ:	0.3668	in
Top distance aℓ:	2.9670	in
Distance a - ℓ:	0.0384	in

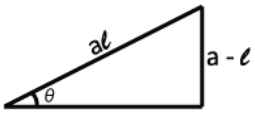

Angle θ 0.742 °

Actual Dimensions:

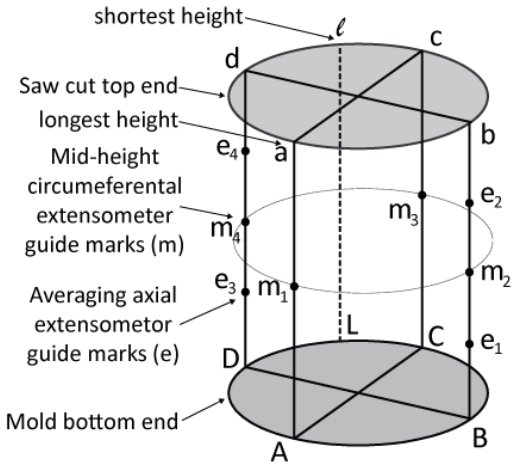

Height Aa:	151.97	mm
Height Bb:	151.46	mm
Height Cc:	151.13	mm
Height Dd:	151.65	mm
Height Lℓ:	151.13	mm
Diam. ac:	75.42	mm
Diam. m_1m_3:	75.45	mm
Diam. AC:	75.41	mm
Diam. bd:	75.39	mm
Diam. m_2m_4:	75.40	mm
Diam. BD:	75.40	mm

Guide Marks

1- Mark points e_1 & e_3 at a distance of 51 mm (2 in) from bottom of cylinder

2- Mark points m_1, m_2, m_3, m_4 at the a distance of 76 mm (3 in) from bottom of cylinder

3- Mark points e_2 & e_4 at a diatance of 102 mm (4 in) from bottom of cylinder

Geometric Comments:

Cylinder Compression Response Test Protocol

BAIV	**Batch**	**Specimen ID**	U13

Geometry & Weight:

Name: Tommy

Date: 2/10/14 Time: 3:36

Nominal Dimensions: 76 × 152 (2 × 6) mm (in) **Weight:** 1.69 Kg

Out-of-Plane Angle:

Dial gage reading at a:	0.4033	in
Dial gage reading at ℓ:	0.3615	in
Top distance aℓ:	2.9370	in
Distance a - ℓ:	0.0418	in

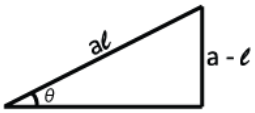

Angle θ 0.815 °

Actual Dimensions:

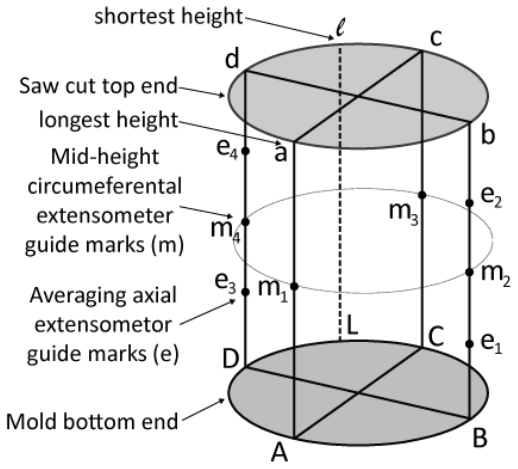

Height Aa:	151.85	mm
Height Bb:	151.41	mm
Height Cc:	150.87	mm
Height Dd:	151.40	mm
Height Lℓ:	150.83	mm
Diam. ac:	75.18	mm
Diam. m_1m_3:	75.17	mm
Diam. AC:	75.25	mm
Diam. bd:	75.22	mm
Diam. m_2m_4:	75.21	mm
Diam. BD:	75.24	mm

Guide Marks

1- Mark points e_1 & e_3 at a distance of 51 mm (2 in) from bottom of cylinder

2- Mark points m_1, m_2, m_3, m_4 at the a distance of 76 mm (3 in) from bottom of cylinder

3- Mark points e_2 & e_4 at a diatance of 102 mm (4 in) from bottom of cylinder

Geometric Comments:

Cylinder Compression Response Test Protocol

BAIV	**Batch**	**Specimen ID**	U14

Geometry & Weight:

Name: Tommy

Date: 2/10/14 Time: 3:36

Nominal Dimensions: 76 × 152 (2 × 6) mm (in) **Weight:** 1.70 Kg

Out-of-Plane Angle:

Dial gage reading at a:	0.4042	in
Dial gage reading at ℓ:	0.3665	in
Top distance aℓ:	2.9330	in
Distance a - ℓ:	0.0377	in

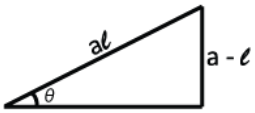

Angle θ 0.736 °

Actual Dimensions:

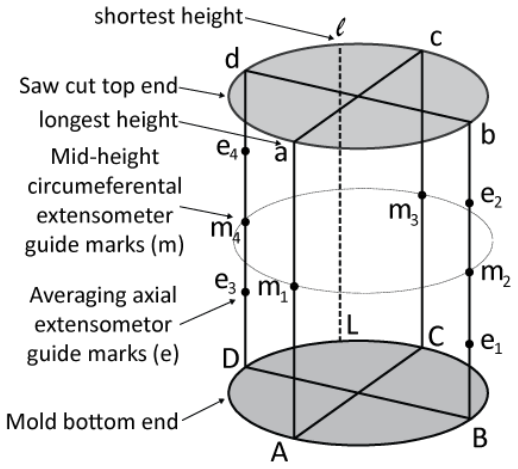

Height Aa:	151.95	mm
Height Bb:	151.50	mm
Height Cc:	151.05	mm
Height Dd:	151.61	mm
Height Lℓ:	151.05	mm
Diam. ac:	75.39	mm
Diam. m_1m_3:	75.31	mm
Diam. AC:	75.34	mm
Diam. bd:	75.30	mm
Diam. m_2m_4:	75.31	mm
Diam. BD:	75.40	mm

Guide Marks

1- Mark points e_1 & e_3 at a distance of 51 mm (2 in) from bottom of cylinder

2- Mark points m_1, m_2, m_3, m_4 at the a distance of 76 mm (3 in) from bottom of cylinder

3- Mark points e_2 & e_4 at a diatance of 102 mm (4 in) from bottom of cylinder

Geometric Comments:

Cylinder Compression Response Test Protocol

BAIV	**Batch**	**Specimen ID**	U15

Geometry & Weight:

Name: Tommy

Date: 2/10/14 Time: 3:37

Nominal Dimensions: 76 × 152 (2 × 6) mm (in) **Weight:** 1.70 Kg

Out-of-Plane Angle:

Dial gage reading at a:	0.4000	in
Dial gage reading at ℓ:	0.3794	in
Top distance aℓ:	2.9610	in
Distance a - ℓ:	0.0206	in

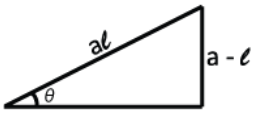

Angle θ 0.399 °

Actual Dimensions:

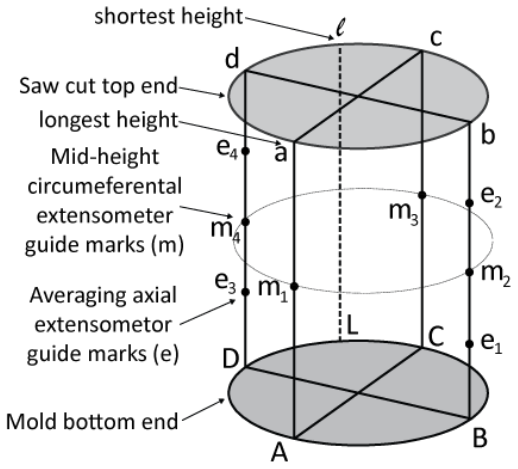

Height Aa:	151.81	mm
Height Bb:	151.54	mm
Height Cc:	151.31	mm
Height Dd:	151.67	mm
Height Lℓ:	151.28	mm
Diam. ac:	75.26	mm
Diam. m_1m_3:	75.33	mm
Diam. AC:	75.35	mm
Diam. bd:	75.34	mm
Diam. m_2m_4:	75.34	mm
Diam. BD:	75.35	mm

Guide Marks

1- Mark points e_1 & e_3 at a distance of 51 mm (2 in) from bottom of cylinder

2- Mark points m_1, m_2, m_3, m_4 at the a distance of 76 mm (3 in) from bottom of cylinder

3- Mark points e_2 & e_4 at a diatance of 102 mm (4 in) from bottom of cylinder

Geometric Comments:

Cylinder Compression Response Test Protocol

BAVIII	**Batch**	**Specimen ID**	U1

Geometry & Weight:

Name: Tommy

Date: 2/10/14 Time: 4:50

Nominal Dimensions: 76 × 152 (3 × 6) mm (in) **Weight:** 1.77 Kg

Out-of-Plane Angle:

Dial gage reading at a:	0.3972	in
Dial gage reading at ℓ:	0.3561	in
Top distance aℓ:	2.8260	in
Distance a - ℓ:	0.0411	in

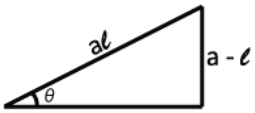

Angle θ 0.833 °

Actual Dimensions:

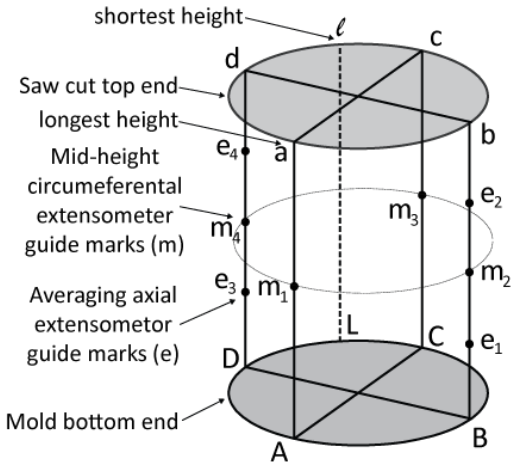

Height Aa:	151.13	mm
Height Bb:	150.65	mm
Height Cc:	150.20	mm
Height Dd:	150.44	mm
Height Lℓ:	150.17	mm
Diam. ac:	75.38	mm
Diam. m_1m_3:	75.37	mm
Diam. AC:	75.40	mm
Diam. bd:	75.31	mm
Diam. m_2m_4:	75.33	mm
Diam. BD:	75.37	mm

Guide Marks

1- Mark points e_1 & e_3 at a distance of 51 mm (2 in) from bottom of cylinder

2- Mark points m_1, m_2, m_3, m_4 at the a distance of 76 mm (3 in) from bottom of cylinder

3- Mark points e_2 & e_4 at a diatance of 102 mm (4 in) from bottom of cylinder

Geometric Comments:

Cylinder Compression Response Test Protocol

BAVIII	**Batch**	**Specimen ID**	U2

Geometry & Weight:

Name: Tommy

Date: 2/10/14 Time: 4:50

Nominal Dimensions: 76 × 152 (3 × 6) mm (in) **Weight:** 1.77 Kg

Out-of-Plane Angle:

Dial gage reading at a:	0.3966	in		
Dial gage reading at ℓ:	0.3522	in		
Top distance aℓ:	2.8610	in		
Distance a - ℓ:	0.0444	in	Angle θ	0.889 °

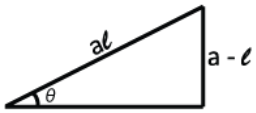

Actual Dimensions:

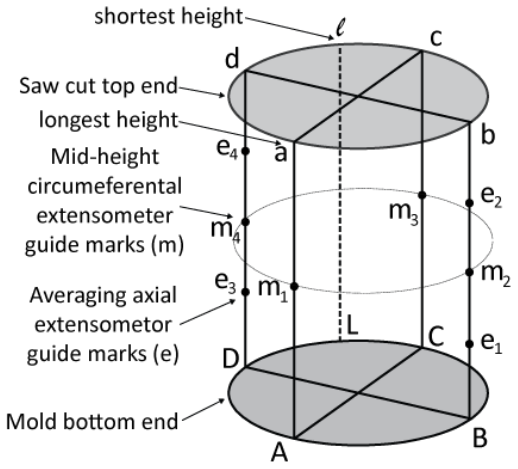

Height Aa:	151.07	mm
Height Bb:	150.49	mm
Height Cc:	150.06	mm
Height Dd:	150.79	mm
Height Lℓ:	150.00	mm
Diam. ac:	75.37	mm
Diam. m_1m_3:	75.36	mm
Diam. AC:	75.33	mm
Diam. bd:	75.22	mm
Diam. m_2m_4:	75.30	mm
Diam. BD:	75.35	mm

Guide Marks

1- Mark points e_1 & e_3 at a distance of 51 mm (2 in) from bottom of cylinder

2- Mark points m_1, m_2, m_3, m_4 at the a distance of 76 mm (3 in) from bottom of cylinder

3- Mark points e_2 & e_4 at a diatance of 102 mm (4 in) from bottom of cylinder

Geometric Comments:

Cylinder Compression Response Test Protocol

BAVIII	**Batch**	**Specimen ID**	U3

Geometry & Weight:

Name: Tommy

Date: 2/10/14 Time: 4:51

Nominal Dimensions: 76 × 152 (2 × 6) mm (in) **Weight:** 1.77 Kg

Out-of-Plane Angle:

Dial gage reading at a:	0.3875	in
Dial gage reading at ℓ:	0.3466	in
Top distance aℓ:	2.9310	in
Distance a - ℓ:	0.0409	in

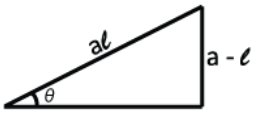

Angle θ 0.800 °

Actual Dimensions:

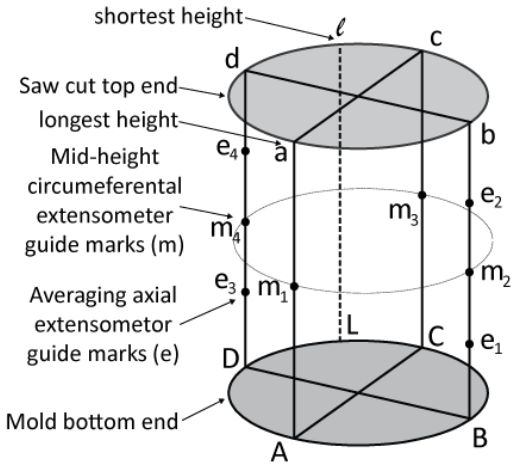

Height Aa:	150.77	mm
Height Bb:	150.45	mm
Height Cc:	149.95	mm
Height Dd:	150.25	mm
Height Lℓ:	149.81	mm
Diam. ac:	75.42	mm
Diam. m_1m_3:	75.50	mm
Diam. AC:	75.37	mm
Diam. bd:	75.34	mm
Diam. m_2m_4:	75.38	mm
Diam. BD:	75.38	mm

Guide Marks

1- Mark points e_1 & e_3 at a distance of 51 mm (2 in) from bottom of cylinder

2- Mark points m_1, m_2, m_3, m_4 at the a distance of 76 mm (3 in) from bottom of cylinder

3- Mark points e_2 & e_4 at a diatance of 102 mm (4 in) from bottom of cylinder

Geometric Comments:

Cylinder Compression Response Test Protocol

BAVIII	**Batch**	**Specimen ID**	U4

Geometry & Weight:

Name: Tommy

Date: 2/10/14 Time: 4:51

Nominal Dimensions: 76 × 152 (2 × 6) mm (in) **Weight:** 1.78 Kg

Out-of-Plane Angle:

Dial gage reading at a:	0.4031	in
Dial gage reading at ℓ:	0.3572	in
Top distance aℓ:	2.9550	in
Distance a - ℓ:	0.0459	in

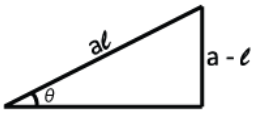

Angle θ 0.890 °

Actual Dimensions:

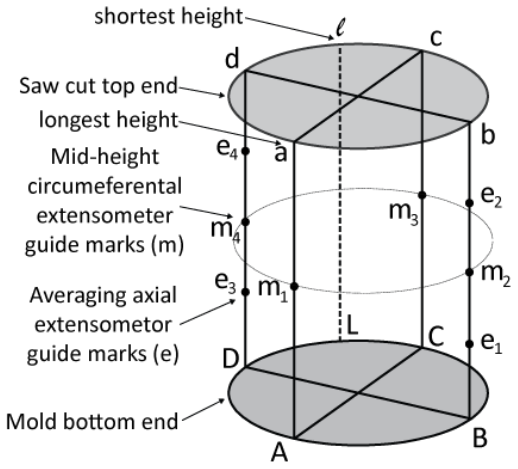

Height Aa:	151.70	mm
Height Bb:	151.02	mm
Height Cc:	150.47	mm
Height Dd:	151.15	mm
Height Lℓ:	150.43	mm
Diam. ac:	75.41	mm
Diam. m_1m_3:	75.37	mm
Diam. AC:	75.39	mm
Diam. bd:	75.44	mm
Diam. m_2m_4:	75.37	mm
Diam. BD:	75.36	mm

Guide Marks

1- Mark points e_1 & e_3 at a distance of 51 mm (2 in) from bottom of cylinder

2- Mark points m_1, m_2, m_3, m_4 at the a distance of 76 mm (3 in) from bottom of cylinder

3- Mark points e_2 & e_4 at a diatance of 102 mm (4 in) from bottom of cylinder

Geometric Comments:

Cylinder Compression Response Test Protocol

BAVIII	**Batch**	**Specimen ID**	U5

Geometry & Weight:

Name: Tommy

Date: 2/10/14 Time: 4:51

Nominal Dimensions: 76 × 152 (2 × 6) mm (in) **Weight:** 1.77 Kg

Out-of-Plane Angle:

Dial gage reading at a:	0.4055	in
Dial gage reading at ℓ:	0.3606	in
Top distance aℓ:	2.9380	in
Distance a - ℓ:	0.0449	in

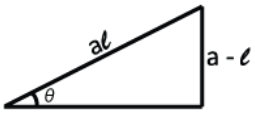

Angle θ 0.876 °

Actual Dimensions:

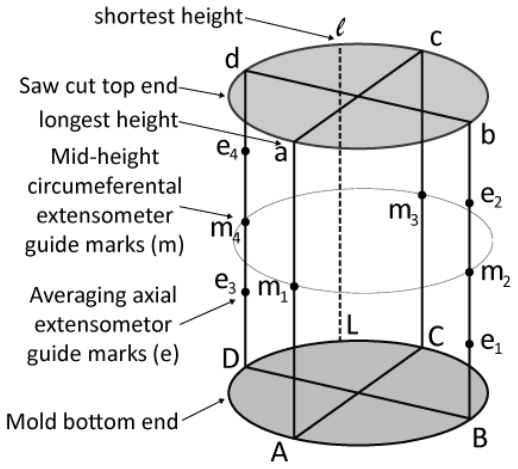

Height Aa:	151.37	mm
Height Bb:	150.70	mm
Height Cc:	150.15	mm
Height Dd:	150.88	mm
Height Lℓ:	150.09	mm
Diam. ac:	75.31	mm
Diam. m_1m_3:	75.29	mm
Diam. AC:	75.31	mm
Diam. bd:	75.27	mm
Diam. m_2m_4:	75.26	mm
Diam. BD:	75.33	mm

Guide Marks

1- Mark points e_1 & e_3 at a distance of 51 mm (2 in) from bottom of cylinder

2- Mark points m_1, m_2, m_3, m_4 at the a distance of 76 mm (3 in) from bottom of cylinder

3- Mark points e_2 & e_4 at a diatance of 102 mm (4 in) from bottom of cylinder

Geometric Comments:

Cylinder Compression Response Test Protocol

BAVIII	**Batch**	**Specimen ID**	U7

Geometry & Weight:

Name: Tommy

Date: 2/10/14 Time: 4:51

Nominal Dimensions: 76 × 152 (2 × 6) mm (in) **Weight:** 1.77 Kg

Out-of-Plane Angle:

Dial gage reading at a:	0.4179	in		
Dial gage reading at ℓ:	0.3785	in		
Top distance aℓ:	2.9320	in		
Distance a - ℓ:	0.0394	in	Angle θ	0.770 °

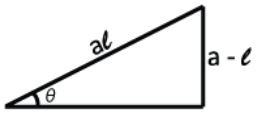

Actual Dimensions:

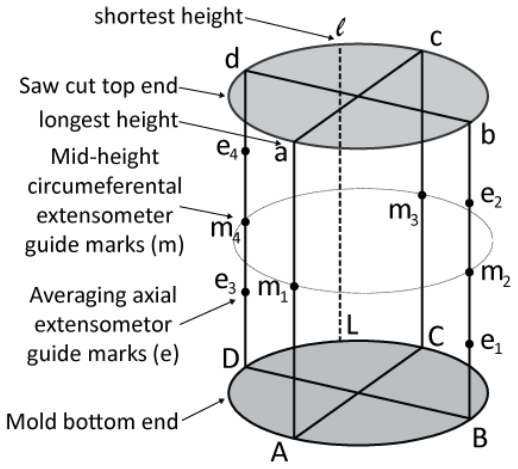

Height Aa:	151.56	mm
Height Bb:	150.76	mm
Height Cc:	150.48	mm
Height Dd:	150.97	mm
Height Lℓ:	150.46	mm
Diam. ac:	75.34	mm
Diam. m_1m_3:	75.27	mm
Diam. AC:	75.25	mm
Diam. bd:	75.25	mm
Diam. m_2m_4:	75.25	mm
Diam. BD:	75.25	mm

Guide Marks

1- Mark points e_1 & e_3 at a distance of 51 mm (2 in) from bottom of cylinder

2- Mark points m_1, m_2, m_3, m_4 at the a distance of 76 mm (3 in) from bottom of cylinder

3- Mark points e_2 & e_4 at a diatance of 102 mm (4 in) from bottom of cylinder

Geometric Comments:

Cylinder Compression Response Test Protocol

BAVIII	**Batch**	**Specimen ID**	U8

Geometry & Weight:

Name: Tommy

Date: 2/10/14 Time: 4:52

Nominal Dimensions: 76 × 152 (2 × 6) mm (in) **Weight:** 1.77 Kg

Out-of-Plane Angle:

Dial gage reading at a:	0.3905	in
Dial gage reading at ℓ:	0.3528	in
Top distance aℓ:	2.9030	in
Distance a - ℓ:	0.0377	in

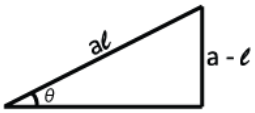

Angle θ 0.744 °

Actual Dimensions:

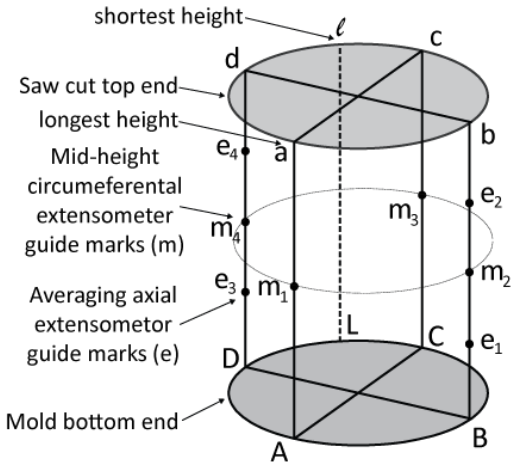

Height Aa:	150.71	mm
Height Bb:	150.41	mm
Height Cc:	149.88	mm
Height Dd:	150.23	mm
Height Lℓ:	149.80	mm
Diam. ac:	75.44	mm
Diam. m_1m_3:	75.46	mm
Diam. AC:	75.39	mm
Diam. bd:	75.14	mm
Diam. m_2m_4:	75.42	mm
Diam. BD:	75.41	mm

Guide Marks

1- Mark points e_1 & e_3 at a distance of 51 mm (2 in) from bottom of cylinder

2- Mark points m_1, m_2, m_3, m_4 at the a distance of 76 mm (3 in) from bottom of cylinder

3- Mark points e_2 & e_4 at a diatance of 102 mm (4 in) from bottom of cylinder

Geometric Comments:

Cylinder Compression Response Test Protocol

BAVIII	**Batch**	**Specimen ID**	U10

Geometry & Weight:

Name: Tommy

Date: 2/10/14 Time: 4:55

Nominal Dimensions: 76 × 152 (2 × 6) mm (in) **Weight:** 1.78 Kg

Out-of-Plane Angle:

Dial gage reading at a:	0.4118	in		
Dial gage reading at ℓ:	0.3916	in		
Top distance aℓ:	2.6750	in		
Distance a - ℓ:	0.0202	in	Angle θ	0.433 °

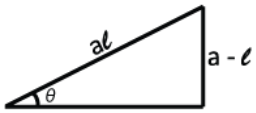

Actual Dimensions:

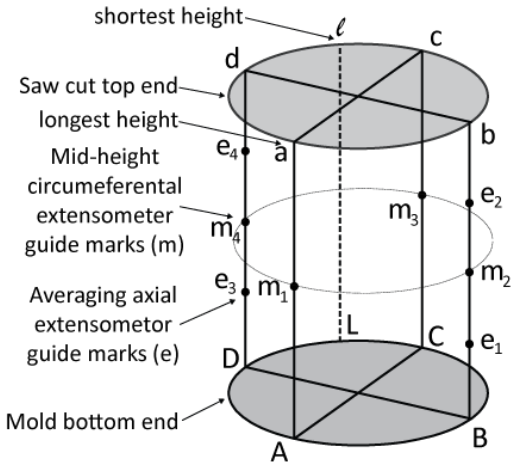

Height Aa:	151.91	mm
Height Bb:	151.40	mm
Height Cc:	151.33	mm
Height Dd:	151.74	mm
Height Lℓ:	151.26	mm
Diam. ac:	75.23	mm
Diam. m_1m_3:	75.25	mm
Diam. AC:	75.21	mm
Diam. bd:	75.15	mm
Diam. m_2m_4:	75.23	mm
Diam. BD:	75.21	mm

Guide Marks

1- Mark points e_1 & e_3 at a distance of 51 mm (2 in) from bottom of cylinder

2- Mark points m_1, m_2, m_3, m_4 at the a distance of 76 mm (3 in) from bottom of cylinder

3- Mark points e_2 & e_4 at a diatance of 102 mm (4 in) from bottom of cylinder

Geometric Comments:

Cylinder Compression Response Test Protocol

BAVIII	**Batch**	**Specimen ID**	U13

Geometry & Weight:

Name: Tommy

Date: 2/10/14 Time: 4:56

Nominal Dimensions: 76 × 152 (2 × 6) mm (in) **Weight:** 1.78 Kg

Out-of-Plane Angle:

Dial gage reading at a:	0.4052	in
Dial gage reading at ℓ:	0.3758	in
Top distance aℓ:	2.9530	in
Distance a - ℓ:	0.0294	in

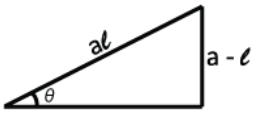

Angle θ 0.570 °

Actual Dimensions:

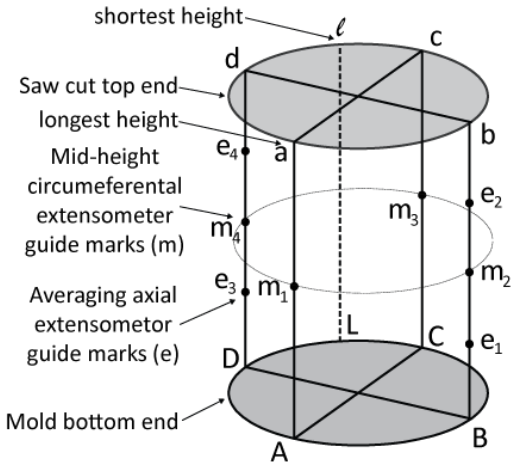

Height Aa:	151.92	mm
Height Bb:	151.56	mm
Height Cc:	151.25	mm
Height Dd:	151.67	mm
Height Lℓ:	151.17	mm
Diam. ac:	75.33	mm
Diam. m_1m_3:	75.33	mm
Diam. AC:	75.37	mm
Diam. bd:	75.34	mm
Diam. m_2m_4:	75.29	mm
Diam. BD:	75.38	mm

Guide Marks

1- Mark points e_1 & e_3 at a distance of 51 mm (2 in) from bottom of cylinder

2- Mark points m_1, m_2, m_3, m_4 at the a distance of 76 mm (3 in) from bottom of cylinder

3- Mark points e_2 & e_4 at a diatance of 102 mm (4 in) from bottom of cylinder

Geometric Comments:

Cylinder Compression Response Test Protocol

BAVIII	**Batch**	**Specimen ID**	U14

Geometry & Weight:

Name: Tommy

Date: 2/10/14 Time: 4:56

Nominal Dimensions: 76 × 152 (2 × 6) mm (in) **Weight:** 1.78 Kg

Out-of-Plane Angle:

Dial gage reading at a:	0.3961	in
Dial gage reading at ℓ:	0.3622	in
Top distance aℓ:	2.9610	in
Distance a - ℓ:	0.0339	in

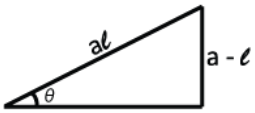

Angle θ 0.656 °

Actual Dimensions:

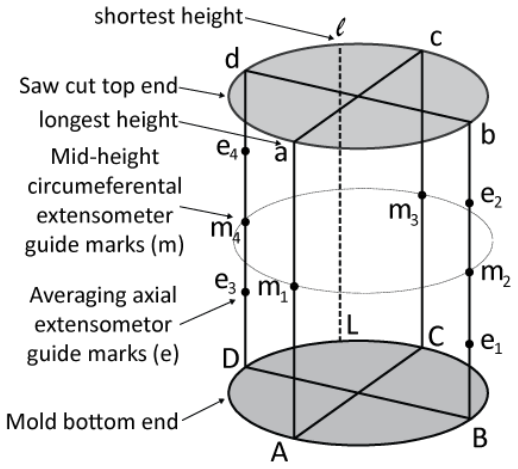

Height Aa:	151.69	mm
Height Bb:	151.28	mm
Height Cc:	150.85	mm
Height Dd:	151.33	mm
Height Lℓ:	150.85	mm
Diam. ac:	75.35	mm
Diam. m_1m_3:	75.34	mm
Diam. AC:	75.37	mm
Diam. bd:	75.29	mm
Diam. m_2m_4:	75.31	mm
Diam. BD:	75.36	mm

Guide Marks

1- Mark points e_1 & e_3 at a distance of 51 mm (2 in) from bottom of cylinder

2- Mark points m_1, m_2, m_3, m_4 at the a distance of 76 mm (3 in) from bottom of cylinder

3- Mark points e_2 & e_4 at a diatance of 102 mm (4 in) from bottom of cylinder

Geometric Comments:

Specimen has a uneven surface at the edge (bump)

Appendix C

UHPC Fracture Beams Experimental Data Sheets

Fracture Toughness Test Protocol

BAI	**Batch**	**Specimen**	B1

Geometry:

Name: Rachel Gordon

Date: 12/3/13 Time: 5:03PM

Nominal Dimensions:

Prism: 51×102×457 (2×4×18) mm (in) Notch: 25×4.76 (1×3/16) mm (in)

Actual Dimensions: Note: Use uncut side of the beam for AakK.

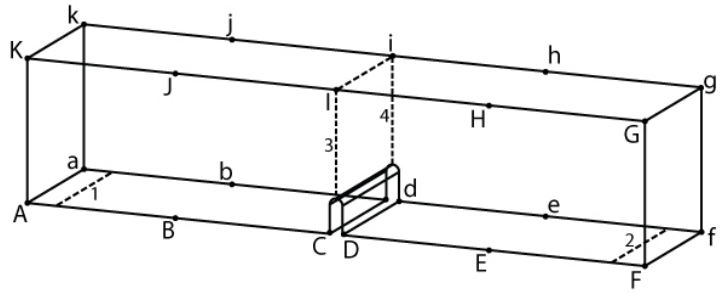

Length AC:	225.60	mm	Width CD:	5.63	mm
Length ac:	225.58	mm	Width cd:	5.62	mm
Length DF:	225.20	mm			
Length df:	225.00	mm			
Length KG:	455.61	mm			
Length kg:	455.61	mm			

Outer Marks

1- Mark points B, b, J, & j at 114.20 mm from point A, a, K, & k respectively.

2- Mark line Ii at 228.40 mm from line Kk.

3- Mark points E, E, H& h at 339.30 mm from point A, a, K, & k respectively.

			Width Aa:	50.90	mm
Height AK:	100.79	mm	Width Bb:	50.78	mm
Height BJ:	100.94	mm	Width Cc:	50.88	mm
Height EH:	101.24	mm	Width Dd:	50.84	mm
Height FG:	101.23	mm	Width Ee:	50.91	mm
Height ak:	100.45	mm	Width Ff:	51.19	mm
Height bj:	100.56	mm	Width Gg:	51.08	mm
Height eh:	100.76	mm	Width Hh:	50.94	mm
Height fg:	100.81	mm	Width Ii:	50.94	mm
			Width Jj:	50.80	mm
			Width Kk:	50.99	mm

Guide Marks

4- Center plexiglass with line 3 & 4 and draw lines 1 & 2.

5- Mark the plane of lines 1 & 2

Width 1:	50.84	mm	Width 2:	51.13	mm
Height 3:	74.92	mm	Height 4:	75.13	mm

Geometric Comments:

Fracture Toughness Test Protocol

BAI	**Batch**	**Specimen**	B2

Geometry:

Name: Rachel Gordon

Date: 12/3/13 Time: 5:03PM

Nominal Dimensions:

Prism: 51×102×457 (2×4×18) mm (in) Notch: 25×4.76 (1×3/16) mm (in)

Actual Dimensions: Note: Use uncut side of the beam for AakK.

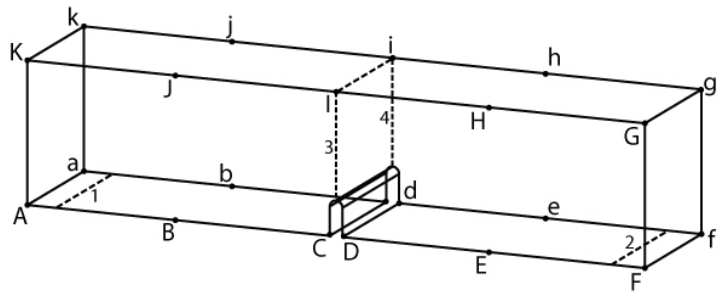

Length AC:	225.08	mm	Width CD:	5.89	mm
Length ac:	225.31	mm	Width cd:	5.71	mm
Length DF:	226.44	mm			
Length df:	225.50	mm			
Length KG:	457.20	mm			
Length kg:	455.61	mm			

Outer Marks

1- Mark points B, b, J, & j at 114.05 mm from point A, a, K, & k respectively.

2- Mark line Ii at 228.10 mm from line Kk.

3- Mark points E, E, H& h at 340.02 mm from point A, a, K, & k respectively.

			Width Aa:	51.41	mm
Height AK:	101.48	mm	Width Bb:	51.13	mm
Height BJ:	101.67	mm	Width Cc:	51.02	mm
Height EH:	101.70	mm	Width Dd:	50.94	mm
Height FG:	101.81	mm	Width Ee:	50.94	mm
Height ak:	101.22	mm	Width Ff:	50.88	mm
Height bj:	101.48	mm	Width Gg:	50.98	mm
Height eh:	101.47	mm	Width Hh:	50.81	mm
Height fg:	101.82	mm	Width Ii:	50.86	mm
			Width Jj:	51.06	mm
			Width Kk:	51.27	mm

Guide Marks

4- Center plexiglass with line 3 & 4 and draw lines 1 & 2.

5- Mark the plane of lines 1 & 2

Width 1:	51.33	mm	Width 2:	50.91	mm
Height 3:	75.77	mm	Height 4:	75.68	mm

Geometric Comments:

Preexisting cracks

Fracture Toughness Test Protocol

BAI	**Batch**	**Specimen**	B4

Geometry:

Name: Rachel Gordon

Date: 12/3/13 Time: 5:03PM

Nominal Dimensions:

Prism: 51×102×457 (2×4×18) mm (in) Notch: 25×4.76 (1×3/16) mm (in)

Actual Dimensions: Note: Use uncut side of the beam for AakK.

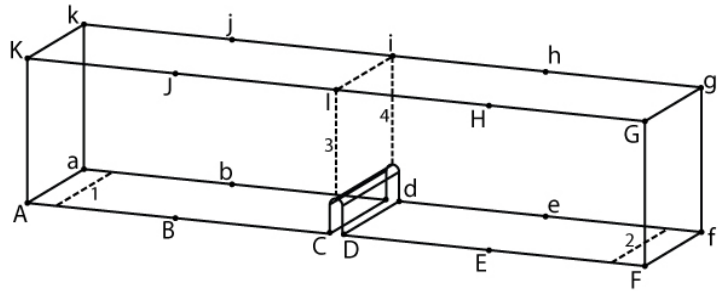

Length AC:	226.61	mm	Width CD:	5.51	mm
Length ac:	226.24	mm	Width cd:	5.86	mm
Length DF:	225.70	mm			
Length df:	225.15	mm			
Length KG:	457.20	mm			
Length kg:	455.61	mm			

Outer Marks

1- Mark points B, b, J, & j at 114.63 mm from point A, a, K, & k respectively.

2- Mark line Ii at 229.27 mm from line Kk.

3- Mark points E, E, H& h at 340.06 mm from point A, a, K, & k respectively.

			Width Aa:	50.88	mm
Height AK:	101.79	mm	Width Bb:	50.95	mm
Height BJ:	101.68	mm	Width Cc:	51.04	mm
Height EH:	101.93	mm	Width Dd:	50.98	mm
Height FG:	101.85	mm	Width Ee:	50.89	mm
Height ak:	101.93	mm	Width Ff:	50.90	mm
Height bj:	101.67	mm	Width Gg:	51.15	mm
Height eh:	101.94	mm	Width Hh:	51.09	mm
Height fg:	101.86	mm	Width Ii:	50.97	mm
			Width Jj:	50.98	mm
			Width Kk:	50.72	mm

Guide Marks

4- Center plexiglass with line 3 & 4 and draw lines 1 & 2.

5- Mark the plane of lines 1 & 2

Width 1:	50.94	mm	Width 2:	50.88	mm
Height 3:	75.96	mm	Height 4:	75.32	mm

Geometric Comments:

Preexisting cracks

Fracture Toughness Test Protocol

BAI	**Batch**	**Specimen**	B5

Geometry:

Name: Rachel Gordon

Date: 12/3/13 Time: 5:03PM

Nominal Dimensions:

Prism: 51×102×457 (2×4×18) mm (in) Notch: 25×4.76 (1×3/16) mm (in)

Actual Dimensions: Note: Use uncut side of the beam for AakK.

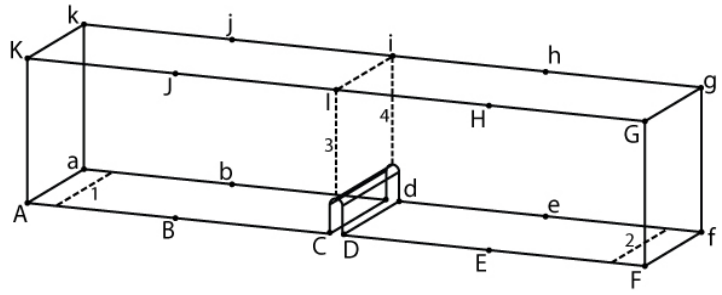

Length AC:	225.00 mm	Width CD:	5.88 mm
Length ac:	224.78 mm	Width cd:	5.50 mm
Length DF:	225.52 mm		
Length df:	225.71 mm		
Length KG:	455.61 mm		
Length kg:	455.61 mm		

Outer Marks

1- Mark points B, b, J, & j at 113.87 mm from point A, a, K, & k respectively.

2- Mark line Ii at 227.74 mm from line Kk.

3- Mark points E, E, H& h at 339.48 mm from point A, a, K, & k respectively.

		Width Aa:	50.96 mm
Height AK:	98.85 mm	Width Bb:	50.70 mm
Height BJ:	100.31 mm	Width Cc:	50.72 mm
Height EH:	101.64 mm	Width Dd:	51.00 mm
Height FG:	101.74 mm	Width Ee:	50.71 mm
Height ak:	98.53 mm	Width Ff:	50.80 mm
Height bj:	99.98 mm	Width Gg:	51.24 mm
Height eh:	101.28 mm	Width Hh:	51.14 mm
Height fg:	101.28 mm	Width Ii:	51.07 mm
		Width Jj:	51.11 mm
		Width Kk:	51.23 mm

Guide Marks

4- Center plexiglass with line 3 & 4 and draw lines 1 & 2.

5- Mark the plane of lines 1 & 2

Width 1:	50.90 mm	Width 2:	50.79 mm
Height 3:	75.11 mm	Height 4:	76.22 mm

Geometric Comments:

Preexisting cracks

Fracture Toughness Test Protocol

BAI	**Batch**	**Specimen**	B6

Geometry:

Name: Rachel Gordon

Date: 12/3/13 Time: 5:03PM

Nominal Dimensions:

Prism: 51×102×457 (2×4×18) mm (in) Notch: 25×4.76 (1×3/16) mm (in)

Actual Dimensions: Note: Use uncut side of the beam for AakK.

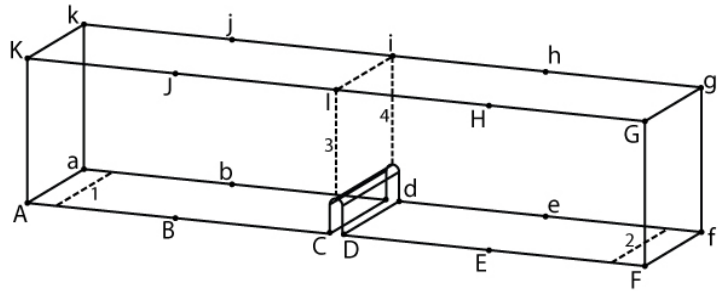

Length AC:	223.36	mm	Width CD:	5.48	mm
Length ac:	225.31	mm	Width cd:	5.66	mm
Length DF:	222.89	mm			
Length df:	223.89	mm			
Length KG:	454.03	mm			
Length kg:	455.61	mm			

Outer Marks

1- Mark points B, b, J, & j at 113.56 mm from point A, a, K, & k respectively.

2- Mark line Ii at 227.12 mm from line Kk.

3- Mark points E, E, H& h at 336.95 mm from point A, a, K, & k respectively.

			Width Aa:	51.51	mm
Height AK:	101.50	mm	Width Bb:	51.66	mm
Height BJ:	101.54	mm	Width Cc:	51.94	mm
Height EH:	101.47	mm	Width Dd:	51.99	mm
Height FG:	101.20	mm	Width Ee:	52.34	mm
Height ak:	100.99	mm	Width Ff:	52.41	mm
Height bj:	101.15	mm	Width Gg:	54.67	mm
Height eh:	101.11	mm	Width Hh:	54.64	mm
Height fg:	100.95	mm	Width Ii:	54.12	mm
			Width Jj:	53.75	mm
			Width Kk:	53.46	mm

Guide Marks

4- Center plexiglass with line 3 & 4 and draw lines 1 & 2.

5- Mark the plane of lines 1 & 2

Width 1:	51.62	mm	Width 2:	52.67	mm
Height 3:	75.90	mm	Height 4:	75.36	mm

Geometric Comments:

Preexisting cracks

Beam is badly uneven

Fracture Toughness Test Protocol

BAII	**Batch**	**Specimen**	B1

Geometry:

Date: 1/28/14 Name: Tommy Time: 2:50PM

Nominal Dimensions:

Prism: 51×102×457 (2×4×18) mm (in) Notch: 25×4.76 (1×3/16) mm (in)

Actual Dimensions: Note: Use uncut side of the beam for AakK.

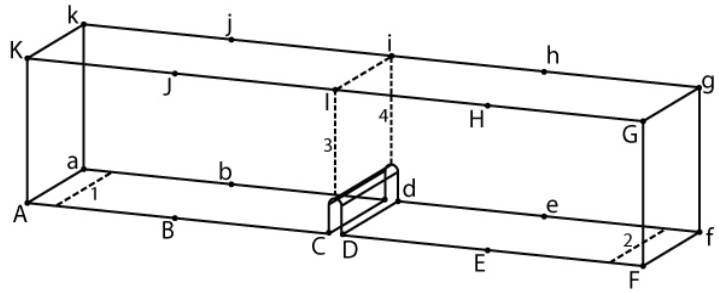

Length AC:	225.72	mm	Width CD:	5.66	mm
Length ac:	226.64	mm	Width cd:	5.90	mm
Length DF:	227.53	mm			
Length df:	226.85	mm			
Length KG:	458.79	mm			
Length kg:	457.99	mm			

Outer Marks

1- Mark points B, b, J, & j at 114.54 mm from point A, a, K, & k respectively.

2- Mark line Ii at 229.07 mm from line Kk.

3- Mark points E, E, H& h at 341.73 mm from point A, a, K, & k respectively.

			Width Aa:	50.90	mm
Height AK:	104.08	mm	Width Bb:	50.83	mm
Height BJ:	103.37	mm	Width Cc:	50.92	mm
Height EH:	101.44	mm	Width Dd:	50.92	mm
Height FG:	100.03	mm	Width Ee:	51.07	mm
Height ak:	103.82	mm	Width Ff:	51.24	mm
Height bj:	103.18	mm	Width Gg:	51.33	mm
Height eh:	101.45	mm	Width Hh:	51.12	mm
Height fg:	100.42	mm	Width Ii:	51.03	mm
			Width Jj:	50.90	mm

Guide Marks

			Width Kk:	51.01	mm

4- Center plexiglass with line 3 & 4 and draw lines 1 & 2.

5- Mark the plane of lines 1 & 2

Width 1:	50.93	mm	Width 2:	51.16	mm
Height 3:	75.19	mm	Height 4:	74.96	mm

Geometric Comments:

Fracture Toughness Test Protocol

BAII	**Batch**	**Specimen**	B2

Geometry:

Date: 1/28/14 Name: Tommy Time: 2:50PM

Nominal Dimensions:

Prism: 51×102×457 (2×4×18) mm (in) Notch: 25×4.76 (1×3/16) mm (in)

Actual Dimensions: Note: Use uncut side of the beam for AakK.

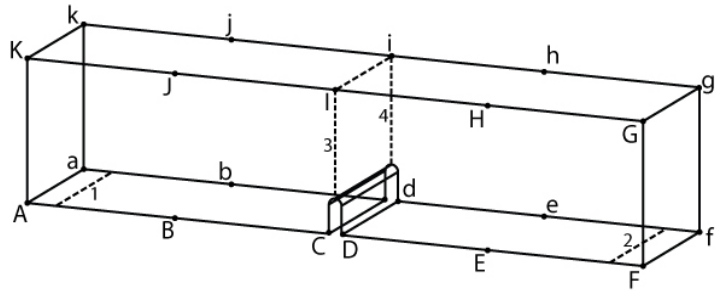

Length AC:	226.25	mm	Width CD:	5.72	mm
Length ac:	226.33	mm	Width cd:	5.62	mm
Length DF:	227.53	mm			
Length df:	227.66	mm			
Length KG:	458.82	mm			
Length kg:	458.79	mm			

Outer Marks

1- Mark points B, b, J, & j at 114.56 mm from point A, a, K, & k respectively.

2- Mark line Ii at 229.13 mm from line Kk.

3- Mark points E, E, H& h at 342.16 mm from point A, a, K, & k respectively.

			Width Aa:	51.39	mm
Height AK:	100.49	mm	Width Bb:	51.14	mm
Height BJ:	101.37	mm	Width Cc:	50.97	mm
Height EH:	103.00	mm	Width Dd:	50.97	mm
Height FG:	103.74	mm	Width Ee:	50.85	mm
Height ak:	100.27	mm	Width Ff:	50.84	mm
Height bj:	101.08	mm	Width Gg:	50.82	mm
Height eh:	102.74	mm	Width Hh:	50.82	mm
Height fg:	103.66	mm	Width Ii:	50.89	mm
			Width Jj:	51.01	mm
			Width Kk:	51.17	mm

Guide Marks

4- Center plexiglass with line 3 & 4 and draw lines 1 & 2.

5- Mark the plane of lines 1 & 2

Width 1:	51.42	mm	Width 2:	50.86	mm
Height 3:	74.98	mm	Height 4:	75.29	mm

Geometric Comments:

Fracture Toughness Test Protocol

BAII	**Batch**	**Specimen**	B3

Geometry:

Name: Tommy

Date: 1/28/14 Time: 2:50 PM

Nominal Dimensions:

Prism: 51×102×457 (2×4×18) mm (in) Notch: 25×4.76 (1×3/16) mm (in)

Actual Dimensions: Note: Use uncut side of the beam for AakK.

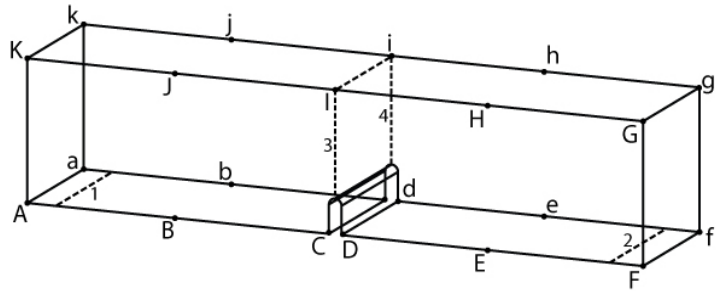

Length AC:	227.67	mm	Width CD:	5.76	mm
Length ac:	227.63	mm	Width cd:	5.59	mm
Length DF:	227.01	mm			
Length df:	226.99	mm			
Length KG:	458.79	mm			
Length kg:	458.79	mm			

Outer Marks

1- Mark points B, b, J, & j at 115.24 mm from point A, a, K, & k respectively.

2- Mark line Ii at 230.49 mm from line Kk.

3- Mark points E, E, H& h at 342.24 mm from point A, a, K, & k respectively.

			Width Aa:	50.77	mm
Height AK:	100.44	mm	Width Bb:	50.77	mm
Height BJ:	100.84	mm	Width Cc:	50.89	mm
Height EH:	101.59	mm	Width Dd:	50.91	mm
Height FG:	101.58	mm	Width Ee:	50.85	mm
Height ak:	100.48	mm	Width Ff:	51.12	mm
Height bj:	100.80	mm	Width Gg:	51.15	mm
Height eh:	101.45	mm	Width Hh:	51.00	mm
Height fg:	101.43	mm	Width Ii:	50.87	mm
			Width Jj:	50.74	mm
			Width Kk:	50.59	mm

Guide Marks

4- Center plexiglass with line 3 & 4 and draw lines 1 & 2.

5- Mark the plane of lines 1 & 2

Width 1:	50.80	mm	Width 2:	51.01	mm
Height 3:	75.01	mm	Height 4:	75.27	mm

Geometric Comments:

Fracture Toughness Test Protocol

BAII	**Batch**	**Specimen**	B4

Geometry:

Date: 1/28/14 Name: Tommy Time: 2:50PM

Nominal Dimensions:

Prism: 51×102×457 (2×4×18) mm (in) Notch: 25×4.76 (1×3/16) mm (in)

Actual Dimensions: Note: Use uncut side of the beam for AakK.

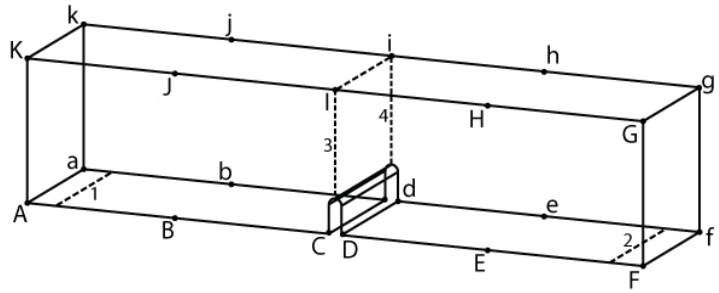

Length AC:	225.17	mm	Width CD:	5.82	mm
Length ac:	225.30	mm	Width cd:	5.55	mm
Length DF:	226.51	mm			
Length df:	226.84	mm			
Length KG:	456.41	mm			
Length kg:	457.20	mm			

Outer Marks

1- Mark points B, b, J, & j at 114.04 mm from point A, a, K, & k respectively.

2- Mark line Ii at 228.08 mm from line Kk.

3- Mark points E, E, H& h at 340.71 mm from point A, a, K, & k respectively.

			Width Aa:	50.97	mm
Height AK:	101.17	mm	Width Bb:	50.95	mm
Height BJ:	101.42	mm	Width Cc:	50.84	mm
Height EH:	101.71	mm	Width Dd:	50.83	mm
Height FG:	101.97	mm	Width Ee:	50.84	mm
Height ak:	101.27	mm	Width Ff:	50.90	mm
Height bj:	101.44	mm	Width Gg:	51.00	mm
Height eh:	101.66	mm	Width Hh:	51.12	mm
Height fg:	101.95	mm	Width Ii:	51.11	mm
			Width Jj:	51.13	mm
			Width Kk:	51.18	mm

Guide Marks

4- Center plexiglass with line 3 & 4 and draw lines 1 & 2.

5- Mark the plane of lines 1 & 2

Width 1:	50.99	mm	Width 2:	50.89	mm
Height 3:	74.81	mm	Height 4:	75.36	mm

Geometric Comments:

Fracture Toughness Test Protocol

BAII	**Batch**	**Specimen**	B5

Geometry:

Date: 1/28/14

Name: Tommy

Time: 2:50PM

Nominal Dimensions:

Prism: 51×102×457 (2×4×18) mm (in)

Notch: 25×4.76 (1×3/16) mm (in)

Actual Dimensions: Note: Use uncut side of the beam for AakK.

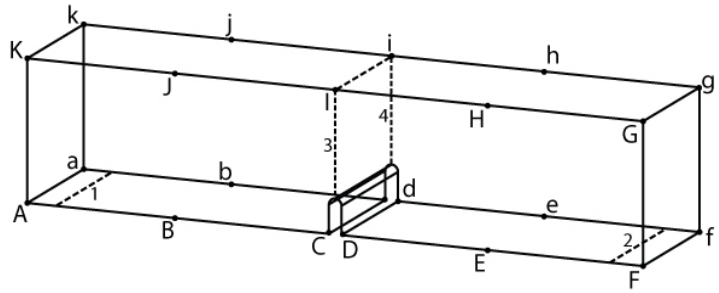

Length AC:	225.88	mm	Width CD:	5.82	mm
Length ac:	225.74	mm	Width cd:	5.64	mm
Length DF:	226.52	mm			
Length df:	226.84	mm			
Length KG:	457.20	mm			
Length kg:	457.99	mm			

Outer Marks

1- Mark points B, b, J, & j at 114.34 mm from point A, a, K, & k respectively.

2- Mark line Ii at 228.68 mm from line Kk.

3- Mark points E, E, H& h at 341.02 mm from point A, a, K, & k respectively.

			Width Aa:	50.96	mm
Height AK:	98.71	mm	Width Bb:	50.71	mm
Height BJ:	100.40	mm	Width Cc:	50.74	mm
Height EH:	102.18	mm	Width Dd:	50.73	mm
Height FG:	102.01	mm	Width Ee:	50.69	mm
Height ak:	98.80	mm	Width Ff:	50.80	mm
Height bj:	100.63	mm	Width Gg:	51.19	mm
Height eh:	102.31	mm	Width Hh:	51.04	mm
Height fg:	102.32	mm	Width Ii:	51.08	mm
			Width Jj:	51.25	mm
			Width Kk:	51.92	mm

Guide Marks

4- Center plexiglass with line 3 & 4 and draw lines 1 & 2.

5- Mark the plane of lines 1 & 2

Width 1:	50.88	mm	Width 2:	50.71	mm
Height 3:	74.87	mm	Height 4:	75.29	mm

Geometric Comments:

Fracture Toughness Test Protocol

BAII	**Batch**	**Specimen**	B6

Geometry:

Name: Rachel & Tommy

Date: 12/12/13 Time: 5:11PM

Nominal Dimensions:

Prism: 51×102×457 (2×4×18) mm (in) Notch: 25×4.76 (1×3/16) mm (in)

Actual Dimensions: Note: Use uncut side of the beam for AakK.

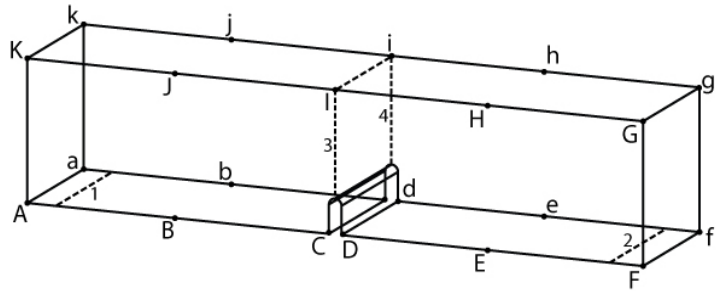

Length AC:	228.41	mm	Width CD:	5.67	mm
Length ac:	227.97	mm	Width cd:	5.49	mm
Length DF:	224.70	mm			
Length df:	226.13	mm			
Length KG:	457.52	mm			
Length kg:	458.15	mm			

Outer Marks

1- Mark points B, b, J, & j at 115.49 mm from point A, a, K, & k respectively.

2- Mark line Ii at 230.98 mm from line Kk.

3- Mark points E, E, H& h at 340.91 mm from point A, a, K, & k respectively.

			Width Aa:	52.41	mm
Height AK:	101.18	mm	Width Bb:	51.88	mm
Height BJ:	101.33	mm	Width Cc:	52.12	mm
Height EH:	101.00	mm	Width Dd:	52.24	mm
Height FG:	100.91	mm	Width Ee:	52.28	mm
Height ak:	100.62	mm	Width Ff:	52.36	mm
Height bj:	100.99	mm	Width Gg:	52.95	mm
Height eh:	101.14	mm	Width Hh:	53.19	mm
Height fg:	101.21	mm	Width Ii:	53.14	mm
			Width Jj:	52.93	mm
			Width Kk:	53.02	mm

Guide Marks

4- Center plexiglass with line 3 & 4 and draw lines 1 & 2.

5- Mark the plane of lines 1 & 2

Width 1:	51.94	mm	Width 2:	52.24	mm
Height 3:	74.88	mm	Height 4:	75.36	mm

Geometric Comments:

Messed up the lettering but it's right now

Fracture Toughness Test Protocol

BAIV	**Batch**	**Specimen**	B1

Geometry:

Name: Rachel Gordon

Date: 12/12/13 Time: 5:46PM

Nominal Dimensions:

Prism: 51×102×457 (2×4×18) mm (in) Notch: 25×4.76 (1×3/16) mm (in)

Actual Dimensions: Note: Use uncut side of the beam for AakK.

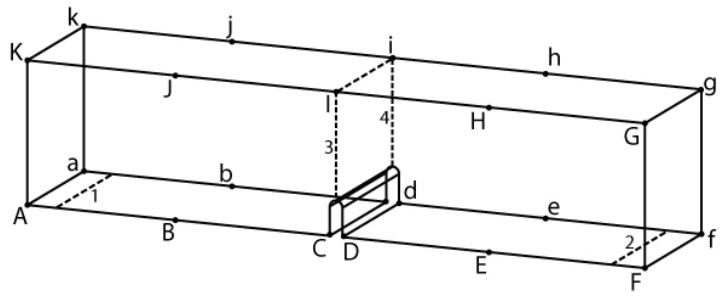

Length AC:	226.64	mm	Width CD:	5.42	mm
Length ac:	226.67	mm	Width cd:	5.82	mm
Length DF:	228.05	mm			
Length df:	226.33	mm			
Length KG:	458.79	mm			
Length kg:	458.63	mm			

Outer Marks

1- Mark points B, b, J, & j at 114.73 mm from point A, a, K, & k respectively.

2- Mark line Ii at 229.47 mm from line Kk.

3- Mark points E, E, H& h at 341.92 mm from point A, a, K, & k respectively.

			Width Aa:	51.48	mm
Height AK:	102.54	mm	Width Bb:	51.12	mm
Height BJ:	102.11	mm	Width Cc:	50.89	mm
Height EH:	101.03	mm	Width Dd:	50.89	mm
Height FG:	100.04	mm	Width Ee:	50.82	mm
Height ak:	102.04	mm	Width Ff:	51.20	mm
Height bj:	101.98	mm	Width Gg:	50.91	mm
Height eh:	101.03	mm	Width Hh:	50.75	mm
Height fg:	99.84	mm	Width Ii:	50.79	mm
			Width Jj:	51.06	mm
			Width Kk:	51.30	mm

Guide Marks

4- Center plexiglass with line 3 & 4 and draw lines 1 & 2.

5- Mark the plane of lines 1 & 2

Width 1:	51.33	mm	Width 2:	50.74	mm
Height 3:	75.56	mm	Height 4:	74.85	mm

Geometric Comments:

Fracture Toughness Test Protocol

BAIV	**Batch**	**Specimen**	B2

Geometry:

Name: Rachel Gordon

Date: 12/12/13 Time: 5:39PM

Nominal Dimensions:

Prism: 51×102×457 (2×4×18) mm (in) Notch: 25×4.76 (1×3/16) mm (in)

Actual Dimensions: Note: Use uncut side of the beam for AakK.

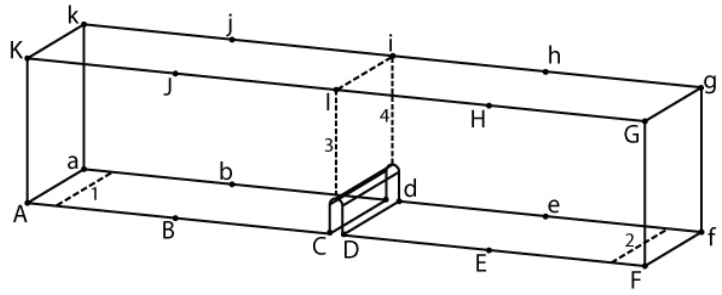

Length AC:	225.07	mm	Width CD:	5.65	mm
Length ac:	225.35	mm	Width cd:	5.83	mm
Length DF:	229.51	mm			
Length df:	228.24	mm			
Length KG:	460.86	mm			
Length kg:	460.53	mm			

Outer Marks

1- Mark points B, b, J, & j at 114.04 mm from point A, a, K, & k respectively.

2- Mark line Ii at 228.08 mm from line Kk.

3- Mark points E, E, H& h at 342.92 mm from point A, a, K, & k respectively.

			Width Aa:	51.47	mm
Height AK:	101.16	mm	Width Bb:	51.30	mm
Height BJ:	101.25	mm	Width Cc:	51.05	mm
Height EH:	101.09	mm	Width Dd:	51.01	mm
Height FG:	101.35	mm	Width Ee:	50.03	mm
Height ak:	101.03	mm	Width Ff:	51.25	mm
Height bj:	101.18	mm	Width Gg:	51.13	mm
Height eh:	100.91	mm	Width Hh:	51.09	mm
Height fg:	101.04	mm	Width Ii:	50.94	mm
			Width Jj:	51.06	mm
			Width Kk:	51.41	mm

Guide Marks

4- Center plexiglass with line 3 & 4 and draw lines 1 & 2.

5- Mark the plane of lines 1 & 2

Width 1:	51.41	mm	Width 2:	50.91	mm
Height 3:	75.01	mm	Height 4:	74.16	mm

Geometric Comments:

Fracture Toughness Test Protocol

BAIV	**Batch**	**Specimen**	B3

Geometry:

Name: Rachel Gordon

Date: 12/12/13 Time: 5:32PM

Nominal Dimensions:

Prism: 51×102×457 (2×4×18) mm (in) Notch: 25×4.76 (1×3/16) mm (in)

Actual Dimensions: Note: Use uncut side of the beam for AakK.

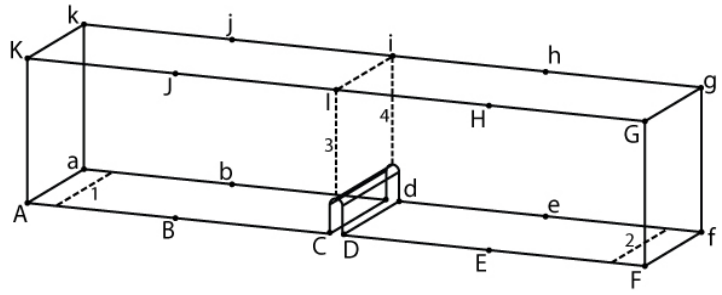

Length AC:	226.35 mm	Width CD:	5.26 mm
Length ac:	226.19 mm	Width cd:	5.92 mm
Length DF:	227.92 mm		
Length df:	226.85 mm		
Length KG:	460.38 mm		
Length kg:	460.22 mm		

Outer Marks

1- Mark points B, b, J, & j at 114.53 mm from point A, a, K, & k respectively.

2- Mark line Ii at 229.07 mm from line Kk.

3- Mark points E, E, H& h at 341.92 mm from point A, a, K, & k respectively.

		Width Aa:	50.85 mm
Height AK:	102.09 mm	Width Bb:	50.80 mm
Height BJ:	102.07 mm	Width Cc:	50.86 mm
Height EH:	101.44 mm	Width Dd:	50.96 mm
Height FG:	100.82 mm	Width Ee:	50.91 mm
Height ak:	102.07 mm	Width Ff:	51.08 mm
Height bj:	101.66 mm	Width Gg:	51.47 mm
Height eh:	101.25 mm	Width Hh:	51.05 mm
Height fg:	100.64 mm	Width Ii:	51.02 mm
		Width Jj:	50.83 mm
		Width Kk:	50.79 mm

Guide Marks

4- Center plexiglass with line 3 & 4 and draw lines 1 & 2.

5- Mark the plane of lines 1 & 2

Width 1:	50.85 mm	Width 2:	51.08 mm
Height 3:	75.50 mm	Height 4:	74.85 mm

Geometric Comments:

Fracture Toughness Test Protocol

BAIV	**Batch**	**Specimen**	B4

Geometry:

Name: Rachel Gordon

Date: 12/12/13 Time: 4:56PM

Nominal Dimensions:

Prism: 51×102×457 (2×4×18) mm (in) Notch: 25×4.76 (1×3/16) mm (in)

Actual Dimensions: Note: Use uncut side of the beam for AakK.

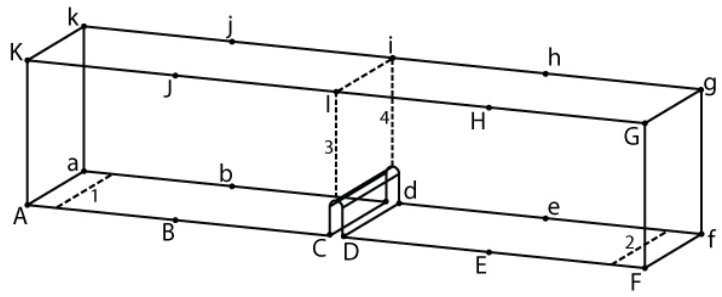

Length AC:	225.70	mm	Width CD:	5.61	mm
Length ac:	225.79	mm	Width cd:	5.85	mm
Length DF:	227.76	mm			
Length df:	226.80	mm			
Length KG:	460.38	mm			
Length kg:	460.07	mm			

Outer Marks

1- Mark points B, b, J, & j at 114.31 mm from point A, a, K, & k respectively.

2- Mark line Ii at 228.61 mm from line Kk.

3- Mark points E, E, H& h at 341.59 mm from point A, a, K, & k respectively.

			Width Aa:	51.05	mm
Height AK:	101.42	mm	Width Bb:	50.96	mm
Height BJ:	102.46	mm	Width Cc:	50.92	mm
Height EH:	102.20	mm	Width Dd:	51.02	mm
Height FG:	101.21	mm	Width Ee:	50.90	mm
Height ak:	101.56	mm	Width Ff:	51.08	mm
Height bj:	101.45	mm	Width Gg:	50.90	mm
Height eh:	101.24	mm	Width Hh:	51.02	mm
Height fg:	100.70	mm	Width Ii:	51.03	mm
			Width Jj:	51.17	mm
			Width Kk:	51.23	mm

Guide Marks

4- Center plexiglass with line 3 & 4 and draw lines 1 & 2.

5- Mark the plane of lines 1 & 2

Width 1:	51.08	mm	Width 2:	50.94	mm
Height 3:	75.57	mm	Height 4:	74.90	mm

Geometric Comments:

Fracture Toughness Test Protocol

BAIV	**Batch**	**Specimen**	B6

Geometry:

Name: Tommy

Date: 2/6/14 Time: 2:33PM

Nominal Dimensions:

Prism: 51×102×457 (2×4×18) mm (in) Notch: 25×4.76 (1×3/16) mm (in)

Actual Dimensions: Note: Use uncut side of the beam for AakK.

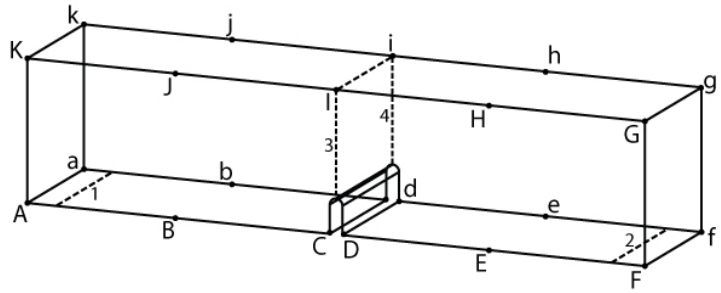

Length AC:	225.45	mm	Width CD:	5.39	mm
Length ac:	225.22	mm	Width cd:	5.91	mm
Length DF:	229.80	mm			
Length df:	228.64	mm			
Length KG:	461.96	mm			
Length kg:	461.95	mm			

Outer Marks

1- Mark points B, b, J, & j at 114.08 mm from point A, a, K, & k respectively.

2- Mark line Ii at 228.16 mm from line Kk.

3- Mark points E, E, H& h at 343.30 mm from point A, a, K, & k respectively.

			Width Aa:	52.60	mm
Height AK:	102.10	mm	Width Bb:	51.70	mm
Height BJ:	101.94	mm	Width Cc:	51.65	mm
Height EH:	101.63	mm	Width Dd:	51.80	mm
Height FG:	101.55	mm	Width Ee:	51.83	mm
Height ak:	100.68	mm	Width Ff:	51.89	mm
Height bj:	100.76	mm	Width Gg:	53.15	mm
Height eh:	101.06	mm	Width Hh:	53.14	mm
Height fg:	100.96	mm	Width Ii:	53.13	mm
			Width Jj:	52.96	mm
Guide Marks			Width Kk:	53.17	mm

4- Center plexiglass with line 3 & 4 and draw lines 1 & 2.

5- Mark the plane of lines 1 & 2

Width 1:	51.79	mm	Width 2:	51.77	mm
Height 3:	75.66	mm	Height 4:	74.90	mm

Geometric Comments:

Fracture Toughness Test Protocol

BAV	**Batch**	**Specimen**	B1

Geometry:

Name: Rachel Gordon

Date: 2/3/13 Time: 3:4000 PM

Nominal Dimensions:

Prism: 51×102×457 (2×4×18) mm (in) Notch: 25×4.76 (1×3/16) mm (in)

Actual Dimensions: Note: Use uncut side of the beam for AakK.

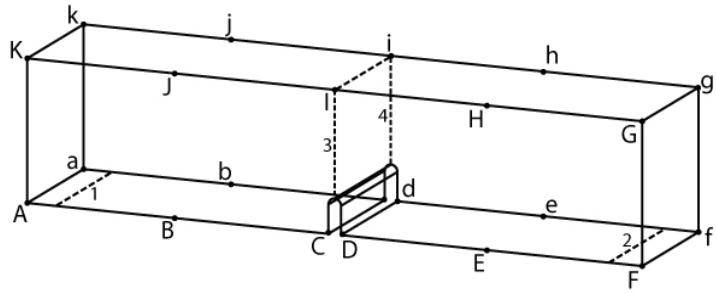

Length AC:	227.19	mm	Width CD:	5.53	mm
Length ac:	226.77	mm	Width cd:	6.15	mm
Length DF:	223.12	mm			
Length df:	223.32	mm			
Length KG:	455.61	mm			
Length kg:	457.20	mm			

Outer Marks

1- Mark points B, b, J, & j at 114.95 mm from point A, a, K, & k respectively.

2- Mark line Ii at 229.90 mm from line Kk.

3- Mark points E, E, H& h at 338.17 mm from point A, a, K, & k respectively.

			Width Aa:	50.85	mm
Height AK:	101.18	mm	Width Bb:	50.77	mm
Height BJ:	101.11	mm	Width Cc:	50.84	mm
Height EH:	100.09	mm	Width Dd:	50.84	mm
Height FG:	99.48	mm	Width Ee:	50.94	mm
Height ak:	101.17	mm	Width Ff:	51.20	mm
Height bj:	101.00	mm	Width Gg:	51.03	mm
Height eh:	100.05	mm	Width Hh:	50.81	mm
Height fg:	99.21	mm	Width Ii:	50.68	mm
			Width Jj:	50.68	mm

Guide Marks

			Width Kk:	50.87	mm

4- Center plexiglass with line 3 & 4 and draw lines 1 & 2.

5- Mark the plane of lines 1 & 2

Width 1:	50.87	mm	Width 2:	51.17	mm
Height 3:	75.95	mm	Height 4:	75.52	mm

Geometric Comments:

Fracture Toughness Test Protocol

BAV	**Batch**	**Specimen**	B2

Geometry:

Name: Rachel Gordon

Date: 2/3/13 Time: 3:4000 PM

Nominal Dimensions:

Prism: 51×102×457 (2×4×18) mm (in) Notch: 25×4.76 (1×3/16) mm (in)

Actual Dimensions: Note: Use uncut side of the beam for AakK.

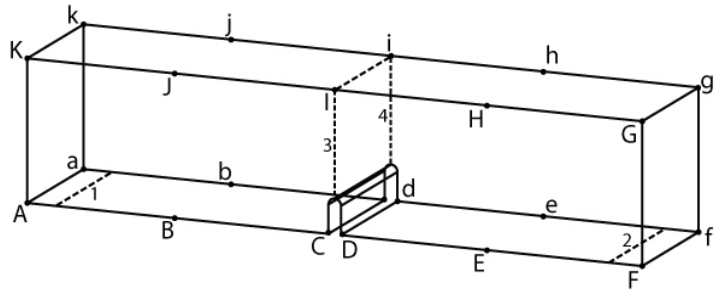

Length AC:	226.57	mm	Width CD:	5.77	mm
Length ac:	226.55	mm	Width cd:	6.49	mm
Length DF:	222.42	mm			
Length df:	222.60	mm			
Length KG:	457.20	mm			
Length kg:	455.61	mm			

Outer Marks

1- Mark points B, b, J, & j at 114.81 mm from point A, a, K, & k respectively.

2- Mark line Ii at 229.63 mm from line Kk.

3- Mark points E, E, H& h at 337.32 mm from point A, a, K, & k respectively.

			Width Aa:	50.96	mm
Height AK:	101.32	mm	Width Bb:	50.89	mm
Height BJ:	101.12	mm	Width Cc:	50.91	mm
Height EH:	100.89	mm	Width Dd:	50.92	mm
Height FG:	100.60	mm	Width Ee:	51.05	mm
Height ak:	101.34	mm	Width Ff:	51.28	mm
Height bj:	101.20	mm	Width Gg:	51.18	mm
Height eh:	100.88	mm	Width Hh:	50.87	mm
Height fg:	100.66	mm	Width Ii:	50.82	mm
			Width Jj:	50.82	mm
			Width Kk:	50.90	mm

Guide Marks

4- Center plexiglass with line 3 & 4 and draw lines 1 & 2.

5- Mark the plane of lines 1 & 2

Width 1:	50.87	mm	Width 2:	51.28	mm
Height 3:	75.49	mm	Height 4:	74.99	mm

Geometric Comments:

Fracture Toughness Test Protocol

BAV	**Batch**	**Specimen**	B3

Geometry:

Name: Rachel Gordon

Date: 2/3/13 Time: 3:4000 PM

Nominal Dimensions:

Prism: 51×102×457 (2×4×18) mm (in) Notch: 25×4.76 (1×3/16) mm (in)

Actual Dimensions: Note: Use uncut side of the beam for AakK.

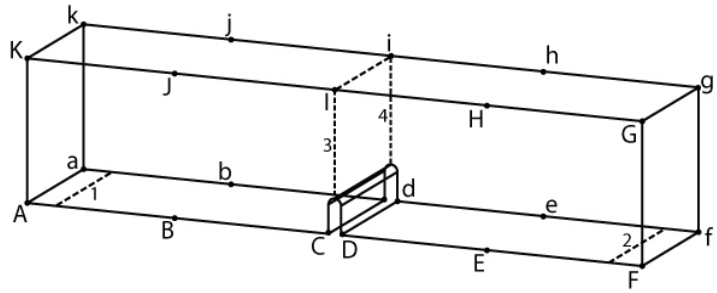

Length AC:	226.33	mm	Width CD:	6.16	mm
Length ac:	225.15	mm	Width cd:	6.31	mm
Length DF:	221.63	mm			
Length df:	222.40	mm			
Length KG:	454.03	mm			
Length kg:	455.61	mm			

Outer Marks

1- Mark points B, b, J, & j at 114.43 mm from point A, a, K, & k respectively.

2- Mark line Ii at 228.86 mm from line Kk.

3- Mark points E, E, H& h at 336.44 mm from point A, a, K, & k respectively.

			Width Aa:	50.78	mm
Height AK:	100.71	mm	Width Bb:	50.77	mm
Height BJ:	100.90	mm	Width Cc:	50.92	mm
Height EH:	100.85	mm	Width Dd:	51.07	mm
Height FG:	100.54	mm	Width Ee:	50.90	mm
Height ak:	100.79	mm	Width Ff:	50.94	mm
Height bj:	100.70	mm	Width Gg:	51.26	mm
Height eh:	100.81	mm	Width Hh:	51.16	mm
Height fg:	100.80	mm	Width Ii:	51.04	mm
			Width Jj:	50.91	mm
			Width Kk:	50.81	mm

Guide Marks

4- Center plexiglass with line 3 & 4 and draw lines 1 & 2.

5- Mark the plane of lines 1 & 2

Width 1:	50.84	mm	Width 2:	51.06	mm
Height 3:	75.41	mm	Height 4:	75.08	mm

Geometric Comments:

Fracture Toughness Test Protocol

BAV	**Batch**	**Specimen**	B4

Geometry:

Name: Rachel Gordon

Date: 2/3/13 Time: 3:4000 PM

Nominal Dimensions:

Prism: 51×102×457 (2×4×18) mm (in) Notch: 25×4.76 (1×3/16) mm (in)

Actual Dimensions: Note: Use uncut side of the beam for AakK.

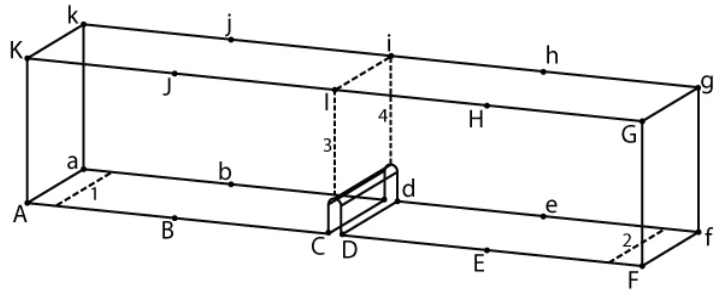

Length AC:	226.37	mm	Width CD:	5.70	mm
Length ac:	226.12	mm	Width cd:	5.97	mm
Length DF:	221.43	mm			
Length df:	221.27	mm			
Length KG:	454.03	mm			
Length kg:	455.61	mm			

Outer Marks

1- Mark points B, b, J, & j at 114.58 mm from point A, a, K, & k respectively.

2- Mark line Ii at 229.16 mm from line Kk.

3- Mark points E, E, H& h at 335.93 mm from point A, a, K, & k respectively.

			Width Aa:	50.79	mm
Height AK:	101.36	mm	Width Bb:	51.07	mm
Height BJ:	101.09	mm	Width Cc:	50.85	mm
Height EH:	100.82	mm	Width Dd:	50.88	mm
Height FG:	100.36	mm	Width Ee:	50.89	mm
Height ak:	101.10	mm	Width Ff:	51.12	mm
Height bj:	100.87	mm	Width Gg:	51.21	mm
Height eh:	100.63	mm	Width Hh:	51.21	mm
Height fg:	100.28	mm	Width Ii:	51.02	mm
			Width Jj:	50.94	mm
			Width Kk:	50.88	mm

Guide Marks

4- Center plexiglass with line 3 & 4 and draw lines 1 & 2.

5- Mark the plane of lines 1 & 2

Width 1:	50.89	mm	Width 2:	50.94	mm
Height 3:	76.01	mm	Height 4:	74.56	mm

Geometric Comments:

Fracture Toughness Test Protocol

BAV	**Batch**	**Specimen**	B5

Geometry:

Name: Rachel Gordon

Date: 2/3/13

Time: 3:4000 PM

Nominal Dimensions:

Prism: 51×102×457 (2×4×18) mm (in)

Notch: 25×4.76 (1×3/16) mm (in)

Actual Dimensions: Note: Use uncut side of the beam for AakK.

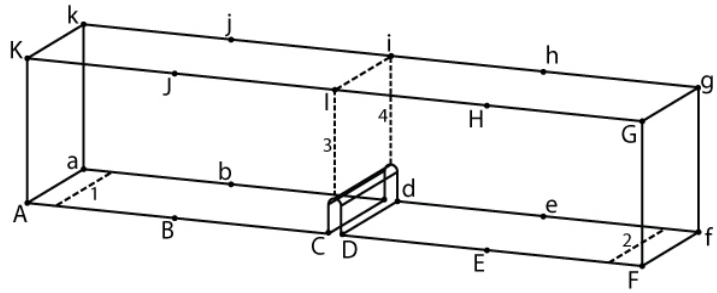

Length AC:	225.81	mm	Width CD:	5.41	mm
Length ac:	225.64	mm	Width cd:	6.36	mm
Length DF:	223.94	mm			
Length df:	223.36	mm			
Length KG:	454.03	mm			
Length kg:	454.03	mm			

Outer Marks

1- Mark points B, b, J, & j at 114.33 mm from point A, a, K, & k respectively.

2- Mark line Ii at 228.67 mm from line Kk.

3- Mark points E, E, H& h at 337.98 mm from point A, a, K, & k respectively.

			Width Aa:	51.07	mm
Height AK:	99.53	mm	Width Bb:	50.68	mm
Height BJ:	100.50	mm	Width Cc:	50.94	mm
Height EH:	100.07	mm	Width Dd:	50.70	mm
Height FG:	98.90	mm	Width Ee:	50.74	mm
Height ak:	99.48	mm	Width Ff:	50.77	mm
Height bj:	100.53	mm	Width Gg:	51.14	mm
Height eh:	100.31	mm	Width Hh:	51.16	mm
Height fg:	99.44	mm	Width Ii:	51.15	mm
			Width Jj:	51.20	mm
			Width Kk:	51.23	mm

Guide Marks

4- Center plexiglass with line 3 & 4 and draw lines 1 & 2.

5- Mark the plane of lines 1 & 2

Width 1:	50.86	mm	Width 2:	50.76	mm
Height 3:	75.19	mm	Height 4:	75.19	mm

Geometric Comments:

Fracture Toughness Test Protocol

BAV	**Batch**	**Specimen**	B6

Geometry:

Name: Rachel Gordon

Date: 12/12/13 Time: 4:36 PM

Nominal Dimensions:

Prism: 51×102×457 (2×4×18) mm (in) Notch: 25×4.76 (1×3/16) mm (in)

Actual Dimensions: Note: Use uncut side of the beam for AakK.

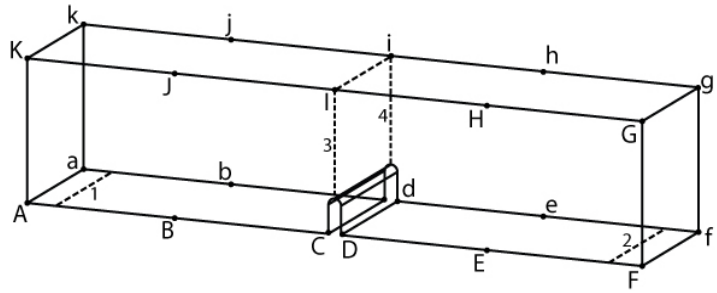

Length AC:	227.02	mm	Width CD:	5.64	mm
Length ac:	226.65	mm	Width cd:	6.11	mm
Length DF:	222.73	mm			
Length df:	222.25	mm			
Length KG:	456.18	mm			
Length kg:	455.93	mm			

Outer Marks

1- Mark points B, b, J, & j at 114.89 mm from point A, a, K, & k respectively.

2- Mark line Ii at 229.77 mm from line Kk.

3- Mark points E, E, H& h at 337.38 mm from point A, a, K, & k respectively.

			Width Aa:	49.91	mm
Height AK:	101.77	mm	Width Bb:	50.04	mm
Height BJ:	101.24	mm	Width Cc:	50.49	mm
Height EH:	100.83	mm	Width Dd:	50.07	mm
Height FG:	100.23	mm	Width Ee:	50.49	mm
Height ak:	100.89	mm	Width Ff:	50.32	mm
Height bj:	100.81	mm	Width Gg:	53.79	mm
Height eh:	100.41	mm	Width Hh:	53.58	mm
Height fg:	100.16	mm	Width Ii:	53.50	mm
			Width Jj:	53.64	mm
			Width Kk:	53.57	mm

Guide Marks

4- Center plexiglass with line 3 & 4 and draw lines 1 & 2.

5- Mark the plane of lines 1 & 2

Width 1:	49.86	mm	Width 2:	50.87	mm
Height 3:	75.29	mm	Height 4:	74.51	mm

Geometric Comments:

Fracture Toughness Test Protocol

BAVIII	**Batch**	**Specimen**	B1

Geometry:

Name: Rachel Gordon

Date: 12/12/13 Time: 5:53PM

Nominal Dimensions:

Prism: 51×102×457 (2×4×18) mm (in) Notch: 25×4.76 (1×3/16) mm (in)

Actual Dimensions: Note: Use uncut side of the beam for AakK.

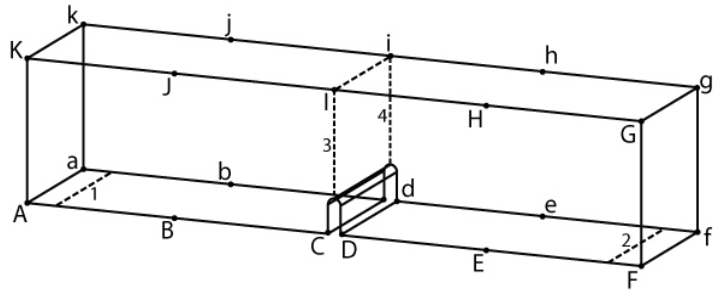

Length AC:	225.30	mm	Width CD:	5.29	mm
Length ac:	225.63	mm	Width cd:	5.84	mm
Length DF:	226.10	mm			
Length df:	226.83	mm			
Length KG:	458.63	mm			
Length kg:	458.95	mm			

Outer Marks

1- Mark points B, b, J, & j at 114.12 mm from point A, a, K, & k respectively.

2- Mark line Ii at 228.25 mm from line Kk.

3- Mark points E, E, H& h at 340.59 mm from point A, a, K, & k respectively.

			Width Aa:	51.46	mm
Height AK:	101.66	mm	Width Bb:	51.11	mm
Height BJ:	101.61	mm	Width Cc:	51.08	mm
Height EH:	101.30	mm	Width Dd:	51.00	mm
Height FG:	100.78	mm	Width Ee:	50.84	mm
Height ak:	101.10	mm	Width Ff:	51.04	mm
Height bj:	100.91	mm	Width Gg:	51.00	mm
Height eh:	100.89	mm	Width Hh:	50.87	mm
Height fg:	100.26	mm	Width Ii:	50.91	mm
			Width Jj:	51.09	mm
			Width Kk:	51.35	mm

Guide Marks

4- Center plexiglass with line 3 & 4 and draw lines 1 & 2.

5- Mark the plane of lines 1 & 2

Width 1:	51.36	mm	Width 2:	50.76	mm
Height 3:	75.27	mm	Height 4:	74.39	mm

Geometric Comments:

Fracture Toughness Test Protocol

BAVIII	**Batch**	**Specimen**	B2

Geometry:

Name: Rachel Gordon

Date: 12/12/13 Time: 6:00PM

Nominal Dimensions:

Prism: 51×102×457 (2×4×18) mm (in) Notch: 25×4.76 (1×3/16) mm (in)

Actual Dimensions: Note: Use uncut side of the beam for AakK.

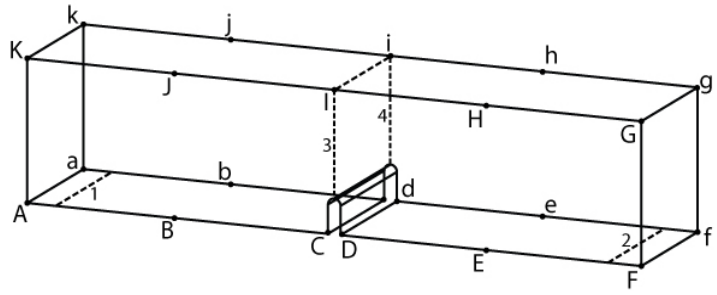

Length AC:	225.15	mm	Width CD:	5.59	mm
Length ac:	225.26	mm	Width cd:	6.52	mm
Length DF:	228.03	mm			
Length df:	227.08	mm			
Length KG:	458.95	mm			
Length kg:	460.38	mm			

Outer Marks

1- Mark points B, b, J, & j at 114.12 mm from point A, a, K, & k respectively.

2- Mark line Ii at 228.23 mm from line Kk.

3- Mark points E, E, H& h at 341.67 mm from point A, a, K, & k respectively.

			Width Aa:	51.41	mm
Height AK:	101.12	mm	Width Bb:	51.12	mm
Height BJ:	100.85	mm	Width Cc:	50.99	mm
Height EH:	99.94	mm	Width Dd:	50.94	mm
Height FG:	97.46	mm	Width Ee:	50.87	mm
Height ak:	101.02	mm	Width Ff:	51.15	mm
Height bj:	100.65	mm	Width Gg:	50.92	mm
Height eh:	99.81	mm	Width Hh:	50.82	mm
Height fg:	98.46	mm	Width Ii:	50.88	mm
			Width Jj:	51.06	mm
			Width Kk:	51.26	mm

Guide Marks

4- Center plexiglass with line 3 & 4 and draw lines 1 & 2.

5- Mark the plane of lines 1 & 2

Width 1:	51.32	mm	Width 2:	50.91	mm
Height 3:	75.06	mm	Height 4:	74.16	mm

Geometric Comments:

Fracture Toughness Test Protocol

BAVIII	**Batch**	**Specimen**	B3

Geometry:

Name: Rachel Gordon

Date: 12/12/13 Time: 6:07PM

Nominal Dimensions:

Prism: 51×102×457 (2×4×18) mm (in) Notch: 25×4.76 (1×3/16) mm (in)

Actual Dimensions: Note: Use uncut side of the beam for AakK.

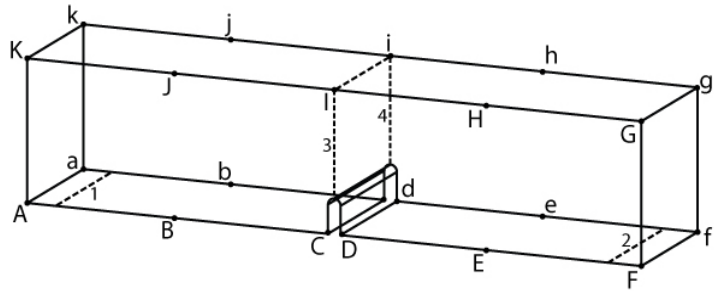

Length AC:	225.28	mm	Width CD:	5.60	mm
Length ac:	225.09	mm	Width cd:	6.19	mm
Length DF:	226.64	mm			
Length df:	226.01	mm			
Length KG:	457.20	mm			
Length kg:	547.52	mm			

Outer Marks

1- Mark points B, b, J, & j at 114.07 mm from point A, a, K, & k respectively.

2- Mark line Ii at 228.13 mm from line Kk.

3- Mark points E, E, H& h at 340.39 mm from point A, a, K, & k respectively.

			Width Aa:	50.93	mm
Height AK:	100.91	mm	Width Bb:	50.86	mm
Height BJ:	101.00	mm	Width Cc:	50.90	mm
Height EH:	100.87	mm	Width Dd:	50.89	mm
Height FG:	100.25	mm	Width Ee:	50.83	mm
Height ak:	100.96	mm	Width Ff:	51.09	mm
Height bj:	100.91	mm	Width Gg:	51.26	mm
Height eh:	100.73	mm	Width Hh:	51.08	mm
Height fg:	99.92	mm	Width Ii:	50.92	mm
			Width Jj:	50.82	mm
			Width Kk:	50.63	mm

Guide Marks

4- Center plexiglass with line 3 & 4 and draw lines 1 & 2.

5- Mark the plane of lines 1 & 2

Width 1:	50.86	mm	Width 2:	51.05	mm
Height 3:	75.10	mm	Height 4:	74.64	mm

Geometric Comments:

Fracture Toughness Test Protocol

BAVIII	**Batch**	**Specimen**	B4

Geometry:

Name: Rachel Gordon

Date: 12/12/13 Time: 6:13PM

Nominal Dimensions:

Prism: 51×102×457 (2×4×18) mm (in) Notch: 25×4.76 (1×3/16) mm (in)

Actual Dimensions: Note: Use uncut side of the beam for AakK.

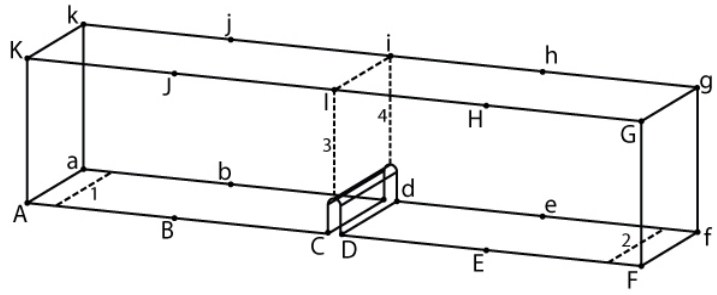

Length AC:	225.34	mm	Width CD:	5.48	mm
Length ac:	225.30	mm	Width cd:	6.23	mm
Length DF:	226.89	mm			
Length df:	226.55	mm			
Length KG:	459.26	mm			
Length kg:	459.58	mm			

Outer Marks

1- Mark points B, b, J, & j at 114.12 mm from point A, a, K, & k respectively.

2- Mark line Ii at 228.25 mm from line Kk.

3- Mark points E, E, H& h at 340.84 mm from point A, a, K, & k respectively.

			Width Aa:	51.17	mm
Height AK:	101.12	mm	Width Bb:	50.97	mm
Height BJ:	100.98	mm	Width Cc:	50.85	mm
Height EH:	100.46	mm	Width Dd:	50.95	mm
Height FG:	100.11	mm	Width Ee:	50.94	mm
Height ak:	100.83	mm	Width Ff:	50.90	mm
Height bj:	100.82	mm	Width Gg:	50.89	mm
Height eh:	100.14	mm	Width Hh:	50.96	mm
Height fg:	99.67	mm	Width Ii:	51.02	mm
			Width Jj:	51.15	mm
			Width Kk:	51.25	mm

Guide Marks

4- Center plexiglass with line 3 & 4 and draw lines 1 & 2.

5- Mark the plane of lines 1 & 2

Width 1:	51.00	mm	Width 2:	50.91	mm
Height 3:	75.33	mm	Height 4:	74.44	mm

Geometric Comments:

Fracture Toughness Test Protocol

BAVIII	**Batch**	**Specimen**	B5

Geometry:

Name: Rachel Gordon

Date: 12/12/13 Time: 6:20PM

Nominal Dimensions:

Prism: 51×102×457 (2×4×18) mm (in) Notch: 25×4.76 (1×3/16) mm (in)

Actual Dimensions: Note: Use uncut side of the beam for AakK.

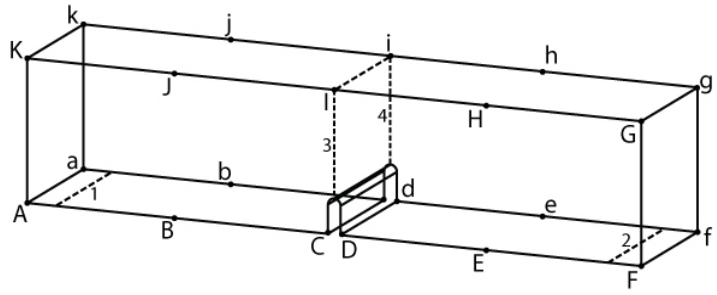

Length AC:	223.74	mm	Width CD:	5.86	mm
Length ac:	223.92	mm	Width cd:	6.38	mm
Length DF:	227.80	mm			
Length df:	227.38	mm			
Length KG:	456.57	mm			
Length kg:	456.88	mm			

Outer Marks

1- Mark points B, b, J, & j at 113.45 mm from point A, a, K, & k respectively.

2- Mark line Ii at 226.89 mm from line Kk.

3- Mark points E, E, H& h at 341.04 mm from point A, a, K, & k respectively.

			Width Aa:	51.06	mm
Height AK:	100.38	mm	Width Bb:	50.67	mm
Height BJ:	100.77	mm	Width Cc:	50.71	mm
Height EH:	99.92	mm	Width Dd:	50.69	mm
Height FG:	98.63	mm	Width Ee:	50.76	mm
Height ak:	100.28	mm	Width Ff:	50.90	mm
Height bj:	100.77	mm	Width Gg:	51.03	mm
Height eh:	99.94	mm	Width Hh:	51.06	mm
Height fg:	98.81	mm	Width Ii:	51.07	mm
			Width Jj:	51.17	mm
			Width Kk:	51.37	mm

Guide Marks

4- Center plexiglass with line 3 & 4 and draw lines 1 & 2.

5- Mark the plane of lines 1 & 2

Width 1:	50.89	mm	Width 2:	50.79	mm
Height 3:	75.18	mm	Height 4:	74.29	mm

Geometric Comments:

Fracture Toughness Test Protocol

BAVIII	**Batch**	**Specimen**	B6

Geometry:

Name: Rachel Gordon

Date: 12/12/13 Time: 3:34PM

Nominal Dimensions:

Prism: 51×102×457 (2×4×18) mm (in) Notch: 25×4.76 (1×3/16) mm (in)

Actual Dimensions: Note: Use uncut side of the beam for AakK.

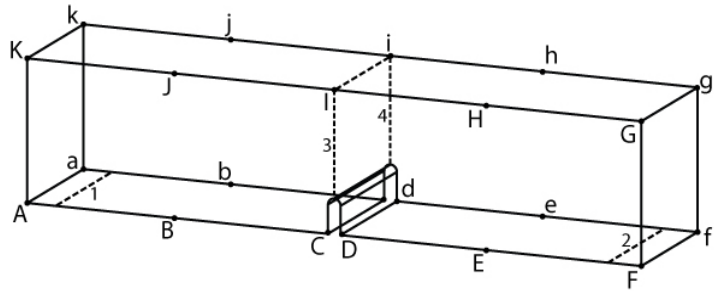

Length AC:	223.66	mm	Width CD:	5.73	mm
Length ac:	223.80	mm	Width cd:	6.26	mm
Length DF:	228.01	mm			
Length df:	227.03	mm			
Length KG:	458.72	mm			
Length kg:	457.96	mm			

Outer Marks

1- Mark points B, b, J, & j at 113.36 mm from point A, a, K, & k respectively.

2- Mark line Ii at 226.73 mm from line Kk.

3- Mark points E, E, H& h at 340.88 mm from point A, a, K, & k respectively.

			Width Aa:	52.26	mm
Height AK:	102.38	mm	Width Bb:	51.52	mm
Height BJ:	102.34	mm	Width Cc:	51.76	mm
Height EH:	102.08	mm	Width Dd:	51.74	mm
Height FG:	102.03	mm	Width Ee:	51.84	mm
Height ak:	100.28	mm	Width Ff:	52.11	mm
Height bj:	100.00	mm	Width Gg:	52.85	mm
Height eh:	100.95	mm	Width Hh:	52.98	mm
Height fg:	100.91	mm	Width Ii:	53.05	mm
			Width Jj:	52.87	mm
			Width Kk:	52.98	mm

Guide Marks

4- Center plexiglass with line 3 & 4 and draw lines 1 & 2.

5- Mark the plane of lines 1 & 2

Width 1:	51.57	mm	Width 2:	51.96	mm
Height 3:	75.22	mm	Height 4:	74.52	mm

Geometric Comments:

Screwed up letters but it's right now

Fracture Toughness Test Protocol

BAVIII	**Batch**	**Specimen**	B7

Geometry:

Name: Rachel Gordon

Date: 12/12/13 Time: 3:34PM

Nominal Dimensions:

Prism: 51×102×457 (2×4×18) mm (in) Notch: 25×4.76 (1×3/16) mm (in)

Actual Dimensions: Note: Use uncut side of the beam for AakK.

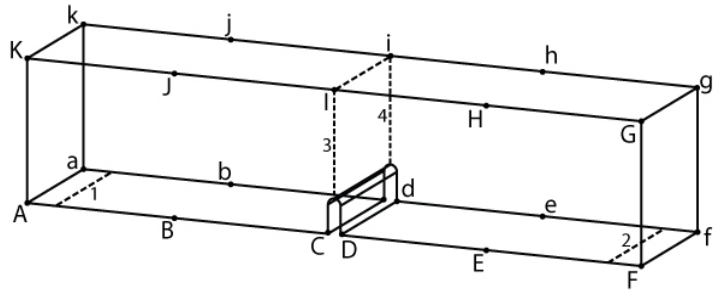

Length AC:	225.32	mm	Width CD:	5.52	mm
Length ac:	225.55	mm	Width cd:	6.23	mm
Length DF:	227.01	mm			
Length df:	226.51	mm			
Length KG:	458.77	mm			
Length kg:	458.79	mm			

Outer Marks

1- Mark points B, b, J, & j at 114.19 mm from point A, a, K, & k respectively.

2- Mark line Ii at 228.37 mm from line Kk.

3- Mark points E, E, H& h at 340.95 mm from point A, a, K, & k respectively.

			Width Aa:	51.85	mm
Height AK:	100.46	mm	Width Bb:	51.76	mm
Height BJ:	101.31	mm	Width Cc:	51.79	mm
Height EH:	101.76	mm	Width Dd:	51.73	mm
Height FG:	101.19	mm	Width Ee:	52.05	mm
Height ak:	100.24	mm	Width Ff:	52.01	mm
Height bj:	100.29	mm	Width Gg:	55.30	mm
Height eh:	101.09	mm	Width Hh:	54.99	mm
Height fg:	100.96	mm	Width Ii:	54.88	mm
			Width Jj:	55.00	mm
			Width Kk:	55.48	mm

Guide Marks

4- Center plexiglass with line 3 & 4 and draw lines 1 & 2.

5- Mark the plane of lines 1 & 2

Width 1:	51.68	mm	Width 2:	52.30	mm
Height 3:	74.88	mm	Height 4:	74.49	mm

Geometric Comments:

Fracture Toughness Test Protocol

BAVIII	**Batch**	**Specimen**	B8

Geometry:

Name: Rachel Gordon

Date: 12/12/13 Time: 3:34PM

Nominal Dimensions:

Prism: 51×102×457 (2×4×18) mm (in) Notch: 25×4.76 (1×3/16) mm (in)

Actual Dimensions: Note: Use uncut side of the beam for AakK.

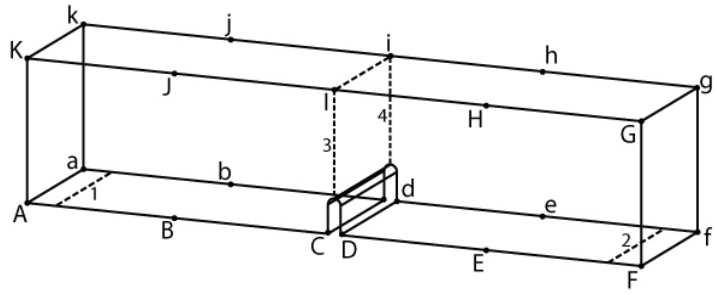

Length AC:	224.67	mm	Width CD:	5.42	mm
Length ac:	225.26	mm	Width cd:	6.12	mm
Length DF:	229.52	mm			
Length df:	228.98	mm			
Length KG:	460.38	mm			
Length kg:	460.50	mm			

Outer Marks

1- Mark points B, b, J, & j at 113.93 mm from point A, a, K, & k respectively.

2- Mark line Ii at 227.85 mm from line Kk.

3- Mark points E, E, H& h at 343.18 mm from point A, a, K, & k respectively.

			Width Aa:	51.78	mm
Height AK:	100.89	mm	Width Bb:	51.42	mm
Height BJ:	100.93	mm	Width Cc:	51.09	mm
Height EH:	100.75	mm	Width Dd:	51.06	mm
Height FG:	100.64	mm	Width Ee:	51.16	mm
Height ak:	100.62	mm	Width Ff:	51.45	mm
Height bj:	100.55	mm	Width Gg:	51.95	mm
Height eh:	100.92	mm	Width Hh:	51.74	mm
Height fg:	100.76	mm	Width Ii:	51.56	mm
			Width Jj:	51.50	mm
Guide Marks			Width Kk:	51.60	mm

4- Center plexiglass with line 3 & 4 and draw lines 1 & 2.

5- Mark the plane of lines 1 & 2

Width 1:	51.65	mm	Width 2:	51.24	mm
Height 3:	75.33	mm	Height 4:	74.45	mm

Geometric Comments:

Fracture Toughness Test Protocol

BAIX	**Batch**	**Specimen**	B1

Geometry:

Name: Rachel Gordon

Date: 2/3/13 Time: 4:47PM

Nominal Dimensions:

Prism: 51×102×457 (2×4×18) mm (in) Notch: 25×4.76 (1×3/16) mm (in)

Actual Dimensions: Note: Use uncut side of the beam for AakK.

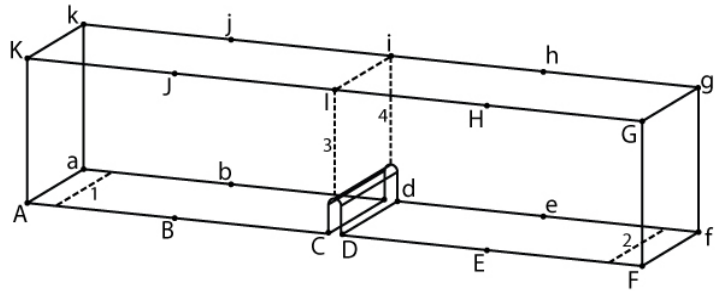

			Length AC:	226.39	mm
			Length ac:	225.77	mm
			Length DF:	224.27	mm
			Length df:	223.04	mm
			Length KG:	455.61	mm
			Length kg:	455.61	mm
Width CD:	5.70	mm	Width cd:	6.66	mm

Outer Marks

1- Mark points B, b, J, & j at 114.59 mm from point A, a, K, & k respectively.

2- Mark line Ii at 229.17 mm from line Kk.

3- Mark points E, E, H& h at 338.24 mm from point A, a, K, & k respectively.

			Width Aa:	50.94	mm
Height AK:	101.39	mm	Width Bb:	50.82	mm
Height BJ:	101.59	mm	Width Cc:	51.11	mm
Height EH:	101.29	mm	Width Dd:	50.91	mm
Height FG:	100.61	mm	Width Ee:	50.95	mm
Height ak:	101.17	mm	Width Ff:	50.39	mm
Height bj:	101.30	mm	Width Gg:	51.14	mm
Height eh:	100.72	mm	Width Hh:	51.12	mm
Height fg:	100.27	mm	Width Ii:	50.93	mm
			Width Jj:	50.94	mm
			Width Kk:	51.26	mm

Guide Marks

4- Center plexiglass with line 3 & 4 and draw lines 1 & 2.

5- Mark the plane of lines 1 & 2

Width 1:	50.93	mm	Width 2:	51.18	mm
Height 3:	75.88	mm	Height 4:	74.41	mm

Geometric Comments:

Fracture Toughness Test Protocol

BAIX	**Batch**	**Specimen**	B2

Geometry:

Name: Rachel Gordon

Date: 2/3/13 Time: 4:47PM

Nominal Dimensions:

Prism: 51×102×457 (2×4×18) mm (in) Notch: 25×4.76 (1×3/16) mm (in)

Actual Dimensions: Note: Use uncut side of the beam for AakK.

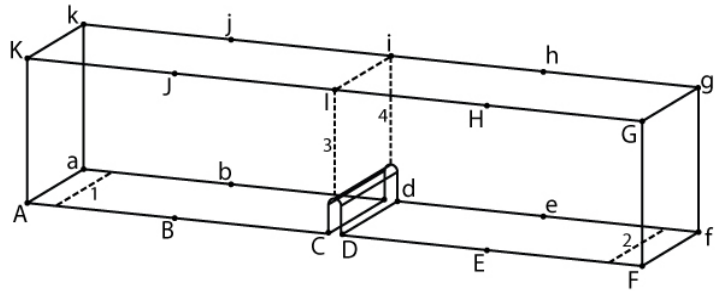

Length AC:	225.97	mm	Width CD:	5.67	mm
Length ac:	225.60	mm	Width cd:	9.60	mm
Length DF:	225.62	mm			
Length df:	224.51	mm			
Length KG:	455.61	mm			
Length kg:	455.61	mm			

Outer Marks

1- Mark points B, b, J, & j at 114.80 mm from point A, a, K, & k respectively.

2- Mark line Ii at 229.60 mm from line Kk.

3- Mark points E, E, H& h at 339.87 mm from point A, a, K, & k respectively.

			Width Aa:	50.18	mm
Height AK:	101.28	mm	Width Bb:	50.89	mm
Height BJ:	101.06	mm	Width Cc:	50.96	mm
Height EH:	100.94	mm	Width Dd:	50.93	mm
Height FG:	100.47	mm	Width Ee:	51.02	mm
Height ak:	100.86	mm	Width Ff:	51.15	mm
Height bj:	100.97	mm	Width Gg:	51.13	mm
Height eh:	100.73	mm	Width Hh:	51.00	mm
Height fg:	100.60	mm	Width Ii:	50.93	mm
			Width Jj:	50.98	mm
			Width Kk:	50.98	mm

Guide Marks

4- Center plexiglass with line 3 & 4 and draw lines 1 & 2.

5- Mark the plane of lines 1 & 2

Width 1:	50.85	mm	Width 2:	51.13	mm
Height 3:	75.64	mm	Height 4:	74.34	mm

Geometric Comments:

Fracture Toughness Test Protocol

BAIX	**Batch**	**Specimen**	B3

Geometry:

Name: Rachel Gordon

Date: 2/3/13

Time: 4:47PM

Nominal Dimensions:

Prism: 51×102×457 (2×4×18) mm (in)

Notch: 25×4.76 (1×3/16) mm (in)

Actual Dimensions: Note: Use uncut side of the beam for AakK.

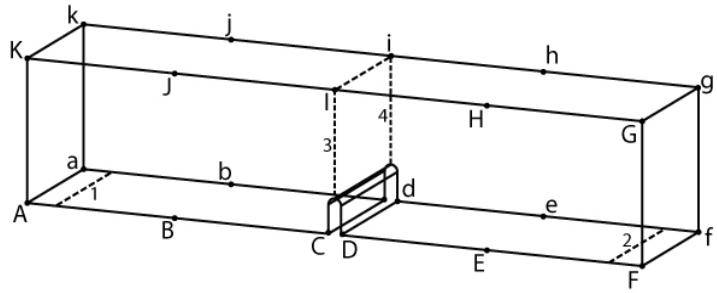

Length AC:	226.04	mm	Width CD:	5.68	mm
Length ac:	225.62	mm	Width cd:	7.21	mm
Length DF:	224.05	mm			
Length df:	223.20	mm			
Length KG:	455.61	mm			
Length kg:	454.03	mm			

Outer Marks

1- Mark points B, b, J, & j at 114.53 mm from point A, a, K, & k respectively.

2- Mark line Ii at 229.05 mm from line Kk.

3- Mark points E, E, H& h at 338.15 mm from point A, a, K, & k respectively.

			Width Aa:	50.79	mm
Height AK:	100.33	mm	Width Bb:	50.77	mm
Height BJ:	100.30	mm	Width Cc:	51.23	mm
Height EH:	100.23	mm	Width Dd:	50.98	mm
Height FG:	99.58	mm	Width Ee:	50.87	mm
Height ak:	100.31	mm	Width Ff:	50.77	mm
Height bj:	100.21	mm	Width Gg:	51.25	mm
Height eh:	100.04	mm	Width Hh:	51.06	mm
Height fg:	99.80	mm	Width Ii:	50.97	mm
			Width Jj:	50.95	mm
			Width Kk:	50.92	mm

Guide Marks

4- Center plexiglass with line 3 & 4 and draw lines 1 & 2.

5- Mark the plane of lines 1 & 2

Width 1:	50.86	mm	Width 2:	51.07	mm
Height 3:	76.58	mm	Height 4:	74.21	mm

Geometric Comments:

Fracture Toughness Test Protocol

BAIX	**Batch**	**Specimen**	B4

Geometry:

Name: Rachel Gordon

Date: 2/3/13 Time: 4:47PM

Nominal Dimensions:

Prism: 51×102×457 (2×4×18) mm (in) Notch: 25×4.76 (1×3/16) mm (in)

Actual Dimensions: Note: Use uncut side of the beam for AakK.

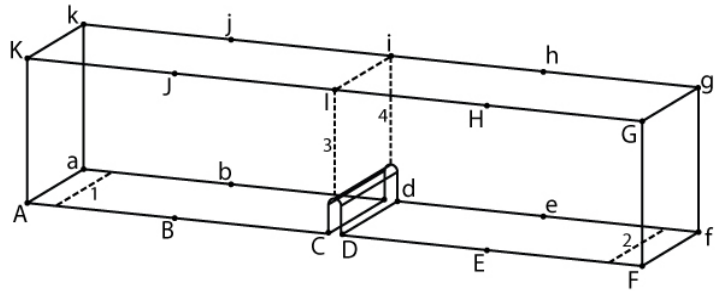

Length AC:	223.07	mm	Width CD:	6.45	mm
Length ac:	223.53	mm	Width cd:	5.49	mm
Length DF:	226.97	mm			
Length df:	227.27	mm			
Length KG:	455.61	mm			
Length kg:	454.03	mm			

Outer Marks

1- Mark points B, b, J, & j at 113.14 mm from point A, a, K, & k respectively.

2- Mark line Ii at 226.29 mm from line Kk.

3- Mark points E, E, H& h at 340.26 mm from point A, a, K, & k respectively.

			Width Aa:	50.84	mm
Height AK:	100.47	mm	Width Bb:	50.99	mm
Height BJ:	100.77	mm	Width Cc:	50.83	mm
Height EH:	101.15	mm	Width Dd:	50.96	mm
Height FG:	100.86	mm	Width Ee:	50.91	mm
Height ak:	101.01	mm	Width Ff:	51.06	mm
Height bj:	100.97	mm	Width Gg:	50.95	mm
Height eh:	101.44	mm	Width Hh:	51.25	mm
Height fg:	101.25	mm	Width Ii:	51.02	mm
			Width Jj:	51.01	mm
			Width Kk:	50.86	mm

Guide Marks

4- Center plexiglass with line 3 & 4 and draw lines 1 & 2.

5- Mark the plane of lines 1 & 2

Width 1:	50.95	mm	Width 2:	50.99	mm
Height 3:	74.16	mm	Height 4:	75.92	mm

Geometric Comments:

Fracture Toughness Test Protocol

BAIX	**Batch**	**Specimen**	B5

Geometry:

Name: Rachel Gordon

Date: 2/3/13 Time: 4:47PM

Nominal Dimensions:

Prism: 51×102×457 (2×4×18) mm (in) Notch: 25×4.76 (1×3/16) mm (in)

Actual Dimensions: Note: Use uncut side of the beam for AakK.

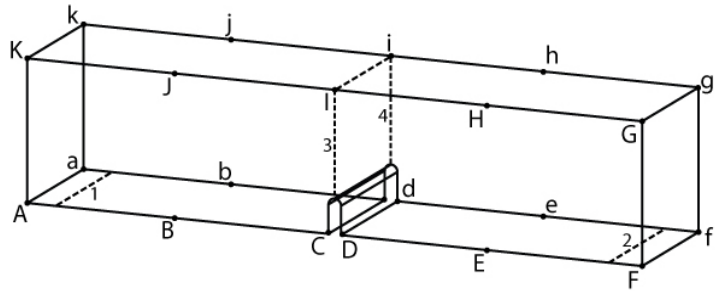

Length AC:	225.89	mm	Width CD:	5.72	mm
Length ac:	225.60	mm	Width cd:	6.98	mm
Length DF:	225.06	mm			
Length df:	224.37	mm			
Length KG:	455.61	mm			
Length kg:	455.61	mm			

Outer Marks

1- Mark points B, b, J, & j at 114.46 mm from point A, a, K, & k respectively.

2- Mark line Ii at 228.92 mm from line Kk.

3- Mark points E, E, H& h at 339.18 mm from point A, a, K, & k respectively.

			Width Aa:	51.06	mm
Height AK:	99.37	mm	Width Bb:	50.69	mm
Height BJ:	100.20	mm	Width Cc:	50.70	mm
Height EH:	100.14	mm	Width Dd:	50.66	mm
Height FG:	99.41	mm	Width Ee:	50.72	mm
Height ak:	99.26	mm	Width Ff:	50.92	mm
Height bj:	100.22	mm	Width Gg:	51.25	mm
Height eh:	100.47	mm	Width Hh:	51.04	mm
Height fg:	99.66	mm	Width Ii:	51.11	mm
			Width Jj:	51.14	mm

Guide Marks

			Width Kk:	51.26	mm

4- Center plexiglass with line 3 & 4 and draw lines 1 & 2.

5- Mark the plane of lines 1 & 2

Width 1:	50.88	mm	Width 2:	50.74	mm
Height 3:	75.47	mm	Height 4:	74.32	mm

Geometric Comments:

Fracture Toughness Test Protocol

BAIX	**Batch**	**Specimen**	B6

Geometry:

Date: 12/12/13

Name: Rachel Gordon

Time: 4:47PM

Nominal Dimensions:

Prism: 51×102×457 (2×4×18) mm (in)

Notch: 25×4.76 (1×3/16) mm (in)

Actual Dimensions: Note: Use uncut side of the beam for AakK.

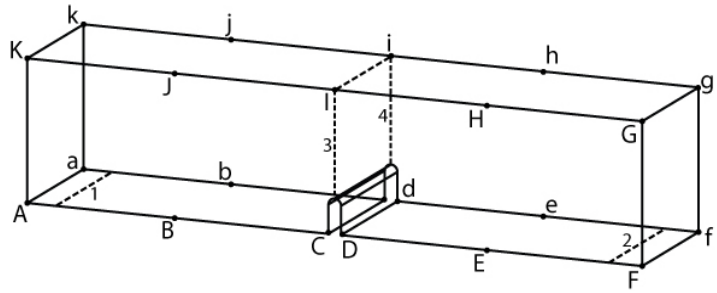

Length AC:	225.75	mm	Width CD:	5.52	mm
Length ac:	225.67	mm	Width cd:	6.24	mm
Length DF:	223.62	mm			
Length df:	222.91	mm			
Length KG:	455.30	mm			
Length kg:	454.98	mm			

Outer Marks

1- Mark points B, b, J, & j at 114.33 mm from point A, a, K, & k respectively.

2- Mark line Ii at 228.65 mm from line Kk.

3- Mark points E, E, H& h at 337.59 mm from point A, a, K, & k respectively.

			Width Aa:	51.53	mm
Height AK:	101.69	mm	Width Bb:	51.39	mm
Height BJ:	101.69	mm	Width Cc:	50.89	mm
Height EH:	101.04	mm	Width Dd:	51.59	mm
Height FG:	100.73	mm	Width Ee:	51.26	mm
Height ak:	101.06	mm	Width Ff:	50.17	mm
Height bj:	100.85	mm	Width Gg:	48.45	mm
Height eh:	101.07	mm	Width Hh:	48.57	mm
Height fg:	100.96	mm	Width Ii:	48.66	mm
			Width Jj:	48.50	mm
			Width Kk:	48.56	mm

Guide Marks

4- Center plexiglass with line 3 & 4 and draw lines 1 & 2.

5- Mark the plane of lines 1 & 2

Width 1:	51.75	mm	Width 2:	50.83	mm
Height 3:	75.08	mm	Height 4:	73.86	mm

Geometric Comments:

Appendix D

Fracture Test Fixture Design and Dimensions

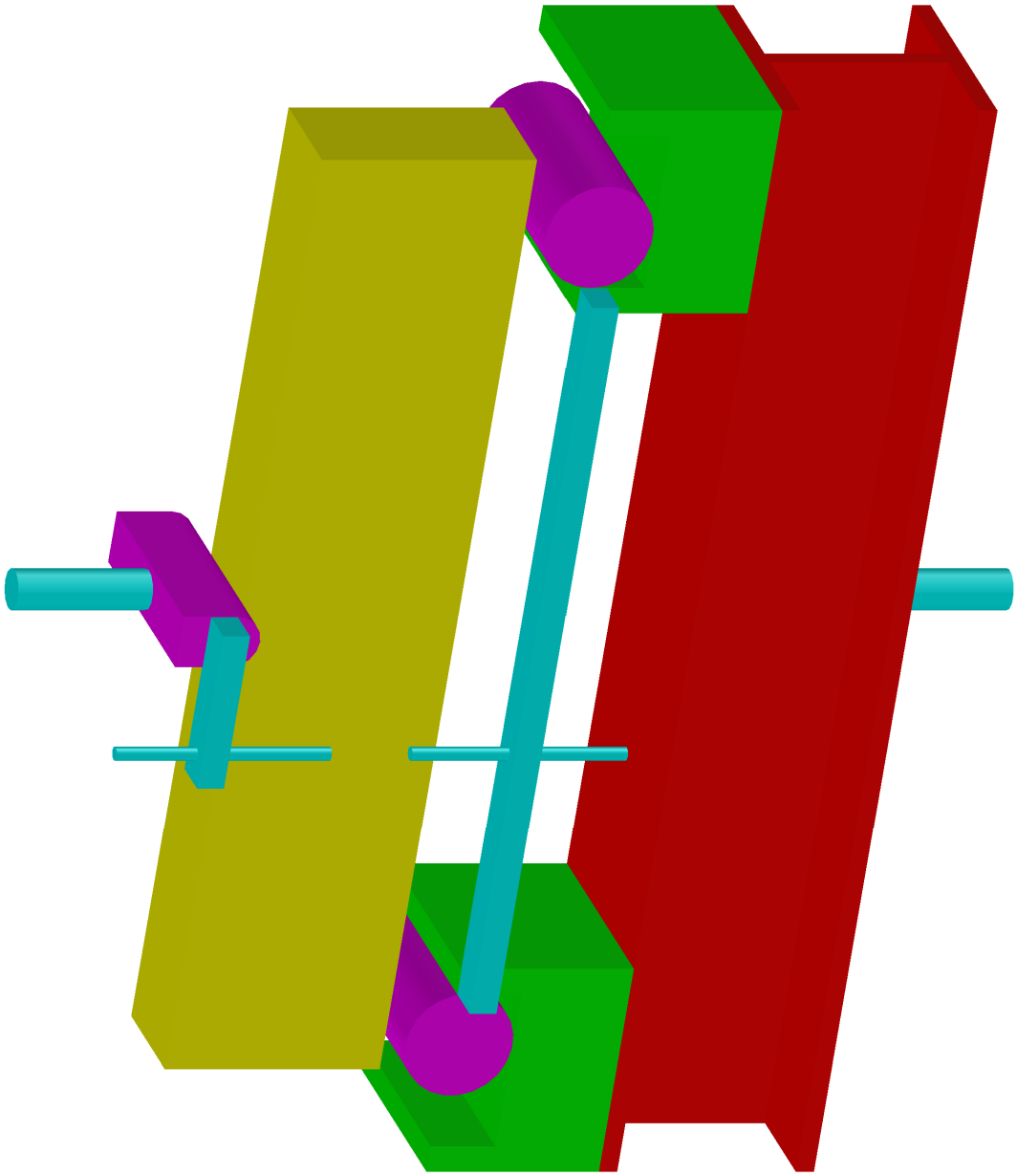

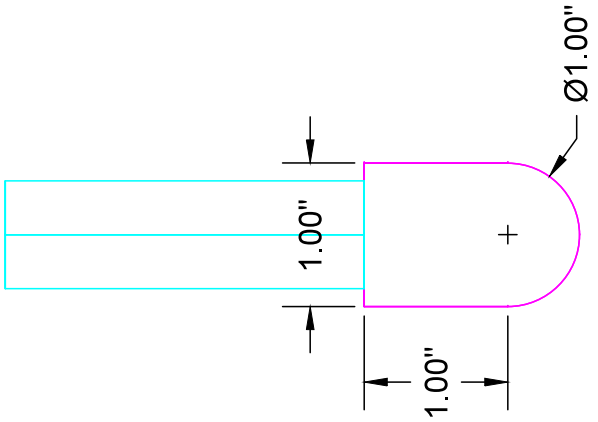
Ø1.00"
1.00"
1.00"

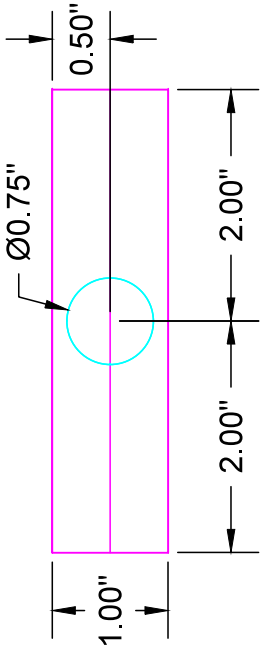
0.50"
Ø0.75"
2.00"
2.00"
1.00"

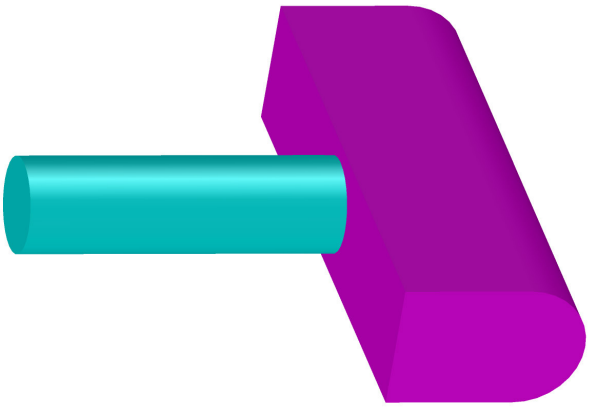

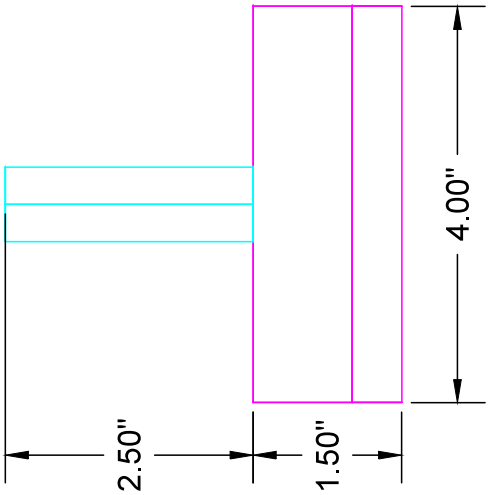
4.00"
2.50"
1.50"

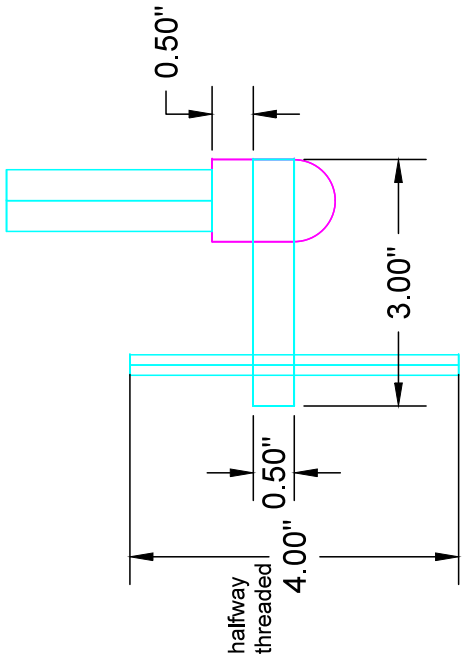
0.50"
3.00"
0.50"
4.00"
halfway
threaded

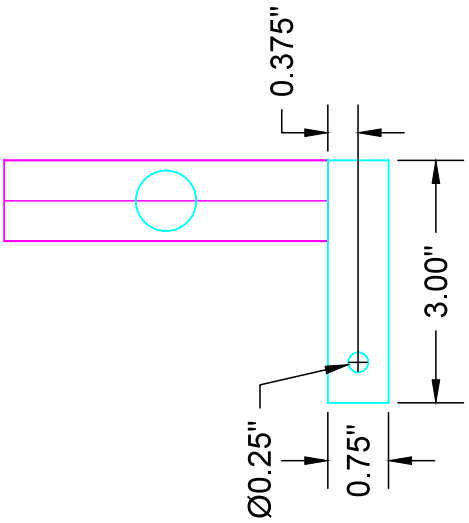
0.375"
3.00"
Ø0.25"
0.75"

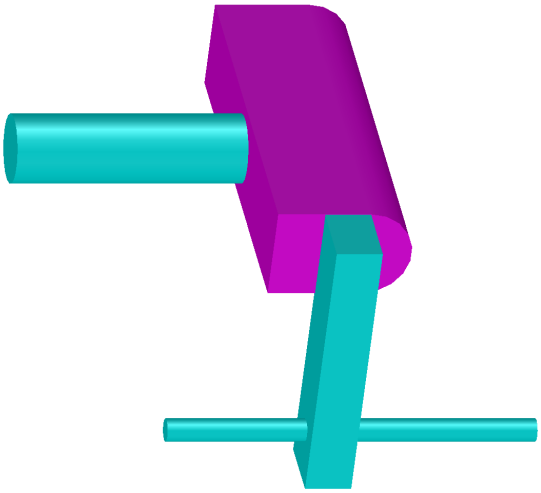

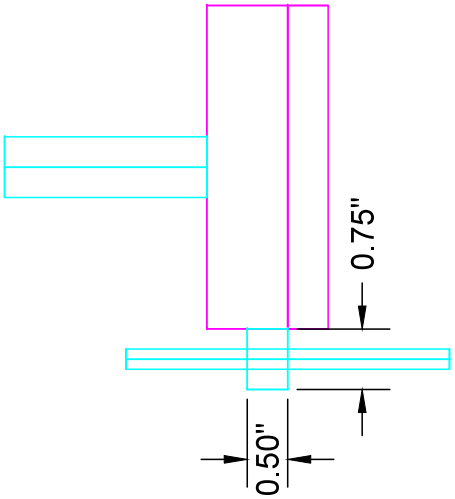
0.75"
0.50"

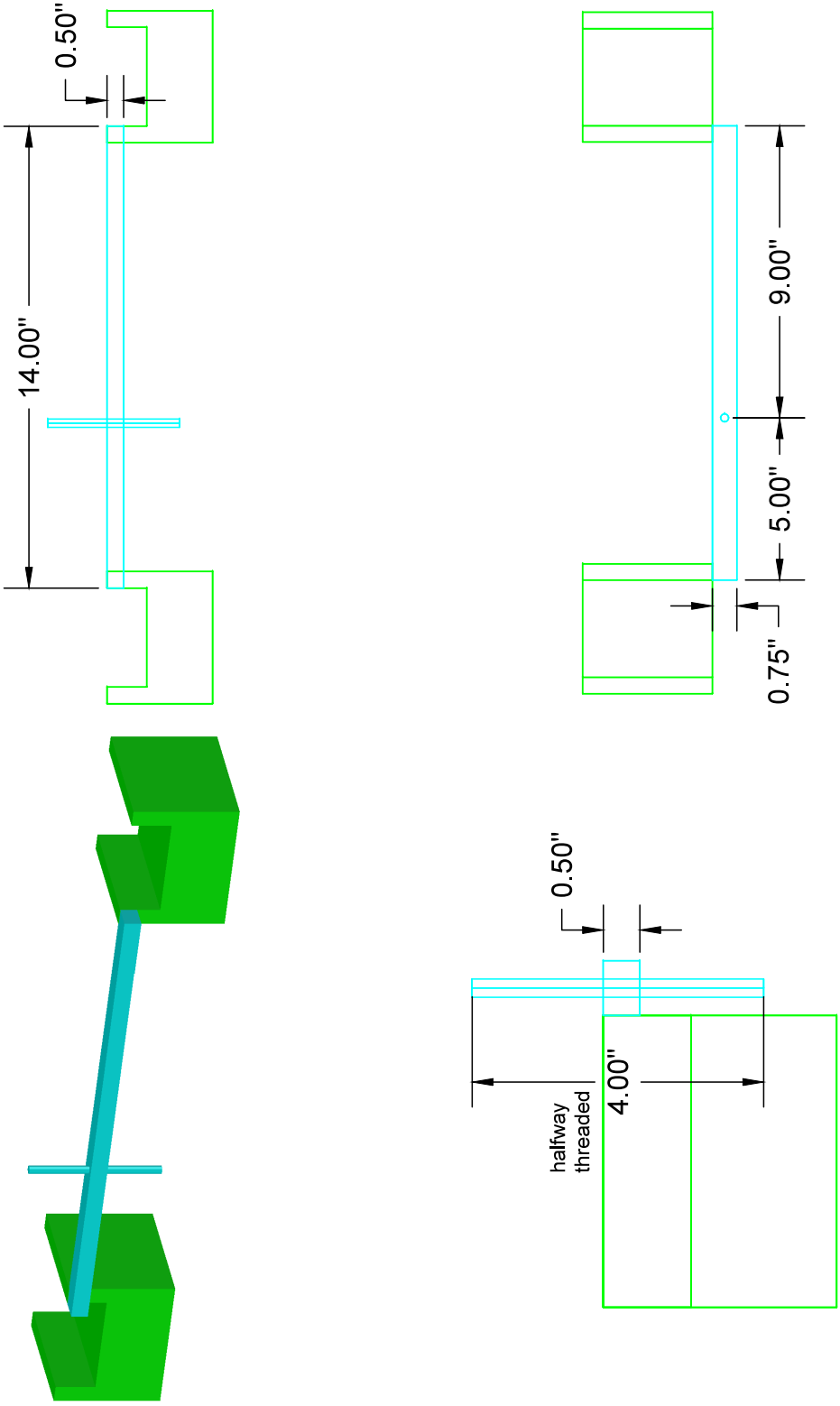
0.50"
14.00"
9.00"
5.00"
0.75"
0.50"
4.00"
halfway
threaded

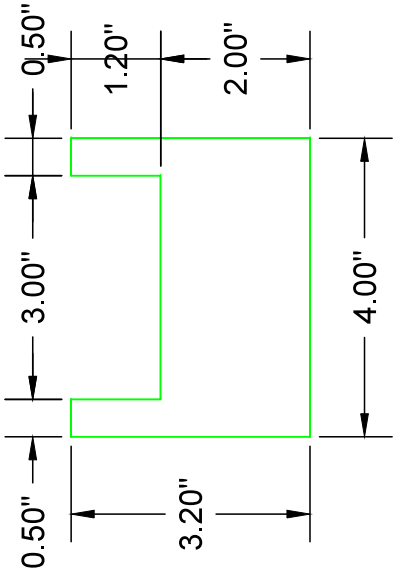
0.50"
1.20"
2.00"
3.00"
4.00"
0.50"
3.20"

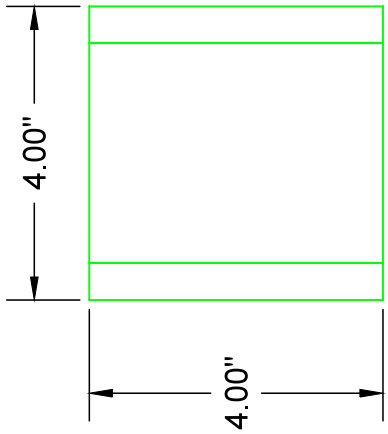
4.00"
4.00"

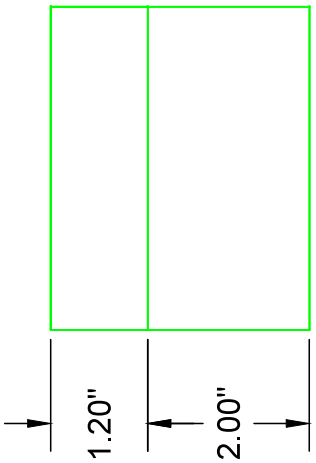
1.20"
2.00"

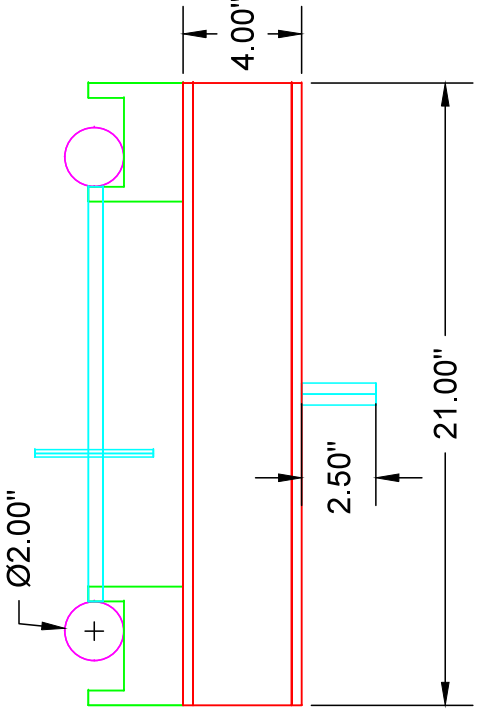
4.00"
21.00"
2.50"
Ø2.00"

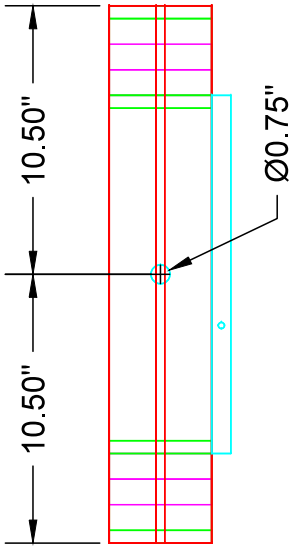
10.50"
10.50"
Ø0.75"

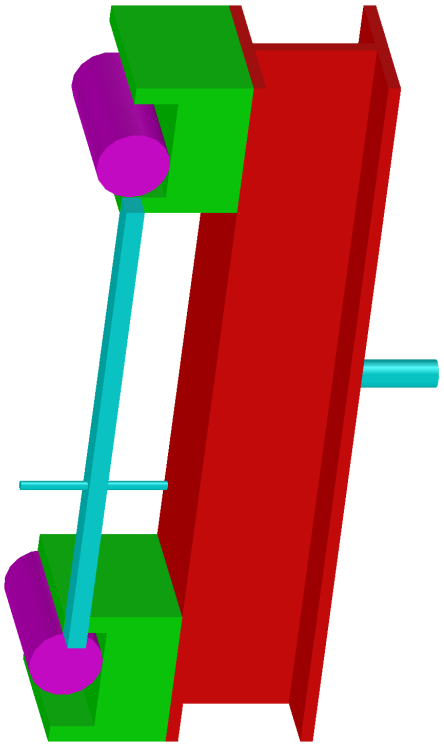

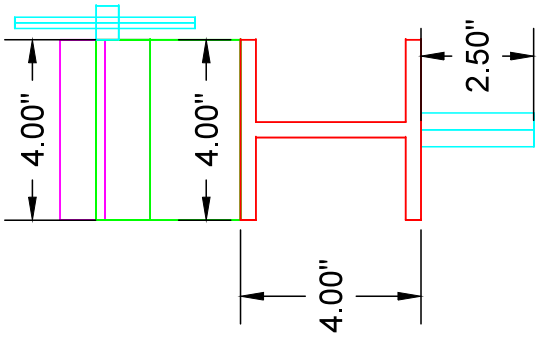
4.00"
4.00"
2.50"
4.00"

Appendix E

UHPC Split Cylinders Experimental Data Sheet

Split Cylinder Length Measurements

Batch	BAI

Specimen	Length A (in)	Length B (in)	Length C (in)	Length D (in)	Diameter D (in)	Diameter D (in)	Diameter D (in)	Average D/2 (in)
S1	7.960	7.970	7.985	7.982	4.002	4.018	3.998	2.003
S2	7.881	7.888	7.892	7.882	4.008	4.019	3.999	2.004
S3	7.987	7.987	7.993	8.018	4.044	4.019	4.002	2.011
S4	7.942	7.941	7.938	7.964	4.012	4.026	4.002	2.007
S5	8.012	8.026	8.010	8.006	3.997	4.019	4.003	2.003

Batch	BAII

Specimen	Length A (in)	Length B (in)	Length C (in)	Length D (in)	Diameter D (in)	Diameter D (in)	Diameter D (in)	Average D/2 (in)
S1	7.950	7.948	7.944	7.967	4.000	4.007	4.015	2.004
S2	7.892	7.895	7.881	7.880	4.012	4.007	4.002	2.004
S3	7.949	7.947	7.951	7.955	4.005	4.004	4.002	2.002
S4	7.950	7.967	7.957	7.952	3.992	4.009	4.004	2.001
S5	7.933	7.919	7.921	7.906	3.973	3.992	3.996	1.994

Batch	BAIV

Specimen	Length A (in)	Length B (in)	Length C (in)	Length D (in)	Diameter D (in)	Diameter D (in)	Diameter D (in)	Average D/2 (in)
S1	7.880	7.874	7.872	7.858	3.997	4.011	4.001	2.002
S2	7.874	7.894	7.872	7.867	4.020	4.010	4.008	2.006
S3	7.950	7.980	7.964	7.966	4.018	4.019	3.998	2.006
S4	7.898	7.915	7.907	7.902	4.035	4.021	4.005	2.010
S5	7.997	7.988	7.985	7.986	4.046	4.025	4.000	2.012

Batch	BAVIII

Specimen	Length A (in)	Length B (in)	Length C (in)	Length D (in)	Diameter D (in)	Diameter D (in)	Diameter D (in)	Average D/2 (in)
S1	7.873	7.859	7.783	7.802	3.982	3.999	4.003	1.997
S2	7.847	7.840	7.842	7.879	3.999	3.999	4.003	2.000
S4	7.862	7.862	7.767	7.791	4.004	4.003	4.001	2.001
S5	7.888	7.887	7.883	7.878	3.998	4.004	4.031	2.006
S6	7.868	7.913	7.919	7.904	4.005	4.004	4.025	2.006

Appendix F

Finite Element Model Analysis of the Confined Fiber Pullout Test Setup

As described in section 9.3, for tests with an external confinement stress applied, the specimens were centered in an engineer's bench vise where the top 25 mm of the specimen's height was in contact with the vise's movable jaws at a width of 50 mm (Fig. 9.3b). Two 44 kN button load cells with an accuracy of 0.2% were used to read the confinement load as the vise was manually tightened using the lever arm.

It is hypothesized that confining the fiber pullout specimens on the top 25 mm by 50 mm will create a uniform compression field in the middle section of the specimens and along the fiber embedment length ($L_e = 6.5$ mm). For this purpose, a finite element analysis of the UHPC specimen was modeled as solid elements assuming a linearly elastic material with modulus of elasticity of 55 GPa and a Poisson's ratio of 0.16 as shown in Fig. F.1. The vise movable steel jaws in contact with the concrete were modeled as solid elements with a modulus of elasticity of 200 GPa and a Poisson's ratio of 0.3 (Fig. F.1) . Perfect bond was assumed between the vise steel blocks and concrete. The boundary conditions were assigned to the concrete FEM nodes on the 4 corners of the specimen as shown in Fig. F.2. A prescribed pressure of 17 MPa is applied to the outside surface of the steel blocks. The simulations were carried out with the Simulia Abaqus software.

The stress contours in the transverse, longitudinal, and vertical directions are shown in Figs. F.3, F.5, and F.4, respectively. The model results confirmed the hypothesis where the transverse stress ($\sigma_x x$) of an element located in the middle section of the specimens where

the fibers are installed was equal to the confinement pressure applied ($\sigma_c = 17$ MPa). A tensile stress field of $0.11\sigma_c = 1.87$ MPa is generated at the same location in the longitudinal direction ($\sigma_z z$). The stresses in the vertical direction are negligible.

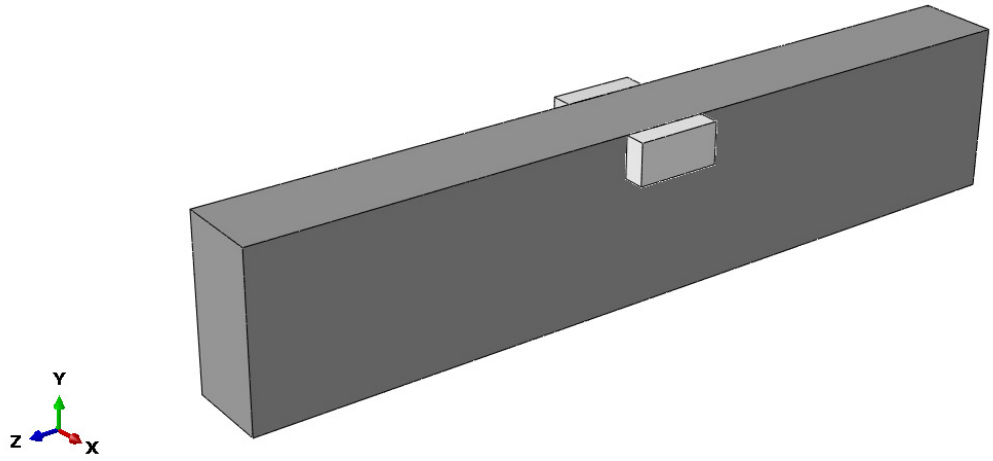

Figure F.1: Confinement fiber pullout specimen model geometry.

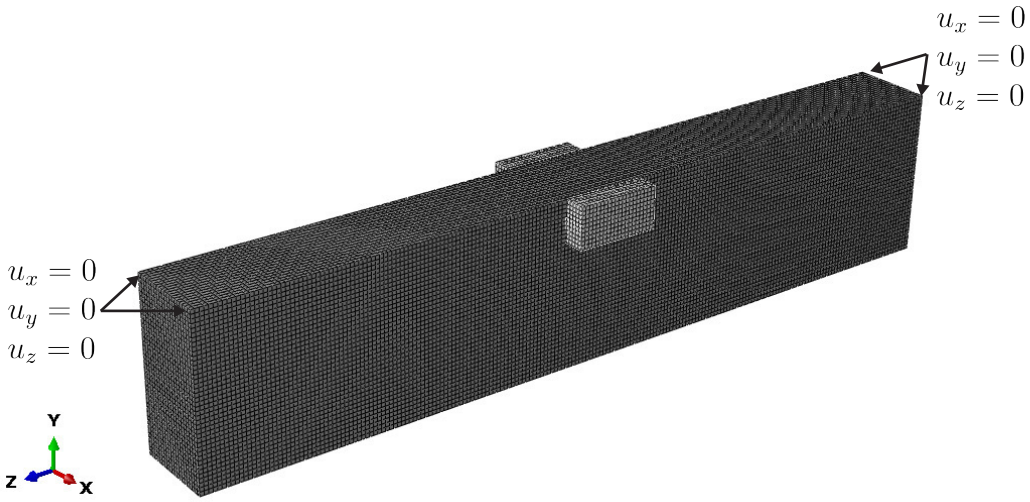

Figure F.2: Confinement fiber pullout specimen model mesh elements.

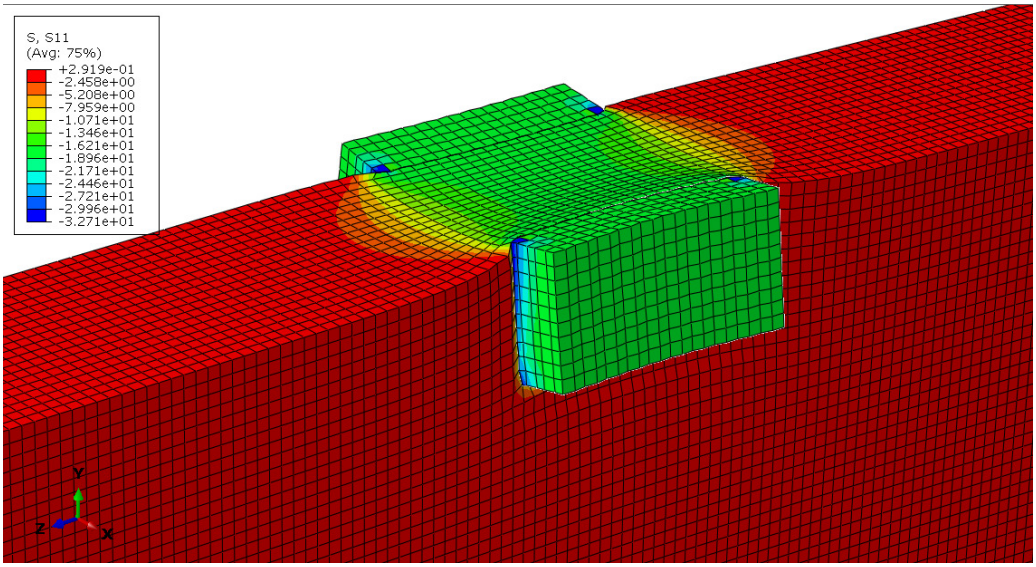

Figure F.3: Stress field along the transverse direction σ_{xx} showing compression stresses in the middle section of the specimen.

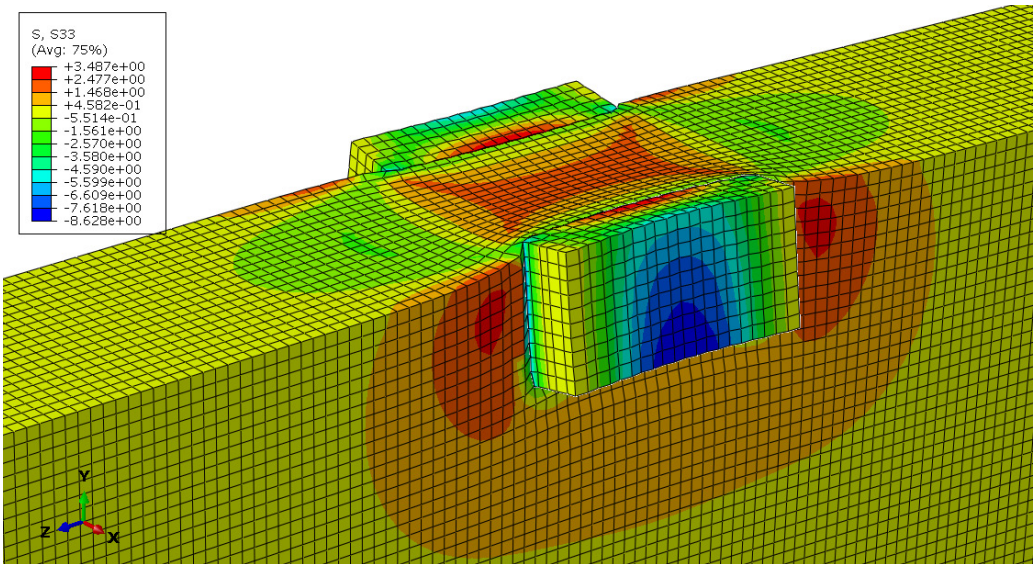

Figure F.4: Stress field along the longitudinal direction σ_{zz} showing tension stresses in the middle section of the specimen.

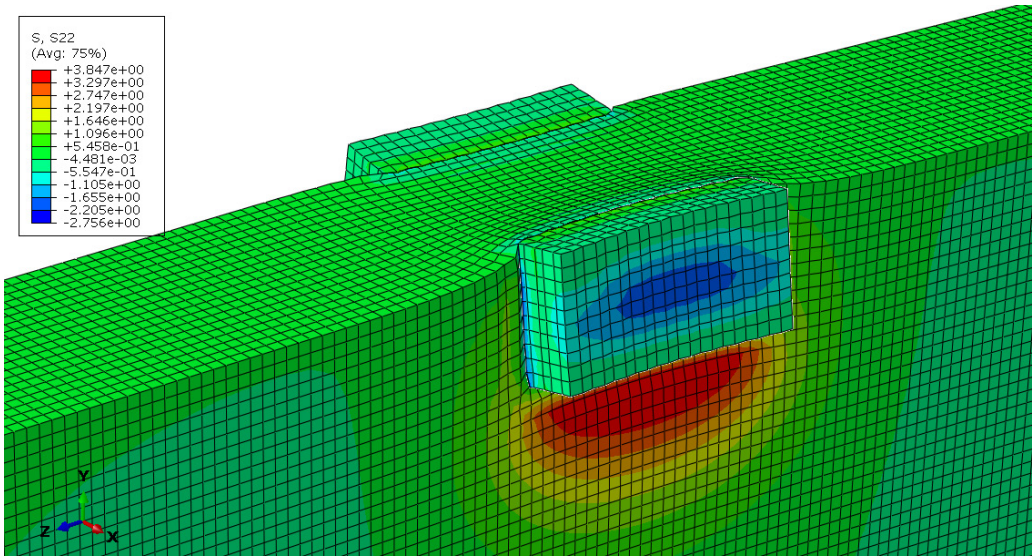

Figure F.5: Stress field along the vertical direction σ_{yy} showing negligible stresses in the middle section of specimen.